

PHASE CONTROL OF THE SPIN-TRIPLET STATE IN S/F/S JOSEPHSON  
JUNCTIONS

By

Eric C. Gingrich

A DISSERTATION

Submitted to  
Michigan State University  
in partial fulfillment of the requirements  
for the degree of

Physics - Doctor of Philosophy

2014

## ABSTRACT

### PHASE CONTROL OF THE SPIN-TRIPLET STATE IN S/F/S JOSEPHSON JUNCTIONS

By

**Eric C. Gingrich**

For decades, the proximity effect in superconductor/ferromagnetic (S/F) hybrid systems was thought to be very short-ranged, with coherence lengths on the order of a nanometer. That changed in 2003 when Bergeret *et al.* suggested systems involving s-wave superconductors and ferromagnets with non-collinear magnetizations could generate spin-triplet supercurrent. This was a significant prediction that radically changed the outlook for these systems, with the possibility of bringing the ferromagnetic coherence length up to ranges similar to the normal metal coherence length. With the experimental confirmation of the spin-triplet state in S/F/S Josephson junctions in 2010, the flood-gates opened into a range of interesting studies.

We have performed measurements on the magnetic and superconducting properties of the multilayer Ni/[Co/Ni]<sub>n</sub>. This arrangement of ferromagnetic materials, when grown with thicknesses of 0.4 nm Ni and 0.2 nm Co, demonstrate a magnetization that lies perpendicular to the plane of the films. Because it will, in the virgin state, possess a non-collinear magnetization with ferromagnets which have magnetizations that lie within the plane, it is a convenient multilayer for the generation of spin-triplet supercurrent. Our measurements of S/F'/F/F'/S Josephson junctions, where F' is a hard ferromagnet and F is the Co/Ni multilayer, confirmed the presence of the spin-triplet state, and demonstrated the viability of the Co/Ni multilayer as a triplet generating ferromagnet.

We have also performed studies on the characteristics of a number of soft ferromagnetic

alloys. These alloys are important for their potential as a soft ferromagnetic switching layer for application in our triplet control devices. To that end, we have created sputtering targets for four different ferromagnetic alloys: Molybdenum-doped Permalloy, Niobium-doped Permalloy, Copper-doped Permalloy, and Palladium Iron. These studies have included: atomic concentration measurements using EDS, magnetic measurements using a commercial MPMS measurement system and GMR, and superconducting studies done by fabricating S/F'/F''/S Josephson junctions with F'' the soft ferromagnet of interest.

Lastly, we have performed measurements to study the relative phase of two S/F'/F''/F''/S Josephson junctions patterned into a Superconducting Quantum Interference Device (SQUID). The phase of the junctions is determined by the relative rotation of the magnetizations through the junction. By applying an external field to the junctions, and utilizing shape anisotropy to control the switching fields, the F'' layer can be switched in a single junction. The switch in the state can be observed by measuring the interference in the current driven through the SQUID, which responds to the relative phase of the two junctions in the loop. These measurements have yielded promising early results for the prospect of controlling the spin-triplet state.

Copyright by  
ERIC C. GINGRICH  
2014

This thesis is dedicated to the memory of  
**Colonel Franklin John Gingrich, Jr., USAF Ret. (1936-2010)**

## ACKNOWLEDGMENTS

A large number of people have played a role in the long development of this work, and I hope that I am not remiss in accounting for anyone.

I would first like to thank my advisor, Professor Norman Birge, for his many years of teaching. Your patience in helping me to learn in my way, and in allowing me to learn from the many, many mistakes that a graduate student will inevitably make, was always greatly appreciated. I could not imagine having a better teacher, advisor, and friend.

I would also like to thank Professor William Pratt, who took me under his wing as a TA in 170 and 451. I may have learned more about low temperature physics and experimental engineering from you in those two courses than in the rest of my time at MSU. Your knowledge and passion for science and engineering are absolutely infectious, and I'm glad to have had an opportunity to see your latest project, the He3 cryostat, in action.

The basement would be a much different place without the tireless efforts of Dr. Reza Loloee, who appears repeatedly in this thesis; particularly in Chapter . Without your help none of our projects would be anywhere near as successful as they are. I will greatly miss our regular morning sports discussions, and I hope you can find someone to talk about them with you on a regular basis. Thank you for all of your help, and for your advice in the writing of this dissertation.

No less critical to our success is Dr. Baokang Bi, who keeps the Cleanroom and its equipment operating. I can't count the number of times I have run into some problem with lithography or some other fabrication step, and every time you were more than willing to take a look and offer your suggestions. I might still be trying to find a solution to the problems with my SQUID bottom leads if you hadn't been there.

I would be remiss not to acknowledge the wonderful companionship and assistance of my many group mates over the years. I owe a debt that can never be repaid to Yixing Wang, Mazin Khasawneh, and Trupti Khaire for their friendship and for mentoring me in the early stages of my career. I'd also like to acknowledge William Martinez, Joseph Glick, Zack DeLand, Patrick Quarterman, Kurt Boden, Kevin Werner, and Andrew Keller for the fun times. I want to also add Rakhi Acharyya and Yen Nguyen to this list. They were not a part of our group, but with how closely we all worked together and helped out with each other's experiments, it often felt like we were.

A couple group mates deserve a little extra recognition for helping to make significant contributions to this work. The early work on characterizing our soft ferromagnets was performed by Simon Diesch, a visiting student from the University of Konstanz. The few months we got to spend as roommates were not nearly enough, and I dearly hope I get a chance to visit with him again in the future. Later work on the soft ferromagnet characterization was performed by Bethany Niedzielski. We would have been overwhelmed without her help. We asked a lot of her, and she proved equal to the task. Finally, Alex Cramer put a lot of hard work into improving our Co/Ni multilayers. Of course, he'll probably spend the rest of his life trying to get those multiplexers of his to work.

I have gotten to know a huge group of wonderful people that have studied in the physics department - Charles Kuehn, Steve Wolf, Steve DeCamp, Kevin Berry, Sean Wagner, Josh Veazey, Sanela Lampa-Pastirk, Megan Romanowich, Kiseok Chang, Kritsada Kittimanapun, and Ian Dayton. You have all made the basement a brighter place, and I greatly enjoyed the times we got to spend together at Michigan State.

I want to thank my family, particularly my Mother and Father, for their encouragement and support. I would never have been able to do this without you. Being the first Ph.D. in

the family is something I hope inspires others to follow in my footsteps. I also want to thank my close friends Jay Parry, Jordan Page, and Sayak Mukherjee. It has always been nice to have a base of the old friends to come back to once in a while. I hope there are many, many more Ohio State Basketball games in our future.

A number of years ago, in preparation for writing this thesis, I joined a blog run by Jeff Seeman to work on my writing. I wanted to thank him for the opportunity to express my opinions on my favorite team. I also wanted to thank all of the friends I've met over the years at that site, particularly Chuck Strawn, Joseph Dexter, and Ken Kohl. Ken deserves a little extra thanks for covering the Basketball team so I could keep writing this dissertation, and then for volunteering on his own to read it.

I would lastly like to thank Malcolm Reynolds, Inara Serra, Jayne Cobb....I'm out of space? Oh, I suppose I'll stop there then.

Thank you, each and everyone one of you, for making all of this possible.

# TABLE OF CONTENTS

<b>LIST OF TABLES</b> . . . . .	<b>xii</b>
<b>LIST OF FIGURES</b> . . . . .	<b>xiii</b>
<b>Chapter 1 Introduction</b> . . . . .	<b>1</b>
1.1 This Work . . . . .	7
<b>Chapter 2 Theory</b> . . . . .	<b>10</b>
2.1 Ferromagnetism . . . . .	10
2.1.1 Demagnetizing Field . . . . .	11
2.1.2 Anisotropy . . . . .	13
2.1.2.1 Shape Anisotropy . . . . .	13
2.1.2.2 Magnetocrystalline Anisotropy . . . . .	15
2.1.3 Magnetic Domains . . . . .	16
2.1.4 Magnetization . . . . .	18
2.1.5 Stoner-Wohlfarth Switching . . . . .	22
2.2 Superconductivity . . . . .	25
2.2.1 DC Josephson Effect . . . . .	26
2.2.2 Resistively and Capacitively Shunted Junction (RCSJ) Model . . . . .	27
2.2.3 Overdamped Junctions . . . . .	31
2.2.4 Magnetic Behavior . . . . .	32
2.2.5 Proximity Effect in S/N and S/F Systems . . . . .	36
2.2.6 Origin of Long Range Triplet Component (LRTC) . . . . .	41
2.2.7 Spin-Triplet Phase . . . . .	44
2.3 SQUIDs . . . . .	46
2.3.1 DC SQUID . . . . .	47
<b>Chapter 3 Experimental Equipment</b> . . . . .	<b>52</b>
3.1 Introduction . . . . .	52
3.2 Metal Deposition . . . . .	52
3.2.1 Thermal Evaporation . . . . .	53
3.2.1.1 Design . . . . .	54
3.2.1.2 Procedure . . . . .	56
3.2.2 Sputtering . . . . .	58
3.2.2.1 Principle . . . . .	58
3.2.2.2 Design . . . . .	60
3.2.2.3 Procedure . . . . .	65
3.2.3 Ion Mill . . . . .	73
3.2.3.1 Design . . . . .	76

3.2.3.2	Procedure . . . . .	77
3.3	Microscopy . . . . .	80
3.3.1	Scanning Electron Microscopy . . . . .	80
3.3.1.1	Design . . . . .	84
3.3.2	Atomic Force Microscopy . . . . .	85
3.4	Lithography . . . . .	88
3.4.1	Optical Lithography . . . . .	89
3.4.1.1	Procedure . . . . .	90
3.4.2	Electron Beam Lithography . . . . .	93
3.4.2.1	Pattern Creation and Control . . . . .	94
3.4.2.2	Procedure . . . . .	97
3.5	Measurement . . . . .	101
3.5.1	SQUID Current Comparator . . . . .	101
3.5.1.1	Measurement Setup . . . . .	105
3.5.1.2	Procedure . . . . .	106
3.5.2	SQUID Magnetometer . . . . .	109
3.5.2.1	Procedure . . . . .	110
<b>Chapter 4 Sample Fabrication . . . . .</b>		<b>113</b>
4.1	Photolithographic Pillars . . . . .	113
4.1.1	Substrates and Cleaning . . . . .	115
4.1.2	Bottom Layer Sputtering . . . . .	116
4.1.3	Photolithographic Definition of Pillars . . . . .	116
4.1.4	Ion Milling and Silicon Monoxide Deposition . . . . .	118
4.1.5	Liftoff . . . . .	119
4.1.6	Top Lead Sputter . . . . .	120
4.2	Electron-Beam Lithographic Pillars . . . . .	120
4.2.1	Substrates and Cleaning . . . . .	121
4.2.2	Photolithographic Definition of Base Multilayer . . . . .	121
4.2.3	Sputter and Liftoff . . . . .	124
4.2.4	EBL Definition of Pillars . . . . .	125
4.2.5	Aluminum Evaporation . . . . .	128
4.2.6	Ion Mill and Silicon Oxide Deposition . . . . .	129
4.2.7	Side Milling . . . . .	130
4.2.8	Aluminum Etch . . . . .	132
4.2.9	Top Lead Ion Mill Cleaning and Sputter . . . . .	132
4.3	SQUID Samples . . . . .	133
4.3.1	Photolithographic Definition of Bottom Leads . . . . .	134
4.3.2	O <sub>2</sub> Plasma Etch . . . . .	135
4.3.3	Sputtering, and E-Beam Lithography . . . . .	136
4.3.4	Aluminum Evaporation . . . . .	137
4.3.5	Milling and Etching . . . . .	137
4.3.6	Top Lead Photolithography and Sputtering . . . . .	138
4.3.7	Negative E-Beam Resist . . . . .	140

<b>Chapter 5</b>	<b>Characterization of Co/Ni Multilayers</b>	<b>144</b>
5.1	The Co/Ru/Co Trilayer	144
5.2	The Co/Ni Multilayer	146
5.3	Samples	148
5.4	Magnetization Measurements	149
5.5	Field Dependent Measurement of Critical Currents	156
5.5.1	Samples Without F'	159
5.5.2	Samples With F'	167
5.6	Viability of the Co/Ni Multilayer	172
5.7	Multilayer Improvement	173
<b>Chapter 6</b>	<b>Characterization of Soft Ferromagnets</b>	<b>177</b>
6.1	Targets	179
6.2	Molybdenum-doped Permalloy	182
6.3	Copper-doped Permalloy	187
6.4	Niobium-doped Permalloy	188
6.5	Palladium Iron	197
6.6	Conclusion	202
<b>Chapter 7</b>	<b>Phase Sensitive Measurements</b>	<b>204</b>
7.1	Spin-Triplet Phase	206
7.2	Phase Measurement Strategy	208
7.3	First Measurements	216
7.4	Flux Trapping	220
7.5	Smaller Junctions	222
7.6	Co/Ru/Co Central Ferromagnet	227
7.7	Full Milling	232
7.8	Conclusion	235
<b>Chapter 8</b>	<b>Outlook</b>	<b>238</b>
8.1	Summary of Results	238
8.2	Future Work	242
<b>Appendix</b>		<b>246</b>
<b>BIBLIOGRAPHY</b>		<b>271</b>

## LIST OF TABLES

Table 3.1	List of thermally evaporated materials and deposition rates, used in this work. . . . .	57
Table 3.2	List of sputtered materials and deposition rates for 2.25 inch guns. .	70
Table 3.3	List of sputtered materials and deposition rates for 1 inch guns. . . .	72
Table 3.4	Values for converting material thickness to an equivalent thickness of Gold. . . . .	77
Table 3.5	Operating parameters for each ion mill. . . . .	79
Table 3.6	A list of the key resistors on each of the two SQUID-based Quick Dippers. . . . .	104
Table 5.1	List of singlet decay lengths in Co and Ni from Khasawneh <i>et al</i> [73] and Robinson <i>et al</i> [74]. . . . .	165
Table 5.2	Comparison of data from S/F'/F/F'/S samples in the virgin state and after being magnetized to .32T. . . . .	170
Table A.1	List of thin film Sb <sub>2</sub> Te <sub>3</sub> sample properties. . . . .	259

## LIST OF FIGURES

Figure 2.1	Diagrammatic demonstration of the formation of domains. . . . .	17
Figure 2.2	Diagram of the process of magnetizing a ferromagnetic material in an external field. . . . .	19
Figure 2.3	Diagrams of magnetic hysteresis in the easy and hard axes. . . . .	21
Figure 2.4	Setup for the Stoner-Wohlfarth problem. . . . .	22
Figure 2.5	Resistively and Capacitively Shunted Junction (RCSJ) model circuit.	28
Figure 2.6	The tilted washboard potential model. . . . .	30
Figure 2.7	Current-Voltage relation for an overdamped Josephson junction. . .	31
Figure 2.8	Diagram of a Josephson junction with a square cross-section. . . . .	32
Figure 2.9	Diagram of a Josephson junction with a circular cross-section. . . .	35
Figure 2.10	Fraunhofer and Airy Patterns. . . . .	36
Figure 2.11	Diagram of normal and inverse Andreev reflection. . . . .	38
Figure 2.12	Dispersion Relations for a: A) normal metal, and B) idealized ferromagnet. . . . .	39
Figure 2.13	A schematic diagram of the Pair correlation function $F$ in both the: A) Normal Metal, and B) Ferromagnet. . . . .	41
Figure 2.14	The spin-triplet generating system proposed by Bergeret, Volkov, and Efetov in 2003. . . . .	42
Figure 2.15	The geometry proposed by Houzet and Buzdin. . . . .	42

Figure 2.16	A superconducting material adjacent to two ferromagnets with non-collinear Magnetization, similar to the geometry proposed by Houzet and Buzdin. . . . .	43
Figure 2.17	The origin of phase in spin-triplet generating systems. . . . .	45
Figure 2.18	DC SQUID Geometry. . . . .	48
Figure 2.19	Predicted Curves for DC SQUID Output. . . . .	51
Figure 3.1	The Edwards Auto306 Evaporator. . . . .	54
Figure 3.2	The main chamber of the Sputtering System showing all seven guns and the small ion mill. . . . .	61
Figure 3.3	The sputtering system SPAMA plate. . . . .	62
Figure 3.4	Top view of a DC Triode Magnetron Gun. . . . .	63
Figure 3.5	Side view of a DC Magnetron Gun. . . . .	64
Figure 3.6	Images of the sputtering sample holders. . . . .	66
Figure 3.7	Diagram of an Ion Mill with its circuit diagram. . . . .	74
Figure 3.8	Top view of the inside of the ion mill chamber. . . . .	75
Figure 3.9	Diagram of the guts of an SEM. . . . .	82
Figure 3.10	A picture of the Hitachi S-4700II SEM. . . . .	84
Figure 3.11	A picture of the Dimension AFM. . . . .	87
Figure 3.12	The ABM Mask Aligner. . . . .	90
Figure 3.13	The JEOL 840A. . . . .	93
Figure 3.14	SEM images of 10 $\mu\text{m}$ diameter pinwheels after evaporation of Ti and Au, following liftoff. . . . .	96

Figure 3.15	A picture of a written SEM pattern imaged at 2k magnification showing the versatility of electron beam lithography. . . . .	101
Figure 3.16	Diagram of pseudo-four terminal measurement arrangement. . . . .	102
Figure 3.17	Diagram of the Current Comparator Circuit. . . . .	103
Figure 3.18	Diagram of the sample measurement scheme. . . . .	105
Figure 3.19	Diagram of the SQUID Magnetometer. . . . .	110
Figure 4.1	Cartoon of the sample fabrication procedure using Optical Lithography.	114
Figure 4.2	Images of photolithographic pillars. . . . .	117
Figure 4.3	Cartoon of the sample fabrication procedure using Electron Beam Lithography. . . . .	122
Figure 4.4	Cartoon of the sample fabrication procedure using Electron Beam Lithography continued. . . . .	123
Figure 4.5	Optical image of sample 2120 4A-2, a 4 $\mu\text{m}$ by 2 $\mu\text{m}$ Elliptical Pillar defined by Electron Beam Lithography. . . . .	128
Figure 4.6	Images of a 4 $\mu\text{m}$ by 2 $\mu\text{m}$ aluminum pillar after liftoff. . . . .	129
Figure 4.7	Images of the Aluminum Etch process. . . . .	131
Figure 4.8	Optical Image of a SQUID sample after Electron Beam patterning. . . . .	135
Figure 4.9	Aluminum pillar growth compared to the deposition rate. . . . .	137
Figure 4.10	A completed pair of SQUIDs, after top leads have been sputtered on and liftoff has been finished. . . . .	139
Figure 4.11	The benefits of Plasma Etching. . . . .	140
Figure 4.12	Cartoon of the sample fabrication procedure using Optical Lithography.	142
Figure 5.1	Magnetization curves of the 0.4/0.6 Co/Ni Multilayers. . . . .	151

Figure 5.2	Magnetization curves of the 0.4/0.8 Co/Ni Multilayers. . . . .	152
Figure 5.3	Magnetization curves of the 0.2/0.4 Co/Ni Multilayers. . . . .	153
Figure 5.4	More magnetization curves of 0.2/0.4 Co/Ni Multilayers. . . . .	155
Figure 5.5	High field magnetization measurements of the n=10 0.2/0.4 Co/Ni multilayer. . . . .	156
Figure 5.6	Example of an $I-V$ Curve and a Fraunhofer Pattern. . . . .	158
Figure 5.7	Fraunhofer patterns measured in Josephson junctions with the 0.4/0.6 Co/Ni multilayer. . . . .	160
Figure 5.8	Fraunhofer patterns measured in Josephson junctions with the 0.2/0.4 Co/Ni multilayer. . . . .	162
Figure 5.9	Fraunhofer patterns measured in Josephson junctions with the 0.2/0.4 Co/Ni multilayer. . . . .	164
Figure 5.10	Semi-log plot of $I_c R_N$ product for samples without F'. . . . .	165
Figure 5.11	Fraunhofer patterns measured in Josephson junctions with the 0.2/0.4 Co/Ni multilayer as well as two 1.2 nm Ni F' layers. . . . .	168
Figure 5.12	Semi-log plot of $I_c R_N$ product versus the thickness of the central ferromagnetic layer. . . . .	169
Figure 5.13	Plots of a 0.3/0.4 Co/Ni multilayer grown directly on 20 nm Pt. . .	175
Figure 6.1	A diagram of the structure of a target modified by Reza Loloee for alloy sputtering. . . . .	181
Figure 6.2	A diagram of the Molybdenum-doped Permalloy target fashioned by Reza Loloee. . . . .	183
Figure 6.3	Data from 10 $\mu\text{m}$ and 20 $\mu\text{m}$ Josephson junction pillars with Molybdenum-doped Permalloy as both the F' and F'' layers. . . . .	184
Figure 6.4	Measurements of 7 percent (Green curve), and 14 percent (Blue curve), Molybdenum-doped Permalloy. . . . .	185

Figure 6.5	Measurement of the change in magnetic behavior of 14 percent Molybdenum-doped Permalloy while changing the Iron content of the Permalloy. . . . .	186
Figure 6.6	A diagram of the Copper-doped Permalloy target fabricated for this experiment. . . . .	188
Figure 6.7	A diagram of the target created for Niobium-doped Permalloy sputtering. . . . .	189
Figure 6.8	Plot of the atomic measured atomic concentration of Nb in NbPy films versus the number of Nb plugs used in the target. . . . .	190
Figure 6.9	Hysteresis curve from a 3mm x 3mm NbPy film 500 thick. . . . .	190
Figure 6.10	Diagrammatic demonstration of Giant Magnetoresistance. . . . .	192
Figure 6.11	Geometry of large scale samples used for Giant Magnetoresistance (GMR) measurements. . . . .	193
Figure 6.12	Giant Magnetoresistance data from a Single Exchange-Biased Spin Valve with 3 nm NbPy as the switching layer, and 24 nm Py as the polarizer. . . . .	194
Figure 6.13	Giant Magnetoresistance data from a Single Exchange-Biased Spin Valve with 3 nm NbPy as the top ferromagnetic layer, and 10 nm of Copper for the spacer layers. . . . .	195
Figure 6.14	Giant Magnetoresistance data from a Single Exchange-Biased Spin Valve with 3 nm NbPy as the free layer, and 10 nm of Copper for the spacer layers. . . . .	196
Figure 6.15	Plot of the critical current versus NbPy thickness in an S/F'/F/F''/S Josephson junction with F'=Ni, F=Co/Ru/Co, and F''=NbPy, in pillar sizes ranging from 3 to 12 $\mu\text{m}$ . . . . .	196
Figure 6.16	Plot of the critical current versus PdFe thickness in an S/F'/F/F''/S Josephson junction with F'=Ni, F the Co/Ni multilayer, F''=PdFe, in pillar sizes of 10 and 20 $\mu\text{m}$ . . . . .	198
Figure 6.17	Plot of the critical current versus PdFe thickness in an S/F'/F/F''/S Josephson junction with F'=Ni, F=Co/Ru/Co, F''=PdFe, in pillar sizes of 3, 6, and 12 $\mu\text{m}$ . . . . .	199

Figure 6.18	Giant Magnetoresistance data from a 1 mm <sup>2</sup> SEBSV with 24 nm PdFe, and an 8 nm Py polarizer pinned by 8 nm FeMn. . . . .	199
Figure 6.19	Giant Magnetoresistance data from 0.25 μm <sup>2</sup> elliptical pillars with PdFe as the switching layer. . . . .	201
Figure 7.1	A diagram of a Josephson junction designed to switch between the Singlet and Triplet states. . . . .	205
Figure 7.2	A diagram of a Josephson junction designed to switch between the 0 and π phase states of the triplet supercurrent. . . . .	207
Figure 7.3	A diagram presenting two different methods of controlling a Josephson junction. . . . .	209
Figure 7.4	A diagram of the Josephson junctions in their initial configuration. . . . .	214
Figure 7.5	A diagram of the Josephson junctions when one of the two junctions has switched. . . . .	215
Figure 7.6	The first measurement of our SQUID design. . . . .	217
Figure 7.7	The first measurement of our SQUID design with a maximum at zero flux. . . . .	218
Figure 7.8	Measurements of $I_c$ vs. $I_\Phi$ for the 1 μm <sup>2</sup> SQUID. . . . .	219
Figure 7.9	A measurement of a SQUID to positive field from 0 to 25 mT. . . . .	222
Figure 7.10	A plot of the behavior of the SQUID in positive fields with 12 nm PdFe for the top ferromagnet. . . . .	223
Figure 7.11	The same SQUID as Figure 7.10 measured to negative fields from 0 to -25 mT. . . . .	224
Figure 7.12	A plot of the repeated measurement of the SQUID to positive fields, again up from 0 to 25 mT. . . . .	225
Figure 7.13	A plot of critical current through a SQUID containing Josephson junctions with a Co/Ru/Co central ferromagnet. . . . .	229

Figure 7.14	A plot of critical current through the same SQUID shown in Figure 7.13. . . . .	230
Figure 7.15	A plot of the second measurement of positive fields of the SQUID plotted in Figure 7.13. . . . .	231
Figure 7.16	Plot of critical current against external field and flux field for a SQUID that has had all 3 ferromagnets patterned. . . . .	234
Figure A.1	The behavior of Landau levels as the magnetic field is increased. . .	251
Figure A.2	Resistivities of samples fabricated by Ctirad Uher's group at the University of Michigan. . . . .	254
Figure A.3	Geometry of the hall bar measurements of our semi-metal materials.	255
Figure A.4	Longitudinal Resistances for thin film $Sb_2Te_3$ samples. . . . .	256
Figure A.5	Hall Resistances for thin film $Sb_2Te_3$ samples. . . . .	257
Figure A.6	Plot of the derivative of Resistivity with respect to field against inverse field for sample 20100717. . . . .	260
Figure A.7	Raw data from sample 20100717 taken at the National High Magnetic Field Laboratory. . . . .	261
Figure A.8	Plot of the Temperature dependence of hall resistance plotted against inverse field for sample 20100717. . . . .	262
Figure A.9	Angular dependence measurements for sample 20100717. . . . .	263
Figure A.10	Analysis of the angular dependence of the amplitude of a peak in the oscillations of sample 20100717. . . . .	264
Figure A.11	Determination of effective mass of carriers in sample 201007177. . .	265
Figure A.12	Raw longitudinal resistance of a bulk sample of $Sb_2Te_3$ . . . . .	266
Figure A.13	Temperature dependence of longitudinal resistance of a bulk $Sb_2Te_3$ sample. . . . .	267

Figure A.14 Determination of the effective mass of carriers in a bulk  $\text{Sb}_2\text{Te}_3$  sample. 267

Figure A.15 Angular dependence of resistance in a bulk  $\text{Sb}_2\text{Te}_3$  sample. . . . . 268

# Chapter 1

## Introduction

Since 1911, when Heike Kamerlingh Onnes discovered the zero resistance state in samples of Mercury [1], superconductivity has fired the imagination of scientists hoping to unlock its secrets and develop it into a mature and useful field of study. However, it was not until 1957 that an accurate theoretical model of the effect came into being. Bardeen, Cooper, and Shrieffer, building on earlier work from Fröhlich [2] and Cooper [3], developed a theory that appropriately accounted for the many superconducting properties that had been observed over the years, including the zero resistance state, the Meissner effect, and others [4]. This BCS theory, as it came to be known, set the stage for a rapid development in our understanding of the superconducting state.

However, BCS theory deals only with s-wave superconductivity. This was not a limitation, as that was the only form of the superconducting state that had ever been observed, a fact which remained true for many years after the theory's development. However, in 1986, Bednorz and Muller discovered the first high  $T_c$  superconductor in the cuprates [5]. Further research into the cuprates, such as Scalapino (1995) [6], and Tsuei *et al.* (2000) [7], among others, has suggested that the pairing in these systems may include a mixture of s- and d-wave superconducting states. Both of these states possess a spin-singlet wave state, but this opened the possibility of other unique variations of superconductivity, and drove a renewed interest in the field.

It was well known that there is a symmetry to the superconducting wavefunction. Under exchange of the two electrons in the Cooper pair, particles that are identical, the superconducting wavefunction must be odd. In s-wave and d-wave superconductors the momentum term of the wavefunction is even. These states then obtain the necessary odd symmetry from an odd spin state, which is satisfied by the spin-singlet.

Much more recently, another superconducting state was discovered, this time in Strontium Ruthenate,  $\text{Sr}_2\text{RuO}_4$  [8]. This state possesses a p-wave characteristic, which means that it has an odd symmetry in momentum. This allows the spin state to exist in the *spin-triplet* configuration, which is even in spin. That the spin-triplet state had not been observed in superconductivity before is simply because it is much easier to produce an odd symmetry in spin than in any other component of the wavefunction.

But are there other ways for the superconducting wavefunction to be odd? Work done by Berezinskii in 1975 predicted another possibility [9]. In attempting to explain the superfluidity effect in liquid He3, Berezinskii suggested that the bound state in He3 be odd under time-reversal (e.g. odd in frequency). This turned out not to be the correct explanation for He3, which happens to be a p-wave spin-triplet state. However, his theory found new life in superconducting systems.

In 2001, and later in 2003, Bergeret *et al.* suggested that a system of s-wave superconductors could generate spin-triplet pair correlations in the presence of a strong exchange field [10, 11]. In these systems, a series of ferromagnetic materials with magnetizations pointing non-collinear to each other could form this s-wave spin-triplet state, often referred to as *odd triplet correlations*.

This was a critical theoretical prediction. Until this point, studies involving the interplay of superconductors and ferromagnets focused on the rapid destruction of the superconducting

state at the interface of a superconductor/ferromagnet (S/F) junction. This was because the exchange energy in the ferromagnet forces the two electrons of a spin-singlet pair into different spin-bands at different momenta. This imposes a phase gradient on the pair wavefunction that causes oscillations in both the critical temperature and critical current, and causes a much more rapid suppression of supercurrent than seen in superconductor/normal (S/N) metal junctions [12].

However, the two electrons in the spin-triplet pair can possess the same spin state. This means that, when this state emerges in these systems, the spins will enter the same spin band in the ferromagnet, and at the same momentum. Therefore, with no momentum difference, no phase gradient is imposed on the state, and the pair correlation can propagate unimpeded by the exchange energy. Because of this, the spin-triplet states with electrons in identical spin states are referred to as *long range triplet correlations*.

Experimental confirmation of this theory proved particularly elusive. Work done in the late 1990s by several groups suggested the possibility of a long range proximity effect in S/F systems. Giroud *et al.* in 1998 performed transport experiments on Co wires in good contact with superconducting Al, and observed a much longer decay length than was expected [13]. Lawrence *et al.* (1999) looked at a similar system using a 40 nm wide Ni wire connected to Sn superconducting contacts, and saw an unexpectedly long proximity effect length [14]. Lastly, Petrashov *et al.* (1999) observed a proximity-induced conductance in the ferromagnetic material that was a factor of two larger than it should have been in 100 nm wide Ni bars, using Al as the superconducting material [15]. None of these works were able to explain what they were seeing, and it remains only suggestive that they might have been observing the spin-triplet state.

Another work performed in 2006 by Keizer *et al.* also suggested signs of the spin-triplet

state [16]. They performed measurements of Josephson junctions formed using NbTiN as the superconductor, and a film composed of the half-metallic material CrO<sub>2</sub>. The half-metallic material is considered a fully spin-polarized magnetic material, meaning that the material is conducting for electrons pointing in the direction of its magnetization, while it is insulating for anti-aligned electrons. This material should therefore strongly suppress supercurrent, as one half of each electron pair would not be able to enter the material. However, Keizer observed a significant supercurrent in these materials, which was a reasonable indication of triplet supercurrent. Unfortunately, the work was not readily reproduced due to complications with the growth of CrO<sub>2</sub>.

More recently a number of groups, including our own, succeeded in confirming the presence of the spin-triplet state arising from s-wave superconductors. Sprungmann *et al.* (2010) created Josephson junctions using the ferromagnetic Heusler alloy Cu<sub>2</sub>MnAl, along with Nb superconductors and an AlO<sub>x</sub> insulating barrier. They were able to observe an enhancement in the critical current when they annealed their samples at 240 °C, which changed the magnetic behavior of the Heusler layer [17]. Robinson *et al.* performed measurements of Josephson junctions using Nb for their superconductors, Co as a central ferromagnet, and Holmium on either side of the Co. Because of the spiral magnetic ordering of the Holmium, they achieved a non-collinear magnetization, and saw a longer range decay in critical current than expected for a standard Co Josephson junction [18]. Lastly, Anwar *et al.* performed measurements on CrO<sub>2</sub> similar to the work by Keizer [19].

Our own group performed experiments on Josephson junction pillars using Nb as the superconducting material, and a synthetic anti-ferromagnetic (SAF) as the central ferromagnet. A SAF is a pair of ferromagnetic materials separated by a normal metal buffer. When the buffer is at a critical thickness, the magnetizations of the two ferromagnets will

lock into an anti-aligned configuration. By adding an additional magnetic layer above and below the SAF we were able to observe the difference of critical current carried through samples with and without the extra magnetic layers [20]. This geometry had been predicted to produce triplet supercurrent by Houzet *et al.* in 2007 [21].

However, this is not the end of the story. While the effect has been observed indirectly, by comparing similar samples both with and without ferromagnets, there are many more interesting experiments that should be done. In particular, a single sample fabricated with three different ferromagnetic materials could be used to control the state of the spin-triplet junction. By changing the magnetic alignment, one could conceivably switch between singlet and triplet generating configurations. Or, based on the Houzet paper, it should be possible to change the phase state of the junction, which could be measured with a phase sensitive method.

While control is interesting from a scientific perspective, it is potentially even more interesting from an applications stand-point as well. Today's society depends on large-scale computing farms to store and retrieve vast quantities of information. These farms require immense cost to operate, requiring air conditioning systems and low temperatures to aid in cooling, and large power requirements to operate. Eliminating the heat released from these systems reduces both losses from the systems themselves, and the required energy to keep built up heat from rapidly spiraling out of control [22].

The goal is to build an entire super-computer of superconducting materials and contacts. This would allow for a system to be entirely plunged in Liquid He4. Because all aspects of the computer are constructed of superconducting parts, there are no resistive wires to communicate between the processor and the memory or hard-drive. All processes would be performed among devices with a minimum of necessary resistance. This reduces the cooling

costs, reduces the amount of heat produced, and reduces the amount of power required to run the device.

Such a computer requires an entire new family of logic, and memory, devices. The logic devices themselves are outside the purview of this thesis and we will not discuss them in detail here. However, the methods include “Single Flux Quantum” (SFQ), “Rapid Single Flux Quantum” (RSFQ), and “Reciprocal Quantum Logic” (RQL) logic families. These are a significant and active area of modern research, in both academia and in the private sector, and a wide body of knowledge is available on the subjects. The reader is directed to the referenced works for more detail [23, 24, 25].

Memory devices involving superconducting materials have a number of different possible sources. One of those is from the field of *Spintronics*. Spintronics, short for Spin Electronics, is an emerging method of information storage and exchange. Like its name suggests, instead of only carrying charge current as in typical electronics, spintronic devices also carry spin currents. This provides another degree of freedom in the control and transmission of information. By taking advantage of the properties of spin polarized currents, and their behavior in systems containing ferromagnetic materials, it is theoretically possible to both control and read the states of the spin current. There are a large amount of research into devices utilizing the spin current for memory applications, which is typically called “Magnetic Random Access Memory” or MRAM [26, 27, 28]. One such application that is already commercially available has been designed and marketed by Everspin Technologies [29].

There is another method of constructing memory bits which uses some of the same concepts as MRAM technology, but utilizes superconducting materials to reduce heat losses. Josephson Magnetic Random Access Memory (JMRAM), developed by employees of Northrop Grumman Corporation, depends on the phase of the current passing through a Josephson

junction instead of using the spin of the current to dictate the transfer and storage of information [30]. Theoretically, it is possible to control the phase in both spin-singlet and spin-triplet S/F/S Josephson junctions, and recent work has shown some indications of control in singlet devices [31].

## 1.1 This Work

The control of the spin-triplet state can be achieved through two different methods. One option is to switch between the singlet and triplet states of the junction, the “on/off” method. The other method to switch between the 0 and  $\pi$  phase states of the junction. We will use a pair of Josephson junctions and measure the interference between them with a Superconducting Quantum Interference Device (SQUID). The interference is generated by changing the phase state of the junction in relation to each other, between the 0 and  $\pi$  states. This is achieved in junctions with an S/F'/F/F''/S structure, where S is a superconductor, F' is a hard ferromagnet, F'' is a soft ferromagnet, and F is a hard ferromagnetic multilayer that arranges its magnetization orthogonally to the outer F' and F'' layers.

In the next chapter, we will outline the theory underpinning the work. We will touch on the critical concepts of magnetic materials, namely demagnetizing factors, magnetocrystalline anisotropy, and Stoner-Wohlfarth theory. We will also cover the aspects of superconducting theory that are necessary in order to understand the working of our samples, such as the proximity effect, the Josephson effect, and the theory of spin-triplet generation. The chapter ends with a discussion of the basics of DC SQUIDS.

Chapter 3 covers the Equipment used during the course of this work, and their procedures of operation. This includes metal deposition systems (thermal evaporation, sputtering),

lithographic methods (optical, electron beam), imaging techniques (SEM, AFM), and our sample measurement systems. This chapter was included primarily for the benefit of future students. It may also be helpful for understanding the methodology of the experiments.

Chapter 4 discusses our sample fabrication methods for the various experiments performed. Because of the development in our studies, each experiment has a slightly different fabrication process. To ensure that all of the details of a given experiment are outlined, and to ensure reproducibility, every step of each process is faithfully recorded.

The first experimental data is presented in Chapter 5, which covers our studies of the  $[\text{Co/Ni}]_n$  multilayer. This multilayer is well known to possess strong perpendicular magnetic anisotropy when the layers of Co and Ni are very thin, on the order of a few angstroms, and in a ratio of 1 to 2 respectively. We studied the magnetic properties of the multilayer in large area ( $1 \text{ mm}^2$ ) films to ensure that we were growing films with a perpendicular magnetization. We also studied the multilayer's superconducting properties in S/F/S, and S/F'/F/F'/S Josephson junctions with Ni as the F' layer, and the Co/Ni multilayer as the F layer to verify the generation of spin-triplet supercurrent.

Chapter 6 covers the studies performed by the group towards characterizing soft ferromagnetic materials. These studies were critical for understanding the properties of the magnets we would be using as the switching layer in our control experiments. We performed studies on a number of ferromagnetic alloys including: Molybdenum-doped Permalloy, Copper-doped Permalloy, Niobium-doped Permalloy, and Palladium Iron.

The magnum opus of this work is detailed in Chapter 7, which covers our experiments towards controlling the spin-triplet superconducting state. We start by outlining our control strategy, utilizing two pillars of different aspect ratios to define the switching fields of the pillars. We then outline the various experiments we have performed on these systems. These

discussions include a large number of changes to the system in order to improve the magnetic behavior of the switching layer.

The appendix covers preliminary experiments performed on semi-metallic samples expected to be common strong Topological Insulators. We studied the magnetic oscillations generated in these materials to attempt to see the predicted two-dimensional conducting surface state of the 3D topological insulator. The goal was to eventually grow ferromagnets and superconductors on the surface of the materials in an attempt to observe Majorana fermions, or other interesting physical phenomena.

# Chapter 2

## Theory

Systems generating spin-triplet supercurrent from s-wave superconductors are unique in physics, combining two types of materials that were long considered an anathema to one another. The first, Ferromagnets, tend to prefer to align the spins of their electrons in a single direction. S-wave superconductors, however, typically have paired electrons with spins that are anti-aligned. Thus, the interaction of the two materials has been occasionally dismissed to no more than a footnote until about thirty years ago.

### 2.1 Ferromagnetism

Ferromagnetic materials have long been known to man. Ferromagnetism was originally discovered in *lodestone*, a naturally magnetized piece of Magnetite (Iron Oxide), which exhibited the unusual property of attracting small pieces of iron at a distance. Over time applications for the material were discovered, such as when it was realized that a needle-shaped piece of magnetite will consistently point towards north (specifically, magnetic north). But despite the interest and mystery surrounding the effects, a rigorous theory continued to elude scientists for centuries. Only with more recent advances in physics was an explanation for the strange behaviors found.

### 2.1.1 Demagnetizing Field

Ferromagnets tend to arrange their magnetic dipoles to lie parallel to each other due to the *exchange interaction*, which is a quantum mechanical result with no classical analog [32]. With the spins pointing in the same direction, they possess a net magnetization. In finite samples, this generates a magnetic field  $\mathbf{H}$  inside the ferromagnet that points directly opposite to the magnetization  $\mathbf{M}$ . This behavior is called the *Demagnetizing Field*, since it directly opposes the magnetization. The existence of this field creates some of the unique properties of ferromagnets.

This field forms because magnetic fields travel from “north” poles to “south” poles of a magnet. When a magnetic material is magnetized, one end assumes the north pole. Outside the material, the lines radiate out and around the magnet. Inside, however, the  $\mathbf{H}$  field travels directly through the magnet, in precisely the opposite direction of the magnetization. This demagnetizing field is proportional to the magnetization that creates it. It is therefore defined as,

$$H_d = -NM, \tag{2.1}$$

where  $N$  is called the *demagnetizing factor*, and is generally a tensor related to the shape of the sample [33, 34].

Typically, for an arbitrary material shape, the demagnetizing factors are too complicated to solve explicitly, and must instead be experimentally measured. However, it turns out that the factors can be derived for ellipsoidal geometries, as the induction inside the material is completely uniform. For these shapes, the demagnetizing tensor is diagonal, and the factors

along the principle axes sum to 1 in SI units,

$$\sum_{j=1}^3 N_j = 1. \quad (2.2)$$

There are several special cases worth mentioning. A sphere possess no directional favorability,  $a = b = c$  with all axes the same length, this results in the demagnetizing factors along each axes being equally one third,

$$N_a = N_b = N_c = \frac{1}{3} \quad (2.3)$$

For an oblate ellipsoid,  $c \neq a = b$  and,  $a/c = r$ , it can be shown that the demagnetizing factor along the short axis is[35],

$$N_c = \frac{r^2}{r^2 - 1} \left( 1 - \sqrt{\frac{1}{r^2 - 1}} \sin^{-1} \frac{\sqrt{r^2 - 1}}{r} \right) \quad (2.4)$$

and along the long axes are,

$$N_a = N_b = \frac{1 - N_c}{2} \quad (2.5)$$

For a disk, where  $c \ll a, b$ , then  $N_c \rightarrow 1$ , while the other two factors become zero. The samples measured in this thesis (see Chapters and ) are similar to oblate spheroids, but meet the condition  $c \ll b < a$ . The form of the demagnetizing factors here are,

$$N_c = 1 - \frac{c}{b} E \quad (2.6)$$

where  $E$  is an elliptical integral that depends on the ratio  $a/b$ , and

$$N_a + N_b = 1 - N_c = \frac{c}{b} E \quad (2.7)$$

This will be discussed in more detail in Chapter 7.

## 2.1.2 Anisotropy

The definition of the word *anisotropy* is “the property of being directionally dependent”. Magnetic anisotropy specifically is a material’s desire to orient its magnetization along a particular direction. Such anisotropy can result from a number of different properties of ferromagnets, such as: material shape, crystalline structure, and stress.

### 2.1.2.1 Shape Anisotropy

Anisotropy due to the shape of the material has its origins in the demagnetizing field [34]. The anisotropy energy can be readily calculated. The internal energy of the system is [33],

$$U_{int} = -\frac{\mu_0}{2} \int \mathbf{M} \cdot \mathbf{H}_d dV, \quad (2.8)$$

where  $H_d$  is the field induced inside the ferromagnet by  $M$ , as discussed in Section 2.1.1. If we assume a uniform magnetization, then this becomes nothing more than a volume integral with a simple solution,

$$U_{int} = -\frac{\mu_0}{2} \mathbf{M} \cdot \mathbf{H}_{int} V. \quad (2.9)$$

Replacing  $H_d$  with Equation 2.1 yields,

$$U_{int} = \frac{\mu_0}{2} N_d M^2 V. \quad (2.10)$$

If we consider an elliptical ferromagnet with axis lengths  $c \ll b < a$ , and with demagnetizing factors  $N_c \gg N_b > N_a$ , then the energy difference due to shape anisotropy between

the two orthogonal directions  $a$  and  $b$  is,

$$U_b - U_a = \frac{\mu_0}{2} (N_b - N_a) M^2 V. \quad (2.11)$$

More generally, for an arbitrary magnetization direction an angle  $\theta$  from the easy axis  $N_a$ ,

$$U(\theta) = \frac{\mu_0}{2} (N_b - N_a) M^2 V \sin^2 \theta. \quad (2.12)$$

This can be written,

$$U(\theta) = K_u V \sin^2 \theta. \quad (2.13)$$

where,

$$K_u = \frac{\mu_0}{2} (N_b - N_a) M^2, \quad (2.14)$$

is the anisotropy parameter, which has units of energy per unit volume.

This implies that the only geometry that possesses no shape anisotropy is a perfectly spherical body, where the demagnetizing factors are identical for all axes. Any deviation from a sphere will lead to a favorability of the magnetization direction. The implications of this are significant. Ferromagnets can be fashioned into shapes that will drive the magnetization into a particular direction. This resulted in the earliest uses of magnetic materials, as lode stones were fashioned into long narrow structures that pinned the magnetization into a very specific direction. It could then be used as a tool to measure the direction of the earth's local magnetic field - the compass.

Shape anisotropy has found more modern usage in magnetic memory technology. By using a variety of shapes, the magnetic states of a thin film of magnetic field can be controlled

by an external field. The field required to drive the magnetization into its opposite direction, the *switching field*  $H_S$ , can then be controlled by careful choice of material shape. This allows for arrays of pillars to be fashioned, and specific elements of the array to be switched reliably.

### 2.1.2.2 Magnetocrystalline Anisotropy

Whereas Shape Anisotropy results from long-range dipolar interactions, Magnetocrystalline anisotropy is primarily a result of spin-orbit coupling[32]. Specifically, the orbital shape and orientation of electronic states can couple to the crystalline electric field. From a Chemistry perspective, this implies that because the orbitals are strongly coupled to the lattice due to bond formation, then any attempt to rotate the spin is resisted. This is a result of the coupling between the spin and orbital components[34]. If both the crystalline electric field and the orbitals are asymmetric, then the spins will tend to align to crystallographic directions. However, if either one of these terms is symmetric, then the spins are capable of aligning in any random orientation.

There are multiple forms of magnetocrystalline anisotropy[34]. For simplicity, we'll discuss uniaxial anisotropy, which is most frequently used as an example in calculations. It is not expected to be a dominant effect in our devices, but could provide enough change to the predicted switching fields to be noticeable.

The energy density of uniaxial crystal anisotropy can be expressed as,

$$u = \frac{U}{V} = \sum_n K_{un} \sin^{2n} \theta, \quad (2.15)$$

where  $K_{un}$  are the anisotropy parameters, with units of energy per unit volume, and  $\theta$  is the angle between the magnetization and the easy axis of the crystal. Typically, only the first

three terms of this expansion are kept,

$$u = K_{u0} + K_{u1} \sin^2 \theta + K_{u2} \sin^4 \theta + \dots \quad (2.16)$$

Additional terms in this sum only become important when  $K_{u1} < 0$ .  $K_{u0}$  does not depend on the directionality of the magnetization, and therefore is unrelated to anisotropy.

### 2.1.3 Magnetic Domains

In ferromagnets, it is possible for the regions of the material to possess magnetizations pointing in different directions. This occurs despite the existence of the exchange energy which seeks to force all of the spins in the material to align in a single direction. These regions of differing magnetization are called *domains*, and are the result of a complicated and delicate balancing act. The key is that there are multiple competing factors at play inside a ferromagnet, and each contributes to domain formation[32].

We have already seen in Section 2.1.2 that there are multiple energy terms within a ferromagnet. The two considered there, the Shape Anisotropy, and the Magnetocrystalline anisotropy, play significant roles in domain formation. Other terms that factor into the effect include magnetostrictive energy and the exchange energy. The balance of all of these energies drives the shapes and behaviors of the domains.

The energy of a magnetic material can be described by Equation 2.8, which describes the field energy internal to the material. It can also be described by the integral of the external field over all space, which is an equivalent expression. Thus, when discussing the minimization of energy in the system, one can consider either minimizing the internal or external terms. This helps explain some of the behavior of the ferromagnetic material.

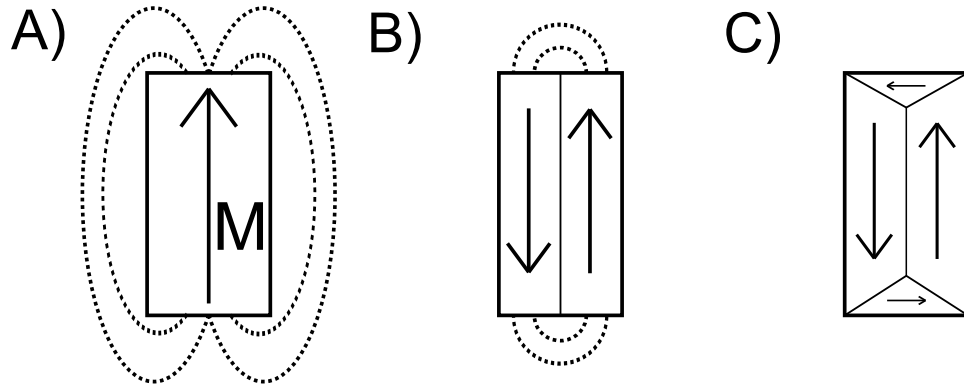


Figure 2.1: *Diagrammatic demonstration of the formation of domains.* A) If the spins in the material are entirely aligned, the exchange energy is minimized. However, a very large magnetostatic energy exists. B) Forming a single domain wall reduces the magnetostatic energy at the cost of a small increase in exchange energy and domain wall energy. C) Some materials can form closure domains, which lowers the magnetostatic energy further at the cost of additional exchange energy. (For interpretation of the references to color in this and all other figures, the reader is referred to the electronic version of this thesis.)

Magnetostatic energy, which is related to shape anisotropy, is the result of the demagnetizing field. If the ferromagnetic material shown in Figure 2.1 possesses a uniform magnetization, the system also has a large demagnetizing field. This creates a large magnetostatic energy term. Even though the sample has a minimum exchange energy, it turns out that the total energy can be reduced by suppressing the magnetostatic energy while simultaneously increasing the exchange energy slightly. This can be done by forming magnetic domains, at the cost of a few interfaces where spins of differing alignment sit next to each other. These interfaces are known as *domain walls*. Figure 2.1 demonstrates the formation of these walls. The domains are formed in such a way that the fringing fields emerging from the magnetic material are minimized. This is a consequence of the equivalence between the internal and external field energies.

The next term is the magnetocrystalline energy, which is related to the magnetocrystalline anisotropy. This drives the ferromagnet to form its domains along the easy axes present within the material. This is because the energy is larger when the spins point along a hard

axis, and smaller when pointing along an easy axis. If there are multiple easy axes, it is possible, and sometimes convenient, for the material to form domains that orient themselves in multiple directions, as in Figure 2.1c. For example, rectangular BCC Iron tends to create *closure domains* at the short edges, where the magnetization points perpendicular to the domains along the long edge. This is done to completely eliminate the magnetostatic energy at no cost in magnetocrystalline energy.

The last term is the magnetostrictive energy, which is the result of the stretching and contracting of a ferromagnet due to its magnetization. This occurs in materials like Iron, which tend to expand slightly along their magnetization direction, and Nickel, which tends to contract along its magnetization. Because the ferromagnet is a single material, these motions induce strain when they compete, increasing the energy of the system.

Between the domains exist the domain walls, which are regions where the spins are rotating between the domain states on either side of the wall. Domain wall size is just as much an energy balancing game as the domain formation itself. Recall that the exchange energy is optimized when the spins are aligned, meaning that the exchange energy favors very wide domain walls with adjacent spin directions very close to being aligned. On the other hand, magnetocrystalline energy is minimized when the spins align to the easy axis. Thus, the magnetocrystalline term favors very narrow domain walls.

#### **2.1.4 Magnetization**

When a ferromagnetic film is exposed to an external magnetic field, the film reacts to align its magnetization to the direction of the field. Figure 2.2 diagrammatically demonstrates the process of this effect. In general, this process follows three different stages that each require more energy than the last. As the field increases, the aligned state becomes increasingly

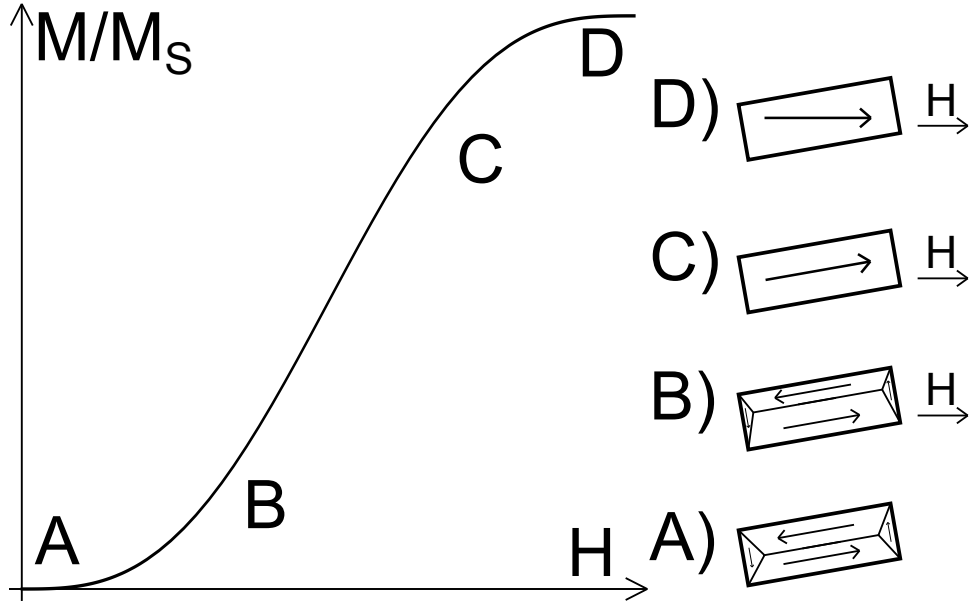


Figure 2.2: *Diagram of the process of magnetizing a ferromagnetic material in an external field.* A) The material is in its original demagnetized state. B) When the field is first applied, the ferromagnet responds by domain wall motion until the walls become pinned. C) Sufficient field will cause the remaining domains themselves to rotate, eventually aligning the magnetization with the easy axis. D) Saturation of the magnetization occurs when the magnetization aligns directly along the direction of the applied field.

energetically favorable, until all the spins become aligned. This is the point at which the magnetization is maximized, or saturated, known as the *saturation magnetization*,  $M_S$  [32, 33, 34].

The film's first reaction to the external field is the smallest energy change possible. At zero external field, and assuming the sample has no net magnetization, the film will arrange itself in magnetic domains, as discussed earlier, such that the external flux loops are minimized. As the external field increases, the initial behavior of the film is to increase the size of the domains that are most closely aligned with the field. This is done by moving domain walls, the region of spins that rotate over a finite spatial distance from one domain alignment to the adjacent alignment. The distance the domain wall moves is related to the strength of the applied magnetic field.

Domain wall motion can be an entirely reversible process in a perfect crystal, i.e. one with no locations available for the domain wall to pin itself on. Exposing a demagnetized ferromagnet to a field small enough to move the domain walls but not pin them does not place the material in a permanently magnetized state. It turns out that the hysteretic effects characteristic of ferromagnetism are a result of the various places where domain walls cannot cross, and instead are pinned. Such locations include lattice defects, inclusions, and grain boundaries.

Once the domain walls become pinned, it is possible to move them with significantly more energy. This can result in other, smaller domains known as “spike domains”, which are not simply removed by domain wall motion. These spike domains tend to remain completely pinned to the lattice defect, even though the bulk wall has swept past. These result from the formation of domains of closure around imperfections that stretch themselves to maintain contact with the pinned domain wall. Eventually, the domain wall will move far enough that it frees itself, separating from the closure domains, and leaving spiked domains in its wake.

At some point, the magnetization cannot be increased by moving domain walls. Now, as the field increases, the film responds by rotating the alignment of the various domains that remain until all of the spins in the sample point in the same direction. During this phase, the domain walls will be removed by spin rotation rather than motion. Once the domain walls vanish through this process then the system is no longer in a reversible state. Subsequent applications of magnetic fields will lead through a hysteretic path.

Eventually there will be no more domains, which results in the magnetization direction pointing directly along the easy axis of the material. If the external field is applied at some angle to the easy axis, then the magnetization will not point directly along the field direction. In the third stage of magnetization the sample rotates its spins coherently. The

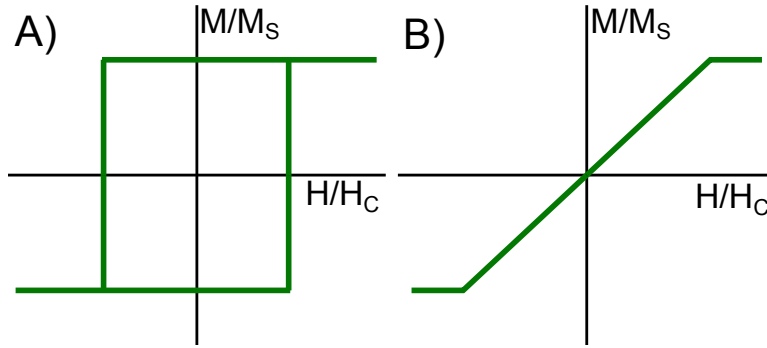


Figure 2.3: *Diagrams of magnetic hysteresis in the easy and hard axes.* A) When magnetized along the easy axis, the ferromagnet responds sharply, and possesses a large remanent magnetization where the magnetization crosses at  $H = 0$ . B) Along the hard axis, there is no coercive field, and the system responds sluggishly to the field.

sample reaches saturation once the spins are completely aligned to the field.

Consider the simplest case of a single-domain sample possessing only magnetocrystalline anisotropy. How this process occurs depends on how the sample is oriented with respect to the external field. Most magnetic films have a particular orientation that is most favorable to being magnetized. This is known as the easy axis of the sample. The axis that is the most difficult to magnetize, which is sometimes directly perpendicular to the easy axis, is referred to as the hard axis. Each axis behaves significantly differently to the applied field.

When the field is applied along its easy axis, the system reacts sharply as in Figure 2.3a. Once magnetized, assuming the system is a perfect single crystal and is small enough to be single-domain, the ferromagnet will remain fully magnetized, or saturated, until the external field reaches the switching field in the opposite direction. The ferromagnet will then suddenly rotate coherently to align its magnetization with the field. Because the system is non-reversible, it will maintain its new magnetization until the opposite switching field is reached. This forms the idealized hysteretic loop.

When this process is repeated along the hard axis, the system responds without hysteresis. The magnetization slowly rises towards saturation as the spins are forced away from their

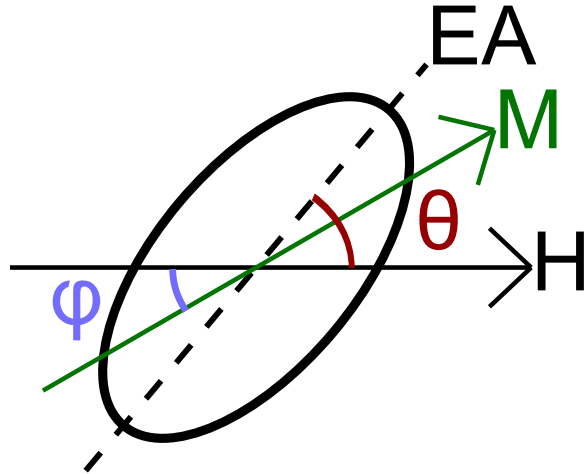


Figure 2.4: *Setup for the Stoner-Wohlfarth problem.* The ferromagnetic particle has the form of an ellipse with easy axis  $EA$  and magnetization  $M$ . A field  $H$  is applied externally at angle  $\theta$  from the easy axis, and  $\phi$  from the magnetization.

preferred orientation. Once the saturation magnetization is reached, further increase in the field yields no additional magnetization. When the field is decreased, the spins will cant back to their preferred direction until the magnetization reaches zero. The same pattern is repeated in the negative direction.

Samples with a large number of defects and impurities are very difficult to magnetize, i.e. they have a high coercive field. Subsequently, they tend to also have a very high remanent magnetization, or the fraction of the magnetization that remains at zero applied field. These materials are known as *hard* ferromagnets. Ferromagnets that are very easy to magnetize, with low coercive fields and generally very little remanent magnetization, are referred to as *soft* ferromagnets.

### 2.1.5 Stoner-Wohlfarth Switching

Consider a ferromagnet material with some form of anisotropy and uniform magnetization as shown in Figure 2.4[34, 36]. For simplicity, the magnetization is assumed to reside in the

plane of the film. The magnetostatic energy of the ferromagnet can be written,

$$U_{tot} = K_u V \sin^2(\phi - \theta) - MH_{ext} V \cos \phi, \quad (2.17)$$

where  $K_u$  is the relevant anisotropy parameter,  $\theta$  is the angle between the applied field  $H$  and the easy axis of the particle EA, and  $\phi$  is the angle between the applied field and the magnetization  $M$ . The first term is the internal energy of the ferromagnet (note the similarity to Equation 2.13), while the second term is the external energy resulting from the applied field. Stoner-Wohlfarth simplified this equation as,

$$\mu = \frac{1}{4} - \frac{1}{4} \cos(2(\phi - \theta)) - h \cos \phi, \quad (2.18)$$

where  $\mu$  is  $U_{int}/2K_u V$ , and  $h$  equals  $MH/2K_u$ . The conditions for stable magnetization direction are when the first derivative of Equation 2.18 with respect to  $\phi$  is zero,

$$\frac{d\mu}{d\phi} = \frac{1}{2} \sin(2(\phi - \theta)) + h \sin \phi = 0, \quad (2.19)$$

and when the second derivative is positive,

$$\frac{d^2\mu}{d\phi^2} = \cos(2(\phi - \theta)) + h \cos \phi > 0. \quad (2.20)$$

When the field is zero, ( $h = 0$ ), this finds its minimum when the magnetization is aligned with the easy axis. For large field, the minimum exists where the magnetization is aligned with the external field.

We can solve for the switching field of a magnetic particle by solving equations 2.19 and

2.20 when the latter is equivalent to zero. This is the crossover point where the magnetization becomes unstable in its orientation and must reverse direction. Using a technique suggested in Landau and Lifshitz [37], the boundary of the hysteretic region is found to be,

$$h_{\parallel}^{2/3} + h_{\perp}^{2/3} = 1 \quad (2.21)$$

where  $h_{\parallel}$  is the component of the field aligned with the magnetization, and  $h_{\perp}$  is the component orthogonal to the magnetization. This explains the switching behavior seen in Figure 2.3. When the field points along the easy axis, as in Figure 2.3a, the  $h_{perp}$  component is zero, and the switching field becomes,

$$h_{parallel} = 1 = \frac{MH}{2K_u} \quad (2.22)$$

which tells us that the coercive field is,

$$H_c = \frac{2K_u}{M} \quad (2.23)$$

which is the values of field where Figure 2.3a crosses the field axis. The perpendicular field requires a bit more explanation. While the value of the switching field is the same as for the parallel case, which suggests a hysteretic behavior, Figure 2.3b suggests no hysteresis at all. This is because we're measuring the component of the magnetization parallel to the applied field. It is hysteretic in that it can rotate to either the right or left of the field, but these two states appear identical in the measurement.

## 2.2 Superconductivity

Superconductivity is an effect originally discovered in 1911 by Kamerlingh Onnes [1]. He noticed the resistance of a sample of Mercury suddenly drop to zero at 4.9 K. Most interesting, further measurements confirmed that the resistance of the Hg sample was in fact perfectly zero, and not merely suppressed to very close to zero. This was a shocking result that has turned out to be one of the most important and useful discoveries in physics.

However, a theory that described the physical phenomenon turned out to be illusive. For forty years, no-one was able to successfully describe, in one grand theory, the properties that were being observed by experiment. Then, in 1957, Bardeen, Cooper, and Schrieffer hit upon a successful model [4], now called “BCS” Theory. It was experimentally confirmed by a number of experiments, particularly in 1960 by Ivar Giaever [38], who performed a simple tunneling experiment to measure the superconducting density of states, successfully matching the density of states as predicted by the theory.

The genius of BCS theory was in the realization that electrons near the Fermi surface can form bound pairs, now known as “Cooper Pairs”. The pairing occurs when the first electron generates a *virtual phonon* in the lattice, a lattice vibration that is not required to conserve momentum while it exists. When this phonon is absorbed by a second electron, the process acts as an attractive potential between the electrons, defeating Coulomb repulsion and binding the two electrons together.

The drop in resistance that Onnes observed was a result of this electronic pairing. Resistance is a result of scattering events between electrons and their environment; be it either other electrons, lattice defects, or phonons. The Cooper Pairs, however, do not experience these events. In order to scatter one of the electrons in the pair, the event has to have

sufficient energy to overcome the binding energy,

$$E = 2\Delta(0) = 3.528k_B T_C, \quad (2.24)$$

where  $k_B$  is the Boltzmann factor, and  $T_C$  is the temperature above which the superconducting state becomes energetically unfavorable [39]. The term  $\Delta$  is the energy gap for single-particle excitations, i.e. the energy a single particle requires to occupy an available single-particle state, whereas  $2\Delta$  is the total size of the superconducting band gap. Because most scattering events have insufficient energy to overcome the energy gap, the result is a complete lack of scattering events, and therefore a complete lack of resistance in the sample.

### 2.2.1 DC Josephson Effect

In a sample comprised of two superconductors separated by an insulating barrier, a current of Cooper pairs can flow between the two superconducting materials [40]. This current is a result of the phase difference,  $\phi$ , between the superconductors, described by,

$$I_S = I_c \sin \phi, \quad (2.25)$$

where  $I_c$  is the *critical current*, the maximum supportable supercurrent in the sample. This was first predicted by Josephson in 1962, and is known as the dc Josephson effect. The Josephson energy of such a device can be described by,

$$E_J = \frac{\hbar I_c}{2e}. \quad (2.26)$$

Using the Josephson energy, it is possible to compute a lower bound to the measurable

critical current in a device [39]. At sufficiently low critical currents, thermal excitations can overpower the supercurrent flowing in the sample. This tells us that,

$$I_c > \frac{2ek_B T}{\hbar}, \quad (2.27)$$

the lowest measurable critical current is related to the thermal energy by a multiplicative constant.

The devices described by the Josephson effect are called “Josephson junctions”. While the original theory was based on samples with an insulating material (I) separating the two superconductors, Josephson junctions can be fabricated with a number of different internal materials. Other options include: Normal Metals (N), Ferromagnets (F), and constricted superconductors (c).

## 2.2.2 Resistively and Capacitively Shunted Junction (RCSJ) Model

The dynamics of a Josephson junction can be modeled by an idealized system. Figure 2.5 demonstrates this model, which includes an ideal Josephson junction shunted by a resistor (R) and a capacitor (C) [39]. The resistor fills the role of modeling the dissipation in the finite voltage regime, which should have a magnitude roughly equivalent to  $R_N$ , the normal resistance of the junction. The capacitor models the geometric shunting capacitance between the two superconductors.

The dc Josephson relation described in Equation 2.25 implies that an applied current controls the phase difference of the superconductors,  $\phi = \phi_2 - \phi_1$ . If the applied current  $I < I_c$ , the phase difference does not change in time, but if  $I > I_c$  the phase difference will

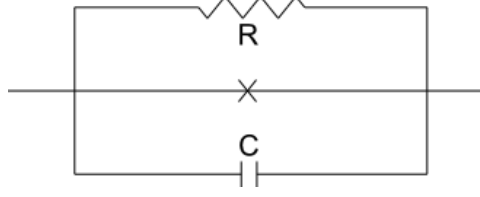


Figure 2.5: *Resistively and Capacitively Shunted Junction (RCSJ) model circuit.* At the center is an ideal Josephson junction. This is wired in parallel with a resistor  $R$ , and capacitor  $C$ .

evolve by,

$$\frac{d(\phi)}{dt} = \frac{2eV}{\hbar}, \quad (2.28)$$

where  $V$  is the voltage difference across the sample [41]. This is known as the ac Josephson relation.

The total current crossing our idealized circuit in the RCSJ model is simply a sum of the currents across each element. This yields,

$$I = I_{c0} \sin \phi + \frac{V}{R} + C \frac{dV}{dt}, \quad (2.29)$$

where  $I_{c0}$  is the critical current of the idealized Josephson junction, which may be different than  $I_c$ , the observable critical current. It is possible for  $I_c$  to be less than  $I_{c0}$ . If we replace  $V$  in Equation 2.29 with the ac Josephson relation 2.28, we get,

$$I = I_{c0} \sin \phi + \frac{\hbar}{2eR} \frac{d\phi}{dt} + \frac{\hbar C}{2e} \frac{d^2\phi}{dt^2}. \quad (2.30)$$

This can be rewritten as,

$$\frac{I}{I_{c0}} = \sin \phi + \frac{1}{Q\omega_p} \frac{d\phi}{dt} + \frac{1}{\omega_p^2} \frac{d^2\phi}{dt^2}. \quad (2.31)$$

where,

$$\omega_p = \left( \frac{2eI_c \phi_0}{\hbar C} \right)^{1/2} \quad (2.32)$$

is the plasma frequency of the junction, and  $Q$  is related to the Stewart and McCumber damping parameter [39]  $\beta_c$  by,

$$Q = \omega_p RC = \beta_c^{1/2}. \quad (2.33)$$

This model can be easily understood qualitatively by the *tilted washboard potential* [39]. We can model the differential equation in 2.31 with a mechanical analog. If we multiply 2.31 by  $E_J$  using 2.26 we get,

$$\frac{I\hbar}{2e} - E_J \sin \phi = \frac{\hbar^2}{(2e)^2 R} \frac{d\phi}{dt} + \frac{\hbar^2}{(2e)^2} C \frac{d^2\phi}{dt^2} \quad (2.34)$$

This problem is identical to that of a particle of mass,

$$M = \left( \frac{\hbar}{2e} \right)^2 C, \quad (2.35)$$

moving in an effective potential,

$$U = -E_J \cos \phi - \frac{\hbar I}{2e} \phi. \quad (2.36)$$

This yields Figure 2.6, where a particle is trapped in a well of the oscillating potential. As the current through the sample is increased, the tilt in the washboard increases. Eventually, the tilt becomes steep enough for the particle to escape. At this limit, there are no longer any stable points to trap the particle, causing it to slide down the washboard. This is the normal state of the system, where a non-zero voltage appears across the junction.

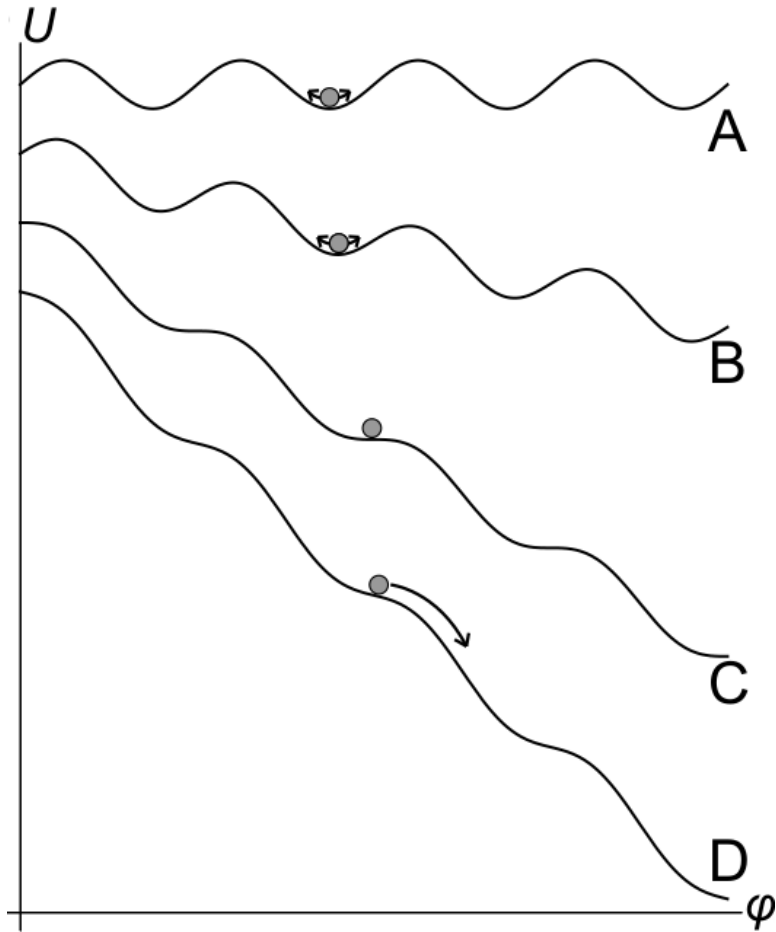


Figure 2.6: *The tilted washboard potential model.* A) With no current applied the washboard has no tilt, and the particle is confined to a well. B) A small current reduces the barrier height, allowing for the possibility of thermal fluctuations to drive the particle over the barrier. C) At the critical point, the particle exists at a metastable state. The slightest fluctuation will send it running to the end of the washboard. D) The current is high enough that the Josephson junction has gone normal, placing it in a state with a dc voltage across the junction.

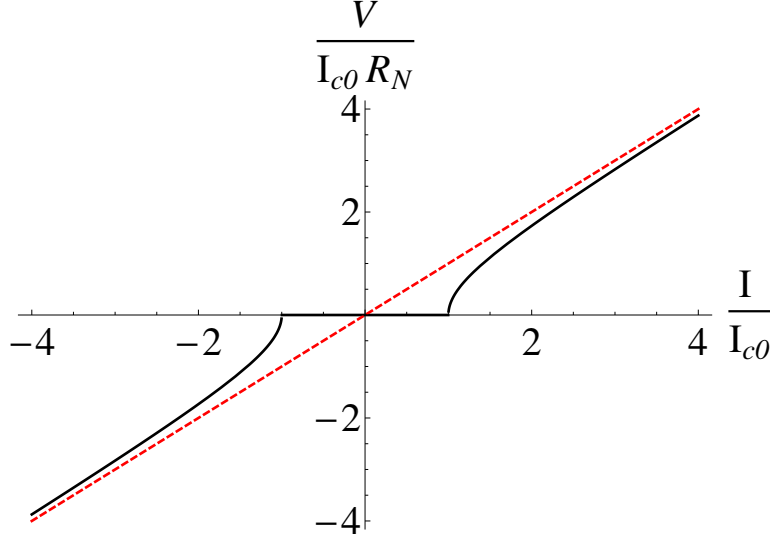


Figure 2.7: *Current-Voltage relation for an overdamped Josephson junction.* The black curve demonstrates the form of Equation 2.38. The system possesses no voltage for currents up to  $I_c$ . Once the critical current has been reached, the system asymptotically approaches an ohmic relation with resistance  $R_N$  plotted by the dashed red line.

### 2.2.3 Overdamped Junctions

If  $C$  is small, so that  $Q \ll 1$ , the second order term in the differential equation 2.31 becomes small enough to be neglected, then,

$$\frac{d\phi}{dt} = \frac{2eI_{c0}R}{\hbar} \left( \frac{I}{I_{c0}} - \sin \phi \right). \quad (2.37)$$

This can be integrated to find the resulting current dependent voltage relation for the junction,

$$|V| = R_N Re \left( I^2 - I_{c0}^2 \right)^{1/2} \quad (2.38)$$

For  $|I| < |I_{c0}|$ ,  $V = 0$ , but for  $I > I_{c0}$  and  $-I < -I_{c0}$ , this smoothly approaches Ohm's law ( $V = IR$ ) as  $I$  increases. Figure 2.7 demonstrates this behavior, where the dashed line is simply Ohm's law with the resistance (the slope of the line) equivalent to the normal resistance  $R_N$  of the junction[39].

## 2.2.4 Magnetic Behavior

The magnetic behavior of the Josephson junction is an important tool for characterization of the junctions. Consider a Josephson junction “pillar” with a square cross section in the  $y$ - $z$  plane as in Figure 2.8 [42]. A uniform external field  $H_{ext}$  applied to the pillar in the  $z$ -direction induces a field  $B(x)\hat{z}$  inside. The vector potential resulting from Landau’s gauge is,

$$\mathbf{A} = -B(x)y\hat{x} \quad (2.39)$$

Within the superconductor, the field will decay as  $\exp(-|x|/\lambda_L)$ , where  $\lambda_L$  is the *London penetration depth*,

$$\lambda_L = \left( \frac{m}{\mu_0 n e^2} \right)^{1/2} \quad (2.40)$$

and  $n$  is the number density of superconducting electrons.

Inside the non-superconducting film, the field can be assumed to be constant,  $B(x) \approx B(0)$ . The phase shift across the junction due to the vector potential is therefore,

$$\Phi_1' = \frac{2e}{\hbar} \int A_x dx = \frac{2e}{\hbar} B(0)yl \quad (2.41)$$

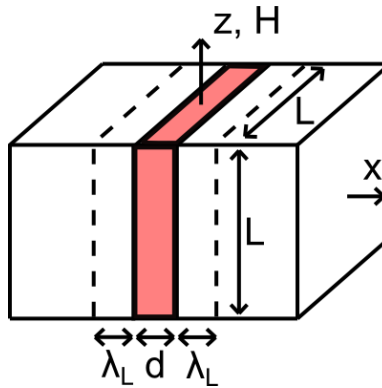


Figure 2.8: Diagram of a Josephson junction with a square cross-section.

where.

$$l = 2\lambda_L + d \quad (2.42)$$

with  $d$  the thickness of the non-superconducting film. This yields a total phase difference of,

$$\Phi = 2\pi \frac{\Phi'_1}{\Phi_0} + \phi \quad (2.43)$$

where  $\phi$  is the natural phase difference between the superconductors, and  $\Phi_0$  is the *flux quantum*,

$$\Phi_0 = \frac{h}{2e} \quad (2.44)$$

The supercurrent density in the junction can then be expressed as,

$$J(y) = J_c \sin \Phi = J_c \sin \left( 2\pi \frac{\Phi'_1}{\Phi_0} + \phi \right) \quad (2.45)$$

or,

$$J(y) = J_c \sin \left( 2\pi \frac{B(0)yl}{\Phi_0} + \phi \right) \quad (2.46)$$

The critical current we measure is the integration of this over the entire junction,

$$I = \int J(y) dy dz \quad (2.47)$$

which becomes, after integration over the  $z$  direction,

$$I = L_z J_c \int_0^{L_y} \sin \left( 2\pi \frac{B(0)yl}{\Phi_0} + \phi \right) dy \quad (2.48)$$

Integrating this yields,

$$I = L_z J_c \frac{\Phi_0}{2\pi B l} \left( \cos \Delta\phi - \cos \left( 2\pi \frac{B(0)L_y l}{\Phi_0} + \phi \right) \right) \quad (2.49)$$

which can be simplified using the trigonometric identity,

$$\cos(u) - \cos(v) = 2 \sin \left( \frac{u+v}{2} \right) \sin \left( \frac{v-u}{2} \right) \quad (2.50)$$

to,

$$I = L_z J_c \frac{\Phi_0}{2\pi B l} \left( 2 \sin \left( \pi \frac{B(0)L_y l}{\Phi_0} \right) \sin \left( \pi \frac{B(0)L_y l}{\Phi_0} + \phi \right) \right) \quad (2.51)$$

which, with  $\Phi_1 = B(0)L_y l$  and  $I_c = J_c L_y L_z$ , can be further simplified to,

$$I = I_c \frac{\Phi_0}{\pi \Phi_1} \left( \sin \left( \pi \frac{\Phi_1}{\Phi_0} \right) \sin \left( \pi \frac{\Phi_1}{\Phi_0} + \phi \right) \right) \quad (2.52)$$

The junction can therefore carry a maximum current of,

$$\frac{I}{I_c} = \left| \frac{\sin(\pi\Phi_1/\Phi_0)}{\pi\Phi_1/\Phi_0} \right| \quad (2.53)$$

This describes a ‘‘Fraunhofer’’ pattern, which is the exact analog to the optical diffraction pattern.

If the pillar is circular [43], as in Figure 2.9, the limits of integration must be altered to account for the geometric difference. Starting with Equation 2.47, and noting that the form

of the gauge and critical current density are the same, we get,

$$I = 2J_c \int_{-R}^R \sqrt{R^2 - y^2} \sin \left( 2\pi \frac{B(0)yl}{\Phi_0} + \phi \right) dy \quad (2.54)$$

after integrating over  $z$ . This is symmetric about zero, and can be simplified by substituting  $u = y/R$ ,

$$I = 4J_c R^2 \int_0^R \sqrt{1 - u^2} \sin \left( 2\pi \frac{B(0)Rl}{\Phi_0} u + \phi \right) du \quad (2.55)$$

This results in,

$$\frac{I}{I_c} = \left| \frac{J_1(RlB/\Phi_0)}{(RlB/\Phi_0)} \right| \quad (2.56)$$

where  $J_1$  is a Bessel's Function of the first kind, and  $I_c = J_c \pi R^2$ . This is an ‘‘Airy Pattern’’ which is plotted with the Fraunhofer pattern described in Equation 2.53 in Figure 2.10.

Typically, our pillars have a circular geometry, but it has become traditional to call the resulting curve a ‘‘Fraunhofer’’ pattern regardless of the shape. Strictly speaking, however, there are differences between these two. That said, with the large quantity of ferromagnetic materials inside our junctions, the differences are minor enough that it would be difficult to observe them in most real samples.

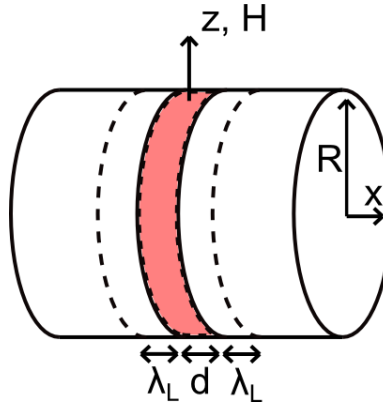


Figure 2.9: *Diagram of a Josephson junction with a circular cross-section.*

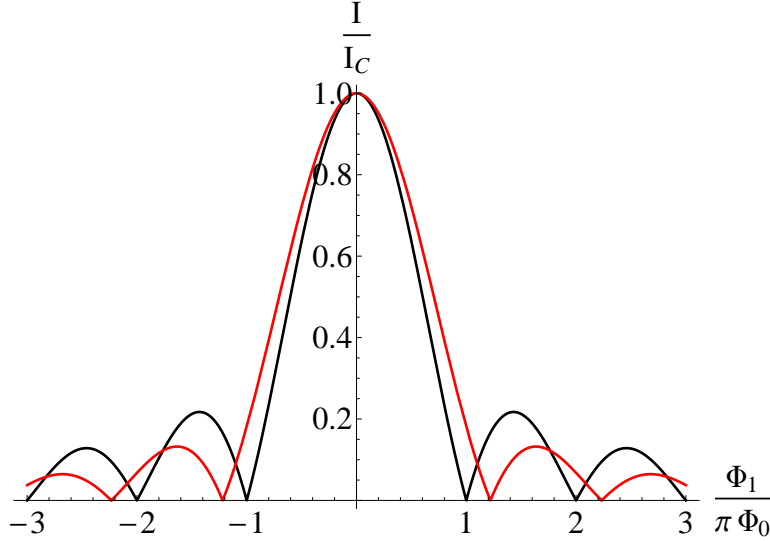


Figure 2.10: *Fraunhofer and Airy Patterns*. Critical current behavior of Josephson junctions with a square (Black) and circular (Red) cross sections. The red curve is the “Airy pattern” described by 2.56, while the black curve is the “Fraunhofer pattern” as described by 2.53.

### 2.2.5 Proximity Effect in S/N and S/F Systems

When a superconductor is placed against a non-superconductor, pair correlations from the superconductor can leak into the abutting material. This results in the new material having superconducting-like properties by proximity to the superconductor, known generally as the “proximity effect”. The superconductor pays for this extension of the superconducting effect, as the pair correlations weaken near the boundary in an effect known as “inverse proximity”. These effects allow for the propagation of pair correlations, which enables the Josephson effect discussed earlier.

However, the normal metal density of states does not include Cooper pair states. At the same time, superconductors possess a band-gap in the single-electron density of states around the Fermi energy. This implies, naively, that neither material should be able to exchange electrons with the other. But, the existence of the Josephson effect in S/N/S junctions proves otherwise. How this is possible is the result of pioneering work by Alexander Andreev in

1964 [44].

Andreev reflection is a microscopic process enabling the motion of electrons across the boundary of the S/N and S/F interface by providing a mechanism for the conversion of single electrons into pairs and vice-versa. Consider an electron in the normal metal traveling towards the S/N interface with spin  $\uparrow$ , momentum  $k$ , and an energy  $\epsilon < \Delta$ , where  $\epsilon$  is measured from the Fermi energy  $E_F$ , and  $\Delta$  is the energy gap in the superconductor (the *order parameter*). Because  $\epsilon$  is smaller than the gap in the single electron density of states, then there are no states available to it, and traditionally it would be expected to reflect off the boundary back into the normal metal.

To overcome this problem the electron can instead find a partner in the normal metal with opposite spin ( $\downarrow$ ), opposite momenta  $-k$  and an energy  $-\epsilon$ . Together, the two electrons can form a Cooper Pair in the superconductor, which resides exactly at the Fermi energy. The result of this process is that a hole is formed inside the normal metal with energy  $\epsilon$  and spin  $\uparrow$ , the exact opposite of the electron's partner. This process is shown in Figure 2.11.

The opposite effect is known as “inverse Andreev reflection”. Here, a Cooper Pair approaches the boundary of an S/N junction from the S side. Like before, there are no available Cooper Pair states across the boundary for the electrons to occupy. Therefore if the two electrons want to cross the boundary, they must occupy states with equal and opposite momenta near the Fermi momentum  $k_F$ . Despite the separation, the electrons maintain memory of their pairing for a time dependent upon the uncertainty principle,

$$\tau \leq \frac{\hbar}{2\epsilon} \tag{2.57}$$

There are two limits in these systems depending on the electronic mean free path  $l = v_F\tau$ ,

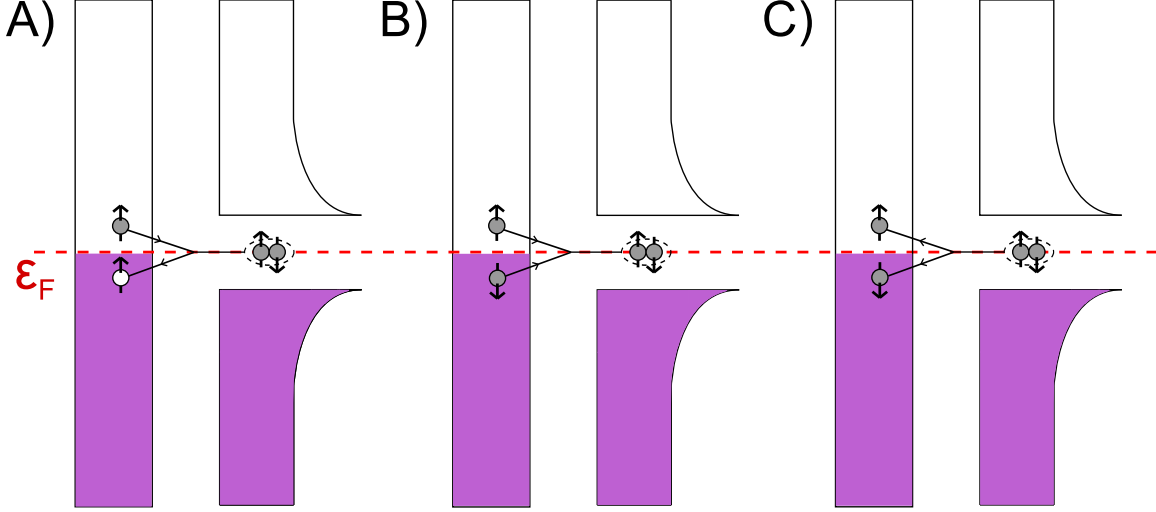


Figure 2.11: *Diagram of normal and inverse Andreev reflection.* A) Andreev reflection involves an electron just above the Fermi energy  $\epsilon_F$  and a Cooper Pair with an electron just below. During the formation of the Cooper pair, a hole is formed below the Fermi energy. B) The alternate picture of Andreev reflection, as two electrons from the normal metal form a Cooper pair in the superconductor. C) Inverse Andreev reflection is a process where a Cooper pair splits into two separate single particle states in a Normal Metal, one above, and one below, the Fermi energy. There must be an empty state below the Fermi energy for this process to occur.

where  $v_F$  is the Fermi velocity, and the pure metal coherence length  $\xi_N$ . In the *clean limit*, where  $l \gg \xi_N$ , the pairs will tend to lose their coherence before scattering inside the metal. If instead  $l \ll \xi_N$ , then the two electrons will scatter many times before losing coherence. This limit is known as the *dirty limit*[45]. Since the energy difference between the electrons,  $2\epsilon$  will be on the scale of the temperature, the coherence length takes the form:

$$\xi_N = \frac{\hbar v_F}{2\pi k_B T} \quad \text{Clean} \quad (2.58)$$

$$\xi_N = \sqrt{\frac{\hbar D}{2\pi k_B T}} \quad \text{Dirty} \quad (2.59)$$

where  $D = \frac{1}{3} N_F l$  is the diffusion constant.

Electrons passing from a superconductor into a ferromagnetic material react much differ-

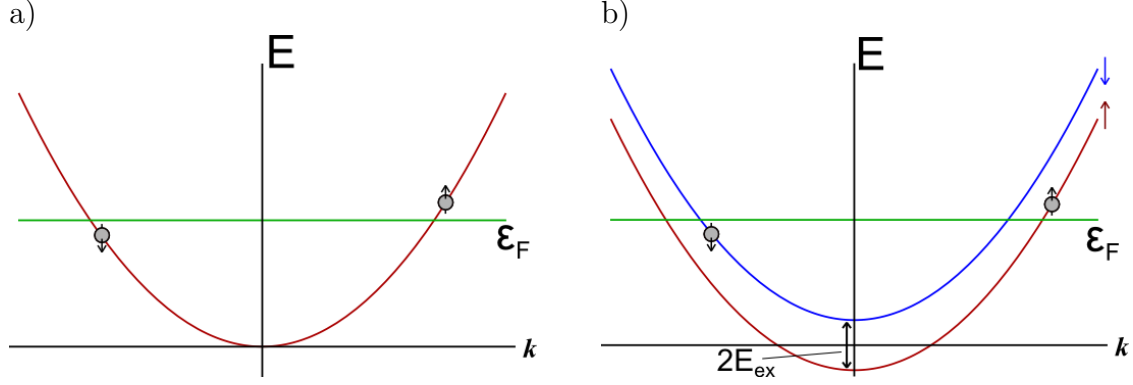


Figure 2.12: *Dispersion Relations for a: A) normal metal, and B) idealized ferromagnet.* When a Cooper pair enters these materials, the electrons must enter the dispersion relation at energies near the Fermi energy  $\epsilon_F$ . In the ferromagnet, this requires a shift in momentum to account for the exchange energy  $E_{ex}$  between the two spin bands.

ently than those passing into a normal metal. This is because of the significant difference in the dispersion relation between these two classes of materials, as can be seen in Figure 2.12. In a normal metal it is largely irrelevant if the incoming electron is spin up or spin down, both types will enter the same energy band. This is not the case for ferromagnets, where the up and down spin bands are separated by an energy  $2E_{ex}$ , where  $E_{ex}$  is the *exchange energy* in the ferromagnet. Because the electrons are seeing a potential energy difference, they must change their kinetic energy to satisfy energy conservation. This results in the pair of electrons acquiring a center of mass momentum [46],

$$Q = \frac{2E_{ex}}{v_F} \quad (2.60)$$

Because the electron entering the majority band gains kinetic energy at the expense of the electron entering the minority band, then when the electrons are exchanged in momentum space the result is a center of mass momentum of  $-Q$ . This results in the addition of a phase

term in the normalized spin singlet wave function in the ferromagnet.

$$\frac{1}{\sqrt{2}} [|\uparrow\downarrow\rangle - |\downarrow\uparrow\rangle] \Rightarrow \frac{1}{\sqrt{2}} [|\uparrow\downarrow\rangle \exp[iQx/\hbar] - |\downarrow\uparrow\rangle \exp[-iQx/\hbar]] \quad (2.61)$$

We also need to account for the fact that not every electron is going to strike the boundary perpendicular to its face. This results in a  $Q/\cos\theta$  dependence on the center of mass momentum, where  $\theta$  is measured from the normal of the interface. It is then possible to integrate over all possible angles of incidence, resulting in a singlet pair correlation amplitude of,

$$F = \frac{\sin(x/\xi_F)}{(x/\xi_F)} \quad (2.62)$$

in the clean limit, where  $x$  is the penetration depth in the ferromagnet, and  $\xi_F = \hbar v_F/2E_{ex}$  is the ferromagnetic correlation length. In the dirty limit, this takes the form,

$$F \approx \exp[(-x/\xi'_F)] \sin(x/\xi'_F + \phi) \quad (2.63)$$

where  $\phi$  is a phase, and,

$$\xi'_F = \sqrt{\frac{\hbar D}{E_{ex}}} \quad (2.64)$$

Interestingly, this implies that pair correlations don't simply decay, but that they also oscillate with increasing depth in the Ferromagnet. This surprising result was predicted by Buzdin *et al.* [47, 48], and Radovic *et al.* [49], and observed by several groups in the form of critical current oscillations in S/F/S Josephson junctions [50, 51, 52, 53, 54, 55].

Figure 2.13 graphically demonstrates the pair correlations in S/N and S/F systems, emphasizing the oscillating behavior of the latter. The actual correlation length for typical

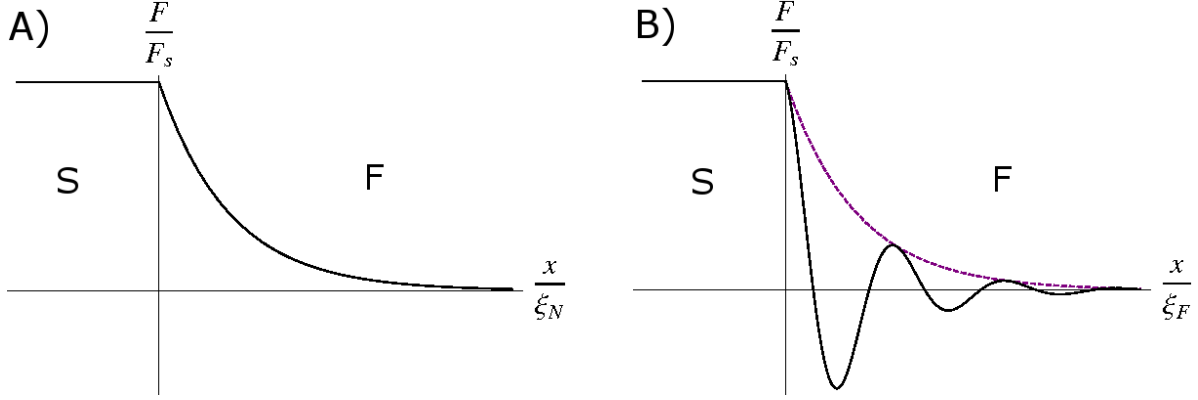


Figure 2.13: A schematic diagram of the Pair correlation function  $F$  in both the: A) Normal Metal, and B) Ferromagnet. The normal metal possesses a decay length  $\xi_N$  on the order of a micron, while the ferromagnet's decay length  $\xi_F$  is roughly a nanometer. Note also the oscillations in the pair correlations inside the ferromagnet.

materials is particularly important. From Equation 2.59, the average normal metal suppresses the pair correlations at a temperature  $T \approx 1K$  on length scales on the order of roughly a micrometer. From Equation 2.64, it can be seen that ferromagnets are much less favorable for pair correlations. Given an exchange energy of  $E_{ex} \approx 1eV$ , they exhibit a length scale about a factor of a thousand shorter, or roughly a nanometer.

## 2.2.6 Origin of Long Range Triplet Component (LRTC)

In 2001, Bergeret, Volkov, and Efetov [10] predicted that certain S/F systems were capable of generating a Long-Range Triplet Component (LRTC). In S/F/S Josephson junctions, this was predicted to manifest itself as an enhancement to the supercurrent as a function of ferromagnet thickness. In 2003 [11], the same group suggested the complicated arrangement of three ferromagnets shown in Figure 2.14. Each ferromagnet possesses non-collinear magnetization to the magnetic films adjacent to it, and are sandwiched among s-wave superconductors. This was predicted to generate pair correlations that could persist for long ranges

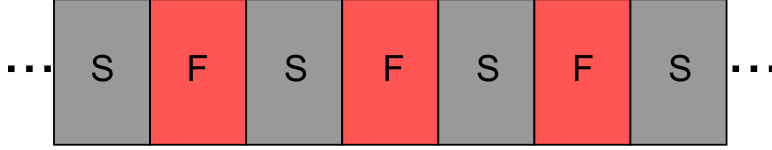


Figure 2.14: *The spin-triplet generating system proposed by Bergeret, Volkov, and Efetov in 2003.*

in the ferromagnets. These pair correlations are “odd-triplet superconductivity” which take the form of  $|\uparrow\uparrow\rangle$  and  $|\downarrow\downarrow\rangle$ . Because the spins of the two electrons point in the same direction, they can occupy the same spin band when penetrating into a ferromagnet. Thus, there is no shift in the center of mass momentum, and therefore no oscillations.

In 2007, Houzet and Buzdin put together a theory describing a slightly different system of ferromagnets [21]. It was predicted that a Josephson junction comprised of three ferromagnets,  $F'$ ,  $F$ , and  $F''$ , would generate the triplet component. This is true so long as the ferromagnets possess non-collinear magnetizations, as before. Figure 2.15 presents this critical geometry, which will play a major role in this thesis.

How the spin-singlet Cooper pairs from the superconductor convert to spin-triplet electron pairs in the ferromagnet was most clearly modeled by Eschrig [56], and is shown in Figure 2.16. This method is not dissimilar to the traditional “Stern-Gerlac” thought exper-

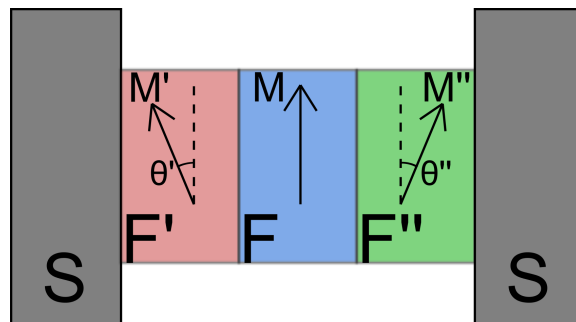


Figure 2.15: *The geometry proposed by Houzet and Buzdin.* The magnetization of the first ferromagnet,  $M'$ , is coming out of the page towards the reader. The magnetization of the last ferromagnet,  $M''$ , is pointing into the page.

iments presented to most early students of Quantum Mechanics. Consider the spin-singlet part of the Cooper pair wavefunction described in Equation 2.61. This can be rewritten as,

$$\Psi = \frac{1}{\sqrt{2}} [(\cos[Qx/\hbar] + i \sin[Qx/\hbar]) |\uparrow\downarrow\rangle - (\cos[Qx/\hbar] - i \sin[Qx/\hbar]) |\downarrow\uparrow\rangle] \quad (2.65)$$

When rearranged and simplified, this yields,

$$\Psi = [(\cos[Qx/\hbar]) |0, 0\rangle + (i \sin[Qx/\hbar]) |1, 0\rangle_z] \quad (2.66)$$

The  $|0, 0\rangle$  component is the standard spin-singlet component which will die out quickly on the scale described by Equation 2.64. This process also generates an  $m = 0$  triplet component, but because this possesses opposite spins, it remains short-ranged. However, when this enters the second ferromagnet, we must perform a change of basis into the direction of the new magnetization. If that is at angle  $\theta$  with the magnetization of the first ferromagnet, this becomes,

$$|1, 0\rangle_z = \left[ \left( \frac{\sin[\theta]}{\sqrt{2}} \right) |1, 1\rangle_\theta + (\cos[\theta]) |1, 0\rangle_\theta - \left( \frac{\sin[\theta]}{\sqrt{2}} \right) |1, -1\rangle_\theta \right] \quad (2.67)$$

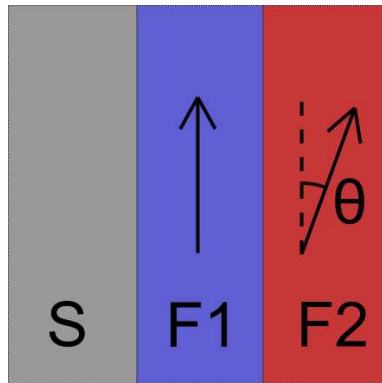


Figure 2.16: A superconducting material adjacent to two ferromagnets with non-collinear Magnetization, similar to the geometry proposed by Houzet and Buzdin.

The terms  $|1, 1 \rangle$  and  $|1, -1 \rangle$  are referred to as the *long range triplet components* (LRTC). Because the spins of the two electrons in the state are identical in the second ferromagnet, they do not experience a splitting due to the exchange energy of the ferromagnet. This means that the ferromagnet treats the LRTC exactly the same way as a normal metal treats the spin-singlet state. The resulting correlation length for the LRTC in ferromagnetic materials increases dramatically to,

$$\xi_{Triplet} = \sqrt{\frac{\hbar D}{2\pi k_B T}} \quad (2.68)$$

identical to the dirty limit coherence length in normal metals.

### 2.2.7 Spin-Triplet Phase

The non-collinearity of all three layers is required, even though triplet supercurrent is generated with only the first two ferromagnets. This is because the triplet has to be reconverted into singlet supercurrent before it can pass back into the s-wave superconductor. The s-wave superconductor has no available states for triplet supercurrent. Failure to reconvert to the singlet state would cause reflection of the triplet current at the superconductor boundary.

If the magnetizations of the three ferromagnets are co-planar then the spin-triplet Josephson junction possesses a phase that is dependent upon the chirality of the rotation angle between adjacent ferromagnets. By tracing the path of the current through the ferromagnetic layers, the direction of rotation between the magnetizations of the first and second ferromagnets, compared to the direction of rotation between the second and third ferromagnets' magnetization, define the phase of the junction. If the rotation is in the same direction, the junction exists in the 0 state. If the rotation direction changes, then the system exists in a  $\pi$  state. This was hashed out in detail in the work done by M. Houzet and A.I. Buzdin in

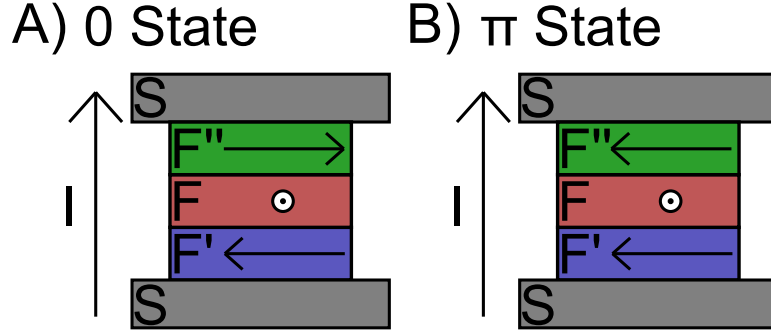


Figure 2.17: *The origin of phase in spin-triplet generating systems.* A) The angle between each adjacent ferromagnet as the current climbs the stack changes in the same direction. This results in a 0 state junction. B) The angle between the bottom and middle magnetizations, and the angle between the middle and top magnetizations, switch between left and right orientation. This creates a  $\pi$  state.

2007 [21], and is shown diagrammatically in Figure 2.17.

The size of the angle, as suggested in the previous section in Equation 2.67, determines the magnitude of the generated triplet supercurrent. The maximum supercurrent is generated with a non-collinear magnetization between the layers of  $\pi/2$ . In the case that two of the layers are perfectly aligned (either parallel or antiparallel), the system remains entirely in the  $|1, 0\rangle$  state, the so-called “Short-range triplet component”, which behaves no differently than the spin-singlet state.

This story gets a little more complicated with the varieties of central ferromagnets used in this work. In the case of a synthetic antiferromagnet (SAF), triplet generation can still occur despite the anti-parallel arrangement between the two magnetic layers. This is allowed because the triplet component is generated between the first ferromagnet (typically called F') and the first of the two ferromagnets in the SAF. It is then reconverted into the singlet component between the second ferromagnet in the SAF and the last ferromagnet in the stack (typically referred to as F''). The phase of these junctions is a little counter intuitive, but the chirality rule remains the same.

The second option for central ferromagnetic layer possesses *Perpendicular Magnetic Anisotropy* (PMA). In this case, the chirality rule remains. However, because the magnetization of the central F layer always possesses an angle of  $\pi/2$  with the other ferromagnets used for the F' and F'' layers, the behavior of the triplet phase is surprising. Rather than a decay in the amplitude with change in angle between the F' and F'' magnetization, along with the possibility of only 0 or  $\pi$  states, instead the system maintains maximum supercurrent, but can possess *any* phase between 0 and  $\pi$ . The experiments described in Chapter provide some evidence for this scenario.

## 2.3 SQUIDS

One of the critical applications of Josephson junctions is the ability to fashion phase sensitive devices. Known as *Superconducting QUantum Interference Devices* (SQUIDS) these tools are ubiquitous for their sensitivity to small changes in the magnetic flux passing through them. This is a result of the interference between the current paths in the two limbs of the device, an interference not unlike coherent optical interference.

Since their invention in 1964 by Robert Jaklevic, John J. Lambe, James Mercereau, and Arnold Silver of Ford Research Labs [57], SQUIDS have found their place in the world as high sensitivity magnetometers. Several examples of this are given in Chapter 3. They have also found a place for phase sensitive measurements, which is how they will be employed in the experiments discussed in Chapter 7.

### 2.3.1 DC SQUID

Consider a loop of superconducting material into which two Josephson junctions have been patterned, as in Figure 2.18. The difference in the gauge invariant phases around this loop can be found by integrating[58],

$$\oint_C \nabla\theta \cdot d\mathbf{l} = 2\pi n \quad (2.69)$$

around a closed path C. This can be divided into four terms for each of the regions specified in Figure 2.18,

$$2\pi n = \theta_{ba} + \theta_{cb} + \theta_{dc} + \theta_{ad} \quad (2.70)$$

where the first subscript denotes the starting point, and the second denotes the end.

For the phase difference across the Josephson junctions, we have,

$$\theta_{ba} = -\phi_1 - \frac{2\pi}{\Phi_0} \int_a^b \mathbf{A} \cdot d\mathbf{l} \quad (2.71)$$

and,

$$\theta_{dc} = \phi_2 - \frac{2\pi}{\Phi_0} \int_c^d \mathbf{A} \cdot d\mathbf{l} \quad (2.72)$$

where  $\phi_1$  and  $\phi_2$  are the phase differences of the superconductors across each junction. The other two terms in Equation 2.70 are the phases generated within the superconducting wires, which can be found using the equation for the current density of Cooper Pairs within a superconductor,

$$\mathbf{J} = -\frac{1}{\mu_0\lambda_L^2} \left[ \mathbf{A} + \frac{\Phi_0}{2\pi} \nabla\theta \right] \quad (2.73)$$

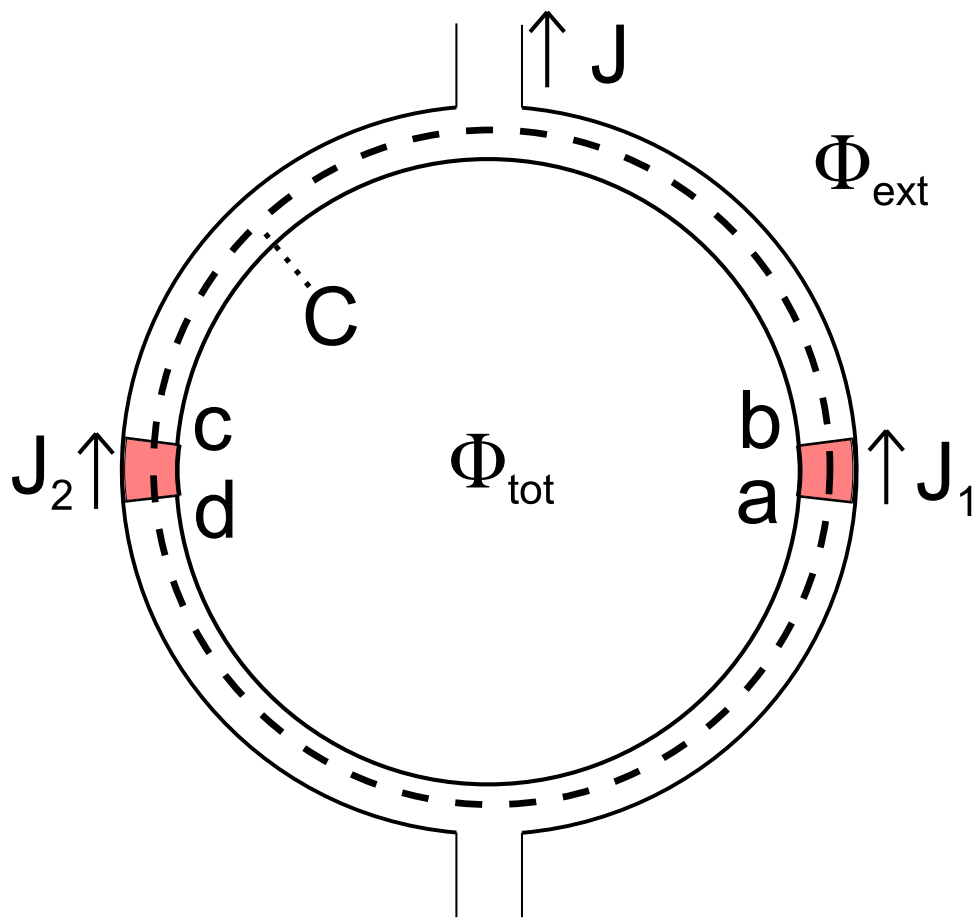


Figure 2.18: *DC SQUID Geometry*. The total current through the device is  $J$ , while  $J_1$  and  $J_2$  represent the supercurrent through the two Josephson junctions.  $\Phi_{tot}$  is the total flux passing through the device, while  $\Phi_{ext}$  is the flux applied to the device.

Rearranging and substituting for  $\nabla\theta$  gives,

$$\theta_{cb} = -\frac{2\pi}{\Phi_0} \int_b^c \left( \mu_0 \lambda_L^2 \mathbf{J} \cdot d\mathbf{l} + \mathbf{A} \cdot d\mathbf{l} \right) \quad (2.74)$$

and identically,

$$\theta_{da} = -\frac{2\pi}{\Phi_0} \int_d^a \left( \mu_0 \lambda_L^2 \mathbf{J} \cdot d\mathbf{l} + \mathbf{A} \cdot d\mathbf{l} \right) \quad (2.75)$$

Plugging these four phase relations into Equation 2.70 and rearranging yields,

$$\phi_2 - \phi_1 = 2\pi n + \frac{2\pi}{\Phi_0} \oint_C \mathbf{A} \cdot d\mathbf{l} + \frac{2\pi}{\Phi_0} \left( \int_b^c \mu_0 \lambda_L^2 \mathbf{J} \cdot d\mathbf{l} + \int_d^a \mu_0 \lambda_L^2 \mathbf{J} \cdot d\mathbf{l} \right) \quad (2.76)$$

Assuming  $\lambda_L$  is small compared to the width and thickness of the superconducting wires, we can choose a path C around the loop deep inside the wire where the integral of the current density vanishes. Since the integral around the entire loop of  $\mathbf{A}$  is simply the total flux through the loop  $\Phi$ , this simplifies the previous expression to,

$$\phi_2 - \phi_1 = 2\pi n + \frac{2\pi\Phi}{\Phi_0} \quad (2.77)$$

This tells us that the phases of the two Josephson junctions are not independent of each other, but are related through the periodic boundary condition. This should not be a surprising result, since the Josephson phase is the difference of the phases of the two superconductors on either side of the junction. The phase within a each superconductor will not vary, so long as  $\lambda_L$  is sufficiently small compared to the dimensions of the superconductor.

The critical current of the SQUID can be found by considering the independent current-

phase relations of each Josephson junction[42],

$$J_n = J_{Cn} \sin \phi_n \quad (2.78)$$

where  $n$  is 1 or 2. We can then say that the supercurrents in each junction of the loop are,

$$J_1 = J_{C1} \sin \phi_1 \quad (2.79)$$

and,

$$J_2 = J_{C2} \sin \phi_2 = J_{C2} \sin \left( \phi_1 + \frac{2\pi\Phi}{\Phi_0} \right) \quad (2.80)$$

where  $\phi_2$  has been replaced using Equation 2.77. Let  $J_s$  be the screening current circulating in the ring due to the flux in the loop, which has value  $\Phi_S = LJ_s$ , where  $L$  is the self-inductance of the loop. In the case that  $LJ_s$  is much smaller than the flux resulting from external sources, total current in the SQUID is,

$$J = J_2 + J_1 = J_{C2} \sin \phi_2 + J_{C1} \sin \phi_1 = J_{C1} \sin \phi_1 + J_{C2} \sin \left( \phi_1 + \frac{2\pi\Phi}{\Phi_0} \right) \quad (2.81)$$

Maximizing this function with respect to  $\phi_1$  provides a relation for the critical current in the SQUID,

$$J_c = \left[ (J_{c1} - J_{c2})^2 + 4J_{c1}J_{c2} \cos^2 \left( \frac{\pi\Phi_{ext}}{\Phi_0} \right) \right]^{(1/2)} \quad (2.82)$$

This function varies with the external flux  $\Phi_{ext}$  applied to the SQUID. The maximum possible critical current is,

$$J_c^{Max} = J_{c1} + J_{c2} \quad (2.83)$$

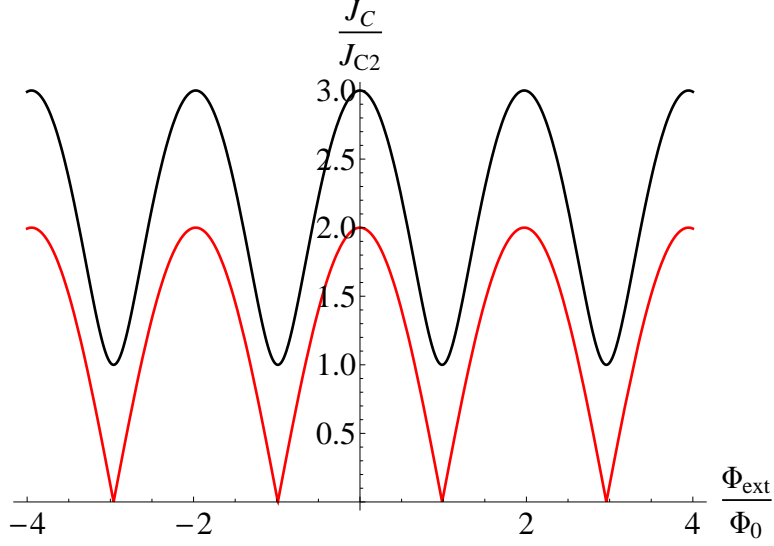


Figure 2.19: *Predicted Curves for DC SQUID Output.* Critical currents for a DC SQUID, normalized to the critical current of the second Josephson junction  $J_{C2}$ , as per Equation 2.82. The red curve is the critical current measured in a SQUID where both junctions possess the same critical current. The black curve has  $J_{C1} = 2J_{C2}$ .

while the minimum possible, which occurs when the cosine term is equal to zero, is,

$$J_c^{Min} = |J_{c1} - J_{c2}| \quad (2.84)$$

For the simplest case, where  $J_{c1} = J_{c2} = J_c$ , we can reduce equation 2.82 to,

$$J = 2J_c \left| \cos \left( \frac{\pi \Phi_{ext}}{\Phi_0} \right) \right| \quad (2.85)$$

which is plotted in Figure 2.19 along with Equation 2.82. Note that if the critical currents are not equivalent, the modulations in the SQUID critical current do not go to zero.

# Chapter 3

## Experimental Equipment

### 3.1 Introduction

The purpose of this chapter is primarily to explain the nature of the equipment we used to perform the experiments that will be described in this thesis. It will also act as a reference for future students to help them learn about the tools they will likely encounter in the lab. The first section discusses the tools used to deposit metals along with the Ion Mill. Section 3.3 looks at the microscopy systems used to characterize samples. Section 3.4 discusses the methods of sample lithography available in the cleanroom facility. Lastly, section 3.5 looks at our magneto-transport measurement systems.

### 3.2 Metal Deposition

One of the critical steps in the fabrication of thin films is the deposition of materials onto the substrate. There are many different film deposition methods, including: Thermal Evaporation, Electron Beam Evaporation, Sputtering, Molecular Beam Deposition, and many more. This section will focus only on those techniques that were used in the process of this study.

Most deposition techniques function on the same basic premise. In order to drive the desired material to the substrate, energy must be delivered to the target source material in some fashion. The user's ability to control the energy delivery results in the rate control of

the metal deposition.

The physical properties and structural quality of the resulting film is dependent on a large number of factors, one of which includes the growth rate. However, substrate temperature, metallic atom energy, material density, deposition angle, residual gas pressure or vacuum quality, and impurity concentration can all impact the deposited film. Each system will have its own advantages and disadvantages in each of these areas.

### **3.2.1 Thermal Evaporation**

Thermal Evaporation is a very straight-forward method of metal deposition. A piece of the desired metal is placed in a conductive *boat*. A current is driven through the boat to produce heating which is conductively transferred to the metal. Once the metal melts it will radiate atoms at a rate related to its temperature, which is controlled by the current applied to the boat. The more thermal energy delivered to the metal, the faster the atoms will radiate away and the faster they will be deposited on the substrate.

The boat itself is typically fashioned from tungsten or molybdenum, which is chosen for its high melting point and relatively high resistivity. Occasionally a boat will be coated with a hard white material called Alumina (Aluminum Oxide). That coating allows some metals, such as aluminum, to be evaporated despite their predilection to alloying with tungsten.

The substrate is placed directly above the metal boat at a distance on the order of tens of centimeters. Because of this, it is generally safe to assume that the metal atoms striking the sample have parallel momenta, which produces relatively uniform films and is convenient for complicated pattern designs.

### 3.2.1.1 Design

The Thermal Evaporator which was used is an Edwards Auto306 Turbo. It possesses three methods of pumping: a mechanical pump for roughing and backing, a turbomolecular pump, and a Meissner trap (cold-trap). Other than the cold-trap, which must be manually filled with liquid N<sub>2</sub>, the pumping system is entirely automatic and is controlled from a keypad at the front of the system. Use of the first two over the course of several hours is capable of dropping the chamber pressure to roughly  $5 \times 10^{-7}$  torr.

The cold-trap is a very simple design. Liquid Nitrogen can be poured into a small cylinder at the base of the chamber. The nitrogen then flows into a pipe inside the vacuum chamber and cools the walls of the pipe. Water atoms coming in contact with the cold finger are

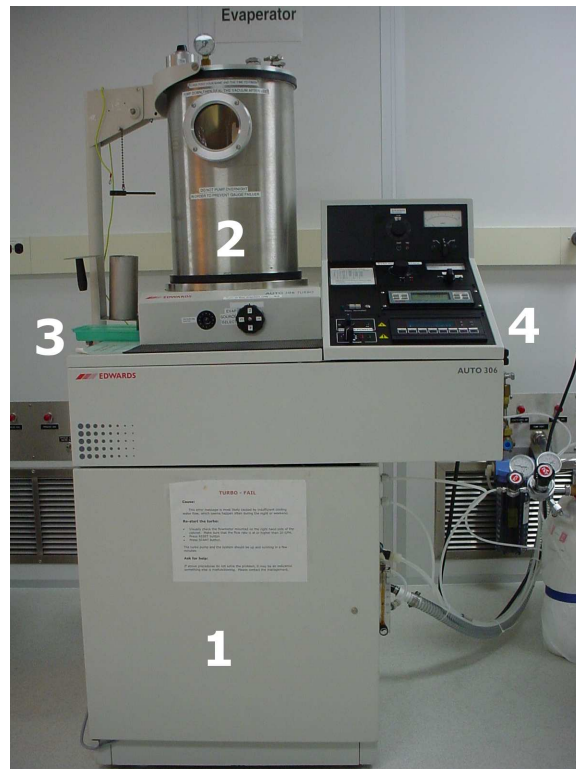


Figure 3.1: *The Edwards Auto306 Evaporator.* 1) Vacuum pump service cabinet. 2) Vacuum chamber. 3) Cold-trap. 4) Control panel. Top to bottom - evaporation current, film thickness monitor, vacuum control.

quickly frozen out of the system, and effectively "pumped out" as long as the finger remains cold.

Use of the cold-trap in tandem with the turbopump can achieve similar pressures as the turbo pump alone in roughly half the time, but can't drop the pressure much further than the turbopump's base. This implies that the system can rapidly reach its pumping limit, the point at which the pumps can't keep up with leaks from the environment.

At these low pressures, the mean free path of gas molecules in the system is on the order of several meters. This implies that any metal atoms released in the evaporation process will follow straight-line paths with little to no scattering events. This makes for a very clean film deposition, as few gas particles will become entrained in the film during growth (though many will strike the sample!), nor will scattering events cause the metal atom momenta to stray from their parallel arrangement.

Film thickness can be monitored *in-situ* during the evaporation process. This is achieved thanks to the spherical radiation of metal atoms in the system (when the material melts into a sphere, if the metal wets over the boat it gains a  $\cos\theta$  dependence). The FTM crystal can be placed off to the side of the sample, out of way of the deposition, and see the same flux of material the sample does. The FTM must be calibrated before-hand with a *tooling-factor* to account for any variation in the distance to the metal source and angle away from vertical. Recall that the flux through a given area around spherical radiator goes as the inverse of the square of the distance (the so-called "Inverse Square Law"). This calibration is done by growing a film in the evaporator and comparing the thickness measured with an AFM or other surface profiling system to the thickness measured on the FTM. The tooling-factor is the ratio of the two.

The evaporator has the capability of rotating the sample stage in two dimensions with

respect to the arriving atoms. The stage can tilt with respect to the oncoming evaporated metal, allowing for deposition angles between 90 degrees and something close to 30 degrees from the substrate face. The sample stage can also rotate about the normal to its surface, which enables the user to tilt the stage and then rotate to get a circularly uniform distribution of deposition. This is particularly helpful in creating sloped edges of the film for improving contact with metals deposited later in the fabrication process.

### **3.2.1.2 Procedure**

The evaporator is particularly simple to operate. The lid is mounted on a hinge, allowing for the system to be top loaded. The substrates are mounted onto sample holders - either tied down with pinching arms, or held down on the edges by a mask that is screwed down over the whole sample plate. The plate is then mounted onto a post in the lid attached to the mechanism that allows for external control of the tilt and rotation.

The boats should be installed into the system in the slots assigned to them. Never use a metal that is not approved for the system, in order to prevent the possibility of ferromagnetic contamination. Open up the knurled nuts slightly and slide the boat between the nut and the post. Tighten down, and take care that the boat doesn't rotate out of position. Once in place, deposit the metal pellets onto the boat. Make certain to rotate the boat stage once through to ensure that no metal falls off a boat. Any pellets that escape could potentially find their way under the gate-valve, propping it open and causing a serious system malfunction when venting.

Close the evaporator shield, close the lid, and cycle the pumping system. This system will automatically open the appropriate valves to first rough the chamber, and then engage the turbopump. The pumping should only take about two hours to reach a reasonable base

Material	Current (A)	Rate (Å/s)
Ag	2.3	1.6
Al	2.4	20.0
Au	2.6	2.9
Cu	2.2	1.5
Ti	3.6	0.2

Table 3.1: *List of thermally evaporated materials and deposition rates, used in this work.*

pressure.

Once the pressure gets down to around low  $10^{-7}$  torr, the metal deposition can be done. Slowly apply current to the boat, increasing by roughly .2 Amps every 20 to 30 seconds. Once above 1.5 Amps, occasionally check the boat to make sure it is emitting a red glow. This ensures that the current isn't shorting away from the boat. Eventually the FTM will begin to register a deposition rate. Continue increasing the current until you achieve the rate you want. Typical evaporation currents and rates are provided in table 3.1. You can find similar data in the cleanroom log books.

Once the metal has begun to evaporate and the rate is stable, simultaneously open the evaporator shield and zero the FTM's thickness and timer. Monitor the current to make certain it doesn't change much during the run, and make any necessary adjustments to maintain the current as closely as possible. As soon as the FTM reads the desired thickness, close the evaporator shield and begin ramping down the current by .2 amps every 10 seconds.

When the current has reached zero, reset the FTM monitor. This gives a convenient timer for how long the system has had to cool. Wait about 15 minutes, then vent the system. Remove the samples and the boats, close the system and pump it down until the gate-valve has opened. Tell the system to seal, so that it maintains a relatively low pressure in standby mode.

## 3.2.2 Sputtering

Sputtering is a metalizing process that operates on the principle of momentum transfer. As opposed to using heat to separate metal atoms from the bulk as with Thermal Evaporation, a positively charged ion is instead slammed into the metal target. This knocks one or more metal atoms off and provides a sufficient momentum for the metal to reach the substrate where it can adhere to the surface.

### 3.2.2.1 Principle

The trick to sputtering is a simple matter of basic electric and magnetic fields crossing at the point of interest. There are two different types of guns, the DC triode magnetron gun, and the DC magnetron gun, that are designed differently but function on the same principle.

In a DC triode magnetron gun, the electric field is generated by a cathode (hot filament) and anode that sit on opposite sides of the interaction region. When a current is driven through the filament, electrons will hop the several-inch-long gap to the anode, passing between two DC magnets that provides a uniform field. Inside the field region, the electric current will form a corkscrew shape, maximizing the volume over which it can interact with Argon gas bled into the system.

When neutral Argon gas flows into the region, the Argon is positively ionized by impacts with the electrons from the cathode, forming a plasma in the region directly above the target. The desired metal *target*, the material to be deposited, is placed between the magnets and the cathode and anode on a water cooled base which acts as the third electrode. The magnetic field passes directly over the target.

To generate the momentum transfer interaction, the target is then charged to a high negative voltage. That voltage is sufficiently high to attract and accelerate the positively-

charged Argon ions onto the target surface. When the Argon strikes, neutral metal atoms are knocked off with sufficient momentum to pass through the interaction region toward the substrate surface about 12 centimeters above the target.

The principle of the DC magnetron gun is functionally identical, but constructed differently. In this design, the target is placed directly above a pair of coaxial cylindrical magnets. This generates the necessary field over the target. The target itself is charged as before, but also acts as the cathode for the ionizing current. The anode is a small cap that is placed a small distance above the surface of the target. The result is a small donut shaped plasma region that collides with the metal surface.

The substrate on which the metal is to be deposited is held directly above the center of the target. This is the place that the deposition rate is a maximum, with about a quarter inch of forgiveness on either side for the small guns, and with more tolerance for larger guns [60]. The metal atoms that are knocked off the target will strike the substrate, condense, and adhere to the surface. With sufficient time, this process will grow a film.

The rate at which the sputtering occurs is related to two different values. The first is the target voltage. If the target voltage is higher, the Argon atoms experience a greater acceleration and strike the target with more energy. This means that more material can be released if the energy of the collision is spread among several atoms. It also means that the released atoms may have more energy, which is not necessarily favorable to film growth.

The second factor affecting the growth rate is the anode. With greater current there are subsequently more electrons flowing in the interaction region. With more electrons, the chance of an Argon atom becoming ionized increases. This means that there are a larger set of Argon atoms to be used to strike the surface of the target, and thus a larger number of metal atoms released by the interaction. This method does not adversely affect the energy

of the collisions.

It is also possible to increase the Argon gas pressure above the target, but that quickly generates diminishing returns. With increased Argon pressure there is also an increased chance of metal atoms scattering off Argon in the plasma above the target, which can quickly suppress the metal deposition rate.

Unlike in Thermal Evaporation, the metal deposited in sputtering is not well collimated. The Argon gas added to the system substantially decreases the mean free path of the metal atoms. Because of the collisions with the Argon gas, the metal can strike the sample surface from a large range of angles. This results in grown films that can be wider than the lithographically patterned features defining the growth region.

### **3.2.2.2 Design**

Our sputtering system is a commercial design produced by Simard in 1985. It includes four primary 2.25 inch DC triode sputtering guns and three 1 inch DC magnetron guns. The system also includes a 1 cm ion mill (see section 3.2.3). The key components of the system are shown in Figure 3.2.

The substrates are loaded into individual sample holders that can hold one or two 1/2" square Silicon chips. Single chip holders are used for large area Giant Magneto-Resistance (GMR) fabrication, while two chip holders are used in the vast majority of our fabrication processes. The chip rests against a slight lip in an opening in the holder. A small block of copper is mounted behind the chip and serves as a heat sink during the fabrication process. Care must be taken when tightening the single bridge screw behind the heat sink as too much pressure can break the sample, but too little will prevent the sample from making good thermal contact with the sample holder.



Figure 3.2: *The main chamber of the Sputtering System showing all seven guns and the small ion mill.* North) 1 cm ion mill. Just above it is the cap on its wobble stick, which allows us to protect the ion mill from material sputtered from the adjacent guns. Northeast) An empty DC triode magnetron gun. East) The newest DC magnetron gun. It has been disabled for the run during which the picture was taken, so it has been coated in aluminum foil to protect the contacts from sputtered material. Southeast) A gun containing a Palladium Iron alloy target. The pip in the center is an Iron plug. South) Another DC magnetron gun that has been disabled. Southwest) A gun containing Copper. West) A DC magnetron gun containing Gold. Further west is the wobble stick used to open and close samples. Northwest) A gun containing Niobium doped Permalloy.

A stainless steel mask with a single opening and four pins is screwed into the front of the sample holder with a small spring. This mask protects the samples from having metal deposited on them until the user is ready to do so. The spring allows the mask to rotate freely around the center of the holder. A small hook in the sputtering system, called the wobble stick, enables the user to rotate the mask during a run, opening and closing samples as necessary.

The sputtering system can hold eight sample holders, equating to a maximum of 16 substrates that can be fabricated in a single run. The sample holders are placed into the openings of the *Sample Positioning and Manipulation Assembly (SPAMA) plate* (see Figure 3.3), and screwed into place to prevent movement while wobbling the mask. This also creates

a good thermal contact between the sample holder and the SPAMA plate. A capillary tube feeds cold nitrogen gas down to the SPAMA plate and is used to maintain the sample temperature during fabrication.



Figure 3.3: *The sputtering system SPAMA plate.* 8 sample holders have been loaded, each with two samples held down by bridges. To the right and left are the film thickness monitors.

The SPAMA plate itself is mounted on an axle through its center, which is connected to a stepper motor at the top of the sputtering system. This motor enables a computer to control the position of each sample during the course of the run, moving them from gun to gun as programmed by the user. Two slots on the SPAMA plate are dedicated for a pair of FTMs to measure the deposition rate of the various materials put off by the guns.

Above the SPAMA plate is a liquid nitrogen cold trap. The trap is fed from a liquid nitrogen dewar connected to the outside of the sputtering system. This trap serves two purposes - one is to provide a cold bath reservoir in order to help maintain the sample plate temperature through the small nitrogen gas coil. The second purpose is to act as an additional cryopump on the system, minimizing the water content as much as possible during a run.

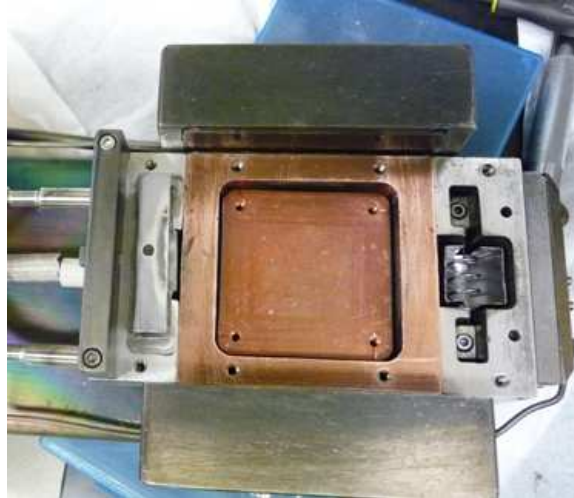


Figure 3.4: *Top view of a DC Triode Magnetron Gun.* The inset copper square in the center flanked by four holes is the target plate, which supplies the target voltage. The dark rectangular regions above and below this area are the poles of the magnet. The filament is clearly visible to the right, while the light colored metal rectangle to the left (with the centered hole) is the anode.

The SPAMA plate, cold trap, and all associated parts are mounted to the removable cap of the sputtering chamber. The top as a whole can be lifted off the chamber, allowing substrates to be mounted to the SPAMA plate, and allowing access to the guns held inside the chamber. Multiple tops can also be employed depending on the particular requirements of the fabrication. The top is vacuum sealed to the main chamber with a rubber O-ring.

The DC triode guns, or “big guns” as they are frequently referred to, are installed in ports in the side of the main chamber. An image of one of these guns is shown in figure 3.4. The target is mounted into the middle of the copper block, which provides the charging voltage for the target itself. The magnetic field is provided by the large bar magnets on either side of the target. Lastly, the ionizing current is driven by the filament to the anode on the far side of the target region.

The DC magnetron guns, one of which is shown in Figure 3.5, are often called “small guns”. They are mounted halfway between the big guns through ports at the very bottom

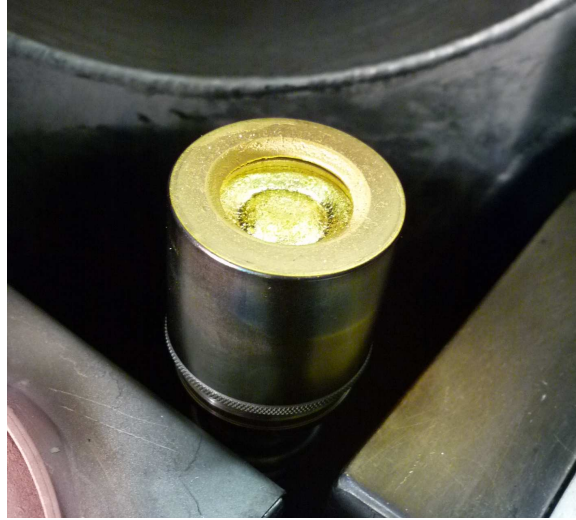


Figure 3.5: *Side view of a DC Magnetron Gun.* The cap surrounding the top acts as the anode while the target itself acts as the cathode.

of the chamber. The target is charged through the copper plate which is also the target holder. With the target installed, typically with silver paste to provide good thermal and electrical contact, the anode is mounted above it. A small piece of wire is used to determine the optimum distance between the target and the anode. The magnets are not visible in these pictures.

A *chimney* is placed above each target, with the big guns also getting a ring of aluminum foil around the chimney. This serves a dual purpose: first to constrain the plasma in the region of the target, and second to provide some measure of collimation to the metal released from the target. It also prevents cross contamination with other sputtering guns.

Another plate is mounted to an axle running in the center of the chamber. This plate, the *shutter plate* has four large holes spaced at 90 degrees around the outside. This allows the user to close off either the large guns or the small guns as necessary to prevent unwanted metal from depositing on the open substrate. The axle is connected to another stepper motor mounted below the chamber, allowing computer control of the shutter plate.

The vacuum in the system is maintained at high pressures by a standard roughing pump, and at low pressures by a cryopump. The cryopump is capable of achieving pressures around  $1 * 10^{-8}$  torr after about 2 days of pumping. Heating tape is wrapped around the outside of the chamber to remove the water that binds to the metal surfaces. Typically the system is baked at 90 °C for four to eight hours after loading the system. This dramatically improves the vacuum quality.

### **3.2.2.3 Procedure**

Loading the system is a careful process of cleaning and preparing the various parts. Since sputtering is a momentum transfer process, the surfaces that the metal and plasma will see must not be contaminated with any other materials. This maximizes the purity of the deposited films.

The sample holders and masks must be thoroughly cleaned to remove the deposited metals of the previous run. They are first soaked in a 1:3 solution of DI water and nitric acid for about 10 minutes. The masks, which are made of stainless steel, can be soaked for longer if necessary. However, the sample holders are made of aluminum which, while not strongly reactive to nitric acid, is susceptible to the cleaning. While this is not a problem for the bulk of the sample holder, it is the screw threads that can suffer the most. Eventually the screws threads will be worn down so much that the screws cannot lock into the holder.

If the deposited metal does not lift off completely, a milliliter or two of hydrofluoric acid (HF) can be added to the nitric acid solution. Make sure to remove the aluminum parts from the nitric acid bath before doing this, as aluminum is particularly susceptible to the HF.

The acid cleaning attacks iron and copper in particular. Since copper is a very common

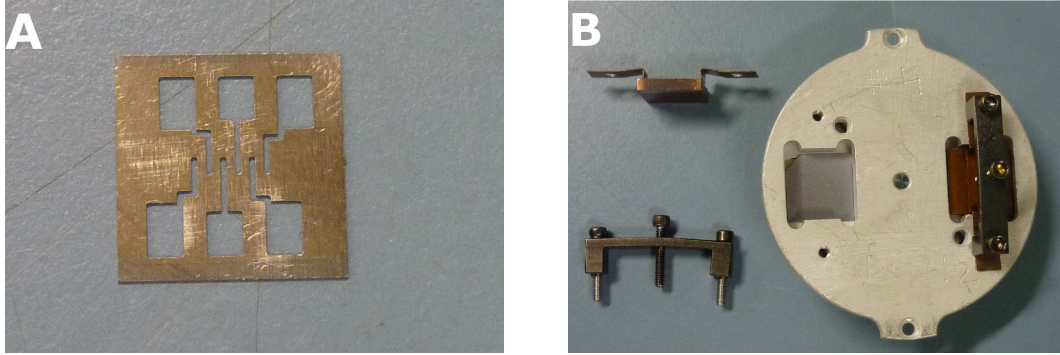


Figure 3.6: *Images of the sputtering sample holders.* A) A stainless steel sample mask used for defining patterns. This is a top lead mask (see 4.2.9). B) A CIP sample holder. In the top left is a copper heat sink. On the lower left is a sample bridge and its screws. A silicon chip (missing a corner) is sitting in the left most sample slot, ready for the heat sink and bridge to be mounted. On the right is a fully mounted chip.

material deposited in our samples, the cleaning tends to be a very quick process. But, make certain that only the stainless steel and aluminum parts are cleaned. Since the heat sinks are made of copper, they tend to vanish rapidly.

When the acid cleaning was complete, the parts were rinsed in DI water twice. They were then scrubbed thoroughly with a metal wire brush. This makes certain that any metal left behind after the acid bath is completely removed. The parts were then soaked in an acetone bath and ultrasonically agitated for 15 minutes, followed by being agitated in alcohol for 15 minutes, and lastly rinsed several times and agitated in DI water. The holders were heat dried with an industrial hair dryer (“heat gun”) to make certain that very little water is added to the sputtering system.

The substrates were then loaded into the holders, which are shown in Figure 3.6. If a mechanical mask was required, it was placed into the holder and the sample placed on top of it, reflective side against the mask. The heat sink is then mounted onto the back of the sample using a bridge. The bridge is a piece of metal with three screw holes: two through holes, and one threaded hole in the center. Screws through the outer through holes hold the

heat sink in place and place it in good thermal contact with the holders. The threaded hole allows a screw to put pressure on the back of the heat sink and make good thermal contact between the sample and the heat sink. Care must be taken when tightening the center screw that not too much pressure is applied, or the sample will crack with a rather distinctive, and frustrating, pop.

Lastly, the rotating mask should be mounted to the face of the sample plate using a special bolt. A spring is placed around the bolt, and the bolt tightened until it makes firm contact with the sample holder. It is important that the mask does not get trapped under the lip of the bolt. Jostling the mask a little from side to side with the screw most of the way in is sufficient to make sure the mask is free. The mask should then be rotated by hand to check the stiffness of the spring. It should rotate easily and not stick in any position.

The chimneys, which help collimate the metal, are kept clean by wrapping them in aluminum foil, which can be replaced between sputtering runs. They are also surrounded by a collar made entirely of aluminum foil which helps constrain the plasma. The chimney can be reused without replacing the foil but only when using the same material, and only when the purity of the film is not absolutely critical.

The shutter plate, the bottom rotating plate in the sputtering system, is also wrapped in aluminum foil for similar reasons. The metal passes through holes in the shutter plate, and those holes have to be kept clean to prevent contamination of the samples. The shutter plate can be reused in multiple runs if the guns in the system are not changed.

The guns themselves are maintained by ensuring that a set of parts is always used for the same material. They are labeled and kept separate from other materials parts to prevent accidental switching of the parts. The parts were inspected before every run for flaking of metal that had been deposited onto the surfaces. The flakes are a hazard for a sputtering

run, as they can cause shorting of the gun that will require the entire system to be opened, cleaned, and reset. A surgical razor blade was usually sufficient to remove any flakes. The SPAMA plate was also checked for flakes and scraped down with a razor blade if any were found.

The guns were loaded first by mounting the filament into place and screwing it down, making certain that it didn't touch the sides of its housing. The target was then placed in the center of the gun and screwed down. The gun parts were placed on top of it in their approximate location to make certain that the target didn't come too close to the gun ring. A close spot could cause intermittent shorting across the gap, or could allow material to build up and completely short the system. The gun parts were then mounted into place over the target. Lastly, a magnetic plate was placed over the entire gun, and the chimney and collar placed around the aperture.

Once all the guns were in place, the shutter plate was mounted into the system. The plate was mounted to the axle by two screws accessible through the center hole of the plate. The screws were initially left a little loose, so that the plate could be rotated until the screws abut the edge of the slots. This helped to guarantee that the shutter plate was in the right position for the computer control. It was also helpful to turn on the computer control and check the motion and positioning of the plates before closing.

The sample holders were mounted onto the SPAMA plate with the pins of the rotating masks pointing down. The holders were screwed down on either side to prevent movement when rotating the masks. Even if the run wasn't full, it was ensured that every sample slot had something in it to help keep things clean, with the remaining holder spots filled by blank holders.

The temperature of the substrates is measured by a thermocouple that is wound around

the axle of the SPAMA plate. The little square piece of copper was mounted between the heat sink and its bridge screw on one of the samples. It was important to avoid using a sample that had been aligned to a mechanical mask, as loosening the bridge screw would cause the alignment to shift. The screw was tightened onto the thermocouple, and care was taken not to accidentally break the substrate chip.

At this point the system was ready to be closed and pumped out. The top of the system has a large number of tubes, pipes, and wires hanging off it that could get trapped into the system. The space between the two halves needs to remain free and clear of anything that could get trapped between. Lastly, the rubber o-ring sealing the joint was checked to make sure it was in place and not damaged.

Once the top was down and it appeared that there were no leaks, the roughing valve was opened slowly to begin pumping on the system. Going slowly protected the pump from seeing too much gas all at once. As soon as the system hit 20 torr, the roughing valve was opened all the way and the system allowed to reach a pressure lower than  $1 \times 10^{-1}$  Torr. At this point, the roughing pump valve was closed and the cryopump's gatevalve was opened the whole way.

Typically the guns were tested, which required the pressure to reach values of low times  $10^{-6}$  torr. This would take a few minutes, during which the cooling water for the guns was turned on, as well as the computer control box for the plasma voltage and filament current. Once low enough, argon gas was leaked into the guns to be tested. Note that the small guns get their argon from the big guns nearby. With the argon on, the gatevalve was closed until the ion gauge shows a pressure a little above  $2 \times 10^{-2}$  torr. The breakers for the guns were powered on, and then the plasma ignited in each gun one at a time. It was checked to make certain the plasma came on by visually inspecting the gun through the window before

Material	Voltage (V)	Current (A)	Rate[1] ( $\text{\AA}/\text{s}$ )
Co[2]	100	.38	.2
Cu	300	.44	5.0-5.5
FeMn	500	.5	4.7
Nb	600	.6	4.5-5.0
Ni[2]	100	.3	.3
PdFe	210	.46	5.4
Py, NbPy	500	.44/.5[3]	5.0

Table 3.2: *List of sputtered materials and deposition rates for 2.25 inch guns.* The voltage is the target voltage, and current is the filament current. [1] Approximate. [2] Co and Ni were intentionally run slowly when growing the Co/Ni multilayers. See Chapter (5). [3] The current applied to Py alloy targets needs to be increased as the concentration of Py increases.

moving on. This was the most common point for problems, so it was worth being careful.

Once the guns were on, the pressure was reduced by opening the gatevalve until the ion gauge read  $2 \times 10^{-3}$ . This was done slowly so as to not shock the guns. After a few minutes, the plasma voltage was slowly increased, at a rate of about 50 V every 30 seconds. It was safest to run the voltage to the value intended for the run, but typically 100 or 200 V was sufficient to detect the majority of issues. This did not catch problems due to the gun heating and expanding - though that was a rare failure mode. See Tables 3.2 and 3.3 for the typical operating parameters of the guns.

As soon as the system had been tested, it was turned off in exactly the reverse order. Once the argon was off, the gatevalve was set at between seven and ten turns from its closed position. The heating tape was turned on using an electronic timer and set to between four and eight hours.

To perform the run, the system was given enough time for the pressure to drop to lower than  $4 \times 10^{-8}$  Torr. Sometimes this was done in a single overnight bake, but it typically required 36 to 48 hours to achieve. If the quality of the films was not particularly critical, for example when doing top leads (see Chapter ), an overnight pump-down was sufficient.

Otherwise a two day pump-down was preferred.

With the pressure sufficiently low, the system was prepared to be run. First, the argon purifier was turned on. This was powered up about an hour before the run to allow the titanium sponge (oxygen grabber) to reach a temperature of 800 °C. This was done to prevent random oxygen molecules in the high purity argon from interacting with the metal and ruining the film.

The dry nitrogen gas line was hooked up to the system, along with the liquid nitrogen line. The dry nitrogen was started first to flush the capillary tube of any air that had bled into the lines so that they didn't become blocked. Then, the dry nitrogen was sealed off and the liquid nitrogen run into the cold trap. This caused the cold trap at the top of the chamber to cool, entraining any water molecules that were still present in the vacuum. Once the cold trap temperature was down to -190 °C, the dry nitrogen line was reopened. This line drives high pressure nitrogen gas into the system past the cold trap and sample plate. This transferred heat away from the sample plate, maintaining the deposition temperature.

When the sample temperature drops below -20 °C, the guns were powered on in the same way as the test. The filament current was not changed by more than 50 milliamps every 30 seconds, and it was never changed soon after changing the plasma voltage. This protected the targets from thermal shock.

With the target voltages and currents at their required values, the run could be started. The computer controlled the majority of the tasks in the system. It was typical for the film thickness monitor to be used after every two samples so that the computer knew the correct deposition rate, which could drift with time during the run. The deposition time is entirely controlled by the computer. It takes the thickness provided to it by the run file - which is setup by the user before the run - and computes the time based on the measured deposition

Material	Power (W)	Rate ( $\text{\AA}/\text{s}$ )
Au	30	3.2
Cu	45	1.7
FeMn	35	1.5
Ru	11	0.4

Table 3.3: *List of sputtered materials and deposition rates for 1 inch guns.* The control parameter for these guns is the target power.

rate.

A “dummy run” or two was performed to eat up about 15 minutes at the beginning of the run. This dummy run, done with all samples closed, allowed for a double check of the alignment of the sample over every gun. This ensured any corrections to the sample position that were required could be performed before the first sample was run. This also acted as an additional pump on the system, a *getter pump*. Comparisons between runs using a dummy run and foregoing the dummy show increased interface resistances in the first sample of the latter.

The order in which the samples are to be grown was decided by the user. It was standard procedure not to grow the samples in numerical order so that any possible change in the system, such as Argon pressure or applied voltages to the guns, didn’t appear as a trend in the resulting data. It was also typical to run the guns through a test substrate or two without opening the samples so that the pressure can be further reduced by the gettering process and the guns can be stabilized.

The computer is told which substrate to run by the user. It then moves the substrate into the position where the *wobble stick* can reach it. The user was then able to rotate the mask plate using the hook at the end of the wobble stick, placing the open section of the mask over the substrate. When ready, the computer moved the selected substrate into the window for inspection, and was then told to either move back to the wobble position for

further adjustment, or told to proceed with the fabrication.

Once all the samples had been made and the guns had been turned off as described above, the dry nitrogen and liquid nitrogen were closed off, the argon purifier turned off, and the gatevalve closed. Nitrogen exchange gas was released into the chamber, to roughly 30 torr, to allow the cold trap and samples to receive heat transferred from the walls. The system was then allowed to warm up naturally to room temperature overnight, or was baked for 45 minutes to bring it up to room temperature. It was important that both the samples and cold trap reached room temperature before opening, so that no water adhered to the parts inside the chamber.

With the system open, the samples and gun parts were removed. With everything out, the top was again closed, and the system pumped out to a couple torr as a standby condition.

### **3.2.3 Ion Mill**

Ion milling is most easily described as “sputtering in reverse”, so while it is not, strictly speaking, a deposition method, it is most closely associated with those techniques. The ion mill generates ionized argon gas that is then accelerated at a sample held above the mill. The charged argon ions then chip away at the material present on the sample through momentum transfer. The material that comes off is carried away from the sample and either deposits itself elsewhere in the system, or is pumped out.

A diagram of the ion mill is presented in figure 3.7. Argon gas is fed into the *discharge chamber*. By applying a current to the cathode the gas is ionized by a discharged electron beam across the gap to the anode. Above the cathode and anode lie two delicate carbon grids. The first grid, called the screen, helps collimate the ions and keeps them from colliding with the second grid, called the accelerator. This is done with a fine adjustment to ensure that

the holes in each grid are perfectly aligned. The accelerator is supplied with a large negative voltage with respect to the discharge chamber in order to drive the positively charged argon ions up out of the discharge chamber and at the sample.

Above the accelerator grid sits a final filament. The *neutralizer* is designed to add electrons into the argon beam. This is not done to neutralize the argon ions, however, and instead acts to prevent the mutual repulsion of the similarly-charged ions. They also serve to balance the ion current in the event that the beam is directed at an insulating surface.

The milling rate of materials is dependent on their density and binding energy, along

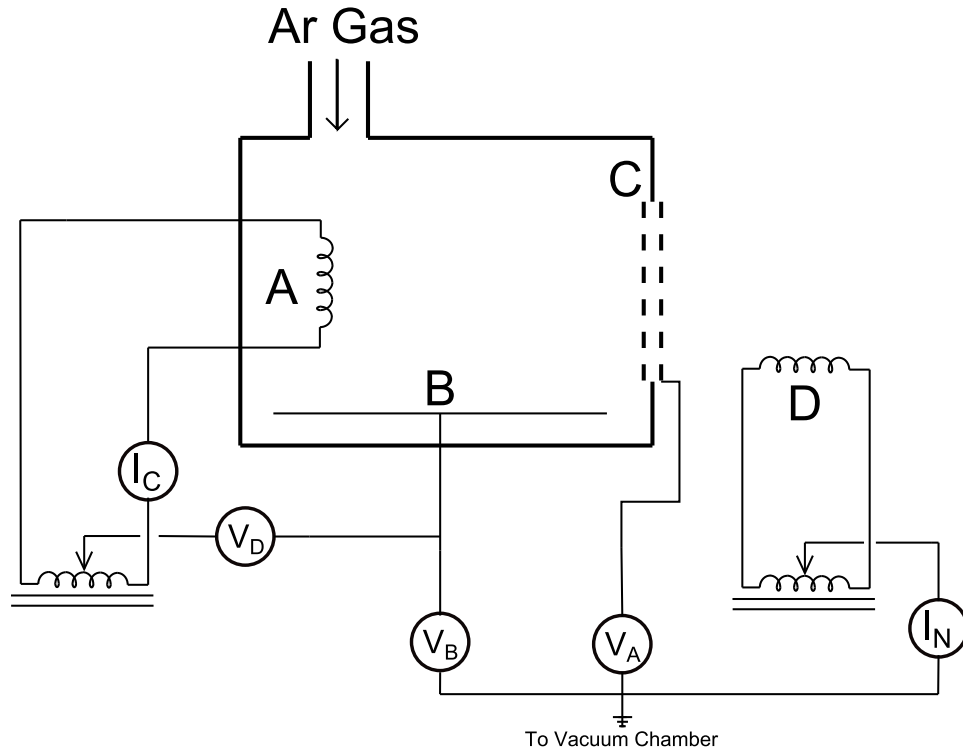


Figure 3.7: *Diagram of an Ion Mill with its circuit diagram.* A) The cathode filament sits inside the discharge chamber, near the argon flow intake. B) The anode. The anode is designed to spread the current out as much as possible, maximizing the area over which argon gas can be ionized. C) The screen (inside) and the accelerator (outside). D) The neutralizer filament, which is held about a centimeter above the accelerator grid.  $I_C$  is the Cathode Current,  $V_D$  is the discharge voltage,  $V_B$  is the beam voltage,  $V_A$  is the accelerator voltage, and  $I_N$  is the neutralizer current. Operating values for these quantities are provided in Table 3.5.

with the energy of the incident Argon atoms. This implies that careful planning must be used when milling complicated structures involving different materials. Care must be taken to ensure that the milling depth of each material is exact.

Unfortunately, unlike with thermal evaporation, the film thickness monitor cannot be simultaneously used while milling. This means that the milling rate must be established before and after the sample is milled. The milling rate is measured by depositing gold on the FTM and then checking the rate at which the gold is milled away. All materials used in our processes have had their milling rates calibrated in such a way that the thickness of each material can be converted to a relative thickness of gold. Using this mathematical equivalent to alchemy, the appropriate milling time can be calculated based on the measured rate of gold milling. This is explained further in Section 3.2.3.2

Any significant variations in the rate during milling should be accounted for. Nothing can be done if the rate has increased during the course of the run. If the rate has decreased however, the user can assume a simple linear decay in the rate over time. By calculating the new milling time with the new rate, taking the difference from the first rate, and dividing by two, the user can approximately regain the lost milling from the rate decay.



Figure 3.8: *Top view of the inside of the ion mill chamber.* North) The 3 cm ion mill. East) The 1.25" DC magnetron gun. South) The Silicon Monoxide evaporation source. West) Another gun that has been permanently disabled.

### 3.2.3.1 Design

Our group possesses a small chamber designed specifically for Ion Milling processes. It contains a 3 cm ion mill, a 1.25" sputtering gun (see 3.2.2), and a boat for thermal evaporation of Silicon Monoxide. Figure 3.8 shows these parts inside the small chamber.

The samples are loaded into specially designed holders, each capable of accepting only a single chip. They are manufactured in three parts. The first is a sample holding disk with a thin inset region for the sample and a circular aperture. Above that sits a copper disk with a square protrusion that rests in the inset of the holding disk and makes contact with the sample. This copper disk acts as a heat sink for the sample. Lastly, an iron disk is mounted on the back of the heat sink. The three parts have holes drilled through them, and the ones in the iron disk are threaded to lock the parts together.

The chamber is capable of holding 5 samples at a time. The samples are loaded into the chamber individually through a load lock above the top of the chamber. The sample is magnetically attached to the end of a long sliding probe controlled by a black magnetic cylinder. This allows the probe to be raised and lowered from outside the system. Once the load-lock is pumped down by roughing pump, the main chamber is opened and the sample lowered onto the sample plate.

The sample plate itself has 5 slots for samples, along with an FTM and a hole. The whole thing is mounted on an axle that runs to a graduated knob that can be rotated by hand. This allows the user to rotate the sample plate inside the chamber. Similar to the sputtering system, there is also a bottom shutter held below the sample plate. It is mounted to an axle that can be rotated by hand from the bottom of the system. This shutter contains only one hole, allowing the user to control exactly what gets exposed at any particular time.

Material	K
Au	1
Cu	1.49/1.9*
Nb	6.71
Ni	3.91
Pd, PdFe, PdNi†	1.33
Py, NbPy†	2.66

Table 3.4: *Values for converting material thickness to an equivalent thickness of Gold.* \* A value of 1.49 Å/s was used in the majority of the experiments. That value was corrected to 1.9 Å/s during the SQUID experiment. † The same value is used when the concentration of the dopant material is sufficiently low.

The system is pumped on by a turbomolecular pumped backed by a mechanical pump. With the system regularly kept under vacuum - made possible by the use of the load lock - the turbo pump is capable of bringing the pressure to about  $2 * 10^{-8}$  torr in a couple hours. If the system is opened, it is necessary to bake the system using heating tape to remove water from the walls of the chamber. Another day of pumping will typically bring the system back to base pressure.

The Silicon Monoxide is used as a protective layer after ion milling, and as a resistive barrier for the formation of specific features in the sample fabrication. Typically a feature is defined lithographically (see 3.4), then the sample is milled away with the defined region protected by the resist. Once the milling is done, the Silicon Monoxide can be evaporated on *in-situ*, preventing the possibility of oxidation of any layers inside the sample.

### 3.2.3.2 Procedure

Before running the ion mill, Gold was sputtered onto the FTM. By milling the Gold off the FTM the milling rate was measured. However, this rate applies specifically to Gold. In order to know the milling rate for other materials, a measurement of the relative rate of milling compared to the Gold rate was needed. This was done by sputtering a film of the material

and milling away a small region for a set amount of time. By measuring the resulting step height, the ratio of milled material to milled gold could be computed.

This ratio, referred to as the "K-factor", can be conveniently used to calculate the appropriate milling time for a stack of known materials. The milling time is,

$$T = \frac{1}{R_{Au}} \sum_{i=1}^n K_n t_n, \quad (3.1)$$

where  $R_{Au}$  is the measured milling rate of Gold,  $K_n$  is the material's relative thickness to Gold, and  $t_n$  is the true thickness of the material in Angstroms. The Gold milling rate should be measured between each sample, and the time recalculated if the milling rate changes. The K-factors used in our experiments can be found in table 3.4.

Setting the ion mill was a procedure requiring some care. Since two different mills were used with the same power supply, an ID 2500 Ion Beam Drive built by Commonwealth Scientific, it was possible to destroy the filaments if the wrong settings were applied. Before turning on the power supply, the beam voltage was turned down the whole way so that the sudden power surge wouldn't overload the filaments. When the power supply is turned on, the beam voltage was slowly increased to its proper operating value. The other values were then adjusted as necessary. See table 3.5 for the typical running parameters. Before turning the power supply on, the argon flow should be started, and the chamber pressure should be kept around  $2 \cdot 10^{-4}$  torr. This ensures sufficient ionized Argon for milling, but a long enough mean free path to minimize scattering.

The sample to be milled was aligned over the Ion Mill with the shutter plate closed after the rate had been measured. Once aligned, the shutter plate should be opened again and the timer started simultaneously. That was typically a convenient moment to calculate the

Parameter	Big IM	Small IM
$V_{Beam}$	300V	175V
$V_{Acc}$	30V	50V
$V_{Dis}$	39.1V	40V
$I_{Beam}$	9mA	2mA
$I_{Cath}$	4.7mA	4.7 mA
$I_{Neut}$	9.7 mA	2.5 mA

Table 3.5: *Operating parameters for each ion mill.*  $V_{Beam}$  is the Beam Voltage,  $V_{Acc}$  is the Accelerating Voltage,  $V_{Dis}$  is the Discharge Voltage,  $I_{Beam}$  is the Beam Current,  $I_{Cath}$  is the Cathode Current, and  $I_{Neut}$  is the Neutralizer Current.

milling time for the sample.

Once the calculated time was reached, the shutter plate was closed and the FTM maneuvered over the ion mill again to remeasure the milling rate. If the rate had changed, the drift was assumed to be linear. An increase in the rate could not be corrected, but could be accounted for by assuming that the true rate was the average of the new value and the measured starting value. If the finishing rate is lower than the starting rate, the difference in the milling times calculated from the two rates was found and divided by two. The sample was remilled for that time to correct for the drift.

All samples were ion milled before moving on to SiOx. Like other evaporators, the SiOx was warmed slowly to prevent damage to the boat. It was also important to make sure that both the turbopump gate valve and the load-lock gate valve were open during this step. The entire chamber needed to be at a uniform pressure to make certain that an accurate measure of the SiOx deposition rate was made. If the load-lock gate valve were closed when the SiOx rate was measured, when that valve was reopened to use the sample insertion arm, the chamber pressure would rise subsequently reducing the SiOx rate.

The deposition rate was measured using the FTM. It was often helpful to lower the sample insertion arm and allow it to rest just above the FTM to allow for easier alignment

to the SiO<sub>x</sub> source. Once the rate had been measured, the shutter was closed and the arm used to lift a sample from the sample plate. The sample needed to be well centered on the arm so that it wouldn't fly off while rotating during the run. The sample plate was rotated so that the hole was beneath the sample. It was then positioned so that it was roughly at the same height as the FTM crystal. Using an O-ring, the handle of the arm was coupled to the motor mounted to the top of the small chamber. When turned on, the motor provided rotation through the magnetic coupling of the arm to the sample. It was important to make sure the motor didn't run too quickly and cause the sample to fly off the arm.

While the sample was rotating, the shutter plate was opened and the timer started simultaneously. The sample was kept rotating through the entire process - this sometimes required a slight manual control to maintain the rate, either slowing or aiding the rotation. Once the appropriate time had elapsed, the shutter plate was closed, the motor turned off, and the FTM moved under the sample arm. The SiO<sub>x</sub> rate was remeasured using the same principles as used with the ion mill to decide if more deposition was necessary. Once the sample was finished satisfactorily, it was returned to its spot on the sample plate.

Once finished with the SiO<sub>x</sub>, the boat was cooled slowly to allow it to gradually equilibrate. The system was given some time to cool before removing the samples from the small chamber.

## **3.3 Microscopy**

### **3.3.1 Scanning Electron Microscopy**

One of the significant achievements in microscopy, the Scanning Electron Microscope (SEM) is an extremely versatile tool for high resolution imaging of microscopic features. Typi-

cally, SEM's today are capable of very high magnification (500000x for our clean room's best system, but better for others) due to their particularly fine resolution. The improved resolution is a combination of using a very small particle, along with improved methods of noise reduction - such as digital signal averaging.

An SEM is designed in a columnar structure, such as in figure 3.9. At the top, in the lowest pressure region ( $1 \cdot 10^{-8}$  torr in the best systems), resides the electron gun. The gun uses a cathode to emit electrons towards an anode placed below it. Between the anode, which has a small hole to allow the beam to pass, and the cathode rests a metal cap with a small hole called the *Wehlnet cap*. The Wehlnet cap is maintained at a large negative bias and acts as an electrostatic lens for the emitted electrons. This confines the beam and brings it to a crossover point just in front of the hole in the anode.

The anode itself is kept at a large positive voltage with respect to the Wehlnet cap, which is also ground with respect to the rest of the SEM. This allows it to act as an accelerator for the electron beam. Many electrons end up striking the anode during the course of operation, but a large number pass through the hole at the center. This improves the beam profile so that a better image can be produced.

Below the anode reside a series of electromagnetic lenses. The first is the condenser lens, which further constricts the electron beam as it travels down the column and helps minimize electrons being driven out of the beam by coulomb repulsion. Below the condenser is the objective lens which is controlled by the user to bring the beam into a cross over point, or focus, on the surface of the sample. Inside the opening of the objective lens resides the scan coils, which are driven by the computer to deflect the beam in a sweeping pattern known as a raster, which is similar to the sweep of a TV screen. Lastly are a set of eight small electromagnets called the stigmation coils, which allow the user to control the beam's shape.

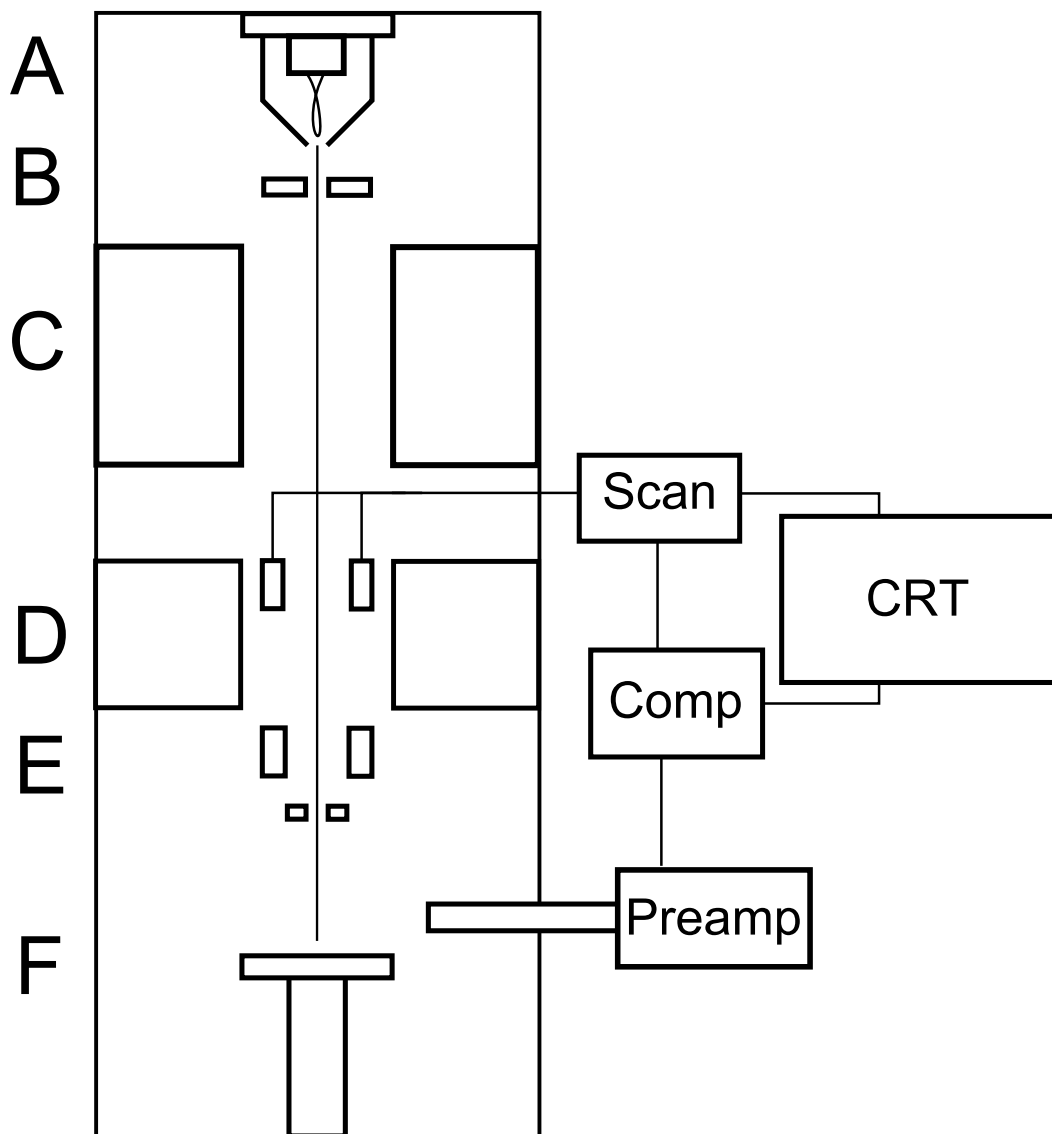


Figure 3.9: *Diagram of the guts of an SEM.* A) The filament sits inside the Wehlnet cap. B) The anode. Along with the parts in A, this comprises the “electron gun”. C) The Condenser Lens. D) The objective lens on the outside, with the scan coils embedded inside. E) The stigmation coils, below which sits the final aperture. F) The sample stage and Everhart-Thornley detector. The computer (Comp) outside drives the generator that controls the scan coils (Scan) and the raster of the screen (CRT). The Preamplifier (Preamp) sends its signals to the computer which is presented on the screen as a variable brightness.

After interacting with the lenses, the shaped beam passes through a final small aperture which again weeds out stray electrons to control the beam shape. The final beam impinges on the sample surface and the electrons interact with the sample material in a region that looks vaguely like a tear-drop. The electrons perform a number of different scattering processes inside this region, producing a variety of measurable emissions. The most important process occurs when an inbound electron strikes a weakly bound conduction band electron in the material. The scattering event releases the bound electron which can escape the sample if close enough to the surface. This released electron is known as a *secondary electron* and is very low energy (3 to 5 eV).

The secondary electrons are measured by a detector placed near the sample region at the bottom of the SEM column. The *Everhart-Thornley detector* uses a low-voltage faraday cage to attract the secondary electrons. This tends to draw the vast majority of secondary electrons in the chamber, regardless of the initial direction of their momentum, due to their low energy. Inside the faraday cage is an accelerator, whose 12000 volts are shielded from the SEM beam by the faraday cage, which drives the secondary electrons into a scintillator. The electrons are converted into light, which pass out of the SEM column into a photomultiplier.

The resulting signal is tied to the same computer driving the raster, and can therefore be combined into an image. The number of secondary electrons detected is presented as brightness on the screen. As the electron beam rasters, the brightness at each point is presented. Features can then be discerned by the variation in emission of secondary electrons which is presented as contrast differences on the screen [61].

### 3.3.1.1 Design

Our SEM is a S-4700II designed by Hitachi. Its maximum sample holder size is 4-inches in diameter, making it capable of imaging even the largest wafers capable of being processed in the cleanroom. The sample is loaded into the system through a load-lock, allowing the SEM to remain under vacuum at all times. Special valves above the sample stage isolate the gun from the sample region, preventing the gun from experiencing pressure variations while loading and unloading samples.

The electron beam is emitted from a Field-Emission gun. The filament has a sharp tip which is exposed to an external electric field. This produces the gas of electrons that can then be accelerated down the column. This type of gun, known as a cold-cathode filament, has many advantages over more common hot cathode gun types, including: a long lifetime typically measured in years rather than months as for tungsten filaments, increased brightness by a factor of a thousand, vastly improved resolution, and higher available magnifications.

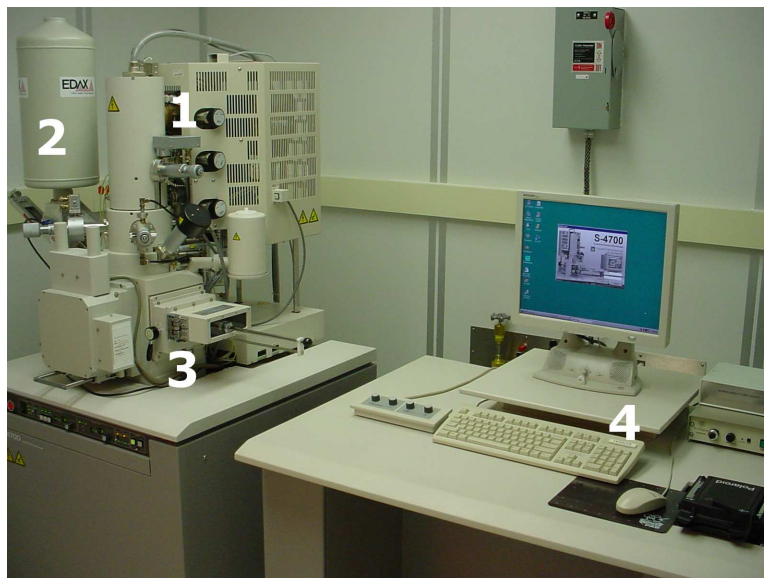


Figure 3.10: *A picture of the Hitachi S-4700II SEM.* 1) The beam column with pumping equipment behind. 2) The EDS system and nitrogen dewar. 3) The sample load-lock. 4) The computer control station.

The system itself is entirely computer controlled. For example, the sample stage is entirely driven by computer hardware. This allows the user to adjust the position and orientation of the stage with point-and-click software, which is a significant advancement over older models. This also allows the computer to better protect the SEM from careless user mistakes that could, for example, crash the stage into a critical part inside the SEM.

The maximum magnification of the system is 500000x with a maximum accelerating voltage of 30 kV. Its maximum resolution is 1.5 nm at 15 kV, which is the usual operating voltage in most cases. It is capable of up to 40 degrees of tilt, which, when combined with a sample holder that gives a perpendicular orientation for the sample, allows the system to take profile images. Such profile images can be extremely useful in fabrication characterization, for example undercuts in lithography procedures.

This SEM also includes an *energy-dispersive spectroscopy* (EDS) system. This allows for the measurement of x-rays emitted by the electron beam's interaction with the sample. The usual x-ray production in that process is the result of inelastic scattering. When an inbound electron from the beam removes an inner orbit electron from the material, a higher orbit electron may fill the gap. This transition emits an x-ray often called a *characteristic X ray* since it is characteristic to the element involved. By measuring the energy of the emitted x rays, it is possible for the system to spatially identify the materials present and their elemental concentrations.

### **3.3.2 Atomic Force Microscopy**

Atomic Force Microscopy (AFM) is a surface probe method originally developed by Gerd Binnig, Calvin Quate, and Christopher Gerber in 1986. The method takes advantage of a force exerted on the surface of a sample by the probe tip which possesses a magnitude on

the order of interatomic forces. Originally discovered in the process of performing Scanning Tunneling Microscopy (STM), the first AFM measurements were done with a STM tip held parallel to the surface. The deflections of the tip were then measured by a second STM tip, and atomically resolved images were possible by plotting the deflection as a function of tip position.

The interactions present between the tip and the sample include electrostatic forces, Van der Waals forces, and dipole-dipole interactions. All of these combine to provide the feedback to the tip that allows it to react to the changes in the surface topography. The ability to detect the resulting reactions of the tip is directly linked to its flexibility, since a more flexible tip will deflect further for a greater applied force. Seen another way, the more flexible the tip, the less force needs to be applied in order to generate a measurable deflection, and the more sensitive the AFM is.

The development of better tips have improved the range of materials measurable by AFM. Along with sensitivity, flexible tips also minimize the damage caused to the surface by the interaction with the probe - a considerable worry for surface science studies. Modern tips are microfabricated from silicon and its oxides, which have a reasonably low spring constant, on the order of 1 N/m, and therefore a reduced effect on the sample. These tips also have resonant frequencies in the tens of kHz which enable faster scanning.

Many different measurement methods are used today to detect the motion in the tip. Our experiments used a system designed for the deflection technique. In this strategy, a laser strikes the surface of the tip and is reflected towards a pair of photodiodes. Shifts in the intensity detected by each photodiode indicate the changes in angle of the tip to the laser and can be interpreted as motion by the computer.

The system employed in the AFM measurements in this work was a Dimension 3100



Figure 3.11: A picture of the Dimension AFM. From left to right are: the vibration isolated sample stage, the computer control station, and the Nanoscope control boxes.

Scanning Probe Microscope (SPM) designed by Veeco. Tip size limits its resolution to between 5 and 15 nanometers laterally, but it has an uncertainty of less than a half angstrom vertically. This makes it extremely useful as a tool to accurately measure the thickness and surface roughness of the films grown, and the remaining thicknesses after ion milling.

All measurements with this system were done in air at room temperature using a tip patterned from Antimony-doped Silicon. This material has a resistivity of 0.01 to 0.025  $\Omega$ -cm. The tip itself was 4  $\mu\text{m}$  in diameter, limiting the resolution of the system. The cantilever as a whole was 125  $\mu\text{m}$  long and 40  $\mu\text{m}$  wide. This gave it a resonant frequency around 320 kHz, and a surprisingly high spring constant of 42 N/m.

The system was always run in dynamic contact mode, or *tapping mode*. In this setting the cantilever tip is vibrated near its resonant frequency at amplitudes of nearly 100-200 nm. As the tip approaches the surface, it is beset by the short range forces which suppress the amplitude of the oscillation. The system then controls the height of the tip above the sample in an attempt to maintain the oscillation amplitude. The tip height can then be

plotted against position to generate an image which represents the surface topography of the sample.

The primary advantage of tapping mode is in the reduction of damage to the sample caused by “dragging” the tip over the features as is done in contact mode. Tapping mode is a less invasive procedure, and tends to preserve the features of the sample better than other methods. This makes it preferable for samples that need to be measured multiple times after different fabrication steps, as the effects of the AFM can be safely ignored.

### **3.4 Lithography**

While the word lithography traditionally denotes a printing technique involving a limestone plate, the methods used here are not quite so archaic. That said, the basic principle is surprisingly similar. Traditional lithography involves drawing an image onto a limestone plate with wax, fat, or oil and then applying an etchant to the stone. The regions that were not protected by the grease based coating would be scored by the etchant. When water was applied to the stone, it would settle into the etched regions. Then an oil-based ink could be applied, and since the oil is repelled by water, only the regions that were unetched would accept the ink. The stone could then be applied to a piece of paper and the image created.

In the lithography of electronic devices, the use of stones has fallen by the wayside. However, the idea of etching out a region to define the important areas remains the same. How this is done depends on the scale of the device to be created.

### 3.4.1 Optical Lithography

Optical, or Photo, lithography is the most common method used for device fabrication. It has a large number of advantages over other methods, and is capable (for a price) of patterning devices with incredibly fine features.

The principle is simple. A sample is coated with a photo-reactive organic compound. When exposed to particular wavelengths of light the compound reacts to the photons. In a positive reaction, the energetic photons break the bonds, shortening the organic molecules. In a negative reaction bonds are formed instead, making the exposed molecules longer.

The sample is placed under a mask that defines the regions to be written. The mask is usually a glass plate that has been coated with a thin layer of chrome. The chrome regions serve to block light from the sample, while the open regions allow the light to pass. The sample is brought into direct, firm contact with the chrome side of the mask and held in place. The sample is then exposed to the light source for a length of time defined by the user.

Once exposed, the sample is rinsed in a chemical solution called a *developer*. Each variety of photoresist has its own unique developing agent, which serves to dissolve the resist. The shorter the bonds in the resist, the faster it will be dissolved away in the process. By accurately timing the development, it is possible for the features to be revealed as presented in the mask. This causes the sample to be opened all the way down to the substrate in the exposed regions, while the unexposed regions remain protected by the resist.

Each chemical has its own properties and procedures for proper exposure and development. Our methods for sample coating are explained thoroughly in Chapter .

Our Optical Lithographer is designed by ABM, Inc, and is shown in Figure 3.12. The

light source emits in both the UV (405 nm) and deep UV (365 nm) spectrums. Using S1813 photoresist it is capable of writing features with dimensions on the order of one micron. It can accept either four or five inch masks, and can write either full wafers or single chips. Any mask size is available for chips up to one inch square. For wafers only five inch masks are available, and it can write wafers up to four inches in diameter.

Alignment is done using a built in split-field microscope with magnifications up to 20x. The sample stage can be positioned using three differential micrometer controls to drive x and y position, as well as rotation. It also uses a micrometer control for controlling the sample distance from the mask.

#### 3.4.1.1 Procedure

Once the samples had been coated and baked (see Section 4.1.3) they were exposed.

The samples were held in place on the wafer chuck with a vacuum. The wafer chuck uses a series of holes spaced a quarter inch apart to apply the vacuum to the back of the chip. Since the chips were never larger than one-half inch on a side, they were smaller than the

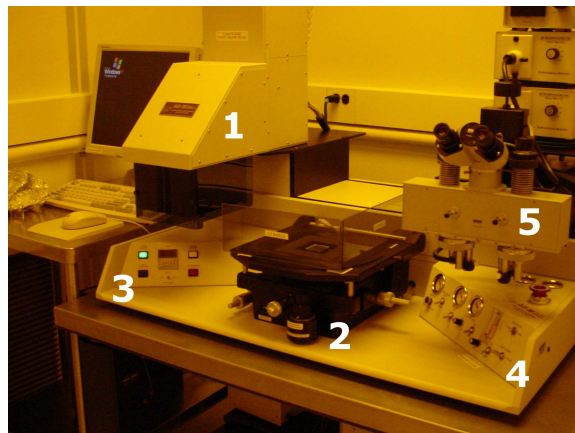


Figure 3.12: *The ABM Mask Aligner.* 1) UV Light Source. 2) Sample region including sample chuck, mask frame, and stage controls. 3) Exposure controls. 4) Vacuum controls. 5) Microscope.

area over which the vacuum was applied. A thin piece of low density polyurethane (LDPE) plastic, like that from a plastic sandwich bag, was cut to fit over the vacuum holes. By cutting out the middle of the plastic, the center hole was exposed and used to hold down the sample.

The mask was hit with a little N<sub>2</sub> gas to blow off any dust that may have accumulated on it. It was important for the quality of the lithography that the sample made contact with the mask at a distance of less than about 2  $\mu\text{m}$ . Any dust in the way may be bigger in radius than this distance, and may therefore ruin the lithography. The mask was then placed on the mask frame and the mask vacuum turned on. The vacuum holds the mask in place so that it can't move during the lithography.

Typically our masks included four different patterns at the corners of a square one inch on a side. It was usually easiest to pick a corner of the mask aligner to use regularly, and then rotate the mask to put the desired design over that corner. This way the lithography was identical every single time, regardless of the design used. All of the writing was done in the upper right corner, and the sample was placed on the mask aligner so that the center of the sample was offset by no more than 5 millimeters from the center of the chuck in that direction.

The sample was slowly raised up to the mask. Once it began to make contact, the open areas of the mask would show Fresnel lines from the thin interface of air between the mask and the sample. At the same time, as the sample approaches the point of good contact, the micrometer control will begin to get tight due to the chip making physical contact with the mask. If the Fresnel lines didn't appear, but the height adjustment was tight, there was likely some piece of dust preventing good contact with the mask.

The sample was typically checked for the Fresnel lines before spending time aligning the

chip. The easiest marks to align are also those that leave large open areas on the design, on the order of a square millimeter at least, so the Fresnel lines are easily visible to the naked eye. The sense of touch on the micrometer control was good enough to detect contact, but not sufficient to guarantee that the writing would come out properly.

If the sample was capable of making good contact, it was aligned to the mask. The chip was backed down in order to ensure it wasn't stuck to the mask before trying to align. Failure to do this would cause the chip to stay in place while the chuck moved beneath it. It was also possible for the chip to move slightly against the mask, scraping resist off onto the mask and causing issues with future writings.

For a writing where the alignment merely needed to be on the chip scale, it was sufficient to use the naked eye to judge the alignment against the edges of the mask. This was most common for bottom lead lithography where there was nothing else on the sample to align to. However, some writing required alignment to small features on the chip itself. This requires the use of the microscope to align the features. Unfortunately, the microscope cannot focus on both the chip and the mask simultaneously. Typically the solution to this was to focus on the mask first and move the chip while it was defocused. By moving the chip up to see where it was with respect to the mask, and then moving it back into a defocused state repeatedly, it was possible to get a sense for what changes needed to be made to align it properly.

Once it was aligned, the sample was brought in contact with the mask again. At this point, the *chuck level* button on the front was depressed to force the chuck to level itself to the mask. The contact vacuum was then turned on and increased to no less than -5 torr and no more than -10 torr. The alignment was double checked with the microscope to make sure it had survived the entire process. Lastly, the chip was exposed to the UV light.

Once the exposure was complete, the contact vacuum was turned off and the N<sub>2</sub> gas



Figure 3.13: *The JEOL 840A.* 1) Electron beam column. 2) Sample exchange chamber and stage controls. 3) Display and controls. 4) Electron beam controls.

switched on. This kept the sample from sticking to the mask as the sample chuck was backed away from the mask. The chuck was backed one full rotation and then the mask frame was raised. The  $N_2$  gas was switched off, followed by the substrate vacuum. The sample was then removed from the mask aligner.

### 3.4.2 Electron Beam Lithography

The Electron Beam Lithographer (E-Beam Lithographer, or EBL) is first and foremost an SEM. Therefore its basic design is fundamentally similar to that of section 3.3.1.

Our E-Beam Lithographer is an 840A SEM built by the Japanese Electron Optics Laboratory (JEOL), now called JEOL, Limited. It uses a hot-cathode filament of tungsten to generate its electron beam. The beam voltage is kept at 35 kV, which generates a spot size at the sample of 8 nanometers. The SEM is capable of loading eight one-half inch chips simultaneously.

The principle of EBL is not dissimilar to photolithography. A resist coated on a sample can be written by breaking bonds in the organic molecules. The high-energy electrons in the beam provide the mechanism for breaking the bonds. While the beam in an ordinary SEM

is controlled by the SEM itself in a raster pattern, an external computer can control the beam in an EBL and direct it in a pre-designed pattern. The sample can then be developed to etch away the exposed pattern.

As opposed to Optical Lithography, which writes large areas in a single shot, electron beam lithography is limited to writing an area of a couple nanometers at any single moment. While the *dwell times*, the amount of time the E-Beam spends on a single spot, are typically on the order of microseconds, the quantity of dots required to write a large pattern tends to make EBL a slow process. This can be sped up by increasing the beam current, but that is limited by the increased effect it has on the nearby patterns. Typically increasing the beam current is only useful as the scale of the pattern increases to microns or even millimeters.

#### **3.4.2.1 Pattern Creation and Control**

The biggest advantage of the E-Beam Lithographer is the ability to create and modify patterns on the fly. Where a photomask has to be made by a company and is therefore a fixed design, the E-Beam pattern can be altered repeatedly at whim. This makes it a particularly versatile method of designing samples.

The software used to control the pattern creation is called the Nanometer Pattern Generation System (NPGS or “Nabity software”). This software reads computer drawings produced by the user and interprets them into a set of beam positions and dwell times. It can then automatically control the beam position to produce the designed pattern in the sample resist. This is done by intermittently *blanking* the beam, or deflecting it away from the sample until the new position is locked into the electromagnetic lenses.

The patterns are written in DesignCAD, a computer assisted design tool. Units in DesignCAD are measured in microns by the NPGS software, convenient for most writing re-

quirements. The software also allows control of the feature color - interpreted by NPGS as different electron beam doses - and layer. This allows the user to include many different types of features with many different desired doses in a single pattern.

NPGS defaults to interpreting solid lines as lines. A box or circle drawn with a solid line border will be written as an outline of the shape. By setting the outline to a dashed line, the system recognizes the shape as filled, and will sweep the beam to completely write the middle of design. It is also possible to define which side of the shape the beam will start writing, and how the beam will move during the writing.

One important detail to include in every writing file is a *pinwheel*. Pinwheels are convenient for checking the focus and stigmatism of the beam during the writing. Any variations in focus will cause the lines in the pinwheel to not come out, typically resulting in an overdosed open center, and spots around the outside where the lines intersect the circle. Poor stigmatism will cause a directional favorability in which lines are developed. This allows for easy diagnosis of any difficulties in the writing.

Once the pattern has been created, a *run file* must be generated for it. NPGS uses the run file to interpret the design as a series of doses for the writing. Inside the run file the user sets the magnification desired for the writing. This is limited by the size of the region created in the design, which NPGS can check. The doses or dwell times can also be set by the user, whichever is convenient, with the other being calculated by the computer based on the input values. There are three different types of doses available and are usually chosen based on the type of writing to be done: line dose (in nC/cm), area dose (in  $\mu\text{C}/\text{cm}^2$ ), and point dose (in nC). Typical line doses are between 2 and 4 nC/cm. Area doses range between 200 and 800  $\mu\text{C}/\text{cm}^2$ .

It is also possible to change the density of points used by the system while writing in

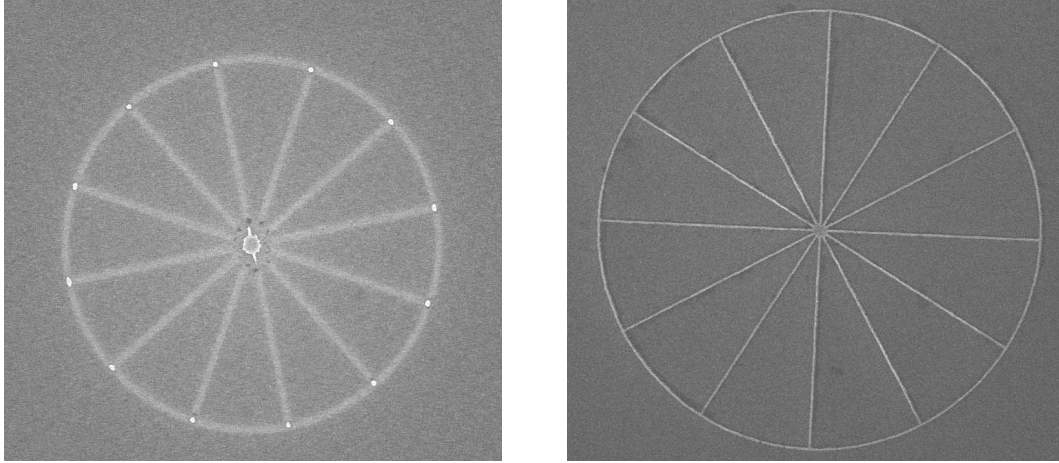


Figure 3.14: *SEM images of 10  $\mu\text{m}$  diameter pinwheels after evaporation of Ti and Au, following liftoff.* A) A 6k magnification image of an under-dosed pinwheel, evident by the bright spots at the junctions of the lines. This was also poorly stigmated, visible by the directional favorability of the center. Note that the written areas remain visible due to leftover resist on the surface. B) A 7k magnification image of a properly focused and stigmated pinwheel.

the run file. The first setting is the *center-to-center* distance, which defines how far apart two beam spots are along a single written line. The second setting is the *line spacing* which determines how far the beam moves between lines written in an area dose. These values can have a significant impact on the resulting shape of the written features. These settings also change the dwell times, as a closer spacing needs less beam dwell per point for the same net dose.

If the dwell time becomes too short, or the beam current becomes too large, a serious problem arises. The *beam blanker*, which moves the beam away from the sample region, was broken during a repair of the SEM. When the command is sent by the computer to turn off the beam blanker, which is done between each point in the writing, there is a delay before the beam blanker responds. That delay is dependent on the beam current, and becomes unmanageable above 500 pA. At the usual writing current of 35 pA, the delay is roughly 1 to 2  $\mu\text{s}$ . The delay should not be more than 10 percent of the dwell time in order for the

dosing to be nominal.

To properly test the possible settings in the run file, it is appropriate to perform a *dose test* with the desired pattern. A DesignCAD file is created with a series of duplicated patterns, using different colors, and possibly different layers, for each one. It is important to make certain that the critical regions are far enough away from each other that they don't experience the *proximity effect*, or increased dosing from nearby written patterns.

When creating a dose test the patterns shouldn't exceed the window of view for the magnification you want to write the pattern at during a normal run. The conditions for the writing should be kept the same at all times. The run file can also be written so that each color represents a different dose, and if desired each layer can work at varying sets of line and center-to-center spacings. By metalizing the dose test sample and observing the features in the SEM, it is possible to determine the best writing conditions.

#### **3.4.2.2 Procedure**

The samples to be written were loaded on the sample stage outside of the EBL. Included among the samples was a specially designed *stigmation sample*. Our stigmation samples are old designs that have been patterned to include gold nanoparticles roughly 10 nm in radius. These nanoparticles are roughly circular, and provide a good basis for checking the stigmation, or circularity, of the electron beam.

The samples were loaded into the chamber, and the chamber allowed to pump for a couple minutes down to under  $4 \times 10^{-6}$  torr. This prevents the possibility of oxidation to the tungsten filament while warming it. This was a good time to check that the system is in its default standby mode so that there were no surprises during the run. Once the pressure was low enough, the filament current was raised slowly. It was typical to raise it by a half step,

as indicated on the panel, every 30 seconds.

While still increasing the current, the collector and detector were turned on, the SEM set to line-scan profile mode, and the contrast adjusted until little spikes could be seen in the line-scan on the screen. These were random electron detections and were visible when the contrast was set correctly to see the secondary electrons from the sample. It was also advisable to reduce the magnification to its minimum value (between 10 and 20 x) so that sample features could be used to help properly saturate the filament.

As filament current increases, the beam current changes in a nonlinear fashion. As the filament current nears the saturation point, the beam current goes through a short peak. This was observable on the SEM in line-scan profile mode by noticing the amplitude of the line-scan increase and suddenly decrease as the filament current passed through the peak. This peak is caused by imperfections in the filament, and is not a stable point for SEM work. Eventually, a second peak would be observed, followed by a plateau. The proper saturation point, the point with the most stability, is at a beam current just below the plateau.

At this point the probe current could be increased to the desired value. The system was switched to picture mode, and the stage moved to one of the holes in the sample holder. These holes act as traps for the electron beam and allow for accurate measurement of the beam current. By zooming into the hole, the probe current could be set to the desired value - 35 picoamps in our case. The system was allowed 15 to 30 minutes to stabilize, which gave the filament time to reach thermal equilibrium, and any fluctuations in the filament emission to cease.

Once stable, the stage was moved to the stigmation sample. Stigmation and focusing was performed at 200000x while looking at the small gold nanoparticles on the surface. The stigmation in each direction (x and y) was adjusted slowly, oscillating around the point of

good focus until it was pinpointed. Then, the stigmation was checked by adjusting the focus back and forth around the focus point. If the feature defocused spherically, uniformly in all directions, then the stigmation was properly set. If the feature defocused in a favored direction, which looked like the sample was stretching along one particular axis, then the stigmation was off and needed to be readjusted.

This method was made possible by the simple, and surprising, fact that the stigmation does not change with beam position in the SEM. It was often suggested that the stigmation should be rechecked with each writing, but even run-to-run the proper stigmation point occurred with very nearly the same settings every time. This consistency was very convenient for ensuring good writing on a regular basis.

Before continuing, the beam current was double checked and, if necessary, reset to 35 pA. Very rarely will the system be so perfectly set as not to drift at all during writing. As long as the beam current didn't drift by more than 10 percent of the desired value, features would develop well. It was, however, worth the extra time to make certain that the beam was more stable than this, and drifted no more than a couple tenths of picoamps during any one sample. The beam current was checked and adjusted after every sample in the run.

The stage was then moved to the top of the sample. The top was often defined by some feature to break the symmetry that was usually present in the sample designs. Since alignment was particularly important, it was critical to make certain that the sample features were perfectly vertical in the SEM window. A long vertical line was found on the sample, and the cross-hairs setting on the SEM (called "B-up") used to align the sample while rotating it so that the vertical feature did appear to be perfectly parallel to the cross-hairs.

It was then time to move to the actual writing. The writing areas were flanked by crosses 40  $\mu\text{m}$  on a side, and 300  $\mu\text{m}$  apart at the four corners of the window at 200x. At 800x (for

the SQUIDS) or 1000x (for the single pillars), 4 L-shaped regions were present at the corners, and were 9  $\mu\text{m}$  on their long side. The sample was first focused on the interior corner of a cross in the upper right corner of the sample region. The upper right was chosen because it was not used in the actual alignment. Unlike the stigmation, the focus did change due to height differences of the stage at various positions. Therefore if moving more than a couple hundred microns the focus was be rechecked.

Once focused, the writing region was centered in the window at 1000x, and then the magnification backed off quickly to 200x. The beam-blanker was then set to external control, followed by the raster set to external control. Failure to have the beam-blanker on while the raster was in external control would stop the rastering and cause the electron beam to drill a hole in the resist. This was something to be avoided at all costs.

Alignment was performed in a video-game like fashion. The SEM scanned over the user-programmed regions for the alignment marks. Before writing, a DesignCAD file with the alignment marks would be drawn so the computer knew what it was looking for. On the computer, the contrast differences in those regions were presented. The alignment marks appeared red against a blue background. On top of the displayed image was a controllable pattern in the shape of the alignment mark that could be maneuvered over the one seen by the SEM. Using this method, fine adjustment of the systems alignment could be done. After being aligned at 200x, it was again aligned at 1000x, without the system ever leaving external mode.

Once the alignment was finished the pattern could be written. It was important that no settings were changed between the end of the alignment and the beginning of the writing. The pattern was written such that the point at  $x = 0$  and  $y = 0$  in the DesignCAD file was at the very center of the alignment.

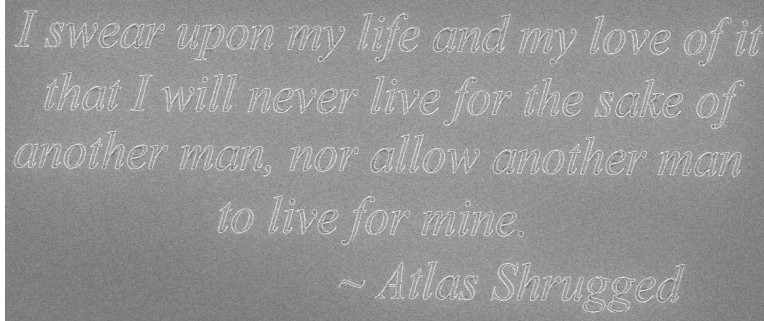


Figure 3.15: A picture of a written SEM pattern imaged at 2k magnification showing the versatility of electron beam lithography. The entire pattern is approximately 20  $\mu\text{m}$  tall and was deposited with Ti and Au.

When all the samples were written, the system was reset to its standby state, and the filament current slowly cooled by a half step every 15 seconds. When the filament current reached zero, the system was given two minutes to cool completely before removing the samples to protect the filament.

## 3.5 Measurement

While many measurement methods were employed in this study, two in particular dominated the work. In a marked recursion, both involved the use of SQUIDS as feedback response schemes. The first uses an RF SQUID to measure Josephson junction samples for transport studies, such as measuring I-V characteristics, Fraunhofer patterns, and SQUID responses. The second uses a DC SQUID to measure magnetic properties of materials.

### 3.5.1 SQUID Current Comparator

The direct measurements of the I-V characteristics of all of our junctions were done using helium probes home-built by Dr. William Pratt in the early 1990's. The *Quick Dippers* are sample probes capable of measuring a single half-inch chip by inserting them directly into

a 60 liter helium storage dewar. The most sophisticated of these can perform only a single four-probe measurement, but with excellent low-noise characteristics.

The current through the sample is driven by an in-house analog current supply built by Dan Edmunds [63]. This supply includes a pair of 12V motorcycle batteries to help stabilize the current during operation. They are recharged when not in use, but can be set to recharge during operation at the cost of a slight increase in system noise.

The current is driven through the pillar from the top leads to the bottom leads. The voltage is then measured across the pillar from the top to the bottom in a pseudo four-terminal measurement scheme. The superconducting top and bottom leads allows this to emulate a four terminal measurement so-long as the I and V contacts on the top lead do not make contact. This is represented in Figure 3.16. The output voltage of the SQUID electronics is measured by a HP 34401A Multimeter.

The circuit used in these dippers is shown in Figure 3.17. The sample is mounted at the bottom of the dewar and is represented by  $R_S$ . When a current is driven across the

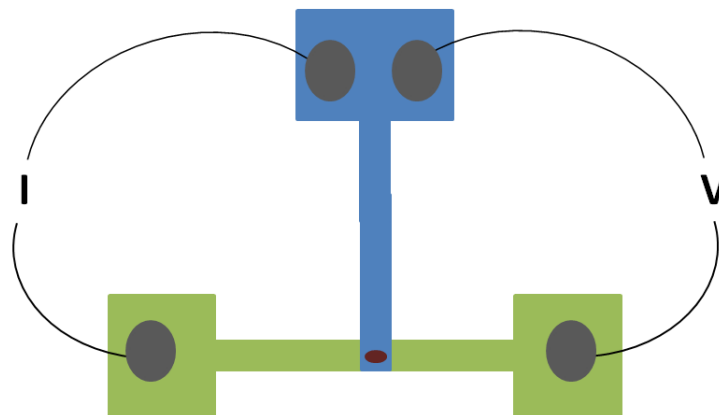


Figure 3.16: *Diagram of pseudo-four terminal measurement arrangement.* The green line represents the bottom lead and pads, while the blue line represents the top lead and pad. The electrical connections are formed to the superconducting leads with pressed indium (gray spots). The red ellipse represents the pillar being measured. This is called a pseudo-four terminal measurement because it depends on the resistance of the blue lead being exactly zero, which is true for a superconductor.

sample, this produces a voltage in the left half of the loop created by  $R_S$  and the reference resistor  $R_{Ref}$ . This creates a current across the inductor that couples to the SQUID. This generates a flux in the SQUID. The SQUID Electronics, a model 2010 SQUID Control built by Quantum Design, reacts to this induced flux by applying a voltage through the feedback resistor  $R_{FB}$  and across the reference resistor until the current through the inductor goes to zero. This is known as a "Current Comparator" circuit.

The signal measured from the SQUID electronics is the output voltage applied to the feedback resistor. This current is amplified with respect to the original signal with a gain proportional to,

$$g = \frac{(V_{out}/R_{FB})}{I_{Prim}}, \quad (3.2)$$

where  $V_{out}$  is the output voltage of the SQUID electronics, and  $I_{Prim}$  is the current generated in the loop between  $R_S$  and  $R_{Ref}$  due to the voltage across  $R_S$ . This gain is on the order of  $10^4$ .

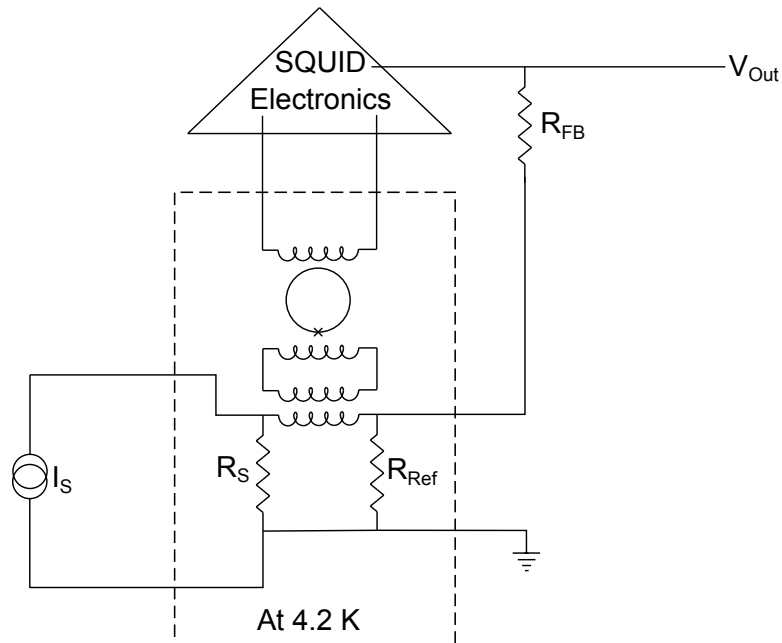


Figure 3.17: *Diagram of the Current Comparator Circuit.*

Resistor	QD-1	QD-2
Feedback $R_{FB}$	10 k $\Omega$	2 k $\Omega$
Reference $R_{ref}$	94.61 $\mu\Omega$	126.0 $\mu\Omega$

Table 3.6: *A list of the key resistors on each of the two SQUID-based Quick Dippers.*

This acts as a particularly sensitive measurement scheme made possible by the inclusion of the SQUID. Recall from Section 2.3 that a SQUID is sensitive to flux changes less than a single flux quantum,

$$\Phi_0 = \frac{h}{2e} = 2.0678 * 10^{-15} \text{ Wb.} \quad (3.3)$$

The noise pickup by the SQUID is roughly  $7 * 10^{-4} \Phi_0$ , which correlates to output noise from the SQUID electronics of less than .1 mV. This gives us a signal-to-noise of nearly 10,000 in the worst case, for our smallest area samples with the lowest  $I_c R_N$ .

The voltage across the sample  $V_S$  is obtained from the measured voltage  $V_0$  by,

$$V_S^* = C (V_0), \quad (3.4)$$

where  $V_0$  is the output voltage of the SQUID, and C is,

$$C = \frac{R_{ref}}{R_{FB}} \quad (3.5)$$

where  $R_{ref}$  is the reference resistor and  $R_{FB}$  is the feedback resistor of the system. The values for these as they are at the writing of these thesis are listed in Table 3.5.1. This means that C depends upon the Quick Dipper used:  $9.461 \times 10^{-9}$  for QD-1, and originally  $12.60 \times 10^{-9}$  for QD-2. Recent changes to QD-2 have changed the feedback resistor of QD-2 to a factor of 5 smaller, making C equal to  $63.0 \times 10^{-9}$ . Due to the finite open-loop gain of the feedback response, this slightly underestimates the sample voltage. This can be corrected

with,

$$V_S = V_S^* \left( 1 + \frac{0.0006}{N} \right), \quad (3.6)$$

where  $N$  is the gain setting on the SQUID electronics. The gain was left at  $N=1$  for all measurements in this study.

### 3.5.1.1 Measurement Setup

The measurement circuit is presented in Figure 3.18. The sample is held so that the external field is parallel to the sample face and along the long axis of the bottom leads. The external field is provided by a superconducting magnet wound in-house with a coil constant of 574 G/A for QD-1, and 560.5 G/A for QD-2. It is protected by a persistent switch driven by a computer controlled relay. The magnet is supplied by a 2A Kepco Bipolar Operational Power Supply (BOPS) for low fields, and a 20A Kepco BOPS for fields up to several thousand Gauss.

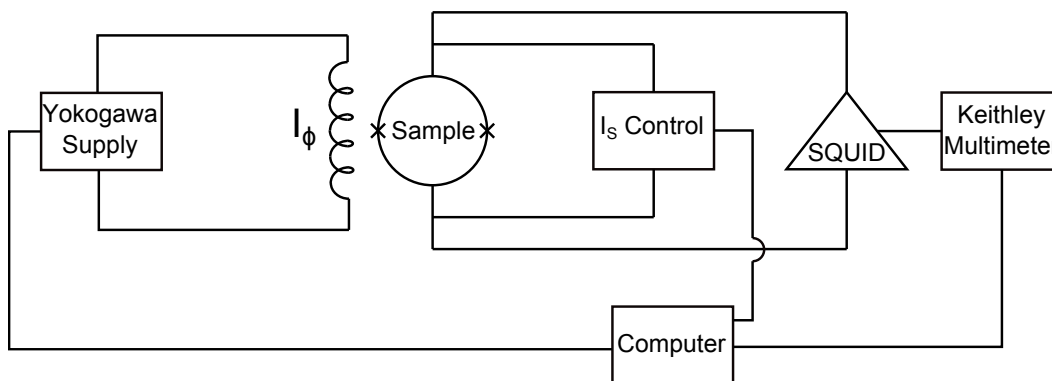


Figure 3.18: *Diagram of the sample measurement scheme.* The flux current control loop at left was present only in experiments testing SQUID samples.

For SQUID samples, an additional line was run on the sample to drive the current for modulating the flux through the SQUID. This line was fed through two of the additional connections on the quick dippers that were originally used for Current-In-Plane (CIP) mea-

surements, and therefore bypass the current comparator circuit. This line was fed by a Yokogawa 7651 programmable DC source. The signal was driven through a  $1000\Omega$  reference resistor in order to emulate a current source.

The entire operation is computer controlled using LabVIEW software developed by former students in the group. The majority of software used for this thesis was designed by Yixing Wang [62]. All aspects of the measurement are completely automated, especially the operation of the persistent switch. This acts as a significant protection for the magnet, minimizing the chance of a user fouling the procedure and destroying the switch.

The samples are measured inside a shielded enclosure to minimize outside interference. This was discovered to be of critical importance when a simple cell phone signal inside the shielded room was detected by the experimental setup. The intermittent attempt of the cell phone to communicate with a cell tower caused random pulsing in the system that made the measurements impossible.

### **3.5.1.2 Procedure**

The samples were mounted to the bottom of the Quick Dipper (QD) with the magnet held off the system. The sample was first tied down with string, looped through a hole at the back, to prevent it from shifting out of position during the run. Indium was then pressed onto the pads to provide a contact point for the wires. The voltage, current, and flux line current leads were pressed into the indium pads, and a small amount of indium added on top to ensure contact and that the wire wouldn't lift out during the measurement.

The magnet was slid over the sample area. The sample was checked for good contact by measuring the resistance down the current supply lines. It was also checked for shorting through the magnet housing, through the probe itself, and to the flux line if present. Lastly,

the flux line was checked for good contact. After this, the magnet was mounted in place with a pair of short screws, and any loose wires tied down with string.

At this point the QD was carried over to the storage dewar. A rope with a hook was mounted to the top of the QD to help maintain control. The vent valve of the Helium dewar includes a flow rate monitor and a long hose. The hose was connected to the QD through the top, and enabled gas flow through the probe helping it to cool. The vent valve was opened and helium gas forced through the probe to remove any air inside the probe. Once finished, the top of the helium dewar was removed and the QD inserted. The probe was lowered slowly so as to not boil off excessive helium, notable by significant spikes in helium gas flow out through the vent valve.

Once completely inserted, the hook was removed from the top of the probe and the dewar rolled into the shielded room. The sample was again tested, both the current leads and flux leads, to check if they had gone superconducting. The values should register between 2 and 7 ohms, which were the lead resistances of the lines in the probe. The sample was also checked using the SQUID electronics to ensure good contact with the voltage lines, and a sufficiently low resistance of the sample. With the RF line of the SQUID controller hooked to the top of the probe, a small multimeter set to read on the 20 k $\Omega$  range was hooked up to the reference resistor side of the QD. When turned on and off, the SQUID should respond with a signal that decayed due to the RL circuit present at the bottom of the SQUID. The decay time was roughly on the order of the pillar size. If the pillars were on the order of several microns in diameter, then the signal would decay on a 5 second time scale. If, however, the pillars are in the hundreds of nanometers in diameter, then the decay time is much shorter due to the larger resistance in the circuit. A response that was too rapid indicated a sample resistance that was too high to be properly measured - the sample was removed and remounted if the

problem was poor contact, or replaced.

If the sample passed the checks, the remaining connections were made. The computer control was then set and programmed to the appropriate current, and field, step sizes. This required a couple test runs on the sample to see what the critical current of the sample was at high and low fields. This way the run time could be optimized to avoid wasting helium.

When measuring Fraunhofer patterns, the field was set and held fixed at each step. The I-V curve was then measured by slowly stepping the current until the voltage exceeded a pre-defined limit. This was done after the curvature of the signal changed sign as it approached the normal resistance part of the overdamped junction curve. If the sample was mounted properly, the signal would have roughly zero voltage (with some minor noise) until it hit the critical current for that field. The field is then swept through a range defined by the user, and the I-V curves measured at each step. See Figure 5.6 for the results of this process on a typical overdamped Josephson junction.

When measuring the SQUIDS, the in-plane field was set, and then dropped to zero again. The I-V curves were measured for a sequence of values of the flux current, which was applied and maintained through each I-V measurement. In this way, the reaction of the magnetic materials in the pillars to the external field could be observed by measuring the changes in the SQUID response to the flux current.

Once finished, the QD was lifted from the dewar in three steps, heating the QD with a hair dryer the whole time. This prevented water from building up inside the QD and possibly destroying solder joints. However, it was important to not overheat the QD, which could destroy the SQUID or its connections.

### 3.5.2 SQUID Magnetometer

The magnetic films used in this study required characterization. Specifically, details such as the saturation magnetization  $M_S$ , the remanent magnetization  $M_R$ , the coercivity  $H_C$ , and the Curie temperature  $T_C$  were important to understanding the properties of the films fabricated in our samples. All of these properties can be easily characterized in modern magnetometers.

Our magnetometer is a Magnetic Property Measurement System (MPMS) built by Quantum Design. The system has a maximum field strength of 5.5 Tesla applied by a helium-4 temperature superconducting magnet. It is also capable of measuring sample temperatures from 2 K up to 400 K. The sample size is strongly limited, with a rough diameter of a half centimeter. Samples typically need to be cut down in size, and so proper planning must be done during fabrication if magnetometry is required.

The MPMS is configured as a balanced coil set known as a second-derivative gradiometer. In this configuration, two axial gradiometers are placed in series, one above the other. This system then measures the response of the loops to changes in the spatial derivative of the flux passing through them. This is convenient for the sensitive measurement of material magnetizations as constant sources of flux, such as earth's magnetic field or the external field applied by the system, or linearly changing fields, do not generate a signal.

The system employs a DC SQUID as a low noise measurement scheme. The current generated by the changing flux is inductively coupled to the SQUID, causing a flux to penetrate the SQUID. The system then responds by applying a bias current across another inductively coupled circuit to cancel the enclosed flux. The system records a voltage related to that bias current and plots it against position. The curve can then be fit to a function

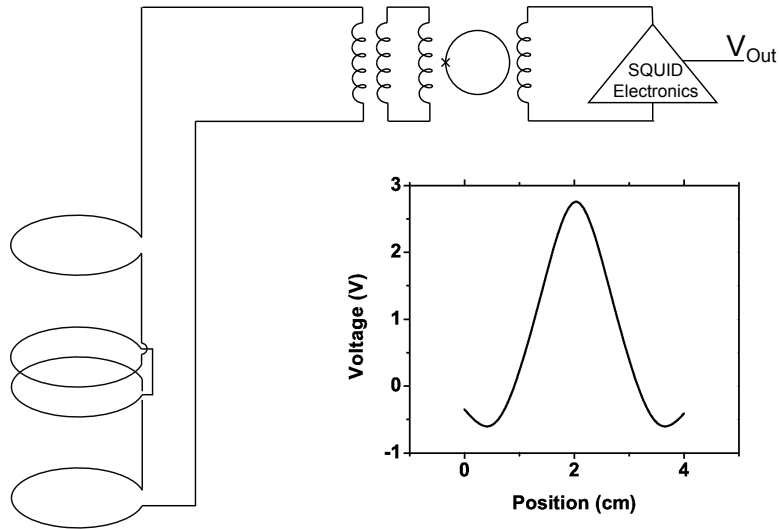


Figure 3.19: *Diagram of the SQUID Magnetometer.* The coils on the left detect the changing magnetic field as the sample is lifted through them. The SQUID sensitively measures the flux change due to the resulting current in the loop. The SQUID electronics output a voltage which can be plotted against position. INSET - A single magnetometer measurement for NbPy with a 9 percent Nb atomic concentration. The large peak in the middle is the result of the alignment of the current pickup in the central coils, while the outer valleys are the result of the outer coils being anti-aligned. The fit to this curve provides the magnetic property data of the sample.

that relates the height of the central voltage peak to the magnetization of the sample.

### 3.5.2.1 Procedure

Since the sputtering system is primarily designed to take one-half inch chips, the samples to be measured first needed to be cut down to size. This was done with a diamond scribe. By scoring the back of the silicon chip several times, the structure could be weakened enough at that spot so that the silicon cleaved roughly along that plane. This was done as many times as necessary to get a chip approximately 5 mm on a side.

If the measurement was to be done with the magnetization oriented along the face of the sample, the sample needs to be only slightly wider than the width of the straw. The straws (literally, plastic drinking straws) can be compressed in one radial direction to enable the

slightly larger chip to pass through up the center. Once it was in position, the straw could be released, and it would attempt to retain its original shape. This compressed the chip at the edges and held it firmly in place.

If the magnetization perpendicular to the face of the sample was to be measured, a little more creativity needs to be employed. It was possible to arrange the chip perpendicular in the straw, but this often destroyed the straw. Instead, a lattice of string was woven across the spot in the straw that the sample was to sit. The sample was then dropped down onto the string netting, and more string woven above it to keep the sample in place.

Depending on the thickness of the ferromagnetic material, sometimes it was necessary to put multiple pieces together for a single measurement. This ensured that there was enough magnetic volume for the system to detect. Sometimes this required planning in the fabrication stage, such as making multilayer films with repetitions of the same ferromagnetic thicknesses, magnetically isolated from one another by layers of copper.

Once the sample was loaded onto the probe, it was inserted into the dewar. At the top resides a load-lock that keeps the system under vacuum and prevents air from getting inside the system. Once pumped out, the probe was slowly lowered into place and locked down to the motor stage at the top of the load lock.

On the computer, the magnetic field was set to 500 Oe. This allowed the sample to be centered properly in the coils, which was critical to get the maximum signal, and the best fit to the data. Once the field had reached its stable value, the program was placed into centering mode. The system would then lift the sample through the coils several times and eventually display the coil voltage versus position data. If the peak in the signal was not centered at 2 cm and was too far to the left, it suggested the sample was too high and must be lowered. Similarly, if it is too far to the right of 2 cm, the sample was too low. A small

silver screw at the top of the sample probe could be loosened and the position of the sample adjusted with respect to the motor. The system could then be rechecked for centering. This process was repeated until the sample was centered at precisely 2 cm above the bottom coil.

Once centered, the field was lowered back to 0 Oe. A run file was created for the measurement that established which fields to measure the magnetization at, along with which temperatures to perform the measurements. It was also possible to set a number of repetitions at each point to generate an average over several data sets. Once complete, the computer was told to run the program, and the system would handle the data taking automatically.

When finished, the sample was slowly removed until it reached the load lock. The valve at the top was closed, and the sample probe removed from the system.

# Chapter 4

## Sample Fabrication

The ability to perform experiments in the mesoscopic regime is a result of the development of tools and procedures that allow for sensitive work on small scales. But while the technologies such as Photolithography, Electron Beam Lithography, and Ion Milling do the job, it is the procedures that make it work. Therefore it is an important task to develop the proper procedures that will allow for the formation of samples that meet the experimental requirements.

Several different sample fabrication processes have been used during the course of these experiments. In the next section I discuss the fabrication of large scale mesoscopic pillars using photolithography. In section 4.2 I discuss the development of an Electron Beam process for use in smaller scale pillar fabrication. Section 4.3 discusses the changes made in fabricating the SQUID design samples.

### 4.1 Photolithographic Pillars

Our first experiments were designed to test Josephson junctions, samples made with two superconductors sandwiching a central material, with a new magnetic multilayer. This was specifically so that we would have as much baseline comparison as possible to the previous experiments performed in the group. The fabrication technique here is similar to the work done by T. Khairi [43]. Figure 4.1 presents a diagram of the entire process.

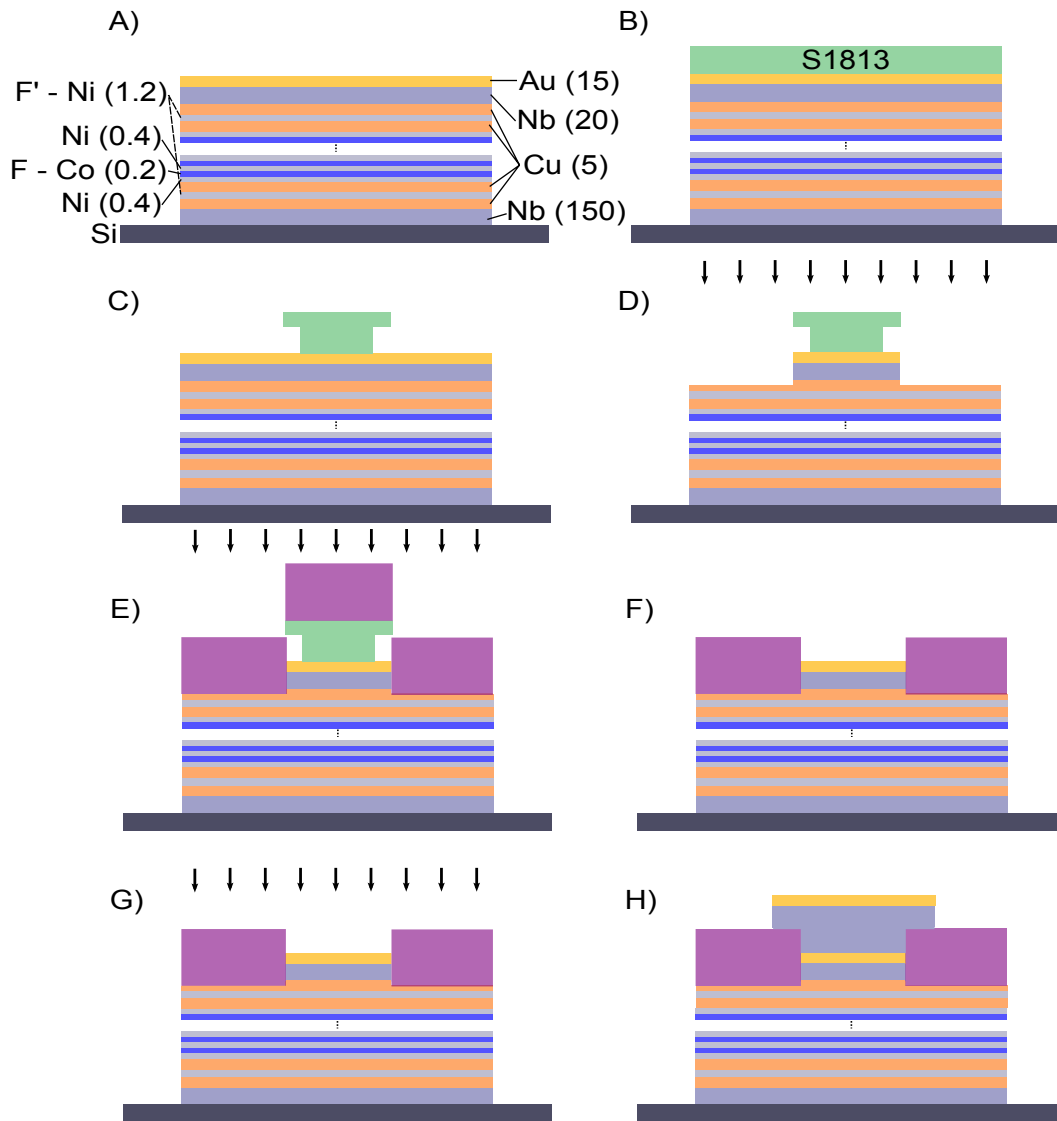


Figure 4.1: *Cartoon of the sample fabrication procedure using Optical Lithography.* A) The Base Multilayer after Sputtering and Liftoff. B) S1813 photoresist is spun onto the sample. C) After writing and development, the polymer has been removed in the exposed region, forming a pillar with an undercut in the S1813 due to the interaction with the top layer with Chlorobenzene. D) The sample is ion milled to the middle of the top Cu layer. E) 150 nm of SiOx are *in-situ* deposited immediately following the ion mill. F) The pillar and the SiOx that has coated it is removed via acetone liftoff. G) The sample is ion milled again to clean the surface. H) Top leads are sputtered onto the pillars.

### 4.1.1 Substrates and Cleaning

The samples were grown on 1/2 inch square chips cut from 3 inch <100> p-type Boron-doped Silicon wafers. The resistivity of the substrates was 1-10 Ohm-cm. They were stored in a Class 100 clean room facility at all times to minimize potential contamination. Since the wafers were diced before fabrication, it was important to minimize the possibility of residual silica dust sticking to your sample surface. A protective layer of S1813 photoresist was coated onto the sample and baked for 1 minute at 110 degrees Celsius on a hotplate. The quality of the film, generally visible by color variations of the sample, is not critical. It is only necessary that the film completely cover the wafer.

Sample and substrate cleaning involves: at least 10 minutes soak in acetone under ultrasonic vibration, remove and spray with Isopropyl Alcohol (IPA) before the acetone dries, at least 10 minutes soak in IPA under ultrasonic, remove and spray with DI water, at least 10 minutes soak in DI water under ultrasonic. Remove the sample, wash it again with DI water, and blow dry with N<sub>2</sub> gas while holding a sample edge against a kim wipe. This ensured the water was properly wicked away from the sample, and that no residue was left over.

An optical microscope is sufficient to determine the cleanliness of the substrate. If particulate matter remains, a soft cotton swab can be used to wipe off the surface of the sample. Wet a the cotton swab with Acetone, then IPA, then DI water to ensure no acetone or IPA residue remains on the sample. Also take care to wipe the sample in a single direction (not back and forth), and to do so while holding the sample against a kim wipe to wick away the fluid. Finish by blow drying with N<sub>2</sub> gas.

### 4.1.2 Bottom Layer Sputtering

The bottom multilayer leads of the sample are sputtered using a mechanical (metal) mask to define the shape. The leads used in this case were roughly  $300\ \mu\text{m}$  wide and 1 cm long, with features to aide in aligning the later steps. Onto the bottom lead was deposited two different S/F/S stacks, the top of which was Cu(5)/Nb(20)/Au(15). This top prevented oxidation and allowed for good contact to be made with the top leads later in the process. The 20 nm of Niobium is enough to ensure that it will superconduct. Doing this allows some breathing room in the fabrication, as it will mask minor defects in the contact between the bottom and top leads. See Chapter for more on Sputtering.

### 4.1.3 Photolithographic Definition of Pillars

After sputtering, the samples were coated with a single layer of S1813. Using a pipette, several drops of resist were deposited on the center of the sample. About seven drops of the photoresist were sufficient for a uniform and complete coating of the substrate. The sample was then spun for 50 seconds at 5000 RPM, which formed a  $1.3\ \mu\text{m}$  thick photoresist layer. Before baking, every sample was inspected to make certain that the resist completely covers the chip and that the coloration was roughly uniform in the center. If this was not the case, the sample was cleaned following section 4.1.1 and re-spun. The resist was baked on a hotplate for 1 minute at 110 degrees Celsius and allowed to cool.

Once cool, the sample could be exposed in the mask aligner. The mask pattern was a simple open box with 6 circular pillars of diameter:  $80\ \mu\text{m}$ , two  $10\ \mu\text{m}$ , two  $20\ \mu\text{m}$ , and  $40\ \mu\text{m}$ , arranged in that order. Using the flag of the bottom lead as a guide, the  $40\ \mu\text{m}$  pillar was centered inside the bottom lead line, and then centered between the sides of the flag

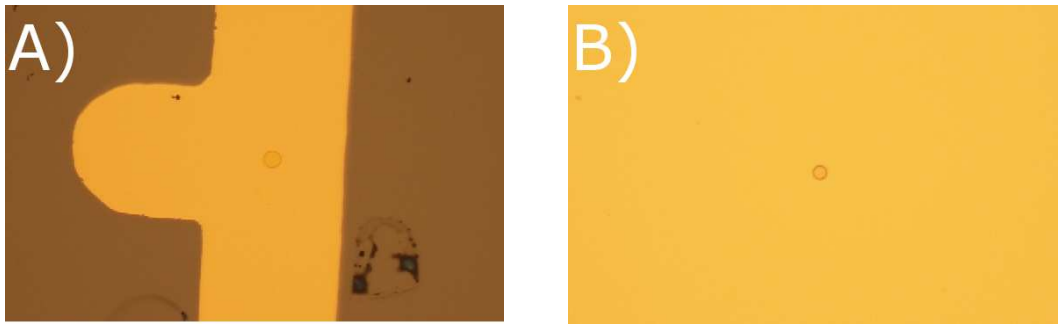


Figure 4.2: *Images of photolithographic pillars.* A) A 40  $\mu\text{m}$  pillar patterned from S1813 onto a multilayer. The tab to the left is the flag to aid alignment. A little unwelcome residue can be seen in the lower right corner. B) A 10  $\mu\text{m}$  pillar from the same sample.

(see figure 4.2a). The rotation was checked by looking at the position of the 80  $\mu\text{m}$  pillar near the bell of the bottom leads. By correcting the rotation to center the 80  $\mu\text{m}$  pillar and adjusting the 40  $\mu\text{m}$  pillar to its proper position, the whole chip could be easily aligned. The sample was finally brought into contact with the mask and exposed to UV light for 10 seconds.

Development of the sample started with a wash in a Chlorobenzene bath. Care must be taken with Chlorobenzene as it is both a carcinogenic chemical and a solvent - it is, in fact, a particularly good plastic glue. Do not accidentally spill the Chlorobenzene, ingest it, or drop any plastic pieces into it. It is probably not suited for plastic modeling either, so don't try using it to put together that P-51 Mustang you have lying around at home.

The sample was washed in the Chlorobenzene for 5 minutes, which caused the top of the S1813 to harden and become more resistant to the developing chemical. This allowed for the formation of an undercut in the photoresist layer, as the inside of the S1813 remains unaffected by the Chlorobenzene. The sample was wafted in the Chlorobenzene for the first 5 seconds, and the last 30 seconds, of the 5 minute cycle. It was then blow dried with  $\text{N}_2$  gas.

The sample was immediately developed in 352 solution for 45 seconds, wafting the whole time. As soon as the development was finished, it was rinsed in DI water and blown dry. If any water-like residue was seen under the microscope, the sample was rinsed again in DI water. It was important to make certain that the 352 was replaced after every single chip in this process, as enough photoresist was removed from the sample that it reduced the developer's effectiveness.

Every pillar needs to be individually checked for quality in an optical microscope. If the lithography was not done properly, it was very easy for the 10  $\mu\text{m}$  pillars to be fouled up by the process. An imperfect lithography might cause the pillar to look like a donut, due to the center of the pillar getting over or under dosed by interference effects from improper mask contact. If any issues were observed, the sample was immediately cleaned following section 4.1.1, Plasma Etched following section 4.3.2 to remove any lingering residue that may affect the resistance of the pillar or adhesion of the photoresist, and then taken through this process again.

#### **4.1.4 Ion Milling and Silicon Monoxide Deposition**

The samples are loaded into individual sample holders for insertion into the Ion Mill (small) Chamber (see Section 3.2.3). No mask was used for these samples, particularly since the outer pillars were at the outer edge of the hole in the ion mill sample holders. In order to make certain that those were properly milled - even though there was no plan to use them - a mask was avoided.

The samples were ion milled halfway through the top most copper layer from the top of the sample. Thus the ion mill cut through the layers Au(15)/Nb(20)/Cu(2.5), with each thickness in nanometers. It simultaneously consumed the top of the photoresist pillar. The

relative milling rates as compared to the milling rate of Au are provided in Section 3.2.3. Typically, each sample required about 4 minutes of milling, primarily due to the very slow mill rate of Nb. In that amount of time, the S1813 suffers minimal damage due to ion milling, as its milling rate is expected to be particularly low.

After all five samples had been ion milled, they were deposited with silicon monoxide (SiO<sub>x</sub>). The SiO<sub>x</sub> was thermally evaporated onto the samples in situ. During the evaporation, the samples were spun about the normal axis to their face so as to provide a more uniform growth and limit the formation of “pin-holes” in the SiO<sub>x</sub> layer. 150 nm of SiO<sub>x</sub> was deposited in this step.

#### **4.1.5 Liftoff**

To remove the photoresist pillar, the samples are placed in a beaker of hot acetone. The acetone is warmed to 90 degrees Celsius to aid the liftoff. It was important that this step be done in a fumehood to prevent this process from becoming explosive due to the extremely low acetone flashpoint in partial acetone atmospheres. After about 10 minutes the acetone beakers with the samples were moved into an ultrasonic bath for 10 minutes. This ensured that the acetone completely attacked the photoresist, and that the SiO<sub>x</sub> cap on top of the resist did not drop back into the pillar.

Once the ultrasonic was complete, the sample was removed, rinsed with IPA, then dipped into an IPA bath. The IPA beaker was left in ultrasonic for 10 minutes to make certain all acetone residues are removed. This was followed by a similar procedure for DI water. Lastly, the sample was removed and blown dry with N<sub>2</sub> gas. This left the pillars clean and open. Inspection in an optical microscope can easily verify a gold coloration inside the pillars, contrasted against the color of the surrounding SiO<sub>x</sub>.

### 4.1.6 Top Lead Sputter

To sputter on the top leads, the samples were loaded into the sputtering sample holders. A mechanical (metal) mask was used to define the top leads. By leaving the bridge screws slightly loose, it was possible to maneuver the mask around on the surface of the sample. This enables the mask to be properly aligned with the pillars. The sample holder could be mounted on the Olympus optical microscope in such a way that it was well balanced, which made it possible to see if the mask was properly aligned to the pillars. Once satisfied, the screws should be tightened down, and the pillars rechecked to make sure no movement occurred while the sample was being secured.

The samples were then loaded into the sputtering chamber. The system was pumped down to between 2 and  $4 * 10^{-8}$  torr. The top leads are simply a thick (150 nm) superconducting Nb film and a 10 nm Au cap to prevent oxidation. The samples were sputtered between -30 degrees Celsius and 30 degrees Celsius to ensure proper film growth.

## 4.2 Electron-Beam Lithographic Pillars

The next step of our experiments required the shrinking of our pillars. While the previous process created at minimum a 10  $\mu\text{m}$  circular pillar, the photolithographic process itself was capable of creating a pillar as small as 3  $\mu\text{m}$  in diameter. However, this was not small enough for our purposes, and was at the limit of the mask aligner. Another major disadvantage is that the mask aligner limits you to those designs for which you have created a mask - often an expensive procedure, particularly when the features get small. The later experiments were going to call for a wide range of possible pillar geometries, making it necessary to have a modifiable pillar design. Therefore, a new procedure was required.

Thankfully, Electron Beam Lithography (EBL) is capable of satisfying both of these requirements. The EBL is limited at minimum to a line size of approximately 50 nm in width. The experiment in question called for pillars that were expected to be no smaller than about five times that minimum limit, well within a reasonable operating range for the device. Also, as mentioned in Chapter , the EBL uses a set of design files that can be edited on the fly, which allows for easy experimental changes as required.

Refer to figures 4.3 and 4.4 for a diagram of the entire fabrication procedure.

### **4.2.1 Substrates and Cleaning**

We grew our samples on 1/2 inch square chips diced from 4-inch diameter <100> p-type Silicon wafers. The wafers used in this section had a resistivity of 10-20 Ohm-cm. They were stored in a class 100 cleanroom at all times, and were diced with a protective layer of photoresist coating the polished surface. The user removes the photoresist and cleans the chips just prior to use, lifting off the dust from the dicing procedure, and any other particulate matter that may have settled on the sample.

The samples are cleaned in accordance with section 4.1.1.

### **4.2.2 Photolithographic Definition of Base Multilayer**

The design for the multilayer wire was defined by photolithography. This is due to the necessity of having alignment marks for the EBL process, which cannot be made small enough with a mechanical mask to be useful. Mechanical mask features fabricated by the Machine Shop possess a minimum size of about 300  $\mu\text{m}$ .

We spun a single layer of S1813 photoresist onto the polished side of a cleaned substrate

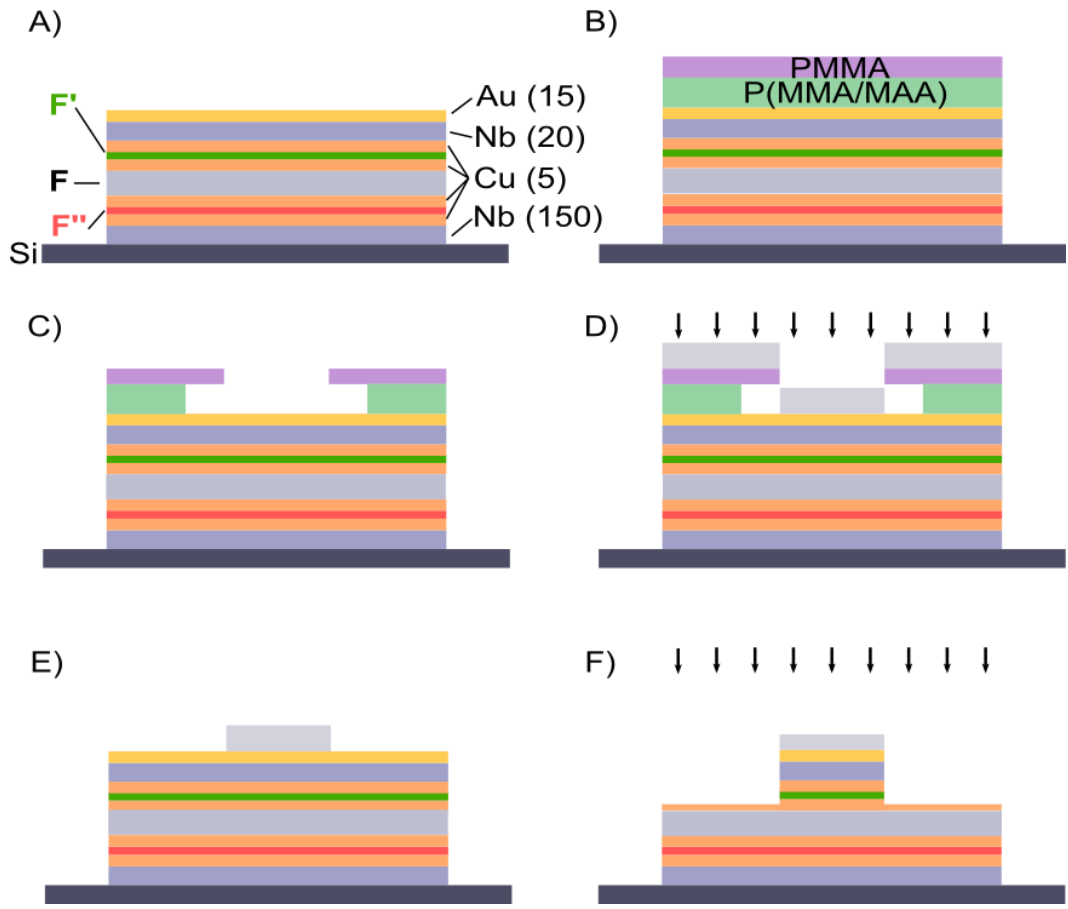


Figure 4.3: *Cartoon of the sample fabrication procedure using Electron Beam Lithography.* A) The Base Multilayer after Sputtering and Liftoff. The central ferromagnet can be either the Co/Ru/Co SAF or the Co/Ni multilayer with perpendicular magnetic anisotropy. B) P(MMA/MAA) and PMMA are spin-coated onto the sample. C) After writing and development, the polymers have been removed in the appropriate region, along with an undercut in the P(MMA/MAA) copolymer. D) Aluminum is evaporated on to the sample. E) Liftoff removes the aluminum that has deposited onto the polymer layers. F) The sample is ion milled to a point halfway through the Cu layer second from the top.

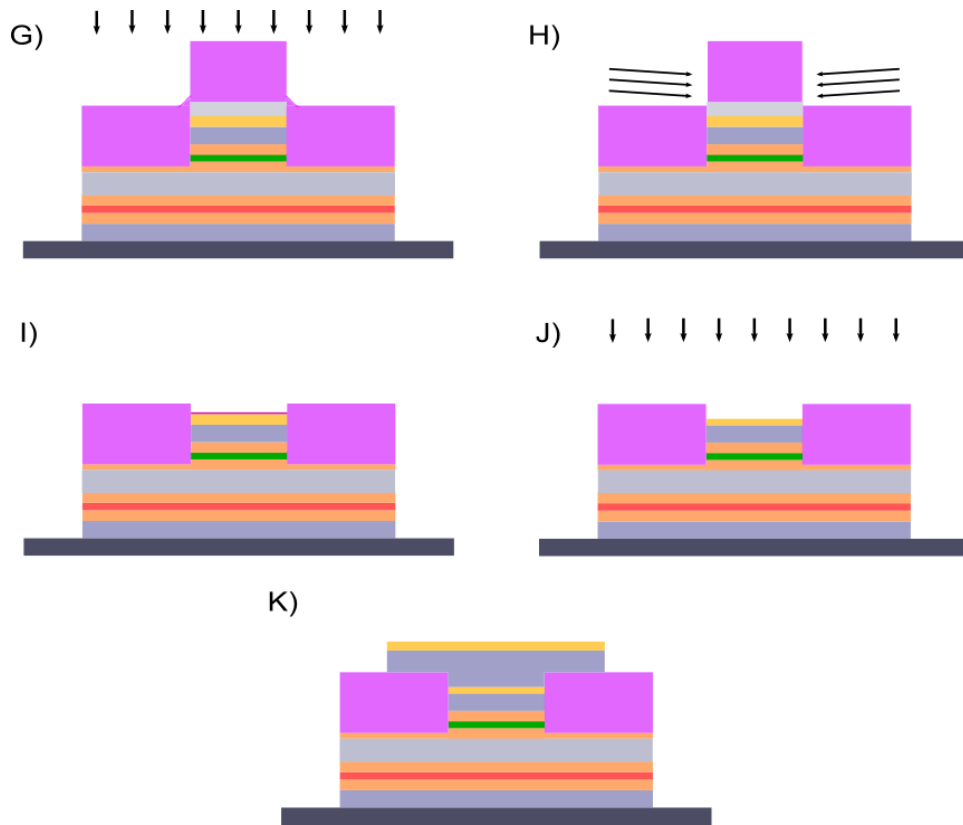


Figure 4.4: *Cartoon of the sample fabrication procedure using Electron Beam Lithography continued.* G) SiOx is deposited on the Ion-Milled sample. Note the SiOx coating the sides of the pillar. H) Side milling removes the SiOx around the sides of the pillar, exposing the aluminum. I) Aluminum etch removes the aluminum pillar and the SiOx on top, but may leave an Al/Au interface. J) Ion-Mill in situ in the Sputtering Chamber removes the Al/Au interface and some of the Au top layer. K) The top leads (Nb and Au) are sputtered.

in the same way as in 4.1.3. After baking, and after allowing the sample to cool for about a minute, it was placed in the mask aligner. The bottom layer requires minimal alignment, only enough to ensure that the pattern was reasonably well centered on the chip, and square to the sides. The sample was then exposed for 12 seconds. Following the exposure, the sample was dipped in Chlorobenzene for 5 minutes to harden the top surface.

Development of the sample was done in 352 solution. The sample was wafted in the 352 for 45 seconds, rinsed in running water for 15 to 20 seconds, and then blow dried with N<sub>2</sub> gas. The larger features should be completely visible to the naked eye at this point. In fact, large features visible to the naked eye should appear roughly 6 to 10 seconds into the development. Any slower indicates that the sample may have been underexposed. An inspection under an optical microscope was necessary to determine if smaller features had developed properly.

It should be noted that running water is not suitable for washing off the 352. Running water tends to leave residues on the sample, particularly in the channels of a patterned line. While rewashing the sample in DI water tends to remove the residues, it is far better to rinse the sample in a beaker of DI water for 20 to 30 seconds. This method was much more effective at removing the 352, and was used in all later processes. The running water method is mentioned here to preserve the proper history of what was done.

### 4.2.3 Sputter and Liftoff

After completion, up to 16 of these samples were loaded into the Sputtering chamber and deposited with the multilayer stack. For this case, the multilayer was of the form Nb(150)/Cu(5)/Ni(1.2)/Cu(5)/Ni(0.4)/[Co(0.2)/Ni(0.4)]<sub>n</sub>/Cu(5)/Ni(1.2)/Cu(10)/Nb(20)/Au(15). Each sample was sputtered to completion, at a temperature between -30

and 30 degrees C, before moving on to the next sample. For a full discussion of the process of sputtering, see Section 3.2.2.

Once the sputtering run was complete, the sample holders were removed from the sputtering chamber and returned immediately to the clean room. The samples were removed from the holders once in the clean environment.

To remove the excess material that was deposited on top of the photoresist, the samples must undergo a liftoff procedure. They were first placed in a beaker of hot acetone, on a hotplate set to 90 °C, for 10 minutes. The beaker was then removed and placed in an ultrasonic shaker for 10 additional minutes. Additional acetone may need to be added to the beaker during this time as the ultrasonic process tends to boil off acetone rapidly. Within moments of the beaker being introduced to the ultrasonic, the vast majority of the undesired material should be completely removed, and the base multilayer geometry should be apparent.

After 10 minutes, the sample should be removed from the acetone, rinsed with IPA, and placed in a beaker of IPA to ultrasonic for 10 minutes. Then rinse the sample with DI water and ultrasonic in DI water. Another DI water rinse should be done before blow drying with N<sub>2</sub> gas. An inspection of the samples in an optical microscope is necessary to ensure that the smallest features - the alignment marks - have properly formed, and have not been removed during liftoff.

#### **4.2.4 EBL Definition of Pillars**

In preparation for EBL writing, the sample was again coated using the spinner. This time, however, a bilayer of resists was used to create a sufficient undercut. The undercut was necessary to prevent future deposited metals from climbing the sidewall or binding to the

resist. If such contact were to occur, the metal would be likely to be torn off during the lift-off process.

We first spun P(MMA/MAA) EL9 resist for 40 seconds at 6000 RPM. Using a pipette, seven drops of the resist were placed on the center of the chip before starting the spinner. This created a thickness of about 200 nm in the center of the chip, with a usable area profile similar to the Photoresist step above. The sample was baked for 120 seconds at 180 degrees C on a hotplate, and allowed to cool before further processing.

The second step was to spin PMMA C2 E-Beam resist on top of the baked P(MMA/MAA) EL9 resist. Again, seven drops were deposited before starting the spinner, which ensured complete coating. The sample was finally baked again for 120 seconds at 180 degrees C on a hotplate. This results in an additional 70 nm of thickness to the e-beam resist layer. While the documentation claims that 100 nm should be expected, AFM measurements suggest that roughly 30 nm of the PMMA C2 forms an interface with the P(MMA/MAA) below it.

Once the E-Beam was properly stigmated following Section 3.4.2.2, the sample itself was written. Each sample had six regions on which a pillar could be patterned. The E-Beam was refocused on an alignment mark near to, but not within proximity effect distance of, the writing area. The *proximity effect* in this usage is not the superconducting variety discussed in Chapter . Because the E-beam creates a tear-drop shaped interaction region that is larger than the beam size, written features that are particularly close can experience extra dosing from each other. This can usually be accounted for by practicing a pattern, but only if it results from systematic writing. Adding extra dosing from the scanning of the screen is non-reproducible, and definitely to be avoided.

Following the refocusing, the EBL window was placed over the center of the writing window at 1000x magnification (the writing magnification) to properly center the writing

area. Failure to do this could result in an error during alignment, due to the alignment marks not falling in the writing window. As soon as it was centered, the window was backed out to 200x magnification (the first alignment mag), before finally “blanking”, or deactivating the raster of, the beam.

Two different alignment sets were used to guarantee accuracy of the final pillar location. The first was a set of crosses placed at the corners of a square 300  $\mu\text{m}$  on a side and centered on the eventual pillar location. Once the computer had locked into those crosses, the magnification was run up to 1000x. Another alignment was performed on a set of L-shaped features that were again placed at the corners of a square, this time 50  $\mu\text{m}$  on a side.

Once the alignment was finished, the pillar was written. The write file always included a “pin-wheel” geometry along with the pillar design. The pin-wheel was used after development to ensure that the beam was properly stigmated and focused when the pillar was written. The writing was done at a beam current of 35 pA, the pillar was written with an area dose of 500  $\mu\text{C}/\text{cm}^2$ , and the pin-wheel was written at a line dose of 2.5 nC/cm. These values remained the same for all pillar dimensions. See Section 3.4.2.1 for more on the pin-wheels and writing values.

Once all the pillars have been written, the sample is removed from the EBL. For development the sample was wafted for 30 seconds in a 1:3 solution of MIBK and IPA. It was immediately moved to a beaker of pure IPA and again wafted for 30 seconds. When it was removed, the sample was sprayed directly with IPA, and then blow dried with  $\text{N}_2$  gas. Examination of the pillars was done in an optical microscope, but only pillars of about 2  $\mu\text{m}$  in diameter or larger could be seen clearly. Smaller pillars could be seen, but not thoroughly enough to gauge their quality. An example of a finished pillar can be seen in figure 4.5.



Figure 4.5: *Optical image of sample 2120 4A-2, a 4  $\mu\text{m}$  by 2  $\mu\text{m}$  Elliptical Pillar defined by Electron Beam Lithography. Note the four L-shaped alignment marks, including the two that have been clearly exposed to the electron beam.*

For a complete discussion of EBL sample writing, see Chapter .

### 4.2.5 Aluminum Evaporation

The Electron Beam lithography acts as a negative mask in our process. In order to actually define the pillar for later steps, we needed something to serve as a mask during the ion mill process. Aluminum was effective in this step because it has a relatively low Ion Mill etch rate, was easy to evaporate, and was easy to etch away.

The samples were placed in the evaporator face down over an alumina-coated tungsten boat with about 3 pellets worth of Aluminum. The evaporator was closed and pumped down for about three hours to attain as low a pressure as possible (preferably a few  $10^{-7}$  Torr at maximum). Current was slowly applied to the tungsten boat, following the discussion of Thermal Evaporator operation in Chapter . The rate of deposition was typically around 3  $\text{\AA}/\text{s}$ , though that was later increased to 20  $\text{\AA}/\text{s}$ . This change was done to improve the quality of the Aluminum pillars grown on the sample.

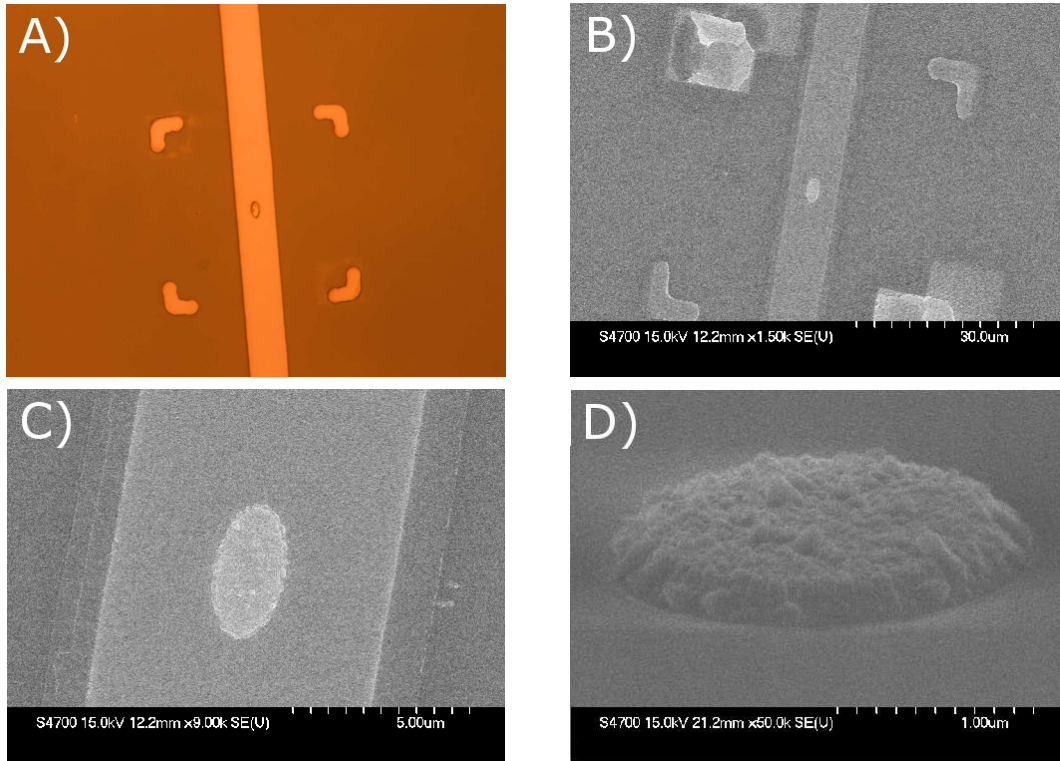


Figure 4.6: *Images of a 4  $\mu\text{m}$  by 2  $\mu\text{m}$  aluminum pillar after liftoff.* A) Optical image at 100X magnification. B) A similar pillar seen from above in the Hitachi SEM at 1.5k mag. C) 9k mag shows fine detail of the pillar, including the rough edge characteristic of the slow evaporation rate (see 4.2.5 and 4.3.4). D) The same pillar seen at 50k mag at an angle of 70 degrees from vertical, demonstrating the surface roughness of the aluminum film.

After allowing the evaporator to cool for about 30 minutes, the samples were removed. They were again exposed to the same liftoff procedure mentioned in section 4.2.3. The pillars were examined in an optical microscope to ensure that no aluminum pillar was ripped away during the liftoff procedure. See the figures in 4.6 for the results of this process.

#### 4.2.6 Ion Mill and Silicon Oxide Deposition

The samples were loaded into individual sample holders for insertion into the Ion Mill (small) Chamber. A small stainless steel mask with a 5 mm by 5 mm square hole was aligned over the six pillars so as to not expose the entire sample to the Ion Mill. This also improved the

thermal contact with the heat sink. Only five samples can be run in the Ion Mill at any one time. See Section 3.2.3 for more on the Ion Mill.

The samples were first Ion Milled halfway through the second copper layer from the top of the sample. Thus the Ion Mill cuts through the layers Au(15)/Nb(20)/Cu(5)/Ni(1.2)/Cu(2.5). It simultaneously consumed the top of the aluminum pillar. The relative milling rates as compared to the milling rate of Au are provided in Chapter . Typically, each sample required about 4 and a half minutes of milling, primarily due to the very slow mill rate of Nb.

The quantity of aluminum deposited in the previous section was calculated carefully based on the goals of the Ion Milling. It was thick enough that it wouldn't be completely consumed in the ion mill, and thick enough that it would be taller than the final SiOx around it. It was also not so thick that it accidentally exceeded the height of the undercut region in the e-beam resist. That way, the aluminum pillar didn't make contact with the top of the e-beam resist, which may have resulted in it being lifted off the sample.

#### 4.2.7 Side Milling

The SiOx deposition had the effect of coating the entire exposed sample with SiOx. Theoretically, this would simply place SiOx straight down on all exposed surfaces and leave a small bit of aluminum exposed. However, because the sidewalls of the materials in these samples were not perfectly vertical, and because the evaporation was not completely collimated, the sides of the aluminum pillar were often coated with SiOx.

Interestingly, this was not a problem for pillars that are "large enough" - on the order of about 3  $\mu\text{m}$  in diameter. If the pillar was at least this size, enough of the sides of the pillar were exposed to enable liftoff (or etching) of the photoresist (or aluminum) pillar. If

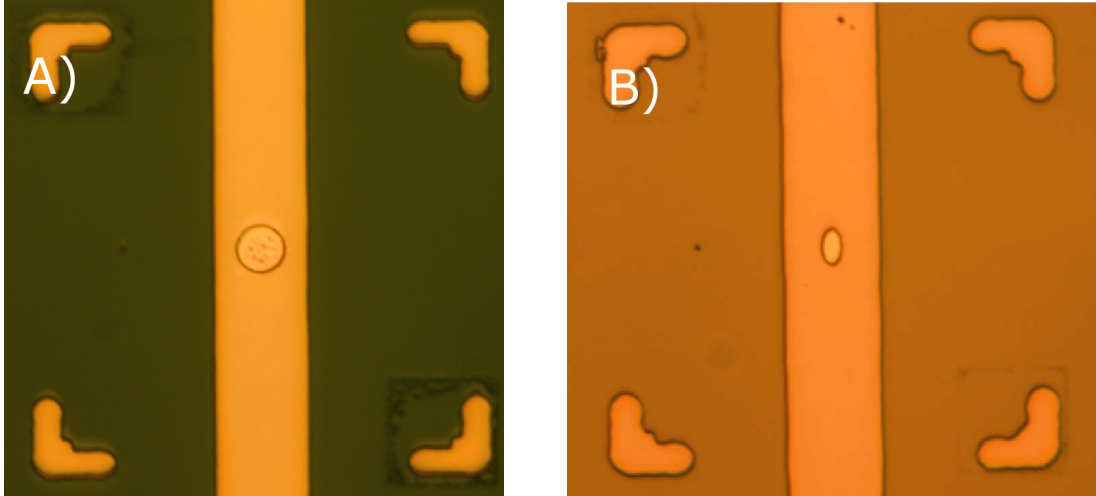


Figure 4.7: *Images of the Aluminum Etch process.* A) Optical image at 100X magnification of a  $5\ \mu\text{m}$  circular pillar. Inside can be seen spotting due to aluminum that has not been completely etched away. B) Optical image of a  $4\ \text{by}\ 2\ \mu\text{m}$  pillar that is completely open after the aluminum etch. The coloration around the pillar is due to the surrounding SiOx that is nearly transparent at this thickness.

it was under this size, there was a reasonable chance that the entire pillar was covered, and therefore immune to the liftoff procedure.

The solution to this problem was to “side mill” the pillar. Special sample holders position the sample such that the face of the sample points 3 degrees from horizontal - or, in another perspective, the Ion Mill beam comes in at 3 degrees from the face of the sample. This process then allowed the Ion Mill to attack the edge of the pillar coated with SiOx while limiting the milling of the face of the sample.

The samples were side milled twice, directly along the long axis of the base multilayer, once from each side. The side mill was done for approximately 2 minutes at a milling rate of roughly  $6\ \text{\AA}/\text{s}$ , which was enough to expose the aluminum buried underneath the SiOx.

### 4.2.8 Aluminum Etch

Unlike S1823 photoresist, aluminum cannot be done away with simply by washing with an acetone liftoff procedure. It turns out, however, that the 352 photoresist developer works as a very effective aluminum etchant. This made for a much more simple liftoff procedure. While we have not measured the exact etching rate of the aluminum in 352, we were able to determine optically how long to etch based upon how long it took the largest pillars to be etched completely.

The sample was placed in a beaker of 352 solution and placed in ultrasonic vibration for an hour. The sample was then rinsed in DI water and blow dried with  $N_2$  gas in the usual way. Once complete, the sample was inspected optically for any color variations within the largest pillars, particularly at the center of the pillar. Any variations in color, such as can be seen in Figure 4.7, requires a repetition of the entire procedure for an additional 10 minutes.

It was also very important to make sure that the sample was blow dried from multiple angles. One of the possible methods of discoloration was for water to dry at the bottom of a pillar instead of being drawn out by the  $N_2$ . This form of discoloration was typically sharper optically (black edges instead of a uniform color) and usually was distributed over multiple areas. Rinsing with water and blow drying the sample again solved the problem.

### 4.2.9 Top Lead Ion Mill Cleaning and Sputter

Once the aluminum pillar was completely etched away, the samples were again loaded into the sputter chamber sample holders. For this step we used a physical mask with six pads and leads. The sample holder could be placed under the microscope so that fine detail could be observed. If the bridge screws are not tightened completely, the mask should be able to

move around on top of the sample allowing easy alignment with a pair of tweezers. Once the bridge screws were properly tightened, the mask was rechecked to ensure that it did not shift while tightening. If the sample is still aligned, it will remain so through the run so long as the screws are not loosened.

With the sputtering chamber ready to go, the samples were first ion milled while in the big chamber. This step was originally used simply to clean the top surface of the Au to eliminate any garbage that might have collected at the top of the pillar. In this process the ion milling is critical, as Al and Au form a particularly problematic interface layer. That layer might have remained after the Aluminum etch, so another strategy had to be employed.

The ion mill was run on each sample for an amount of time sufficient to mill 10 nm of Au, which was typically around a minute and a half. 10 nm was sufficient to completely eliminate the Al/Au interface, while not so long as to eat completely through the Au layer. The Mill was run at a much lower voltage (about 150 V) to minimize the possibility of damaging the sample. See Section 3.2.3 for more.

Once the samples were milled, they were then finished by sputtering leads of Nb(150)/Au(10) on top of the pillar.

### **4.3 SQUID Samples**

The SQUID samples were fabricated in a procedure that was very similar to the E-Beam Lithographic process described in section 4.2. However, some significant changes were made in a couple of critical areas. This section will detail the changes to the process. Figures 4.3 and 4.4 still apply to the fabrication in this section.

### 4.3.1 Photolithographic Definition of Bottom Leads

The design of the bottom leads for the SQUID geometry necessitated long, thin leads down the length of the chip. These lines were between 5 and 10  $\mu\text{m}$  in width and several mm's in length, but spaced by only 7  $\mu\text{m}$ . This means that after the development there needs to be very long channels separated by a very thin plateau of S1813. As it turns out, this was much too thin for the weak bonding between the S1813 and the Silicon substrate, resulting in channel gaps moving around or being ripped off entirely by the development process.

The solution to this problem was to use Hexamethyldisilazane (HMDS). This chemical binds to the surface of the Silicon and provides a much more stable interface for the S1813 to adhere to. After the samples were cleaned following 4.1.1, they should be baked in an oven set to no less than 120 degrees Celsius for no less than 10 minutes. This evaporated any water that had bound itself to the surface of the Silicon substrate.

A little HMDS poured into the bottom of a desiccator will create a gaseous vapor of HMDS in the chamber. If this was done before the chips were placed in the oven, the desiccator would be ready by time the chips had been fully baked. Straight from the oven, and while still warm, the Silicon chips were placed into the desiccator on a platform set above the bottom. The HMDS vapor coats the surface of the chip in a monolayer, providing a stronger binding surface for the S1813.

At that point, 4.2.2 was followed as normal to complete the photolithography for the bottom leads.

### 4.3.2 O<sub>2</sub> Plasma Etch

After development of the photoresist, the HMDS needed to be removed from the sample surface before any metal was deposited. It was also helpful to make certain that any residual photoresist that may have been left over from the lithography was completely removed as well. While the HMDS should not adversely effect the binding of the metal to the surface, this was not something that we wanted to leave to chance.

The plasma etcher must be cleaned before use. Failure to do so can lead to dramatically inconsistent results in the etching, and potentially deposit unknown material onto the sample. It was typical to run the etcher empty at 300 W for 5 minutes in 500 mtorr of O<sub>2</sub> gas to etch away any organic materials left inside the system by previous users. After this, the plate was removed from the system, and cooled by evaporating Acetone on its surface. Once cool, the surface was rinsed with acetone and blown dry, followed by a similar step with IPA.

The samples were placed as close to the center of the plate as possible in order to avoid edge effects in the plasma field. This was done with the plate out of the system so the samples

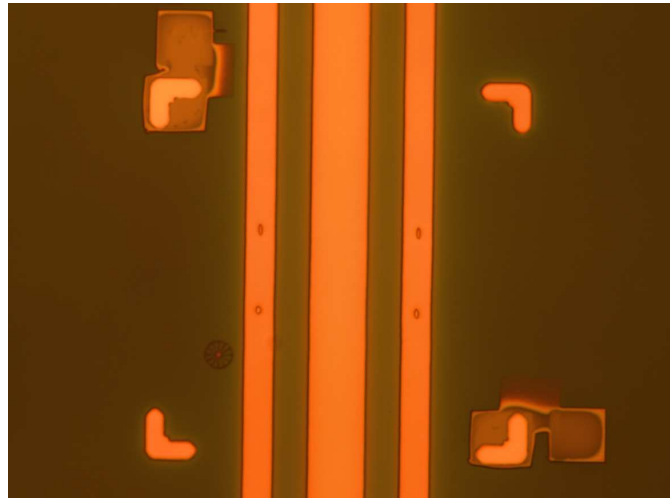


Figure 4.8: *Optical Image of a SQUID sample after Electron Beam patterning.* All four pillars are written simultaneously. Note that the aspect ratios of the ellipses are slightly different in each pair.

could be better controlled, and so that the risk of damaging the sample was minimized.

Once the system had been pumped down, it was run at 100 W for 90 seconds in 500 mtorr of O<sub>2</sub> gas to remove residual photoresist from the sample channels. The coloration of the sample will change slightly - typically from dark green to a pastel green for these samples. If the etcher was being used to completely strip any photoresist from a sample instead, it was run at 300 W for about 2 minutes at 500 mtorr gas pressure.

### **4.3.3 Sputtering, and E-Beam Lithography**

Refer to sections 4.2.3 to 4.2.4 for the processes used to deposit the bottom leads and define the pillars.

The top layer of Au in the bottom leads was sputtered to 20 nm in this experiment rather than 15 nm. This was an extra buffer for performing the additional milling discussed later in the section (see section 4.3.5)

The E-Beam Lithography had several key differences in this process which are shown in Figure 4.8 . First, the SEM magnification used to image the small alignment marks was set to 800x due to the width of the bottom leads. The marks themselves were identical to the ones used in previous experiments. The second difference was that four pillars, each with different aspect ratios, were written instead of just one, since two SQUID's were present in each alignment window. This reduced the writing time by a fair margin. Lastly, the pillars were drastically reduced in size to attempt to approach a single domain in the top ferromagnetic layer. Pillar areas were reduced to nominal sizes as small as  $.094 \mu\text{m}^2$ .

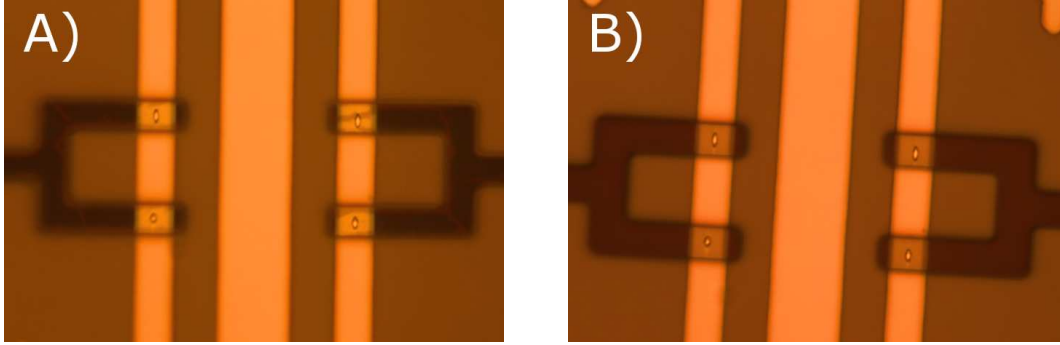


Figure 4.9: *Aluminum pillar growth compared to the deposition rate.* A) 1 by 0.25  $\mu\text{m}$  elliptical pillar deposited at 2-3  $\text{\AA}/\text{s}$ . Note that the pillar shape is not well defined because of aluminum grains that are too large. B) 1 by 0.5  $\mu\text{m}$  pillar deposited at 19-20  $\text{\AA}/\text{s}$ . The pillar is much more well defined, and the grain size is much smaller.

#### 4.3.4 Aluminum Evaporation

This process was similar to 4.2.5. Issues were discovered in the process and changes were made to the evaporating conditions in order to improve the pillar growth.

With the reduction of the overlap region between the bottom and top leads, the  $\text{SiO}_x$  thickness could be safely reduced without a substantial risk of pinholes. This allowed the thickness of the Aluminum pillar to be reduced from 200 nm to only 90 nm. Such a reduction in thickness prevented the grains at the edges from growing out of control and distorting the shape of the pillars.

In a similar vein, the rate at which the Al film was deposited was increased to as much as 20  $\text{\AA}/\text{s}$ . By increasing the deposition rate the size of the grains was reduced significantly. This is a result of the increase in the density of nucleation sites, reducing the available area for a grain to grow before merging with a neighbor.

#### 4.3.5 Milling and Etching

This procedure is repeated following sections 4.2.6 to 4.2.8.

Following the Aluminum Etch an additional top milling must be done. This extra run was to ensure that any leftover aluminum or Al-Au alloy had been completely removed. During the course of this project it was discovered that omitting this milling step may have had dire consequences for the fabrication. Without it the sample resistances were wildly inconsistent, varying between several hundred milliohms at best and several thousand ohms at worst - a five order of magnitude variation. It must also be done before defining the top leads, as the issue arose only when using photolithography to pattern the top.

It should be pointed out that there were multiple issues that could have caused this resistance issue. It is possible that the problem was related to the cleanliness of our photomask, which we were forced to eventually ship back to the company that produced it for cleaning. However, for this to have been the problem, a thin film, transparent to visible light but translucent to the UV light used in writing, would have to have formed on the surface of the mask. Where such a film had come from is a mystery, but may be related to failing to fully back the sample away from the mask before adjusting the position during alignment.

For our process, we calculated a milling time appropriate to mill 10 nm of Au in this last step. Aluminum mills more slowly than Gold, and so the actual thickness removed may have been somewhat smaller than the predicted value.

### **4.3.6 Top Lead Photolithography and Sputtering**

With the change in design to the SQUID layout, the line widths of the SQUID became only 5  $\mu\text{m}$ . This made it necessary to fashion the top leads using photolithography. The process is identical to 4.2.2. The samples must be aligned in the optical lithographer using the crosses as guides for both x and y translation, and for rotation. The SQUIDs only have roughly a half micron to a micron of slack in the lithography, so care must be taken to ensure that the

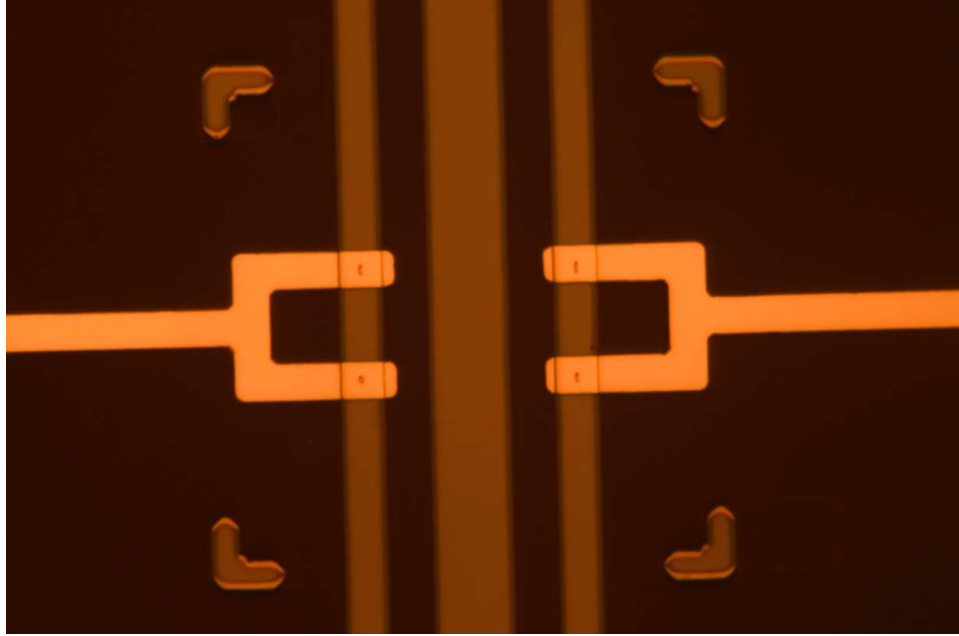


Figure 4.10: *A completed pair of SQUIDs, after top leads have been sputtered on and liftoff has been finished.*

crosses line up across the chip.

It was extraordinarily important that the mask remained as clean as possible. Photomasks can accumulate garbage over time, particularly photoresist from the surface of samples. Sometimes this dirt is visible in an optical microscope. A dark field setting can illuminate dust-like particles on the surface, as light scattering from the particle surfaces will stand out visibly against the dark background. However, it is possible for an insidious film to develop on the surface that is invisible in an optical microscope. The only proof that such a film was present was after development, where the sample would appear underdeveloped, or even after the sample had been completely fabricated with a higher-than-expected sample resistance.

After development another Plasma Etch must be done following 4.3.2. With the SiO<sub>x</sub> deposited on the surface, the reflectivity of the sample was reduced. This in turn reduced the effective dose of the optical lithography and allowed resist residue to be left behind in

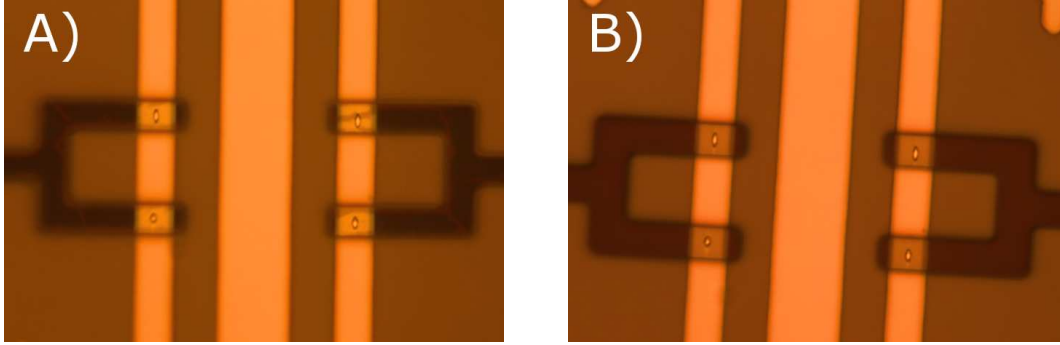


Figure 4.11: *The benefits of Plasma Etching.* A) Optical image at 100X magnification of a pair of SQUID junctions immediately following photolithography. Careful inspection shows an inconsistent color pattern inside the top lead channels. B) Optical image of the same SQUIDS after etching in  $O_2$  plasma. Note the channels have become much more uniform in appearance.

critical regions of the sample. This reduction in dose was compensated for by increasing the exposure time to 12 seconds, which improved the etching during development. This time also preserved the critical features, and did not seriously change the shape of the devices. The  $O_2$  plasma, run at a power of 100W, was also used, and was effective at cleaning the residue. (See figure 4.11)

Finally, the samples were ion milled and sputtered following section 4.2.9. The *in-situ* ion mill in the sputtering chamber was done as a cleaning process only, so only 2 nm Au needed to be removed. Once complete, the samples were lifted off as per section 4.1.5.

### 4.3.7 Negative E-Beam Resist

One of the big concerns in the measurement of the SQUID samples was the roughness of the aluminum pillars. You can see in Figure 4.6 that the evaporated aluminum does not have a particularly smooth profile. Since the top ferromagnet will possess the general shape of the aluminum pillar due to the ion mill process, this could cause issues with the switching of the magnetic moments in the samples. Therefore, it was preferable to replace the aluminum

pillar with a smoother mask.

A negative E-Beam Resist is one in which the written pattern remains after development. Instead of breaking bonds as in traditional E-Beam writing with PMMA, the electron beam forms bonds in the polymers, making them more resistant to the developing agent. This allowed us to skip all of the steps dealing with the aluminum in 4.3.4 and 4.3.5, as the E-Beam resist replaced the aluminum pillar.

The resist we used was ma-N 2401. It was spun coat as a single layer at 3000 rpm for 40 seconds. It was then baked on a hot plate at 90 degrees C for 120 seconds. The writing conditions for the resist are very similar to the PMMA method, so no changes were made in the doses. All pillars were written at  $500 \mu\text{C}/\text{cm}^2$ . Once the writing was finished, the sample was developed in AZ 300 MIF Developer for 30 seconds and then rinsed in DI water for 20 seconds.

The sample could then be placed directly into the ion mill holders. Heat sinking was of paramount importance here so that the pillars could be properly lifted off. A very small dot of Santovac diffusion pump oil was placed on the back of the samples to provide better thermal conduction to the heat sink. Failure to include this would cause the ma-N to overheat, resulting in a poor liftoff. It was crucial to make certain that a very, infinitesimally small amount of Santovac was used, so that it didn't leak out around the edges of the sample and foul up the top of the sample. The Santovac was removed by the PG remover during liftoff.

After the ion mill and silicon monoxide deposition, the sample was side milled like with the aluminum process. The side mill was included as a legacy step, since it was found to be necessary with the small aluminum pillars, it was reasonable to suspect it would be necessary here. That has not been proven, and may not be a necessary step after all. The side milling was done at roughly  $6 \text{ \AA}/\text{s}$  for 2 minutes on a side.

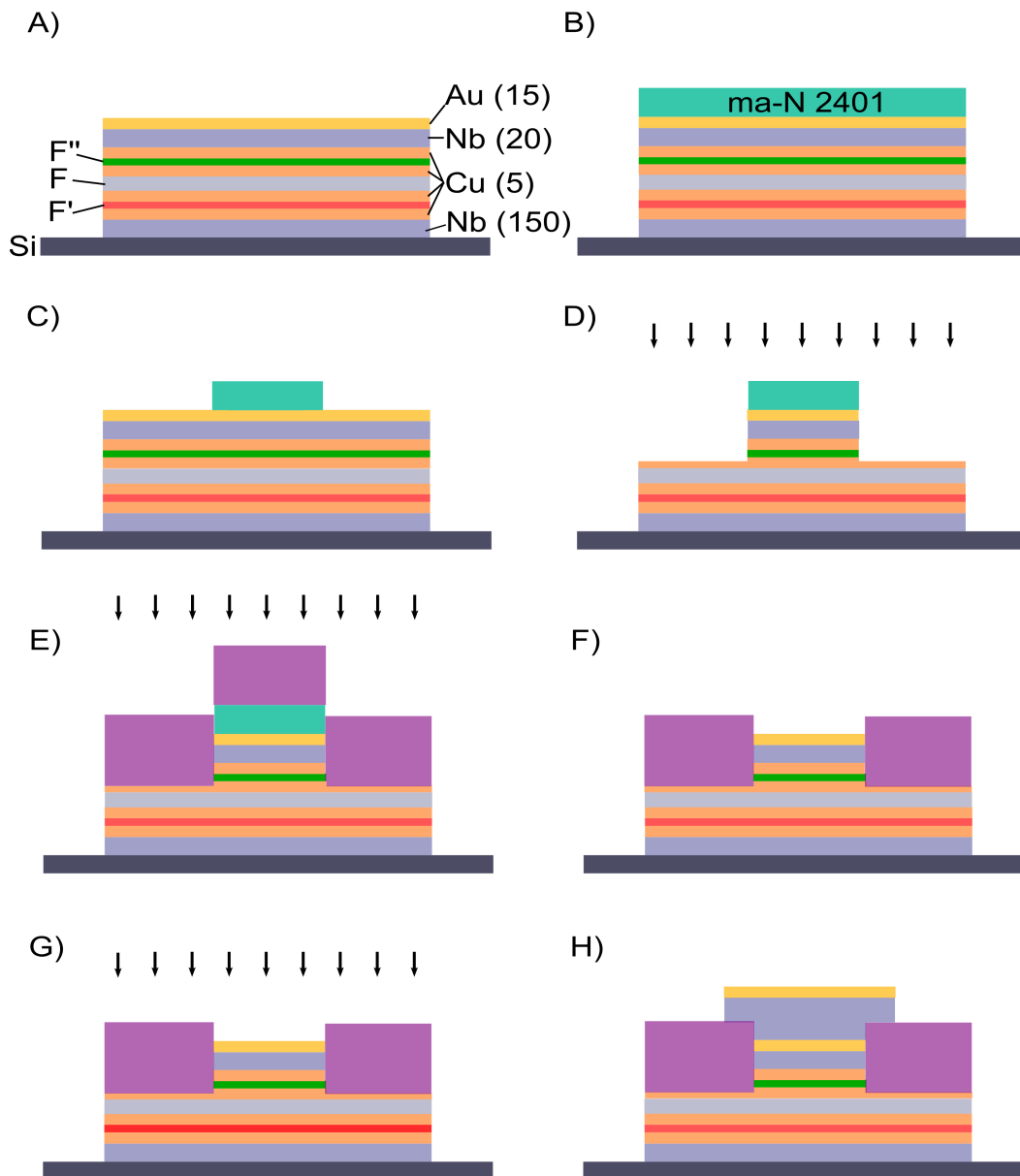


Figure 4.12: *Cartoon of the sample fabrication procedure using Optical Lithography.* A) The Base Multilayer after Sputtering and Liftoff. The F layer can be either the Co/Ru/Co SAF or the Co/Ni multilayer with PMA. B) ma-N 2401, a negative E-Beam resist, is spun onto the sample. C) After writing and development, the polymer has been removed in the unexposed regions, forming a pillar with a slight undercut. D) The sample is ion milled to the middle of the top Cu layer. E) SiOx is *in-situ* deposited immediately following the ion mill. F) The pillar and the SiOx that has coated it is removed via acetone liftoff after side milling both sides of the pillar. G) The sample is ion milled again to clean the surface. H) Top leads are sputtered onto the pillars.

Following the side mill, the ma-N 2401 was lifted off the sample. The sample was placed in a beaker of PG Remover set on a hotplate warmed to 110 C and capped with aluminum foil. The foil allows the temperature inside the beaker to reach roughly 60 °C during the liftoff. The sample was given 15 minutes on the hotplate before being moved to the ultrasonic for another 15 minutes. After liftoff, the sample is rinsed in DI water for 20 seconds and blow dried off.

# Chapter 5

## Characterization of Co/Ni Multilayers

As mentioned in Chapter , previous work in our group focused on the use of the Co/Ru/Co trilayer as the central ferromagnet of our S/F'/F/F'/S Josephson junction structure. This chapter details our studies into a possible replacement of the trilayer with a different ferromagnetic multilayer, Ni/[Co/Ni] $_n$ . The first section will discuss in greater detail the traits of the Co/Ru/Co trilayer. Section 5.2 looks at the advantages of the Co/Ni multilayer as a replacement for Co/Ru/Co. Section 5.3 discusses the variety of samples fabricated for these studies. The fourth section details the magnetometer studies performed in characterizing the magnetic properties of the multilayer. Section 5.5 discusses our measurements of the Fraunhofer patterns and  $I_c R_N$ 's of these pillars. Section 5.6 examines the viability of the Co/Ni multilayer as a central ferromagnet in Spin-Triplet generating samples. Lastly, section 5.7 examines the studies performed on enhancing the magnetic properties of the multilayer.

### 5.1 The Co/Ru/Co Trilayer

The first attempts in our group to measure S/F/S Josephson junctions demonstrated some unexpected results. Work involving weak ferromagnets, such as PdNi [64], demonstrated clear Fraunhofer patterns (see Chapter 2). These patterns were not identical to the perfect patterns you would see in a S/N/S junction, but demonstrated a large central peak along with smaller fringe peaks. Typically, the central peak would be shifted to positive or negative

field, as opposed to being centered at 0 mT as you would expect for an S/N/S junction, due to the necessity for the external field to cancel the magnetic flux of the ferromagnetic layer.

A strong ferromagnet, such as Co, turns out to have a much more significant impact on the resulting Fraunhofer pattern. Early work on S/F/S junctions using Co alone demonstrated that for very thin films of Co the pattern was reasonably well behaved, but for much thicker films the pattern would be functionally random and demonstrate no clear central peak [65]. This was a serious problem in the characterization of these junctions, since it was impossible to identify any systematic patterns.

The choice was made to use Co/Ru/Co because of its synthetic anti-ferromagnetic (SAF) properties. The domain structure in the two Co layers will naturally arrange itself on formation such that the magnetizations of the two Co layers point antiparallel to each other [66]. Any current passing through the Co layers will therefore experience zero net magnetic flux in the trilayer. Thus, the resulting Fraunhofer pattern will be unaffected by the inclusion of the F trilayer.

Another advantage to the Co/Ru/Co layer appeared in later studies by Klose [67]. When magnetizing the Ni F' layers, a significant enhancement in the measured supercurrents were observed compared to the virgin state data. This was due not only to the magnetizing of the F' layers, but also to a significant change in the central trilayer. When Co/Ru/Co is magnetized the Co layers will align parallel to the external field. However, once the field is released, the Co magnetizations will each rotate 90 degrees so that they align opposite each other, preserving their SAF nature. Because the Ni F' layers remain aligned to the direction of the external field, this "Spin-Flop" transition has the effect of providing the precise 90-degree angle between the ferromagnetic magnetizations in order to optimize the triplet.

Considering its properties, the Co/Ru/Co trilayer is remarkably well suited for the study of the spin-triplet pair correlations. It provides no magnetic flux to the current, provides an easy system of arranging its magnetization perpendicular to the F' layers, and is relatively easy to fabricate. However, several issues were discovered that caused concerns with the trilayer. First, my experiment was going to call for Josephson junctions of the form S/F'/F/F''/S. This means the studies would require three different ferromagnetic layer materials, where previous experiments only called for two. This meant that seven total materials had to be sputtered. But, at the time, the sputtering system only had 6 guns. Second, while the Co/Ru/Co exists as a SAF in its virgin state, the perfectly orthogonal magnetizations of the Co and the F' and F'' layers only results from the spin-flop transition that occurs after it has been magnetized [67]. Lastly, Yixing Wang began to have concerns about the uniformity of the Ru layer that was being sputtered. This concern was based on inconsistent results he was seeing in his Josephson junction data.

All three issues combined were enough to force the realization that a new multilayer was necessary. The properties of such meant that it had to: include a material that was already included in the planned multilayer stack, come pre-magnetized in the virgin state, and not involve a Ru interface layer.

## 5.2 The Co/Ni Multilayer

When grown in the FCC arrangement, thin films of Co grown in alternating [111] multilayers with other materials turn out to possess Perpendicular Magnetic Anisotropy (PMA). Originally, the first materials studied for the pair were non-magnetic materials such as Pd, Pt, Au, Ag, and Ir. When Daalderop *et al.* [68] began to study the Magnetic Anisotropy

Energy (MAE) of these films, they discovered that, while there was no dependence on the MAE from the thickness of Cu and Ag, a slight thickness dependence did appear with Pd. This was interpreted as a result of the magnetic polarization of Pd layers close to the Co/Pd interface. Because Pd and Ni contain the same number of valence electrons, this led them to consider the possibility of a ferromagnetic material in place of the non-magnetic ones used in the study.

In 1992 Daalderop *et al.* theoretically predicted and confirmed experimentally that alternating monolayers of Ni and Co possess a strong perpendicular anisotropy [68]. This is a result of the unique electronic properties of Ni and Co that couple to give strong magnetic anisotropy, along with a Fermi level that intersects electron states possessing a magnetization pointing out of the plane of the film. The big advantage of this is that the Co/Ni multilayer possesses much more ferromagnetic material than the other Co/X counterparts. This means that the overall magnetic moment of the film is much stronger than those films containing non-magnetic layers.

This formation of the PMA is a natural property of the Co/Ni multilayer. This means that the system does not need to be exposed to an external magnetic field in order to achieve a magnetization perpendicular to the F' layers, as long as the F' layers are chosen so that their magnetizations lie in the plane of the film. The addition of the Ni makes it favorable for magnetization studies, as the magnetic moment will remain strong even for thinner multilayers, or for samples with very few bilayers.

Because Co/Ni multilayers have a perpendicular magnetization, one can reasonably expect that the effect of the magnetic flux on supercurrents flowing perpendicularly will be negligible. This remains mostly true, but depends on the size of your sample pillar compared to the domain size of the multilayer. If the pillar is larger than the average domain size of

Co/Ni (which is certainly less than 1 micrometer) the current will sample multiple domains and domain walls. This can have drastic effects on the resulting Fraunhofer patterns and significantly reduce their quality.

### 5.3 Samples

In this experiment, three different types of samples were fabricated: Samples without the F' layer, samples including both F' layers, and magnetometer samples.

The samples without F' were formed in the method described in Chapter . The thin film stack was sputtered through a mechanical mask in the form Nb(150)/Cu(5)/Ni(x)/[Co(y)/Ni(x)]<sub>n</sub>/Cu(10)/Nb(20)/Au(15) (all thicknesses in nanometers) without breaking vacuum. For this experiment, the *n*'s were varied between 2 and 22 repeated layers in steps of 2, while the *y/x* combination was 0.2/0.4, 0.4/0.6 or 0.4/0.8. The samples were then removed, and a pillar defined photolithographically. The sample was ion milled to about halfway through the top most Cu(10) layer, and 150 nm of SiO<sub>x</sub> put down as an insulating layer. The photoresist pillar was removed by liftoff in acetone, followed by IPA, and then water, in order to remove all chemical residues. Finally top leads of Nb(150)/Au(10) were sputtered through a mechanical mask.

The samples with F' were fabricated in exactly the same way as the ones without F'. In this case, the thin film stack had the form Nb(150)/Cu(5)/Ni(1.2)/Cu(5)/Ni(0.4)/[Co(0.2)/Ni(0.4)]<sub>n</sub>/Cu(5)/Ni(1.2)/Cu(10)/Nb(20)/Au(15). Only samples with even *n*'s between 8 and 22 inclusive were fabricated. The rest of the process remained the same as before.

The last type of sample to be fabricated were the chips designed for the magnetometer.

A mask was used that had a large open area, on the order of 1 by 1/2 cm, so that plenty of magnetic material was deposited. The quantity of Nb on the top and bottom layers was changed to reduce the diamagnetic response of the superconducting material. Lastly, we removed the gold so that the final stack had the form Nb(50)/Cu(5)/Ni(x)/[Co(y)/Ni(x)]<sub>n</sub>/Cu(10)/Nb(10). The samples were formed with even  $n$  ranging from 2 to 22, and  $y/x$  possessing the values 0.2/0.4, 0.2/0.6, 0.4/0.6, and 0.4/0.8. No other processing occurred for these samples.

## 5.4 Magnetization Measurements

In the beginning, we had very little understanding of the proper thicknesses and quantities of the Ni and Co multilayers in the samples. Many papers [70] [71] [72] presented a variety of possible options, but there was no way to be certain which possibilities would work best until the magnetic properties had been measured. One of the primary reasons for this is that the fabrication can result in varied properties if it is performed under different conditions. Therefore, it was necessary to know how the multilayer would behave when grown in our system.

The samples needed to display a very strong signature indicating that the magnetization was arranged perpendicularly. This would be identified by two measurements on each sample. When the external field ran across the face of the sample, the system would have to respond sluggishly as the magnetization is forced out of its favored alignment. With the external field arranged parallel to the normal of the surface of the sample, it should switch its direction much more rapidly. See Figure 2.3 and the accompanying discussion for more detail.

Also important to the characterization is the *remanent magnetization*. The remanent

magnetization is related to how well the sample wants to maintain its ferromagnetic arrangement when the external magnetic field is released. In the perpendicular case, it is desirable to get the largest remanent magnetization possible. It is best if the remanent has the same value as the saturation magnetization. In the parallel case the remanent should be as close to zero as possible. This would imply that the system wants to arrange itself perfectly normal to the sample face, regardless of what external field is applied to it.

The samples were measured in the SQUID Magnetometer as described in Section 3.5.2. The samples were typically cut into 2 pieces of roughly equal size. This allowed the available magnetic volume to be doubled, and therefore enhance the resulting signal. Each sample was measured twice, once in the parallel arrangement, and once in the perpendicular arrangement. The perpendicular direction was frequently measured first, as a poor perpendicular signal would be sufficient to dismiss the sample as a possible candidate.

The first samples processed involved Co/Ni thickness combinations of 0.4/0.6 and 0.4/0.8 measured in nanometers. They also contained multilayer repetitions of 4 and 8. These were considered to be the upper bound of the multilayers that would display (PMA), and so would indicate where the upper bound for our fabrication would be.

The data from these samples are presented in Figures 5.1 and 5.2. There are a few fascinating facts to glean from what is shown here. First, with the 0.4/0.6 samples, it appears that there is certainly hysteresis in the parallel direction, suggesting that it is not suitable for these experiments. However, the quality of the perpendicular component seems to improve with additional repetitions of the multilayer. The residual magnetization in the perpendicular direction of the  $n=8$  sample was roughly 78 percent, much improved over the  $n=4$  value of 38 percent. This suggests that increasing the repetitions could improve the PMA behavior of the sample. Unfortunately, the parallel field behavior of the sample

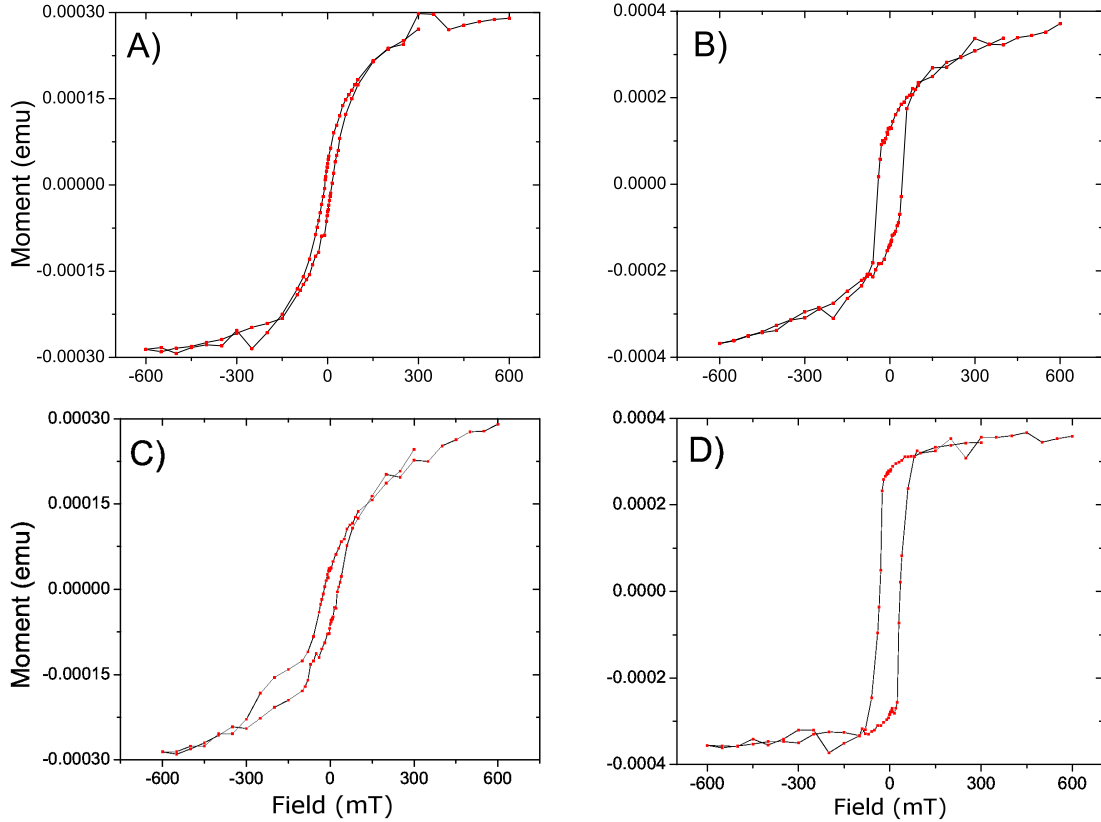


Figure 5.1: *Magnetization curves of the 0.4/0.6 Co/Ni Multilayers.* Plots on the left were measured with the external field along the plane of the sample (parallel), while plots on the right are the same samples with the field pointing perpendicular to the sample face. A)  $n=4$  parallel (in-plane). B)  $n=4$  perpendicular (out-of-plane). C)  $n=8$  parallel. D)  $n=8$  perpendicular.

appears to degrade with increasing  $n$ , becoming more hysteretic and more unusual, with the same changes. This makes this thickness combination less useful for further studies.

The 0.4/0.8 samples, shown in Figure 5.2, are potentially even less useful. The magnetic behavior in these samples appears to greatly favor the parallel arrangement with increasing thickness. It also appears that the PMA vanishes, particularly in the sample with 8 bilayers. It is clear from these data that the magnetization of the 0.4/0.8 arrangement wants to be arranged in the plane of the film. This was particularly surprising, considering other groups have seen PMA in the 0.4/0.8 samples. The source of the noise in 5.2d is not known.

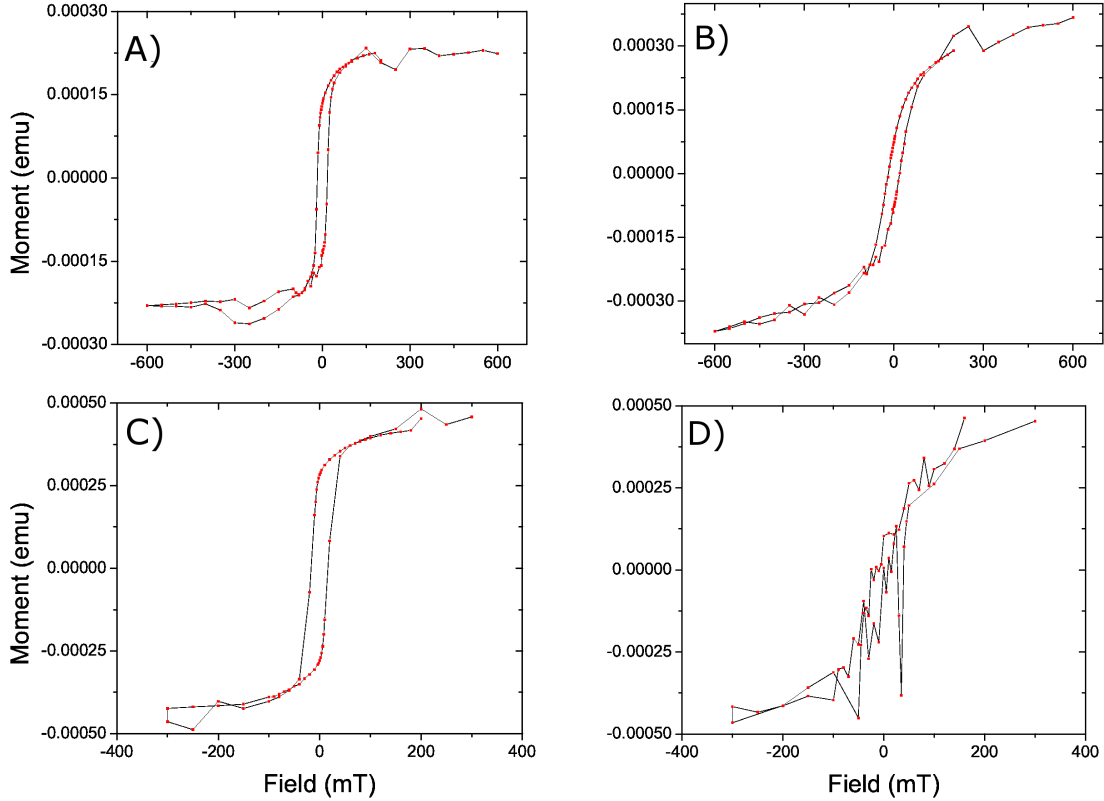


Figure 5.2: *Magnetization curves of the 0.4/0.8 Co/Ni Multilayers.* Plots on the left were measured with the external field along the plane of the sample (parallel), while plots on the right are the same samples with the field pointing perpendicular to the sample face. E)  $n=4$  parallel. F)  $n=4$  perpendicular. G)  $n=8$  parallel. H)  $n=8$  perpendicular.

Following these samples, we analyzed the results of many different repetitions of the 0.2/0.4 multilayer. We began initially with the values 2, 6, and 10 for  $n$ . These results are presented in Figure 5.3. These samples demonstrate much improved magnetic characteristics when compared to the other multilayer configurations. The sample with  $n = 2$  clearly possesses PMA, but the switching is sluggish and begins well before the external field reaches 0 mT. The parallel configuration possesses almost no hysteresis, but it does exhibit a very sharp rise to its saturation magnetization.

Things improve as the repetitions increase. The sample with 6 repetitions has a large remanent magnetization in the perpendicular direction, and very sharp switching charac-

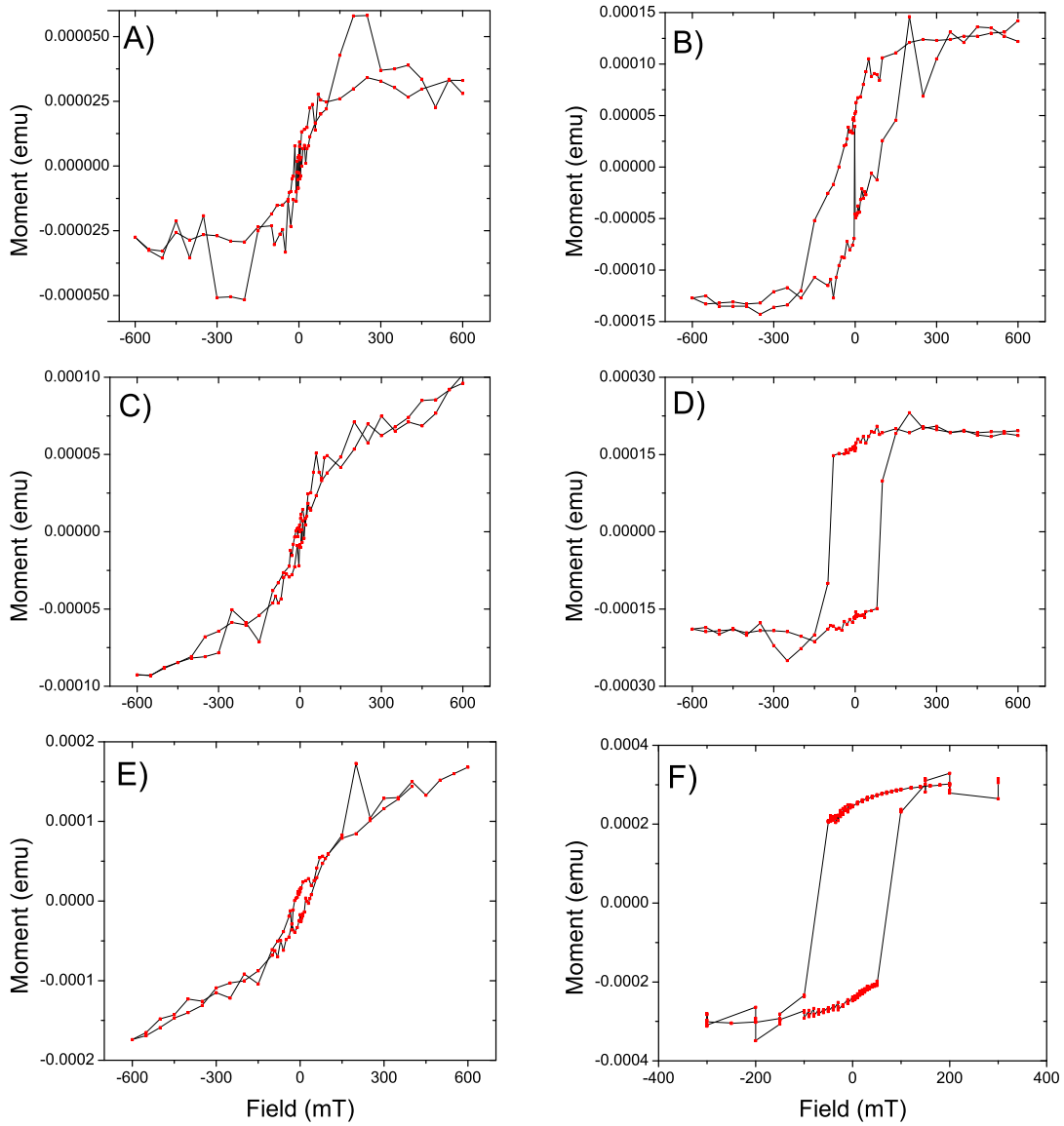


Figure 5.3: *Magnetization curves of the 0.2/0.4 Co/Ni Multilayers.* Plots on the left were measured with the external field along the plane of the sample (parallel), while plots on the right are the same samples with the field pointing perpendicular to the sample face. A)  $n=2$  parallel (in-plane). B)  $n=2$  perpendicular (out-of-plane). C)  $n=6$  parallel. D)  $n=6$  perpendicular. E)  $n=10$  parallel. F)  $n=10$  perpendicular.

teristics. The parallel direction also possesses a nice characteristic, with very little (if any) hysteresis and a very low remanent. The sample with an  $n = 10$  has a similar result, with a large remanent magnetization and a coercive field of roughly 100 mT. Its parallel direction shows a slight hysteresis, suggesting that this is not a perfectly formed PMA. But, the remanent magnetization is very small, so it was expected that the multilayer would still act like a PMA film.

Combining these results with the superconducting properties (discussed later in Section 5.5.1), the decision was made to pursue samples with the 0.2/0.4 magnetic multilayer thicknesses. To further the studies, samples with a larger number of bilayers were fabricated to study the effect of increasing thickness on the Co/Ni multilayer. Some of those results are presented in Figure 5.4.

Interestingly, the magnetic characteristics drastically changed in both the parallel and perpendicular directions from 10 bilayers (5.3e and 5.3f) to 12 bilayers (5.4a and 5.4b). It is not entirely clear why such a large change occurred. Considering the fabrication was done in two separate runs, it is possible that the Co/Ni behavior depends much more on the growing conditions than might be normally anticipated. However, considering how tightly controlled the sputtering conditions are kept, it seems unlikely that there should have been a drastic change in the growing environment.

The sample with 18 bilayers demonstrates the general trend in the run, which included 12, 14, 16, and 18 bilayers. There is a linear progression between 12 and 18, with the coercive field generally increasing with the number of bilayers for both the parallel and perpendicular configurations. The remanent magnetization remains very low in all of the samples suggesting that the samples are breaking up into anti-aligned vertical domains, or perhaps favor a magnetization direction between both parallel and perpendicular directions.

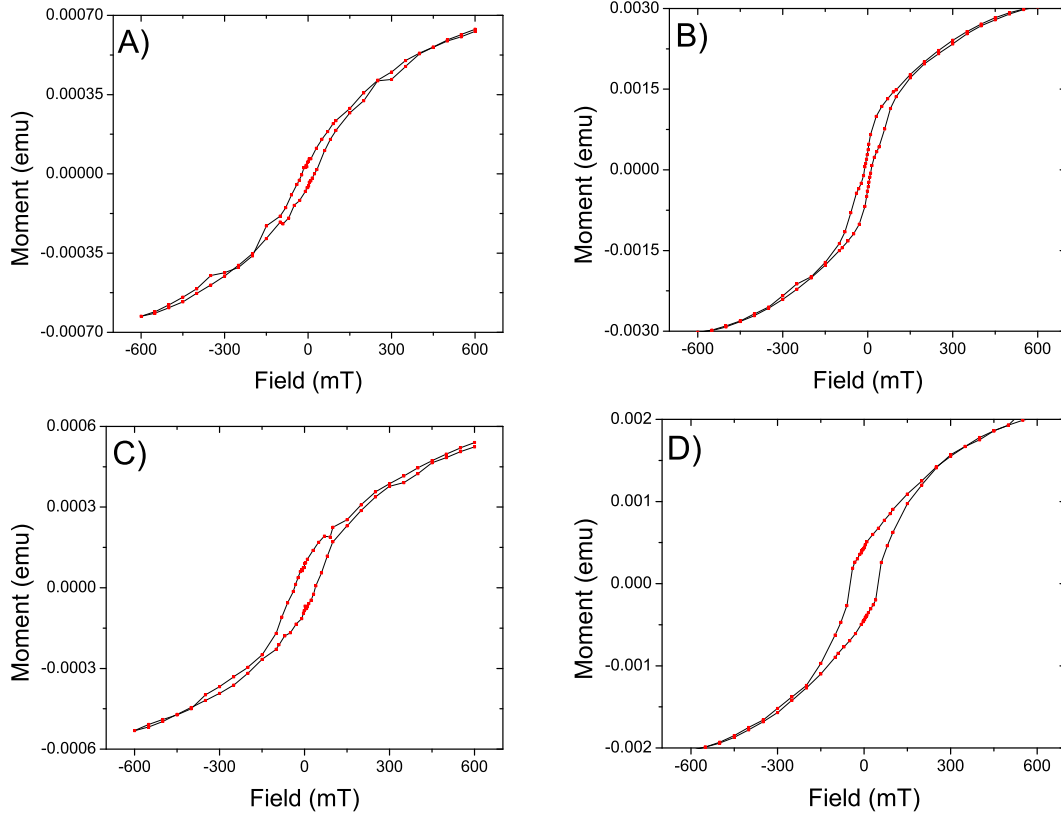


Figure 5.4: *More magnetization curves of 0.2/0.4 Co/Ni Multilayers.* Plots on the left were measured with the external field along the plane of the sample (parallel), while plots on the right are the same samples with the field pointing perpendicular to the sample face. A)  $n=12$  parallel (in-plane). B)  $n=12$  perpendicular (out-of-plane). C)  $n=18$  parallel. D)  $n=18$  perpendicular.

The reader may note the saturation magnetization of the parallel and perpendicular directions. One curious trait of these samples was that the saturation magnetization, which should be related to the total number of spins in the sample, does not seem to approach the same value at high fields. This suggests that some of the spins in the sample are locked in place and unable to rotate, even up to several hundred mT. Figure 5.5 displays magnetometer data from the sample possessing 10 bilayers, magnetized up to 5 T in both the parallel and perpendicular directions. Even here the parallel direction only saturates to half as much as the perpendicular direction. Even to very high field, some of the spins in the sample simply

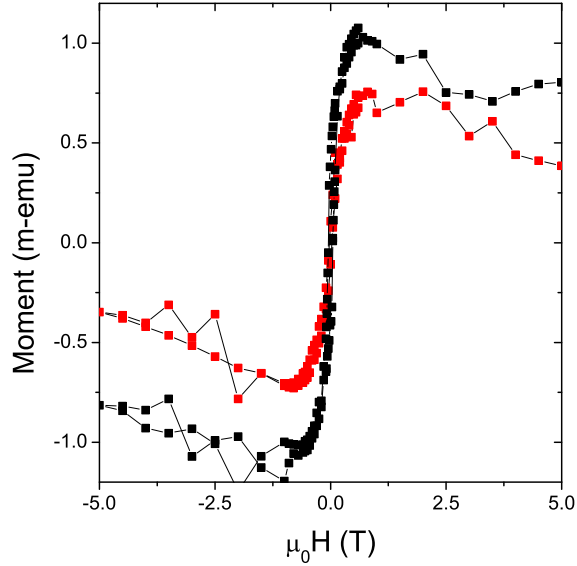


Figure 5.5: *High field magnetization measurements of the  $n=10$  0.2/0.4 Co/Ni multilayer.* The red curve is the parallel configuration, while the black curve is perpendicular. At 5 T, the bilayer demonstrated an inability to align all of its spins in the plane. This suggests some mechanism may be pinning the spins in some intermediate direction.

refuse to cant into the plane. This is a good sign from the context of wanting a film that resists having its magnetization point into the plane, but a bad sign for understanding the properties of the film. The negative slope at high fields is the diamagnetic signal of the Nb films and Si substrate in the sample starting to dominate.

## 5.5 Field Dependent Measurement of Critical Currents

While the magnetic properties of the multilayer must necessarily behave in a predictable fashion, it is equally important that the multilayer carry supercurrent when it is patterned into a Josephson junction. To test this, many samples must be fabricated in order to study the field dependence of the critical current through the varying multilayer thicknesses. When the maximum critical currents of each pillar are plotted against the thickness of the cen-

tral ferromagnet, it is expected to decay exponentially, but preferably it will also exhibit a sufficiently large critical current so that the decay can be measured over a large range of thicknesses.

Since we wish to use this as a layer for the measurement of Spin-Triplet supercurrent, it must also demonstrate an enhancement in its critical current when additional ferromagnets are added with magnetizations that are orthogonal to the Co/Ni. If the material fails to conduct a triplet current, it is useless for any further experiments. Therefore, a systematic investigation of these properties must be done.

These measurements are performed using the Squid Current Comparator circuit discussed in Section 3.5.1. To measure the critical current, the current across the sample is stepped up incrementally until the SQUID reads a voltage. Once that voltage reaches a certain set limit, the current is switched to the negative direction and the process repeated. If the sample is a well behaved Josephson junction, the resulting  $I$ - $V$  curve will look like the one for an overdamped junction as shown in Figure 5.6a. This is discussed in more detail in Chapter 2.

Our measurements are primarily automated, utilizing software programmed by previous students in LabVIEW. The computer sets a value for the field, and then measures an  $I$ - $V$  curve. Once finished, it increments the field by a step size defined by the user at the beginning of the run, and measures another  $I$ - $V$  curve. The  $I$ - $V$  curves are automatically saved into their own individual files after each field step.

A special computer program designed by Yixing Wang extracts the data from those files and applies a fit to the expected  $I$ - $V$  characteristics derived by Ambegaokar and Halperin [69],

$$V = R_N(I^2 - I_C^2)^{(1/2)} \quad (5.1)$$

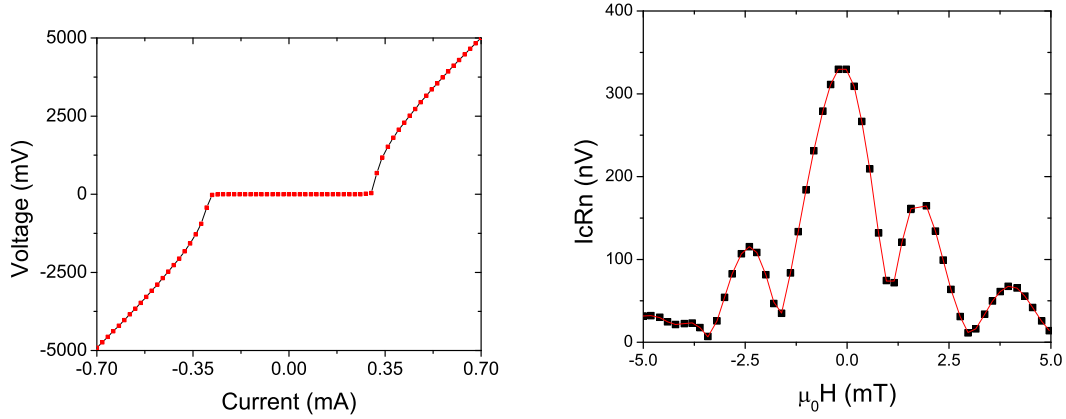


Figure 5.6: *Example of an I-V Curve and a Fraunhofer Pattern.* A) *I-V* curve measured at high field for a typical pillar. The critical current  $I_c$  is the point where the sample transitions from supercurrent (no voltage with finite current) to the ohmic regime. It has been suppressed in this sample by a field on the order of 10 mT. The slope of the linear region is the normal resistance of the sample  $R_N$  B) An example Fraunhofer pattern generated from plotting the  $I_c R_N$  product of the each *I-V* curve against the field at which they are measured.

for  $I > I_c$ , where  $R_N$  is the normal resistance of the junction,  $I$  is the current driven through it,  $V$  is the voltage measured, and  $I_c$  is the critical current. The program then plots the variation of the critical current against the magnetic field. The result is a Fraunhofer pattern as shown in Figure 5.6b. (Since our pillars are circular, the pattern is strictly an Airy pattern, but the differences are subtle. See Chapter .) The critical current of interest in these measurements is the maximum critical current achieved in the sample.

The program can also extract the normal resistance of the sample, which should not be field dependent, but only if the ohmic region of the *I-V* is measured before the voltage cut-off. The voltage cutoff is user defined, and is set to prevent the SQUID electronics from being forced to output a voltage beyond its range. It is possible to find an *I-V* curve with a small enough  $I_c$  so that the ohmic state is at sufficiently low voltage to measure. Typically, the measurement is done to sufficiently high fields that the critical current is suppressed enough so several ohmic *I-V* curves can be sampled.

The traditional method of comparing Josephson junctions is through the product of the maximum critical current and the normal resistance, called  $I_c R_N$ . This is because  $I_c R_N$  possesses no area dependence, since  $I_c$  increases with increasing area while  $R_N$  is inversely related to area. This makes  $I_c R_N$  extremely useful for comparisons of junctions made with different shapes and sizes, even between samples manufactured by different research groups.

### 5.5.1 Samples Without F'

Early in this study the focus was on identifying which version of the multilayer possessed the best superconducting properties. This was done in conjunction with the magnetometer measurements discussed in Section 5.4. Thus, if a sample performed poorly in either one of the two measurements it was quickly dropped from future fabrication runs. The advantage of this was speed, since this was a stepping stone experiment in order to quickly replace the Co/Ru/Co trilayer. The big disadvantage is that we did not systemically explore the entire fabrication space. Therefore, the conclusions drawn here are based on a small statistics set and do not complete the story for these multilayers.

Our first Josephson junction samples were fabricated with the 0.4/0.6 and 0.4/0.8 Co/Ni multilayers. We made samples of each with 4, 6, and 8 multilayer repetitions. Each combination was done twice to allow for the typical problems that can occur in sample fabrication (i.e. breaking a chip). Pillars were patterned onto the chip as discussed in Section 4.1. Once fabricated, the samples' Fraunhofer curves were measured. Several examples of these are presented in Figure 5.7. Measurements of the 0.4/0.8 multilayers were not performed due to the poor quality of the magnetization behavior seen in Section 5.4.

The data is particularly interesting for these samples. Because the Co/Ni multilayer possesses PMA, the resulting Fraunhofer pattern should be well behaved if the magnetization

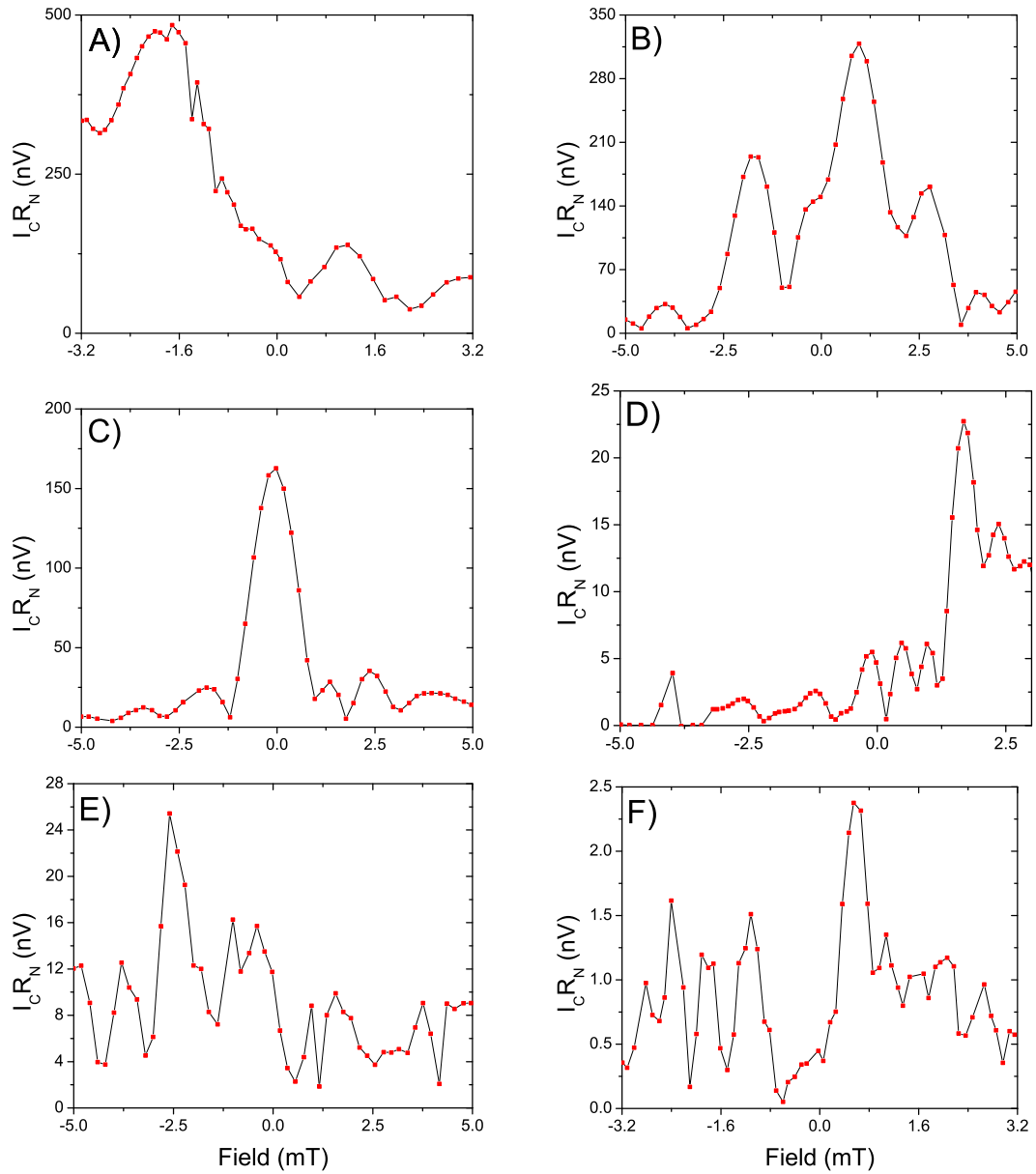


Figure 5.7: *Fraunhofer patterns measured in Josephson junctions with the 0.4/0.6 Co/Ni multilayer. A) 10  $\mu\text{m}$  pillar,  $n=4$ . B) 10  $\mu\text{m}$  pillar,  $n=6$ . C) 10  $\mu\text{m}$  pillar,  $n=6$ . D) 20  $\mu\text{m}$  pillar,  $n=6$ . E) 10  $\mu\text{m}$  pillar,  $n=8$ . F) 20  $\mu\text{m}$  pillar,  $n=8$ .*

is actually pointed along the direction of the current flow. This is because of the lack of any magnetic interactions with the current. It is, however, clear that this is anything but the case for many of the pillars. The peak of most of the pillars is shifted either to the left or the right, implying that the magnetization contains a component parallel to the applied field. Therefore a component of it must be canceled by the external field in order to achieve the true zero field point for the sample.

There are also wild variations in the overall shape of the patterns. This suggests that there are likely multiple domains contained within our pillar region, particularly since the expected domain size must be smaller than the size of our pillars. These domains can cause constructive and destructive interference in the phase difference across the junction due to the spatial variation of the magnetic vector potential [67]. This is supported by Figures 5.7b and 5.7c, which are two pillars of the same size from the exact same chip. The pillar in Figure 5.7c displays a nearly-ideal Fraunhofer pattern that is not duplicated by its mate. This suggests that a complicated domain arrangement has intruded on the pillar in Figure 5.7b.

It is also worth noting that the width of the central peak in field varies with the size of the pillar. In particular, the width of the Airy pattern for a 10  $\mu\text{m}$  pillar is typically 2.4 mT, while the width for a 20  $\mu\text{m}$  pillar is about 1.2 mT. This difference is explained more thoroughly in Chapter . This allows for a quick check of the quality of the Fraunhofer pattern, as any deviation from the expected peak width could suggest magnetic anomalies or, if the pattern does not go to zero at the minima, a short.

With the magnetic data strongly supporting the 0.2/0.4 multilayer, we began fabricating samples of varying thicknesses with that arrangement. Our first batch contained samples with multilayers of 6 through 16 repeats in increments of 2. The resulting Fraunhofer patterns

are presented in Figure 5.8. Much like the previous data, the 0.2/0.4 multilayers display a wide range in Fraunhofer quality, from near textbook in Figure 5.8b, to something less pristine 5.8c, even with nearly the same multilayer arrangement.

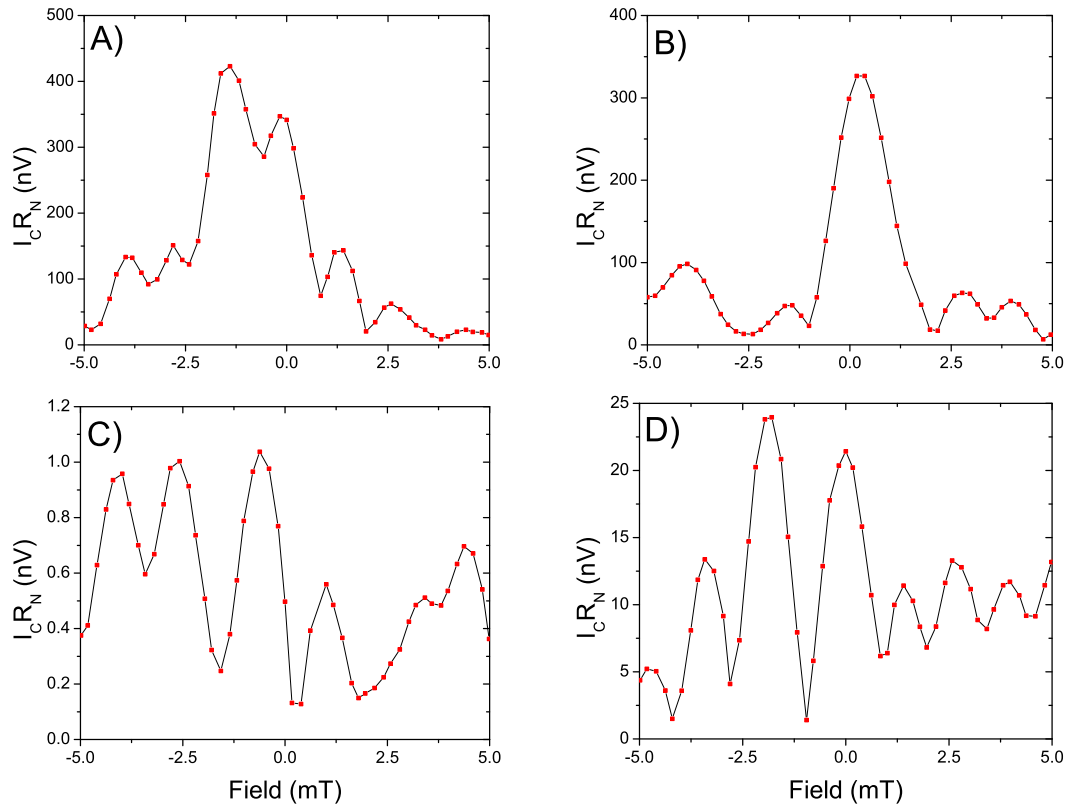


Figure 5.8: *Fraunhofer patterns measured in Josephson junctions with the 0.2/0.4 Co/Ni multilayer. All four pillars were 10  $\mu\text{m}$  in diameter. A) 8 bilayers. B) 10 bilayers C) 12 bilayers. D) 14 bilayers.*

The Fraunhofer quality in this sputtering run seemed to degrade rapidly with increasing repetitions. A further run was done to repeat the thicknesses 12, 14 and 16, as well as to add 18, 20 and 22 to try to extend the range of the measurements. While there was still a wild variation in the data, more of the pillars produced Fraunhofers of at least reasonable quality.

In an attempt to improve the magnetic properties of the Co/Ni film, these samples were

also exposed to a perpendicular magnetic field of 2kG at room temperature. The results are presented in Figure 5.9. The hope was that relatively poor Fraunhofers might be improved by the application of a field, which would rearrange the magnetic moments such that the resulting effect on the current would be minimized.

Unfortunately, there is very little systematic change in the samples. While some samples did show modest improvement, other samples showed none at all, or even showed a decrease in the peak critical current. The inconsistency in the behavior was disappointing, and implied that once fabricated the magnetic characteristics were the luck of the draw. It was unlikely that we would be able to “fix” bad Fraunhofer patterns in this way.

That said, this method of magnetization may not have been the best way to cure the problem. We applied the perpendicular field at room temperature in an attempt to change the behavior. We have no idea if the Co/Ni multilayer is even ferromagnetic at those temperatures, especially since many ferromagnetic thin films have Curie temperatures much lower than room temperature. The fact that the Fraunhofer pattern on some of the pillars changed, however, does support the conclusion that the Curie temperature is sufficiently high.

A better method would be to apply the magnetic field while the sample was cold. Unfortunately, at the time of the experiment, the quick dippers were only able to apply magnetic fields in the plane of the sample. This meant that we had no way to apply a perpendicular field while the samples were in helium. Therefore, further experiments need to be done in order to make any statements regarding the ability to rearrange the magnetic configuration with any certainty.

With the samples measured, the  $I_c R_N$ 's of each pillar were plotted against the thickness of the magnetic multilayer. The results are presented in Figure 5.10. The decay in the signal with increasing number of layers is notable in the data, and is reasonably consistent with

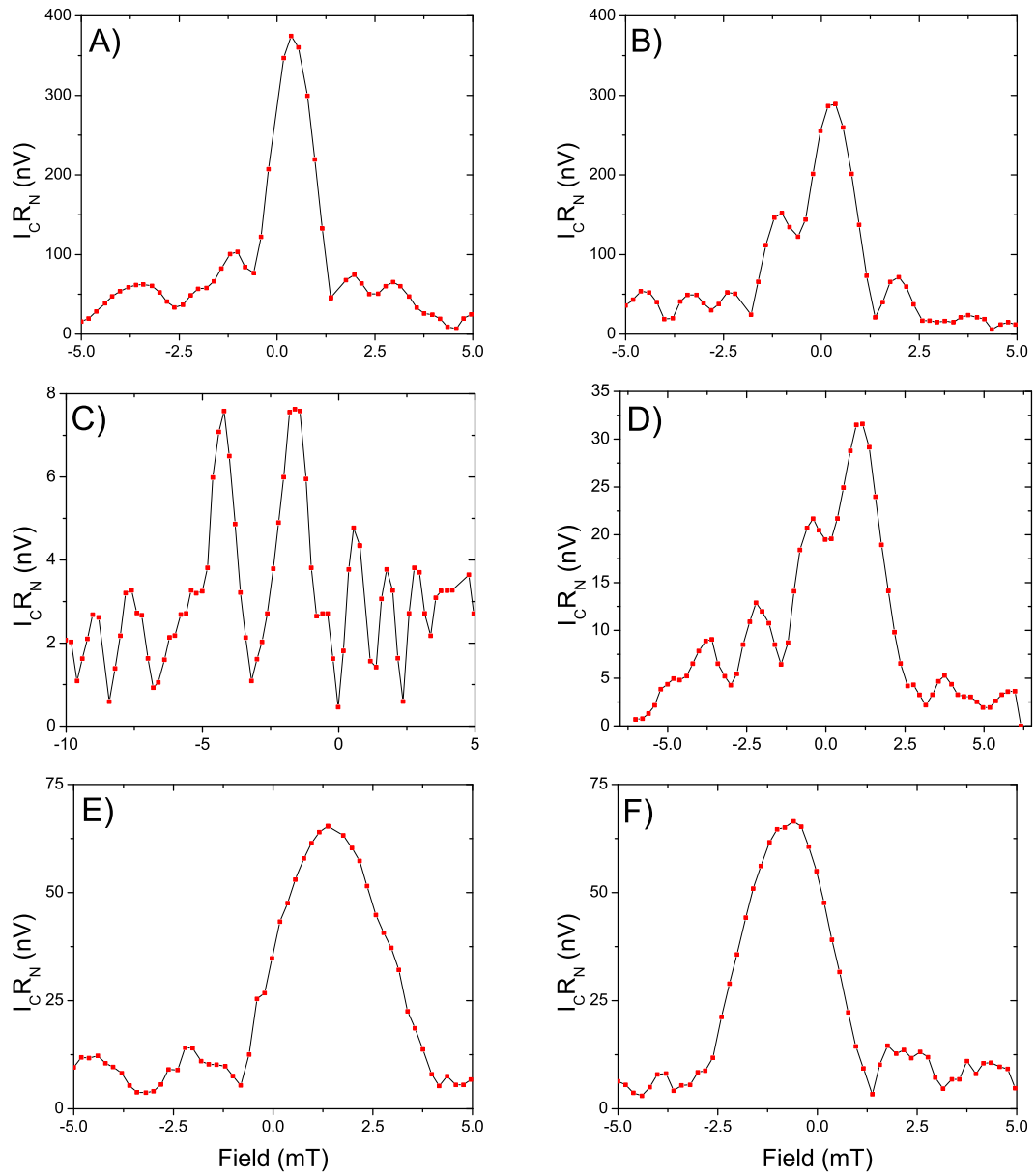


Figure 5.9: *Fraunhofer patterns measured in Josephson junctions with the 0.2/0.4 Co/Ni multilayer.* All pillars were 10  $\mu\text{m}$  circular pillars. Plots on the left are virgin state, while plots on the right are the same pillar after being magnetized to 2kG at room temperature. A) and B) 12 bilayers. C) and D) 18 bilayers. E) and F) 20 bilayers.

Metal	$\xi_1$ (nm)	$\xi_2$ (nm)
Co	2.34	0.3
Ni	4.1	1.2

Table 5.1: *List of singlet decay lengths in Co and Ni from Khasawneh et al. [73] and Robinson et al. [74].*

our expectations that these samples would carry singlet supercurrent. The decay of  $I_c R_N$  with  $n$  can be expressed as an exponential,

$$I_c R_N \propto \exp[-A * n] \quad (5.2)$$

where  $\exp[-A]$  is the decay of the supercurrent per Co/Ni bilayer. From the figure we obtain  $A = 0.29 \pm 0.04$ . The decay can also be written as  $A = .6\text{nm}/\xi_F$  where  $\xi_F$  is an effective decay length, and .6nm is the thickness of each bilayer.

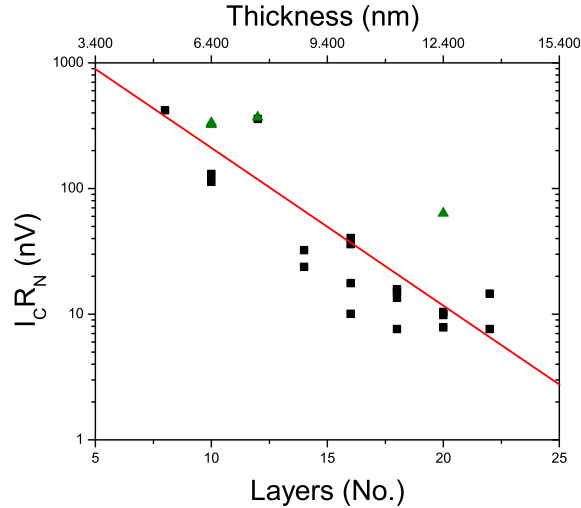


Figure 5.10: *Semi-log plot of  $I_c R_N$  product for samples without  $F'$ . The decay is given by Equation 5.2 with  $A=0.29$ . The green triangles represent pillars with the best quality Fraunhofer patterns.*

The critical current in a singlet Josephson junction behaves with F-layer thickness as,

$$I_c \propto e^{-\frac{d_F}{\xi_1}} \sin\left(\frac{d_F}{\xi_2} + \phi\right) \quad (5.3)$$

where  $d_F$  is the ferromagnet thickness,  $\xi_1$  is the exponential decay constant,  $\xi_2$  is the oscillation period, and  $\phi$  is a phase factor. If we naively assume that the Co/Ni multilayer acts like a single film of Ni and a single film of Co, we can predict the slope of the singlet decay  $A$ ,

$$A = \sum \frac{d_F}{\xi_1} \quad (5.4)$$

where the sum is over the materials in the multilayer. The singlet decay of Co from Khawneh *et al* [73], and the decay length of Ni from Robinson *et al* [74], are presented in Table 5.1. This calculation predicts a slope of  $A = 0.18$  for this system [75]. That value is a bit smaller than the measured value from the samples. However, considering we are not including the effect of spin-memory loss at the Co/Ni interface, this is not terribly surprising.

The green triangles in the plot represent Fraunhofer patterns that were of a quality markedly better than the rest of the pillars. This suggests that if we were able to achieve more consistent results with our patterns that the slope of the decay would not have been as steep as we see in the data when taken as a whole. However, since we saw only three or four very good Fraunhofers out of more than 21 different pillars, this strategy would have required an unreasonable amount of time to pursue. Interestingly, if we fit the slope of the green pillars we receive a decay of  $A = 0.18 \pm 0.05$ , in excellent agreement with our overly simple prediction.

In Chapter , it was discussed that singlet decay should exhibit oscillations due to the change in the phase of the pair correlations across the ferromagnet from 0 to  $\pi$ . The Cooper

pair phase shift  $\theta$  can be calculated in a way similar to the decay length,

$$\theta = \sum \frac{d_F}{\xi_2}. \quad (5.5)$$

This formula gives a value of 1 radian for a bilayer of Co and Ni, which tells us that  $\theta = 0.6$  nm/ $\xi_2^{eff}$ . Since the 0 to  $\pi$  transition is defined in radians, so the transition period  $T_{osc}$  is,

$$T_{osc} = \pi \xi_2^{eff} = 1.9nm. \quad (5.6)$$

This is roughly equivalent to 3 repetitions of our bilayer. This small of an oscillation period would be unobservable in our data, as the sample resolution simply wasn't small enough to resolve it.

### 5.5.2 Samples With F'

After the singlet decay had been measured, samples were fabricated with the same range of Co/Ni thicknesses but with the addition of two 1.2 nm thick Ni layers on either side separated by 5 nm Cu spacer layers. These samples were predicted to show signal of Spin-Triplet supercurrent, which would manifest as an enhancement of  $I_c R_N$  when compared to a sample without the F' layers and the same thickness of Co/Ni. Since these samples also possessed a PMA multilayer, they were also predicted to be fully optimized in the virgin state.

We needed only a single run to obtain the necessary data for these samples. Figure 5.11 shows a series of Fraunhofer patterns from these measurements. Unlike the previous set of data, the Fraunhofer patterns were much more consistent in their overall quality. However,

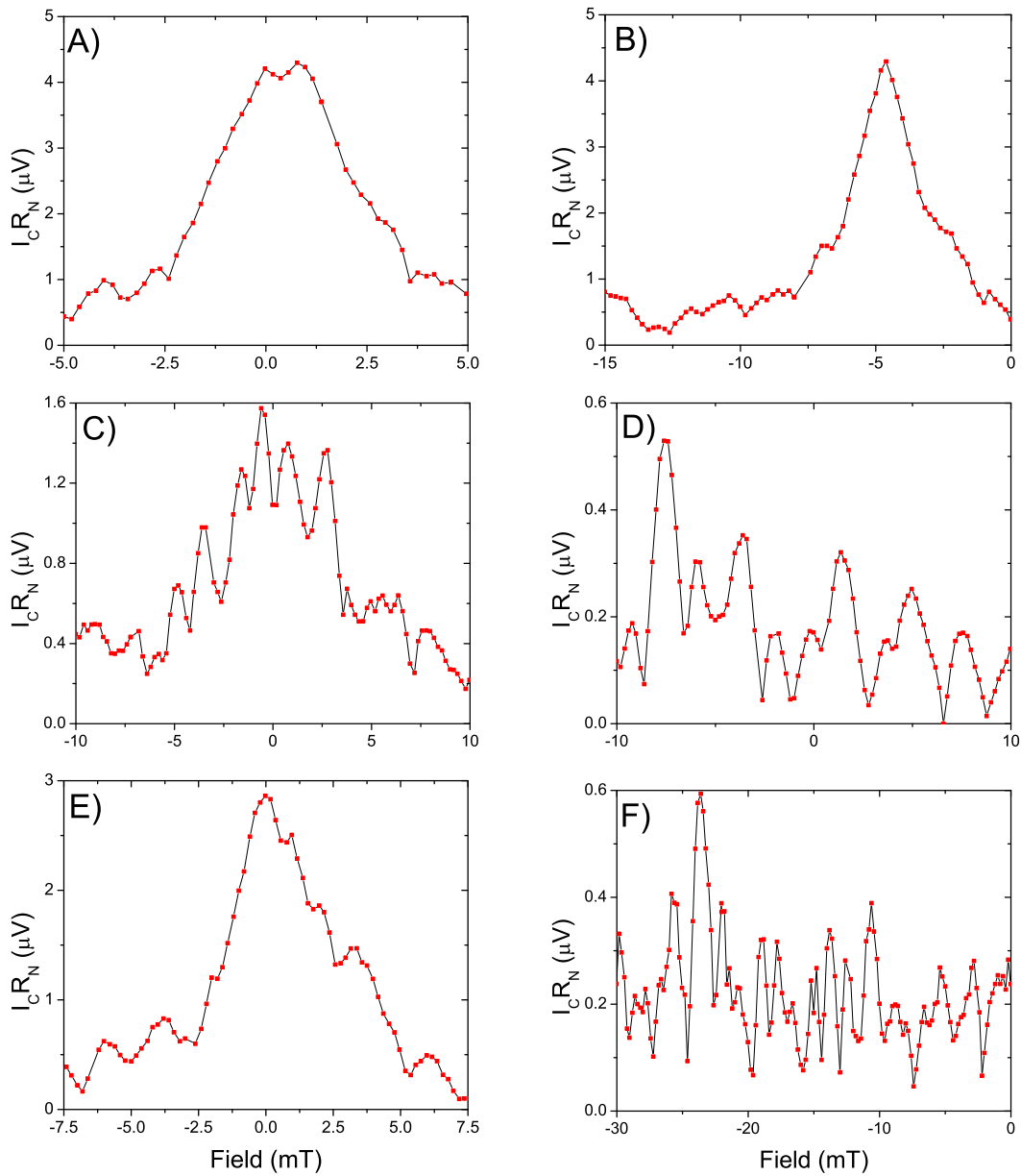


Figure 5.11: Fraunhofer patterns measured in Josephson junctions with the 0.2/0.4 Co/Ni multilayer as well as two 1.2 nm Ni F' layers. All pillars were 10  $\mu\text{m}$  circular pillars. Plots on the left are virgin state, while plots on the right are the same pillar after being magnetized in-plane to 320 mT at 4.2 K. A) and B) 10 bilayers. C) and D) 16 bilayers. E) and F) 18 bilayers.

the average quality was roughly the same, so while no pillar showed a Fraunhofer as bad as 5.7b, there were also no pillars that showed Fraunhofers as good as 5.8b.

One question that arises from these data is why the Fraunhofers are so much more well behaved than their counterparts without F'. One possibility is that the inclusion of the small ferromagnetic layer below the Co/Ni multilayer, namely the 1.2 nm Ni layer, helps the growth of the Co/Ni multilayer such that its PMA is significantly improved. This is supported by the results of Section 5.7, where the application of a field during the growth demonstrated an improvement in the magnetic behavior of the film.

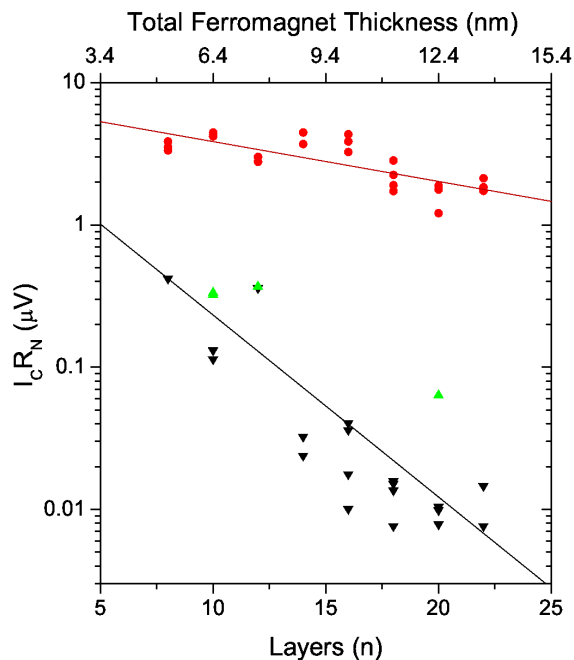


Figure 5.12: *Semi-log plot of  $I_c R_N$  product versus the thickness of the central ferromagnetic layer.* Samples without F' (black squares and green triangles) show a steep decay ( $A=0.29$ ) when compared to the samples possessing F' layers (red squares), which have a much shallower decay ( $A=0.06$ ). The samples with F' also show a significant enhancement in their  $I_c R_N$  products, a distinct signal of Spin-Triplet supercurrent.

The  $I_c R_N$  products of these samples are plotted against the Co/Ni thickness in Figure 5.12 along with the data from the samples without F'. Fitting a line to the data gives a slope of  $A = 0.064 \pm 0.011$ , much smaller than the slope of the singlet decay from the previous data.

n	$H_{shift}$ (mT)	$I_c$ Virgin (mA)	$I_c$ Mag (mA)
8	-3	35	35
10	-4	40	30
10	-5	45	45
16	-6.5	15	5
18	-24	25	5
20	-6	15	9
22	-8	10	7

Table 5.2: Comparison of data from  $S/F'/F/F'/S$  samples in the virgin state and after being magnetized to .32T.  $H_{shift}$  is the position of the Fraunhofer peak in field due to the uncanceled magnetic flux in the sample.

The  $I_c R_N$ 's of the samples including the F' layer are much larger than the one's without F', by as much as a factor of 200 for some of the thicker Co/Ni samples. This is a clear signal of spin-triplet generation in these samples.

To check the optimization of these samples, a 0.32 T magnetic field was applied in the plane of the sample at 4.2 K. The goal was to magnetize the outer Ni layers while hopefully leaving the Co/Ni multilayer unaffected. If the Co/Ni multilayer had textbook magnetization curves, where the parallel magnetization passed through zero with no hysteresis, this assumption would be valid. Unfortunately, as demonstrated in 5.4, this is anything but the case.

As can be seen in Figure 5.11, the magnetized data shows relatively consistent results, quite unlike the results of the magnetization of the Co/Ni multilayer from Section 5.5.1. The  $I_c R_N$  product in these measurements either remained the same or decreased dramatically from the virgin state after magnetizing. Often, if the peak in the critical current dropped, the Fraunhofer pattern also showed a marked reduction in quality from the virgin state.

Table 5.2 shows a comparison of the virgin state and magnetized data for the measured samples, listed with the measured shift in the peak of the Fraunhofer pattern  $H_{shift}$  and the number of bilayers. This data shows conclusively what effect the magnetization process has

on these samples. With the application of an in-plane field, the Co/Ni multilayer wants to cant into the plane of the sample. This effect becomes stronger with increasing  $n$ , apparent from the shift in the location of the peak in field, and in the reduction of the critical current through the sample.

This data emphasizes that these samples are, in fact, optimized in the virgin state. The application of a magnetic field does not improve the critical currents in any sense, and only serves to reduce the supercurrent flow through the pillars. This result is not terribly surprising considering the results of the magnetization data from Section 5.4. As  $n$  increases, the parallel configuration begins to gain a significant remanent magnetization. Thus, as an in-plane field is applied, the sample is removed from its optimized state.

Our early attempts to measure these samples ran into some minor technical difficulties. Because the sample  $I_c$ 's were so high, the flux applied through the SQUID when the pillars would transition to the normal state was spiking much too rapidly for the electronics to handle. The result is that the SQUID would “unlock”, or find itself far from its neutral position. This would require a hard reset of the electronics, which could not be done while the computer was in control, meaning that the samples were functionally unmeasurable.

To solve the problem, a  $2.5 \mu\Omega$  resistor was placed in parallel with the sample in the Current Comparator Circuit. By doing this, the effective resistance of the sample was suppressed by roughly a factor of 40. This caused the output voltage to be similarly suppressed, allowing the SQUID to maintain its lock while measuring the transition to the normal state.

However, because this was short-circuiting the measurement of the normal state resistance of the pillars, a switch was needed in order to turn the shunt resistor on and off. A MoGe film with a superconducting temperature of roughly 6K was fabricated and placed in series with the shunt resistor. A heater was then mounted on the MoGe film which allowed the

user to heat the film and "open" the switch, removing the shunt resistor from the circuit.

## 5.6 Viability of the Co/Ni Multilayer

The purpose of this experiment was to determine if the Co/Ni multilayer was a suitable replacement for the Co/Ru/Co trilayer as the central ferromagnet in samples fabricated to generate Spin-Triplet supercurrent. There is no question that the multilayer works well in this regard. It demonstrates Spin-Triplet generation, possesses a magnetization non-collinear to typical in-plane ferromagnetic films in the virgin state, and it requires fewer guns than the Co/Ru/Co trilayer (assuming Ni is being used as an F' layer).

This means that the Co/Ni multilayer could be used in later studies to measure the behavior of other ferromagnets as the F' or F'' layers (Chapter 6). It could also be used as the central ferromagnet in our future work to build Josephson junctions to try to control of the state of the junction (Chapter 7). Many of the samples in those chapters were fabricated with this multilayer as the central ferromagnet.

Several issues with this multilayer have, however, cropped up during its use. The magnetic characteristics of the multilayer, both in-plane and out-of-plane are not conducive to measurements where large in-plane magnetic fields will be applied. The desire of the multilayer to cant into the plane is strong at higher  $n$ , which fouls the Spin-Triplet generating characteristics of the sample. The solution to this was to use 10 bilayers of Co/Ni in any future sample using the multilayer. This was because the  $n=10$  showed the best overall superconducting and magnetic characteristics of any of the multilayers tested. Unfortunately even the  $n=10$  sample can behave poorly at times.

Lastly, recall the three reasons this multilayer was originally developed: issues with the

Co/Ru/Co fabrication, the number of guns available in the sputtering system, and the want for a multilayer with non-collinear magnetizations with the outer ferromagnetic layers in the virgin state. All three of these issues vanished during the course of our studies. The issues with the Co/Ru/Co were solved, a seventh gun was added to the sputtering system, and some of the future samples required an initial magnetization anyway. Therefore, the Co/Ru/Co multilayer should not be simply discarded, as it remains a useful central ferromagnet in triplet samples.

## 5.7 Multilayer Improvement

In an attempt to gain better control of the Co/Ni multilayer, a study was initiated to discover a way to better fabricate the Co/Ni multilayer and improve the PMA. This work was primarily pursued by Alex Cramer, an undergraduate in the group, under the primary guidance of Reza Loloee, our resident materials guru. The goal was to achieve a textbook magnetic characteristic for the out-of-plane anisotropy with no remanent magnetization when exposed to an in-plane field.

Our early understanding of the problems with the multilayer arose from discussions with several groups during a conference. The strong general consensus was that the issues with our Co/Ni film were a direct result of the roughness of the underlying layers we were trying to grow the multilayer on. By fabricating smoother films, the Co/Ni multilayer would possess more favorable magnetic characteristics. To do this, the suggestion was to use a Tantalum underlayer, since Ta tends to grow very smooth films on Silicon substrates.

This turned out to be not entirely correct. While Ta does grow particularly smooth films, it also grows in a BCC configuration. As mentioned earlier, the perpendicular anisotropy

arises in Co/Ni when the Co grows in an FCC arrangement, which it does in sufficiently thin films (it favors HCP at thicknesses greater than about 30 nm). By growing Co directly on Ta, the BCC underlayer fouled the growth of the FCC Co, which functionally destroyed the PMA. This did not cause a problem in the samples earlier in this chapter because Cu naturally grows in an FCC arrangement, which favored the PMA.

What was ultimately discovered is that the Ta is not used as a smoothing layer for the Co/Ni multilayer, but instead as a sticking layer, much like Ti is used in samples with Au grown on Silicon. While it did provide smoothness, the inclusion of the Ta did not improve the magnetic characteristics of the multilayer in the slightest. Interestingly, comparing samples with and without Nb, which grows a particularly rough surface, the remanent magnetization was not significantly suppressed. Even more interesting was the fact that the coercive field showed an enhancement when Nb was included. This suggested that the roughness of the Nb provided natural positions for grain boundaries and other defects that could pin domain walls, increasing the coercive field by as much as 20 mT. This does not mean that more is better, however, as the roughness would be expected to rise with thickness and eventually have a detrimental impact on the PMA.

There are two methods that work particularly well for generating a strong PMA in the Co/Ni multilayer. The first is the inclusion of Platinum immediately beneath the first Co film of the multilayer. As mentioned in Section 5.2, the Pt/Co interface also possesses perpendicular anisotropy, but it is 6 times stronger than in the standard Co/Ni multilayers. This makes it very effective as a pinning layer for the entire multilayer stack. The data for this type of sample is shown in Figure 5.13. Both figures represent the same measurement, but Figure 5.13a has been narrowed down in order to see the details of the hysteretic behavior.

Despite the excellent improvement in the behavior of the Co/Ni in both the perpendicular

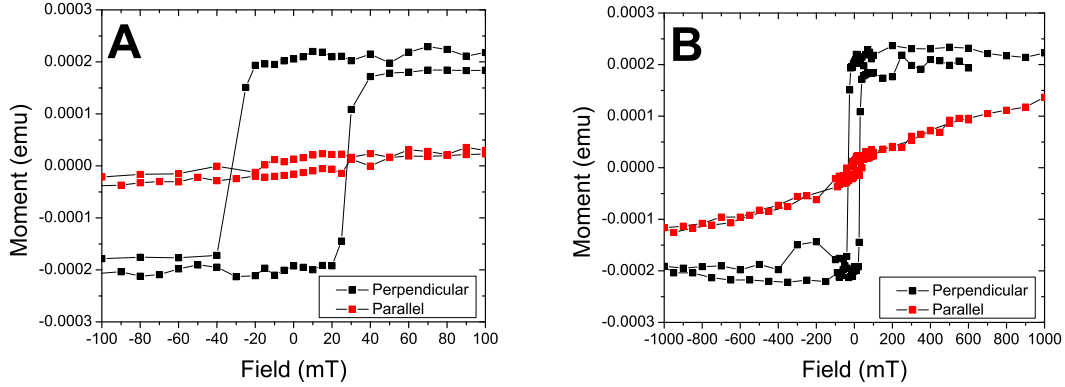


Figure 5.13: Plots of a 0.3/0.4 Co/Ni multilayer grown directly on 20 nm Pt. The black curve represents the perpendicular magnetization direction, while the red curve represents the parallel data. A) The hysteretic behavior in the parallel configuration is small, particularly compared to the nearly square perpendicular hysteresis. B) At fields a factor of 10 higher, the perpendicular direction has entirely saturated, something we could not achieve in our original Co/Ni samples. The parallel configuration demonstrates a very strong pull towards the perpendicular direction. Even to field strengths of 1T, the multilayer has only halfway canted into the plane of the sample. (Credit: Alex Cramer and Reza Loloee)

and parallel directions compared to 5.3, these types of samples are probably not feasible for application in our systems. Unfortunately, the superconducting properties of Pt are very poor due to its large spin-orbit scattering. The normal metal coherence length  $\xi_N$  in Pt is roughly 4.4 nm [76], and the spin diffusion length is on the order of 14 nm [77], so the inclusion of it in a multilayer is likely sufficient to significantly suppress the supercurrent. Luckily, only a thin layer would be required to pin the Co/Ni, but this would be undesirable in samples that already possessed a very low supercurrent, such as very small area pillars.

The second method was to apply a field to the sample during the growth of the multilayer. Unfortunately, the sputtering system does not include an *in-situ* method of applying a controllable field to the samples during growth. The only available method is to place a permanent magnet on the back of the sample during growth. This was shown to dramatically improve the PMA of the Co/Ni multilayer, which makes it a favorable solution to the mag-

netization problems. Since the Co/Ni multilayer will be included with other ferromagnetic layers which require in-plane magnetization, it is hard to be certain if this method will not also have a negative impact on those layers as well. Further study is required before this method could be employed to fabricate transport samples.

# Chapter 6

## Characterization of Soft Ferromagnets

One of the keys to successfully controlling the Spin-Triplet supercurrent is the development of sets of hard and soft ferromagnetic materials that can be used inside Josephson junctions. Some of the materials have already been worked on, such as Ni, Co/Ru/Co, and the  $[\text{Co/Ni}]_n$  multilayer. However, while those materials are great hard ferromagnets, and can work well as fixed layers in the control samples, they can't function well as a free layer at the fields appropriate for applications work. Thus, it is necessary to develop a soft ferromagnetic material which will switch at much lower fields.

A decent switching field isn't the only necessary feature of the magnet, however. It must also act as a good generator for the Spin-Triplet supercurrent. This means that each magnetic material must be put through its paces in order to understand how it will behave in our Josephson junctions. The sequence for the study of each magnetic alloy follows the same path. First, the sputtering target must be fashioned so that we can successfully create the alloy. Then, we sputter a film of at least 500 nm for study by Electron Dispersive Spectroscopy, which allows us to verify the elemental concentrations.

As mentioned in Chapter , the EDS is attached to the Hitachi SEM. It works by taking advantage of the interactions of the electron beam with the sample. When an electron in the beam happens to strike an electron in its orbital within the sample, the second electron can be knocked out if the first electron has sufficient energy. Because the atom in the lattice

is now excited, a higher energy electron will eventually fall into the hole left behind in the orbital. This releases an x-ray of a well defined energy. Because the energy levels of each atom are different, mapping the energy of the x-ray's released provides a means of identifying which types of atoms are present, and their relative quantities.

Once the correct concentrations have been achieved, we then must measure the M versus H of the thick films in a system like our SQUID Magnetometer mentioned in Section 3.5.2. This measurement allows us to find  $H_C$ , the coercive field discussed in more detail in Chapter , which gives us a preliminary indication of whether the material is a hard or soft ferromagnet. Because the films possess large lateral dimensions on the order of millimeters, the magnetization will switch by domain wall motion rather than coherent rotation. However, the shape of the M versus H curve still gives some information on the materials' magnetocrystalline anisotropy.

Giant Magnetoresistance (GMR) measurements need to be performed on samples of both large and small lateral dimensions. We chose GMR for these measurements because the more common methods of performing these measurements, low temperature Magnetic Force Microscopy (MFM), and low temperature Magneto-Optical Kerr Effect (MOKE) are not available to us. However, our work with Bill Pratt and Reza Loloee gives us a large body of expertise for working in GMR. The large scale GMR samples are fabricated first and measured to verify that the GMR signal is sufficiently large to be observable with the ferromagnetic material to be studied. If the large scale GMR samples provide measurable data, then small scale GMR samples are fabricated. These pillars are patterned into ellipses to provide shape anisotropy, and are then measured to observe the change in the switching field of the ferromagnet with changing ellipse shape. GMR will be more fully described in Section 6.4.

Lastly, the ferromagnets must also be efficient at generating the spin-triplet state in our junctions. We pattern S/F'/F/F''/S samples, where F' is a hard ferromagnet, typically Ni, F is one of our central ferromagnetic layers, and F'' is the material to be studied. These are formed into our standard circular Josephson junctions following the procedures in Chapter . We then measure the Fraunhofer patterns and plot the maximum critical current of each junction versus the thickness of the F'' material. We expect that a maximum will appear in the data, signifying the critical thickness for triplet generation.

Each of the ferromagnetic materials discussed below has been considered for the control experiment, and has had some subset of the above experiments performed on them. Some of the materials were considered briefly before being discounted as a possible candidate, and it is noted for each of these where and why it was dropped as a possibility. The experiments were performed by numerous people who have worked for the group, and it is noted on the data and in the text who performed the various experiments if they were not performed directly by the author.

Section 6.1 discusses the creation of our sputtering targets for creating alloys. The second section presents the results of Reza Loloee's studies on Molybdenum-doped Permalloy. The third section gives our EDS data for Copper-doped Permalloy. Section 6.4 presents our magnetic and superconducting data for Niobium-doped Permalloy. Section 6.5 presents similar studies for Palladium Iron. Finally, the last section concludes the discussion.

## 6.1 Targets

The majority of soft ferromagnets considered during this experiment were alloys of ferromagnetic and non-ferromagnetic materials. This is relatively convenient since the strength

and softness of the material can be controlled by varying the relative concentration of the materials in the alloy. There are limits, of course, and it is preferable to study the range of possible concentrations to obtain the best set of material properties. With a large enough concentration of non-magnetic material, it is possible to make the alloy non-magnetic, so knowing where the boundary is can be important for future sample fabrication.

Unfortunately, there are only a few ways to fabricate thin film alloys. The most obvious is to purchase a sputtering target that has been fashioned to have the appropriate atomic concentrations for the alloy. This can be problematic for a number of reasons. First, you have to purchase a new target for each new concentration you wish to try. Since target prices tend to be measured in the thousands of dollars (particularly for special orders), trying to perform a study on a range of alloys can quickly become cost-prohibitive. Second, just because the alloyed target has a particular set of relative concentrations does not mean that the same concentration will appear in sputtered films. Because the sputtering rate varies for each element, one part of the alloy could sputter more slowly than another. A good example of this is Permalloy, an alloy of Nickel and Iron, which tends to sputter at higher concentrations of Nickel than the source target.

To get around this problem, many sputtering systems are built with the ability to *co-sputter*. The idea here is that multiple sputtering targets are presented to the sample. Each target contains a separate element, allowing for the ability to alloy the materials *in-situ*. The relative rates can then be varied so as to set the concentration in the resulting alloyed film. This is a very good solution to the problem of alloying materials, but requires the sputtering system to be designed and built to do it. The sputtering system used in this project does not have co-sputtering ability, and so another solution is required.

Reza Loloee developed a third technique for generating sputtered alloyed films. The

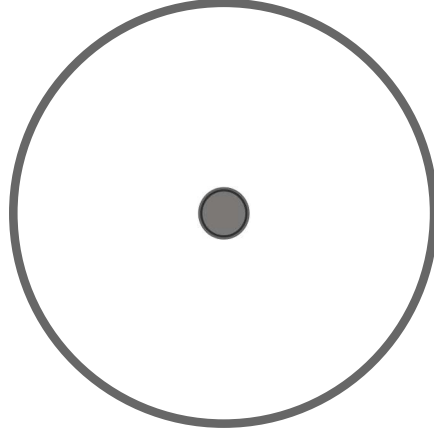


Figure 6.1: A diagram of the structure of a target modified by Reza Loloee for alloy sputtering. The central plug is 1/4" inside a 2.25" circular target.

concept is similar to co-sputtering, but requires only a single sputtering gun to achieve. A base material target is purchased and small holes drilled into its surface. Then, plugs of other materials can be inserted into the holes. The idea is based on the fact that the concentration of the film is related to the surface area of the materials in the target. Therefore, it is possible to roughly predict the concentration of the alloy when designing one of these modified targets. This method does not evade the issue found in alloyed targets, that is relative sputtering rates of the different materials, but that can be more easily solved by changing the number of plugs of the added material.

Typically the plugs used are 1/4" in diameter. The targets themselves are 2.25" across. Knowing these, we can roughly calculate the concentrations of two different materials in a film sputtered from a target with a base material and only a single plug, similar to Figure 6.1. The concentrations are related to the surface area, therefore we can start by calculating the surface area of a 2.25" target  $A_T$ ,

$$A_T = \pi \left( \frac{2.25\text{in}}{2} \right)^2 = 3.9761\text{in}^2 \quad (6.1)$$

and a 1/4" inch plug  $A_P$ ,

$$A_P = \pi \left( \frac{.25\text{in}}{2} \right)^2 = 0.0491 \text{in}^2 \quad (6.2)$$

The difference between these two areas is the surface area of the base material,

$$A_B = A_T - A_P = 3.927 \text{in}^2 \quad (6.3)$$

The concentration of the plug material,  $C_P$ , is the ratio of the area of the plug to the total area,

$$C_P = \frac{A_P}{A_T} = 0.0123 \quad (6.4)$$

while the concentration of the base material,  $C_B$ , is the ratio of the remaining base area and the total area,

$$C_B = \frac{A_B}{A_T} = .9876 \quad (6.5)$$

As an example, our PdFe target uses precisely one quarter inch Iron plug in a 2.25 inch Palladium target. The relative concentrations of the films measured using EDS tells us that the target gives us 1.5 percent Iron in a Palladium matrix. Therefore, the calculation is a good rough estimate of the material concentrations, useful as a starting point for determining what is required for the desired concentration.

## 6.2 Molybdenum-doped Permalloy

The first soft ferromagnet considered for our studies was Permalloy (with .84 Nickel and .16 Iron) doped with Molybdenum, frequently called "Moly-Doped Permalloy" or "Supermalloy". Two varieties of this material were studied. The first, which was studied by Patrick

Quarterman and Simon Diesch with the help of Reza Loloee, was made from a Nickel target with Iron and Molybdenum plugs. This target did not have the proper ratio of Ni to Fe for the Permalloy, so it was later scrapped. The reason for this decision is that fashioning a second target using Permalloy with the proper concentrations is a better method. Therefore, after Simon Diesch attempted to perform superconducting studies on the original MoPy target, a second target was made from a Permalloy target with Mo and Py plugs, giving the correct relative ratios of Ni and Fe. This target, of which a diagram is shown in Figure 6.2 was made by Reza, who also studied its magnetic properties, while its superconducting properties are being studied by Bethany Niedzielski.

One of the key indicators for the viability of these ferromagnetic materials was their superconducting properties. It could be determined how well the material generated Spin-Triplet supercurrent by measuring the variation of critical current with increasing ferromagnetic thickness. It was expected that there should be a peak in the plot of critical current versus thickness due to two competing effects. The first effect is the quantity of supercurrent suc-

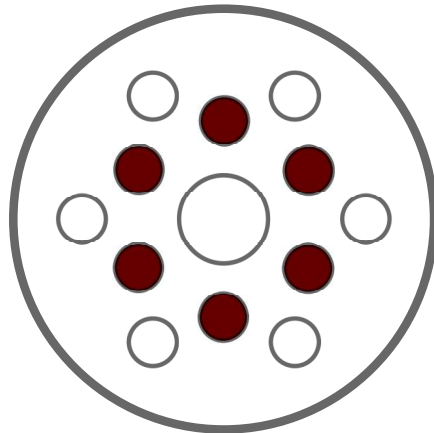


Figure 6.2: A diagram of the Molybdenum-doped Permalloy target fashioned by Reza Loloee. The base material is .81 Ni, and .19 Fe, along with the white circles. This gives a relative concentration of .84 Ni and .16 Fe for the Permalloy after sputtering. The dark circles are Mo.

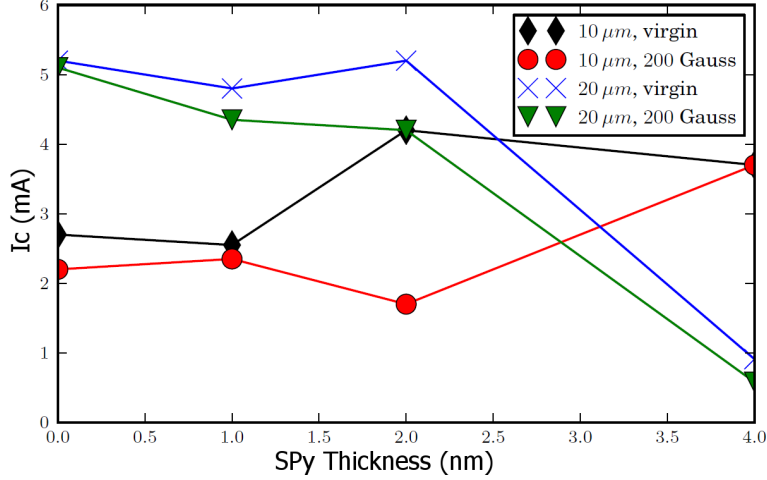


Figure 6.3: Data from 10  $\mu\text{m}$  and 20  $\mu\text{m}$  Josephson junction pillars with Molybdenum-doped Permalloy as both the  $F'$  and  $F''$  layers. Ni/[Co/Ni] $_n$  is the central ferromagnet for these junctions. Note that there appears to be no net change in supercurrent with increasing MoPy thickness for either magnetized or unmagnetized samples. These samples were fabricated with the original MoPy target. (Credit: Simon Diesch)

cessfully converted to triplet current, which is roughly proportional to thickness. The second factor is simply the decay of the spin-singlet with increasing thickness, which simultaneously decreases the quantity of supercurrent available to convert to triplet. The peak occurs where these two effects are balanced, and is the thickness for optimum triplet generation for the ferromagnet. This behavior was observed in several ferromagnetic materials, including PdNi, CuNi [43], and Ni [73].

Unfortunately, the superconducting properties of the original MoPy target were relatively disappointing. Samples were created using MoPy for the  $F'$  and  $F''$  layers of a spin-triplet Josephson junction with [Co/Ni] $_n$  as the central ferromagnetic layer. When patterned into pillars for Josephson junctions, the MoPy did not behave particularly well. Generally, the material seemed to generate poor Fraunhofer patterns, and possessed no clear trend in the data with increasing MoPy thickness, as shown in Figure 6.3. This made it impossible to determine an optimum thickness for the material.

Because of this disappointing result, further work on the material was paused in order to focus efforts on Palladium Iron, discussed in Section 6.5. Recently, work has renewed in an attempt to better understand the material. Part of the reason for this renewed interest is the work Reza has performed on the new target. The other reason has to do with using  $[\text{Co}/\text{Ni}]_n$  as a central ferromagnetic layer for these studies. We have performed studies on both MoPy and PdFe using the Co/Ni multilayer, and neither study generated conclusive data on the thickness dependence of the materials. It is suspected, although not proven, that the reason for this is the use of that multilayer for the central ferromagnet. Bethany Niedzielski is currently performing measurements of samples using Ni for F', Co/Ru/Co for F, and MoPy for F'' to attempt to more accurately measure the superconducting properties relevant to our SQUID samples. This work is also being done with a new MoPy target developed by Reza Loloee in order to improve the relative concentrations of Iron and Nickel.

The magnetic properties of the new MoPy target were carefully studied by Reza Loloee. The target shown in Figure 6.2 was estimated to provided 7 percent Molybdenum in 84/16

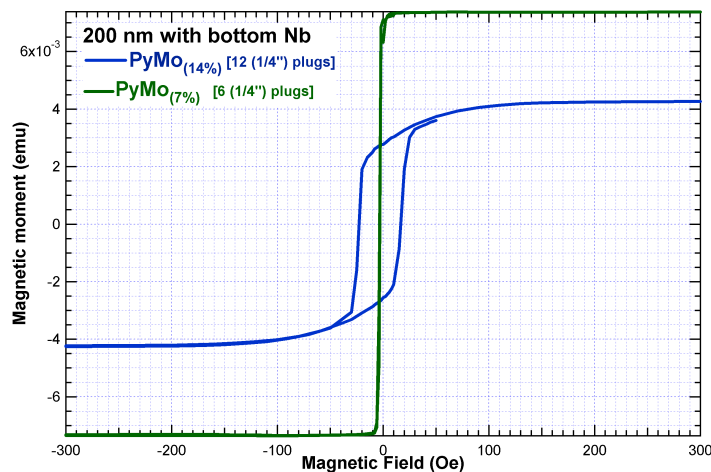


Figure 6.4: Measurements of 7 percent (Green curve), and 14 percent (Blue curve), Molybdenum-doped Permalloy. Note the reduction in saturation magnetization, and the increase in coercivity, with increasing Molybdenum concentration. (Credit: Reza Loloee)

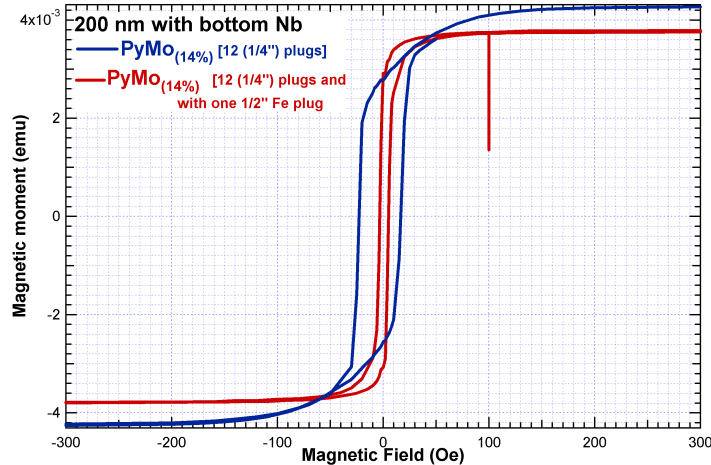


Figure 6.5: *Measurement of the change in magnetic behavior of 14 percent Molybdenum-doped Permalloy while changing the Iron content of the Permalloy.* The Blue curve is the same as in Figure 6.4, and has a 1/2” Py plug in the center. The red curve uses a 1/2” Fe plug at the center. By replacing the center 1/2” Py plug in the target with Iron, the coercivity of the thin film has substantially decreased. (Credit: Reza Loloee)

Permalloy, with 84 and 16 the relative concentrations of Ni and Fe with respect to each other. No measurements have yet been performed to confirm those concentrations, however comparing this to Bozorth [78], this is in the ballpark of his recommendations for MoPy, where “Supermalloy” is 5 percent Molybdenum in 84/16 Permalloy. By replacing all of the small outer plugs in the target with Mo, Reza estimated that he could get 14 percent Molybdenum. The measurements of the magnetization, shown in Figure 6.4 proved particularly interesting. 7 percent MoPy demonstrated very sharp, very soft switching, and looks almost no different than one might expect from pure permalloy - though you would expect the saturation magnetization to have reduced. This is demonstrated with the 14 percent MoPy, which saturates at roughly half the magnetization of the 7 percent MoPy. Also obvious is that the coercive field of the MoPy has dramatically increased, from nearly 0 in 7 percent, to as much as 2.5 mT in 14 percent.

In order to combat the increase in the coercivity, Reza replaced the center 1/2” plug,

which was originally Permalloy, with Iron. This increased the Iron content of the Permalloy which was expected to improve the ferromagnetic ordering. Figure 6.5 shows the data taken comparing the original 14 percent MoPy with the new target with larger Iron concentration. Note that the coercivity has decreased from around 2.5 mT to no greater than 1.0 mT. Also note that the rounding in the hysteresis curve has reduced, suggesting that the domains are more easily aligned with the field.

### 6.3 Copper-doped Permalloy

Copper-doped Permalloy, or CuPy, is a material suggested by our collaborators at Arizona State University, led by Nate Newman. Newman's group used the material in switching studies of S/F/N/F'/S Josephson junctions, which carry only singlet supercurrent. By observing the increase, and eventual decrease, in the critical current through the junction with increasing magnetic field, they were able to ascertain the switching behavior of the CuPy layer. Their data suggested switching fields on the order of 2.5 mT for a 2  $\mu\text{m}$  square junction with 2.4 nm of CuPy [79]. This was recommended as a good candidate for our switching experiments.

We fashioned a target to get 30.0 Py in a 70.0 Cu matrix, which is shown in Figure 6.6. We then grew films at least 500 nm thick for use in Energy Dispersive Spectroscopy (EDS) measurements to verify the relative atomic percentages of the materials in the alloy. The EDS measurements of the Copper Permalloy with the target described here found a ratio of 66.4 Cu to 33.6 Py. The ratio was a little off the expected concentrations, but not so much as to cause serious problems for early studies. The material would have been more strongly magnetic, and probably possessed a slightly lower switching field than seen by Nate

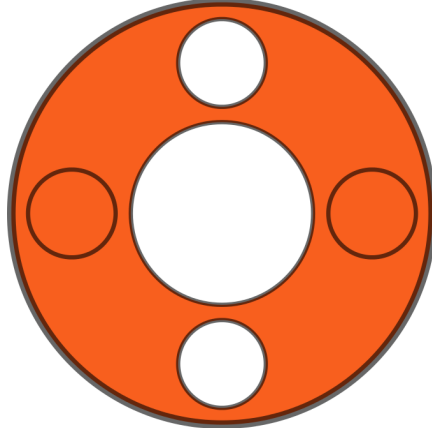


Figure 6.6: A diagram of the Copper-doped Permalloy target fabricated for this experiment. The central plug is 1" in diameter, while the outer plugs are 1/2". They are placed inside a 2.25" circular Copper target. The white plugs are Permalloy, and Orange plugs are Copper.

Newman's group. Magnetic studies were planned for the material, since it is a promising candidate for its magnetic behavior. However, preliminary magnetic characterization data from Newman's group indicate that magnetization switching in CuPy occurs over a broad range of fields, thus making it less attractive than other available options. Therefore, all studies on the material were halted in favor of other more enticing ferromagnetic materials.

## 6.4 Niobium-doped Permalloy

Recent work performed by Burm Baek *et al.* at the National Institute of Standards and Technology in Boulder, suggested the possibility of Niobium-doped Permalloy, or NbPy, as a likely candidate for our soft ferromagnetic layer. Their study, performed in spin-singlet junctions with Permalloy doped with 9 or 13 atomic percent of Niobium, demonstrated excellent switching behavior in the NbPy layers [31]. The work was exciting enough to propel us towards developing this material for our own studies.

The first necessary task was to develop a new target. A Permalloy target was modified to

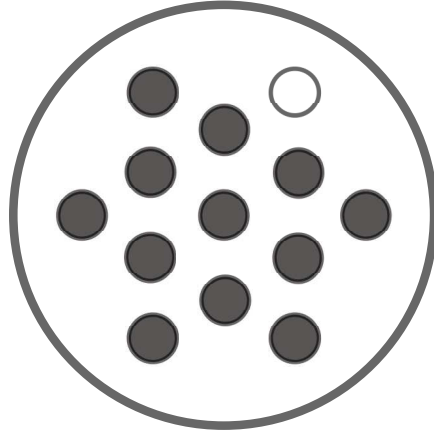


Figure 6.7: *A diagram of the target created for Niobium-doped Permalloy sputtering. All plugs are 1/4" inside a 2.25" circular Py target. The white plug is Py, while the dark plugs are Nb.*

accept plugs of Niobium in a pattern demonstrated in Figure 6.7. The quantity of slots were chosen originally, based on the calculations presented in Section 6.1 so that the Niobium concentration could be varied from 0 to 15 atomic percent. It turns out, however, that Niobium sputters more slowly than Permalloy, which reduced the upper limit to around 10 percent with this target.

The slow sputtering of Niobium was determined and confirmed when checking the concentration of thin films grown from the NbPy target. The concentration measurements were performed using the EDS system mounted to the Hitachi SEM as discussed in Chapter . Three attempts were required to generate the proper Nb concentration in the permalloy, which provided sufficient data to generate a trend of Nb concentration as a function of the quantity of Nb plugs. This is shown in Figure 6.8. This allows more accurate estimates of Nb concentration in this material if further changes are required in the future.

Once the concentration had been properly established, it was possible to use the material for further measurements. First, it was necessary to confirm that the material grown was properly ferromagnetic. At the time, our SQUID magnetometers were not cold, so we asked

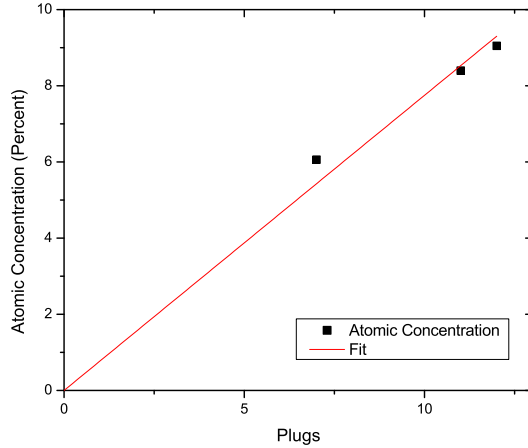


Figure 6.8: *Plot of the atomic measured atomic concentration of Nb in NbPy films versus the number of Nb plugs used in the target.* The fit was forced to go through 0, and has a slope of  $.75 \pm .05$  atomic percent per plug.

Professor Xianglin Ke to perform magnetization studies of a small, 3mm square and 500 nm thick, film of our NbPy in his Physical Properties Measurement System (PPMS). The hysteresis curve of the magnetization is presented in Figure 6.9. The NbPy film switches at a fairly low field, around 0.5 mT. This suggests that the NbPy is, in fact, a reasonably soft ferromagnetic material - not terribly surprising considering that Permalloy is also a very soft ferromagnet, though a very strong one.

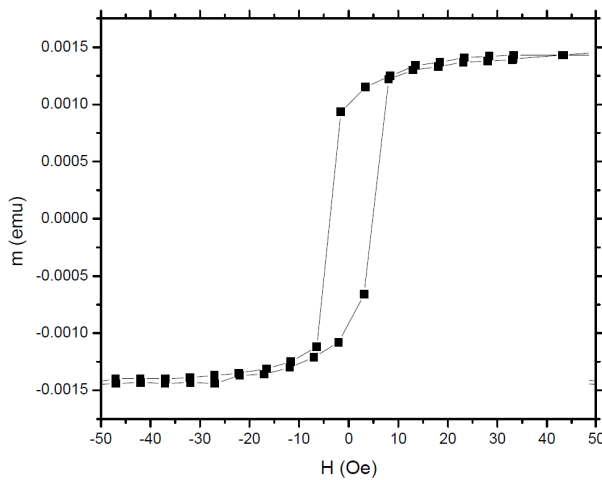


Figure 6.9: *Hysteresis curve from a 3mm x 3mm NbPy film 500 thick.* The switching field is low, roughly 0.5 mT, and fairly sharp.

In earlier studies, which will be discussed later, we had “shot from the hip” and attempted to successfully observe switching in our triplet devices without fully studying the ferromagnetic properties of the material first. Because that had shown limited success, we chose to move more slowly with the NbPy film. Several tasks were required in order to properly vet the material for our studies. The first was to attempt to understand its switching characteristics in small pillars. This would be done with Giant Magnetoresistance studies. The second task was to measure the superconducting properties of the material and verify that sufficient triplet supercurrent could be generated with the ferromagnet.

Giant Magnetoresistance is an effect that has been well studied for the last 25 years due to its applications in magnetic memory technology. The premise of the effect is based on the interaction between electron spins in a current driven through magnetized material layers. Consider a charge current of electrons driven through a system with two ferromagnetic materials, separated by a normal metal to prevent coupling of the magnets. The charge current possesses no spin favorability, so in the simplest concept, we can imagine the current comprised equally of “left” spin electrons, and “right” spin electrons. When this current encounters the first ferromagnet, which has been magnetized to the left, the left spin electrons experience little interaction with the layer and pass through unimpeded. The electrons with right-pointing spins, however, discover fewer available conducting states through the ferromagnet. Thus, they are mostly reflected back at the interface. This has the effect of polarizing the current to the left, and the first ferromagnet is often referred to as a “polarizing layer”.

When the current reaches the second layer, it will see a magnetization direction that could be oriented either to the left, parallel with the polarizer, or to the right, anti-parallel to the first ferromagnet. If the situation is the former case, then the polarized current

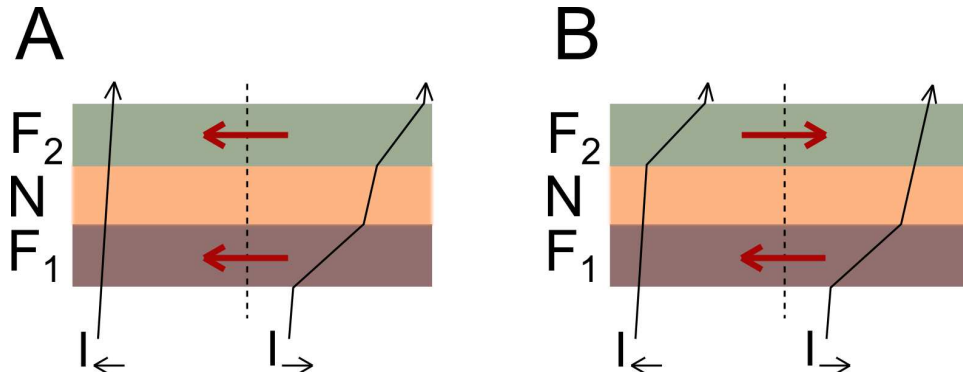


Figure 6.10: *Diagrammatic demonstration of Giant Magnetoresistance.* A) The magnetizations (red arrows) are parallel. The spin current aligned with the magnetizations shows little decay due to typical resistive effects. The anti-aligned current decays rapidly within the two ferromagnetic materials. B) The magnetizations are now anti-parallel. Each current now experiences a severe decay in a single ferromagnet. This leads to a lower overall current than in the previous case.

again passes generally unimpeded. If, however, the latter case is true, then the current sees an unfavorable magnetization state and is mostly reflected. Thus, the quantity of current transmitted through the system is strongly dependent on the relative orientation of the magnetic layers. This is demonstrated diagrammatically in Figure 6.10.

If a four terminal measurement is performed on the stack, the resistance of the stack will be seen to change with the switching of the top magnetic layer. The change in the resistance from the parallel state to the anti-parallel state can be as much as one to two percent of the parallel state resistance. This is a very large effect, even at room temperature, which made it particularly attractive for applications, such as in computer hard drives at the turn of the century. For further information regarding GMR, see the excellent theory work by Valet and Fert [80].

This effect is perfect for measuring the switching field of a magnetic layer. By performing a four terminal measurement on a single pillar, and measuring the change in resistance with applied magnetic field, the switching field can be determined easily. Better yet, this system

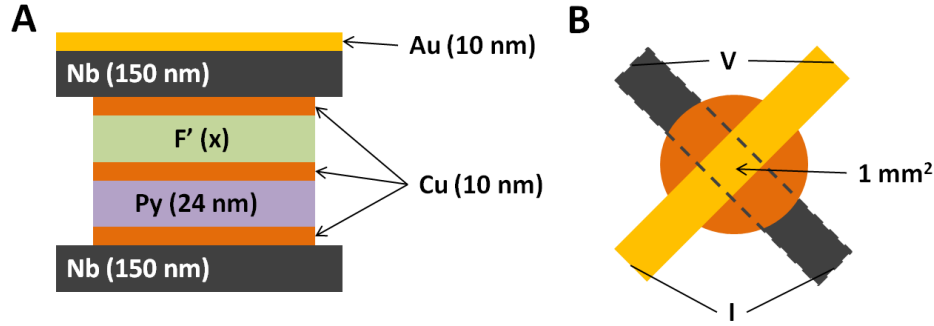


Figure 6.11: *Geometry of large scale samples used for Giant Magnetoresistance (GMR) measurements.* A) Multilayer stack edge on showing ferromagnetic materials spaced by Copper layers. F' is the ferromagnet to be studied, while the 24 nm Py is the polarizing layer. B) Top down view, where the top and bottom leads are Nb, and the center circle contains all Copper and F layers.

is very similar to the pillars we already make, requiring little in the way of modifications to our fabrication techniques.

Before measurements can be performed on small pillars, however, GMR studies need to be performed on large scale samples. Figure 6.11 demonstrates the design of these samples, which have a one square millimeter crossover that defines the junction region. This study must be performed to make certain the material has a sufficiently large GMR signal. If the GMR signal can be measured in the larger samples, then failing to see it in smaller pillars would suggest fabrication problems. That could not be guaranteed if we started by fabricating the small pillars first, as perhaps the material is not a strong enough ferromagnet to generate a large GMR signal.

Our first attempts at measuring the GMR in NbPy utilized a 24 nm Py layer as the polarizer separated from the NbPy by 5 nm of Cu to magnetically decouple the layers. Permalloy is a very soft ferromagnet and switches very close to zero field, so the thinking was that the NbPy would switch at a higher field than the Permalloy. On performing the measurement, however, there was no GMR signal to be found at all, as shown in Figure 6.12.

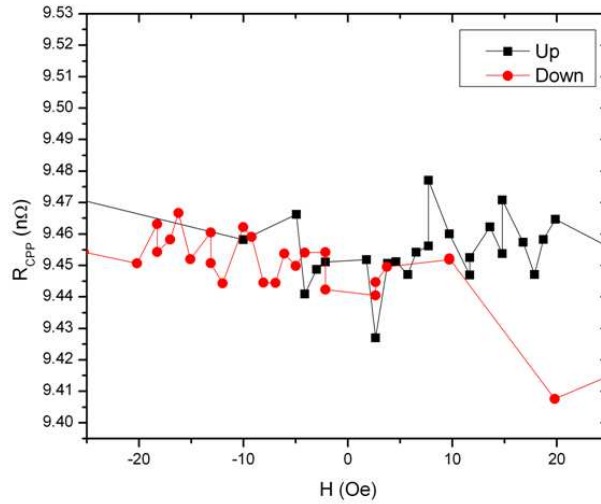


Figure 6.12: *Giant Magnetoresistance data from a Single Exchange-Biased Spin Valve with 3 nm NbPy as the switching layer, and 24 nm Py as the polarizer. The magnets were separated by 5 nm of Cu. No GMR signal was observed in this sample.*

This was particularly surprising, since we expected NbPy to be more than sufficiently strong to generate a GMR signal. This remained true for increasing thicknesses of NbPy, leading us to suspect that something else may have been wrong.

Discussions with Reza Loloee led us to an answer. It turns out that 5 nm of Cu is not sufficient to completely decouple ferromagnetic materials, and that at least twice that thickness is required for proper magnetic isolation. Figure 6.13 demonstrates this in a sample with 24 nm Py, and 3 nm NbPy. Note that there is now a clear resistance change at both positive and negative field. This tells us that in our previous attempts, the magnetic layers were rotating together, and now the two layers are switching mostly independently. However, because we see no plateau in the resistance, that suggests the two layers are still partially coupled. Because we want to see the behavior of the NbPy switching, we need to isolate its behavior from the polarizer.

The effects of the polarizer can be removed from the system by “pinning” the Permalloy

layer using an antiferromagnetic layer, such as Iron Manganese. By growing Py in direct contact with FeMn, the Py switching field will be artificially increased to much higher fields. This allows the NbPy switching behavior to be completely isolated at low fields. Figure 6.14 shows the results of this change. Note that we're now seeing only the switching behavior of the NbPy, as we now see the resistance change until it reaches a plateau. The GMR signal is roughly 0.45 percent, which is a small, but reasonable signal for further studies.

The next task was to determine the superconducting properties of the NbPy [81]. This was done by fabricating spin-triplet generating junctions using NbPy as the top ferromagnetic layer. The pillars measured were circular and had sizes of 3, 6, and 12  $\mu\text{m}$  in diameter. The Fraunhofer patterns were measured for each pillar, and the maximum critical current plotted against the thickness of the NbPy layer. The thicknesses measured ranged from 1.5 nm to 5 nm, and the results are plotted in Figure 6.15. The data ends at 3 nm because samples

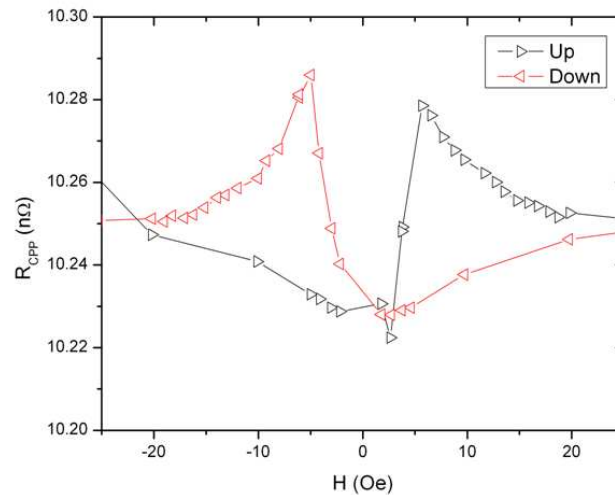


Figure 6.13: *Giant Magnetoresistance data from a Single Exchange-Biased Spin Valve with 3 nm NbPy as the top ferromagnetic layer, and 10 nm of Copper for the spacer layers. 24 nm Py used for the polarizer. A GMR signal is observed, with Py switching first at lowest field, and NbPy switching more slowly after. The lack of a plateau in the resistance suggests the magnets are still experiencing some coupling.*

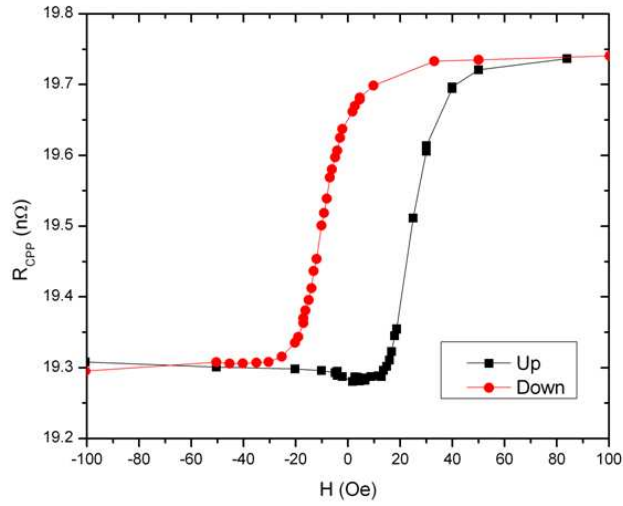


Figure 6.14: *Giant Magnetoresistance data from a Single Exchange-Biased Spin Valve with 3 nm NbPy as the free layer, and 10 nm of Copper for the spacer layers. 8 nm Py pinned by 8 nm FeMn as the polarizer. A GMR signal of 0.45 percent is observed, and the only switching behavior is in the NbPy, as the pinned permalloy does not switch until fields greater than 25 mT*

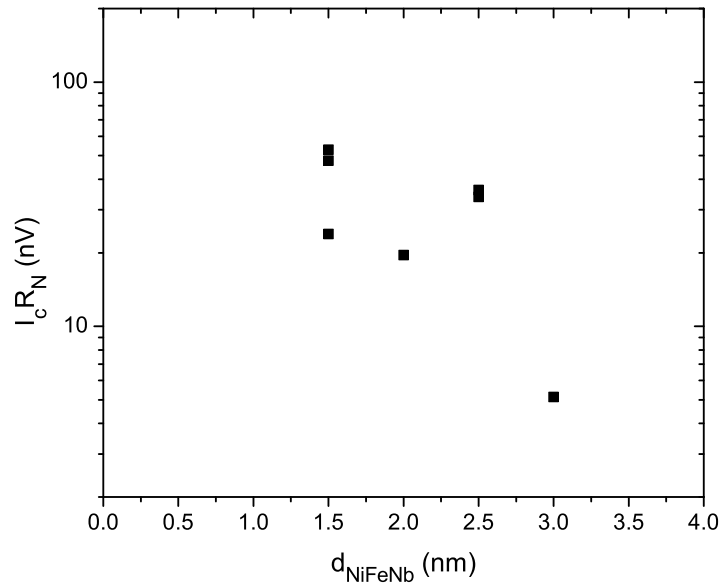


Figure 6.15: *Plot of the critical current versus NbPy thickness in an S/F'/F/F''/S Josephson junction with F'=Ni, F=Co/Ru/Co, and F''=NbPy, in pillar sizes ranging from 3 to 12  $\mu$ m. The  $I_C R_N$  product starts particularly low and decays with increasing thickness for thin NbPy. This suggests that spin-orbit or spin-flop scattering is strong in the material. (Credit: Bethany Niedzielski)*

greater than 3 seemed to carry no supercurrent. It is worth noting that the critical current only seems to decay with thickness. It is possible that the spin-orbit scattering in NbPy is so strong that it overwhelms the triplet generation at the outset. Lower thicknesses were not measured for fear that they would not be magnetic, since we don't know the thickness of the magnetic "dead layer" for NbPy.

The critical currents for this material are surprisingly low, no greater than 55 nV, and it is disappointing that a material with such great switching behavior does such a poor job generating triplet supercurrent. It is still possible to use the material for measurements, but since we need to use very small pillars to control the switching behavior, the critical current in such pillars will be extremely small. This means that NbPy is not the best available candidate for the job, but may still be considered in the future.

## 6.5 Palladium Iron

The most common material used in our studies is Palladium Iron (PdFe), with a 1.5 atomic percent of Iron in Palladium. It is a particularly soft, weak ferromagnetic material that has been studied by our group for several years [82]. It was originally considered for use as the sole ferromagnetic layer in S/F/S junctions back when we hoped to observe spin-triplet supercurrent in samples with that simpler geometry [64]. It was eventually supplanted by the Co/Ru/Co synthetic anti-ferromagnet for that function. The target used here was shown in Figure 6.1.

We attempted to measure the superconducting properties of the PdFe using the Co/Ni multilayer as the central ferromagnet [81]. These measurements showed little obvious variation in the critical current with increasing PdFe thickness, as shown in Figure 6.16. From

this data, it appears that the maximum critical current occurs at 12 nm PdFe. However, given the quality of the data, that was at best an educated guess. The majority of our attempts at triplet control, discussed in the next chapter, use this thickness.

Because we were struggling with the switching behavior of the PdFe in our control experiments, which will be discussed more in Chapter , and due to the questionable data measured before, we attempted to perform another measurement of the supercurrent in PdFe. This time, the samples used the Co/Ru/Co multilayer as the central ferromagnet, which we knew had given us success in other studies [43, 73]. The results of this study are presented in Figure 6.17. There is a more obvious plateau in the data here, which suggests that thicknesses in the range of 16 to 24 nm of PdFe could be used to optimize the triplet supercurrent. Later measurements in our control studies utilized either 16 or 24 nm for the PdFe thickness.

Large scale GMR studies of PdFe were performed by our group several years ago. They

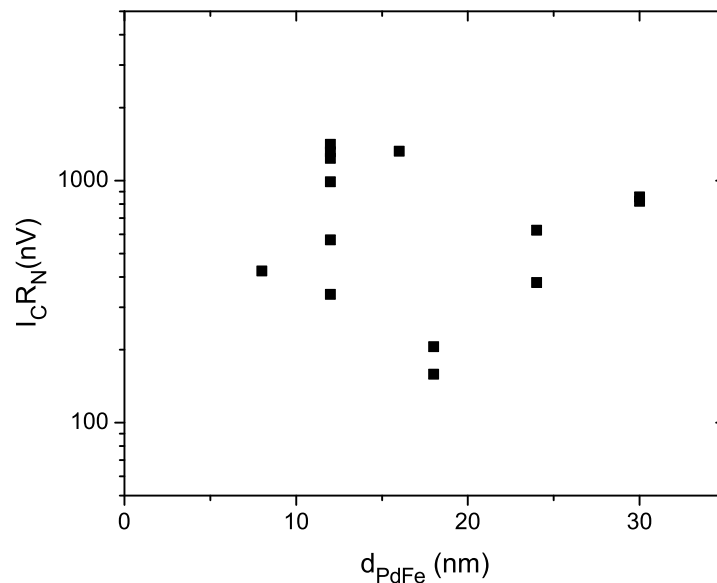


Figure 6.16: *Plot of the critical current versus PdFe thickness in an  $S/F'/F/F''/S$  Josephson junction with  $F'=Ni$ ,  $F$  the Co/Ni multilayer,  $F''=PdFe$ , in pillar sizes of 10 and 20  $\mu\text{m}$ . There does not appear to be any obvious variation in the  $I_C$  with increasing thickness, beyond the sample-to-sample scatter. (Credit: Simon DIESCH)*

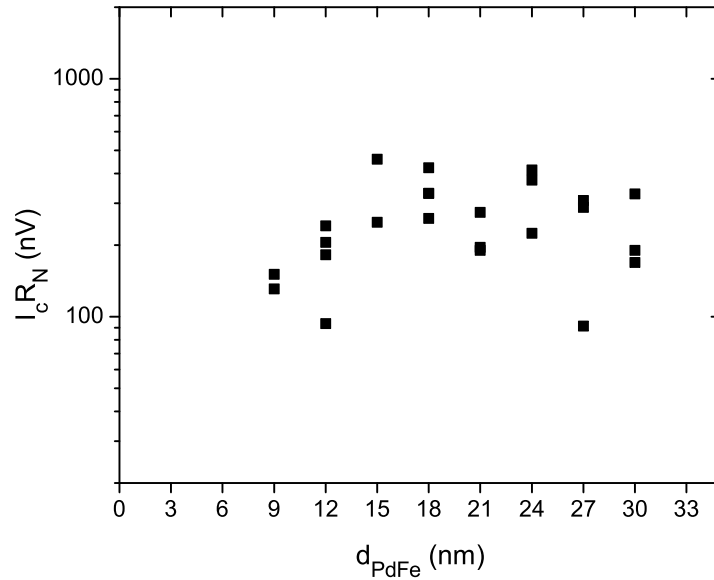


Figure 6.17: Plot of the critical current versus PdFe thickness in an  $S/F'/F/F''/S$  Josephson junction with  $F'=Ni$ ,  $F=Co/Ru/Co$ ,  $F''=PdFe$ , in pillar sizes of 3, 6, and 12  $\mu m$ . There is a trend to the data with increasing thickness, as the  $I_C R_n$  product increases at first, then turns over and appears to start decreasing with increasing PdFe thickness. The range of 16 to 24 nm PdFe were considered a “plateau”, but only 16 and 24 were ever seriously considered as usable. (Credit: Bethany Niedzielski)

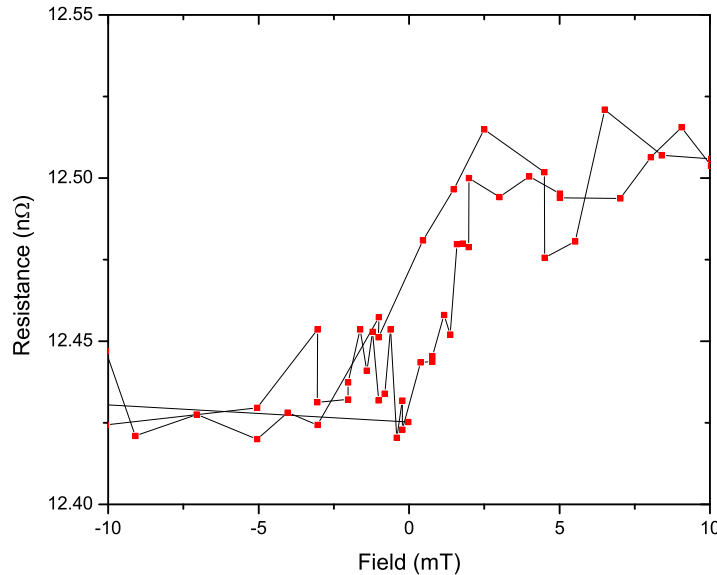


Figure 6.18: Giant Magnetoresistance data from a 1  $mm^2$  SEBSV with 24 nm PdFe, and an 8 nm Py polarizer pinned by 8 nm FeMn. Any hysteresis has been masked by the noise in the data, but a 0.45 percent GMR signal is apparent in the data. Two thinner PdFe layers were also measured, but demonstrated no GMR signal. (Credit: Alex Cramer)

were repeated more recently to verify that the signal would still be measurable with a change in the device design. The samples performed recently were *Single Exchange-Biased Spin Valves* (SEBSV), while the older devices were Double EBSV's. This means that in our samples, we used a single pinned Permalloy layer instead of two, one above and one below the switching layer. DEBSV's have a larger GMR signal than their SEBSV cousins, but are less useful for us in the small scale switching experiment since we need to pattern the switching ferromagnet. Figure 6.18 demonstrates our SEBSV data for 24 nm of PdFe. There is a 0.6 percent change in the resistance in the large scale samples, which is more than sufficient to be useful for small scale measurements. Surprisingly, this is the only sample that displayed a GMR signal, while samples containing 12 and 16 nm gave no discernible signal. It is possible those samples are not ferromagnetic at 4.2K (i.e. the Curie temperature of the PdFe is lower than 4.2K), but other experiments suggest otherwise.

Small scale GMR pillars were also studied to understand the switching characteristics of the PdFe when patterned into elliptical shapes of different aspect ratios. The samples were fabricated using the methods described in Chapter . PdFe thicknesses of 12, 16, and 24 nm were fabricated into pillars of  $0.25 \mu\text{m}^2$  to determine the behavior of the magnetic material with increasing size and different aspect ratio. It was expected that the switching fields would increase compared to the large scale GMR data, but the actual data, shown in Figure 6.19 is a touch more strange than was anticipated. Both the 12 and 16 nm PdFe samples display a shift in the magnetization data. We do not understand that shift in the data, nor why it disappears in the sample with 24 nm PdFe. It is also impossible to say that this shift doesn't occur in other types of samples, or if it only appears in GMR samples.

That issue aside, the switching behavior of the 24 nm PdFe samples are apparently very good. The roundness of the switch emphasizes that there is domain formation in these

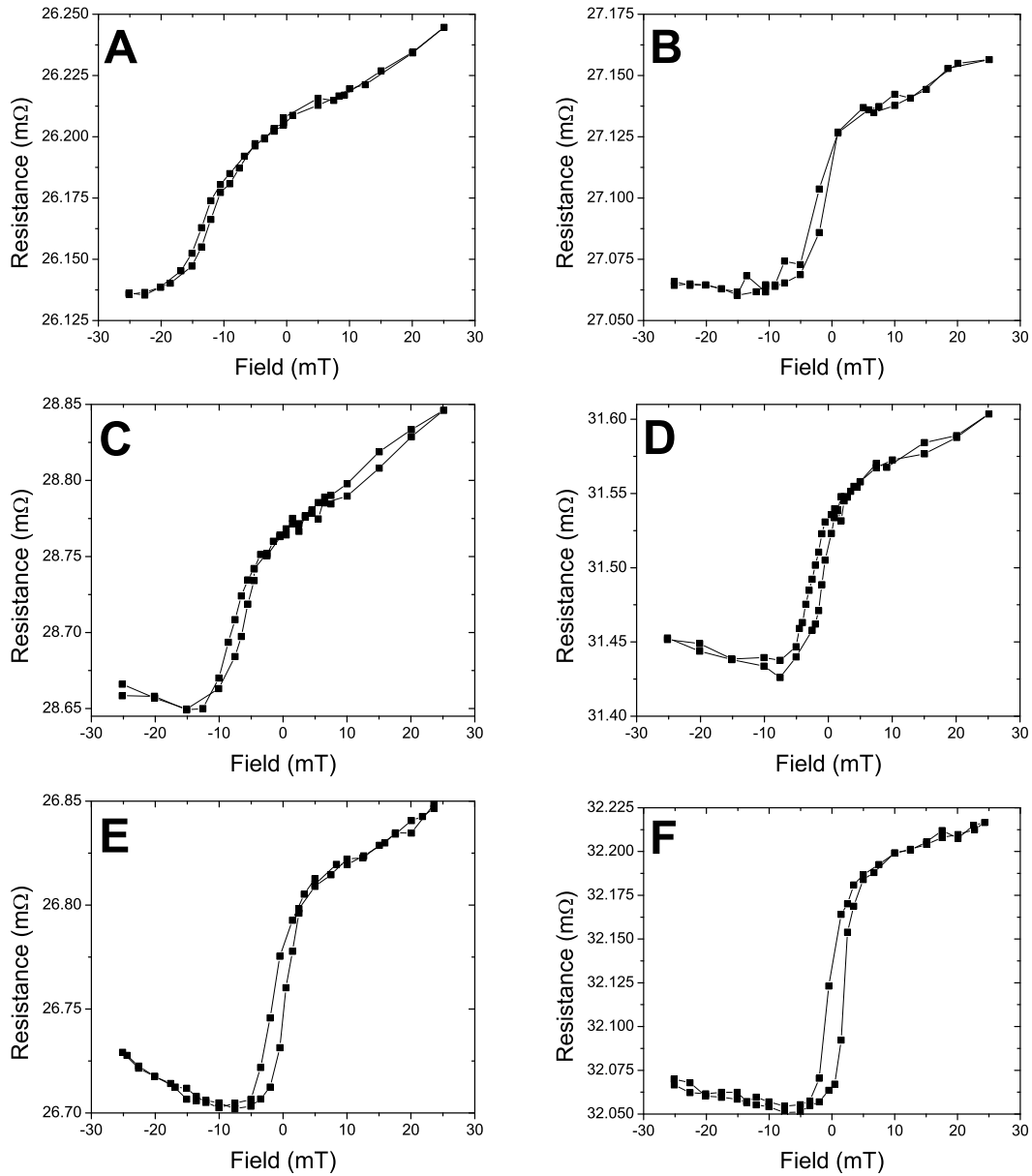


Figure 6.19: *Giant Magnetoresistance data from  $0.25 \mu\text{m}^2$  elliptical pillars with PdFe as the switching layer.* Pillars on the left have aspect ratios of 1.5, while pillars on the right have a 2.4 aspect ratio. Panels A and B show data from samples with 12 nm of PdFe, C and D with 16 nm PdFe, and E and F with 24 nm of PdFe. Pillars on the left show a clear shift to negative field, which is not well understood, whereas pillars on the right have very little shift, or none at all. Also, the hysteresis appears to improve, and the magnitude of the shift minimize, as the thickness increases. (Credit: Bethany Niedzielski)

samples, so the domain size in PdFe is clearly smaller than these pillars. However, the switching is relatively sharp, and is well centered at zero field, which indicates that the PdFe should act as a good soft ferromagnet for switching studies in the spin-triplet. It appears that smaller pillars would be required, both to increase the switching fields a little and gain some separation between pillars of different aspect ratios, and to attempt to get closer to coherent single-domain Stoner-Wohlfarth switching.

## 6.6 Conclusion

No single ferromagnetic material here has demonstrated itself to be the perfect candidate for the soft ferromagnetic layer in the experiments that will be discussed in the next chapter. It's entirely possible that the *perfect* ferromagnet simply doesn't exist. Choosing which aspects of the magnetic behavior can be tolerated is part of the game, and knowing the materials properties is the first step towards being able to decide which ferromagnet may work best.

Most of our work has been done on PdFe because it has thus far been the most promising candidate. Unfortunately, as will be seen in the next chapter, it hasn't proven itself to be as good as the data here suggests. Many of the studies and paths taken in this experiment were driven by the results we were seeing from the PdFe in the control devices. That said, with how promising the PdFe has looked on its own, there hasn't been enough to make it desirable for us to completely switch to a different material.

Whether any of these other materials will be used for this experiment remains to be seen. NbPy remains a particularly promising candidate due to its beautiful switching characteristics, as seen by Baek *et al.* [31]. However, finding a way to work around its severely suppressed supercurrents has been an issue. Major changes to the sample designs for the

control experiment, moving away from needing single-domain ferromagnets, would be required, which are only now becoming a feasible possibility. Unfortunately single-domain NbPy pillars would simply pass too small a supercurrent to be measurable.

As for the other materials, MoPy and CuPy, further studies are required before they would ever be included as ferromagnetic materials in the control devices. The general issues with controlling the PdFe has pushed for a reexamination of the MoPy's superconducting properties, which is currently in progress. Promising data there may lead to GMR studies on the MoPy, and possibly inclusion in control devices. However, it is as yet too early to know for certain.

# Chapter 7

## Phase Sensitive Measurements

With the discovery of the spin-triplet state, people began considering a number of other possible directions for further study. Our group in particular has pursued experiments such as measuring the density of states of the spin-triplet supercurrent by fabricating S/I/F/S Josephson junctions [83], which are still ongoing. Others in the group have also been pursuing experiments into the long-range propagation of the spin-triplet to determine  $\xi_F$ , the ferromagnetic coherence length of the state.

But one other experiment is of particular interest. That experiment is to find methods of developing spin-triplet junctions for applications. One such application, the primary one that would be quickly considered in this modern world driven by computer technology, is to use the properties of the system as a magnetic bit in a superconducting memory array. This makes sense, particularly considering the use of ferromagnetic materials, and since the spin-triplet state depends on the direction of the magnetizations.

The first method one might consider for controlling the spin-triplet state is quite simple. We know that if the magnetizations of two adjacent ferromagnets align parallel to one another, then the spin-triplet state disappears, and the critical current passed through the junction drops by several orders of magnitude. Primarily, we know this indirectly, in the sense that we've observed the change in supercurrent with and without F' layers, and we've seen the enhancement of critical current by magnetizing the junctions [43, 67, 75]

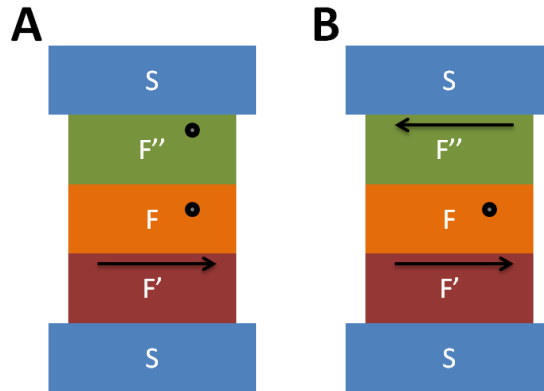


Figure 7.1: A diagram of a Josephson junction designed to switch between the Singlet and Triplet states. A) The top two magnetizations are aligned. In this case no triplet is generated and the system can only conduct singlet supercurrent. This is referred to as the “off” state. B) The top magnetization has been moved to lie orthogonal to the middle magnetization. In this case, because no two adjacent magnetizations are collinear, triplet supercurrent is carried through the junction. This is referred to as the “on” state.

A diagram of the magnetizations of such a control scheme is shown in Figure 7.1. In this experiment, the top magnetic layer would be switched through 90 degrees. When the top layer’s magnetization is aligned with the central ferromagnetic layer, then no triplet is generated, and the system will provide the critical current signature of the spin-singlet state. When the magnetization is switched orthogonal to the central ferromagnet, the system will begin to generate triplet current and an enhancement in the critical current will be seen, commensurate with the generation of the triplet state.

Unfortunately, this scheme, despite being simple on its face, is quite complicated experimentally. The low temperature apparatus used to measure this would require two orthogonal external fields. We would also need two ferromagnet materials that would be capable of orienting their magnetizations to two directions separated by 90 degrees, requiring the magnetocrystalline anisotropy to be identical within the plane. This would then allow the top ferromagnet to be rotated into either a collinear state with the central ferromagnet, or orthogonal to it.

Thankfully there is a much easier scheme from fabrication and measurement standpoints. This scheme, and the measurements of the resulting samples, are described in this chapter. The first section will discuss the property of the spin-triplet Josephson junctions that allows for a change in phase. Section 7.2 will describe our measurement strategy for these junctions. Section 7.3 will describe our first attempts to measure our SQUID devices. Section 7.4 talks about the fields at which our superconducting materials trap flux. Section 7.5 describes the experiments performed when we began to reduce the size of our junctions. The sixth section covers our SQUID devices containing the Co/Ru/Co synthetic anti-ferromagnet. Section 7.7 discusses the most recent studies focusing on samples that have had all three ferromagnetic layers patterned into a single ellipse. Lastly, Section 7.8 concludes the discussion.

## 7.1 Spin-Triplet Phase

A paper written by Houzet and Bouzdin in 2007 hinted at another method of controlling the state of the Spin-Triplet supercurrent [21]. They considered a sample geometry very similar to the one that was eventually used by Trupti Khaire to find the signature of the spin-triplet current [20]. Not only did they predict the generation of the triplet state in these sample geometries, but they also suggested that the orientation of the magnetizations of the various ferromagnets mattered. This was already understood, as discussed in Chapter , to be critical to the triplet generation. However, there was another piece to the story.

It turns out that the relative direction of the magnetizations determines the phase picked up by the supercurrent. This is specifically driven by the *chirality* of the magnetizations. Consider the direction through which the magnetization rotates between the first and second ferromagnetic layers. If the direction is the same between the second and third ferromagnetic

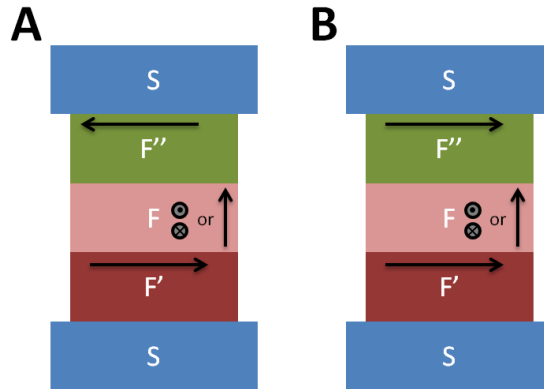


Figure 7.2: A diagram of a Josephson junction designed to switch between the  $0$  and  $\pi$  phase states of the triplet supercurrent. A) The chirality of the rotation between the magnetizations does not change as the current propagates through the layers. In this state, there is no difference in phase between the superconductors, so the state of this junction is referred to as the “ $0$ ” state. B) The top magnetization has been rotated through  $180$  degrees. Now, the chirality of the rotation between the magnetizations changes. The superconductors now experience a phase difference of  $\pi$ , which gives the junction its name. In both cases, the chirality change is most easily understood by considering the perpendicular magnetic anisotropy case for the central ferromagnet.

layers, then the superconductors on either side of the junction have the same phase in the ground state (with no supercurrent flowing through the junction). If the direction of rotation changes, however, then there will be a phase difference of  $\pi$  between the two superconductors. The first such junction is referred to as having a “ $0$ ” phase state, while the second is referred to as being in the “ $\pi$ ” state, where the names are based on the magnitude of the phase shift. These two types of junctions are presented in Figure 7.2.

This provides a very straight-forward method of controlling the spin-triplet state compared to the more simple “on/off” strategy. By changing the magnetization direction of a single ferromagnetic layer in the stack, the phase state of the junction will change. This requires only a magnetic field to be applied in a single direction, which requires no change in our measurement systems. In this way, the junction can be controlled using the external magnetic coils on our quick dippers described in Chapter . The applied field will then act on

the junction in a way that will change its state. The only trick that remains is to measure the phase of a junction, which is discussed in the next section.

There is a small complication that arises when using a central ferromagnet that has perpendicular magnetic anisotropy, as we've done in Chapter . Consider the behavior of the junction when the top ferromagnet rotates in the plane of the sample. The central ferromagnet's magnetization is perpendicular to this rotation, so the system remains optimized regardless of the top magnet's orientation. This means that the junction's phase is determined entirely by the magnetization rotation between the bottom and top ferromagnets. This means that it is possible to have *any* phase state from 0 to  $\pi$ . These other states are referred to as “intermediate states” within this experiment and, when they persist with increasing external field, are deemed as undesirable operation of the junction.

## 7.2 Phase Measurement Strategy

It is not possible to measure the absolute phase of a quantum system directly. Instead, it is necessary to measure the relative phase state of two similar systems. The easiest way to do this for Josephson junctions is to fabricate them into a Superconducting Quantum Interference Device (SQUID), similar to the ones discussed in Section 2.3. Current applied to the SQUID splits into the two legs of the loop. Each current will pick up a phase in its junction, and the two currents will then interfere either constructively or destructively. By measuring the magnitude of the current through the device, it is then possible to measure the relative phase between the two junctions.

This, suggests a strategy for measuring the switching of a junction between the 0 and  $\pi$  state. By building a SQUID with two junctions, one “fixed” that cannot change its state, and

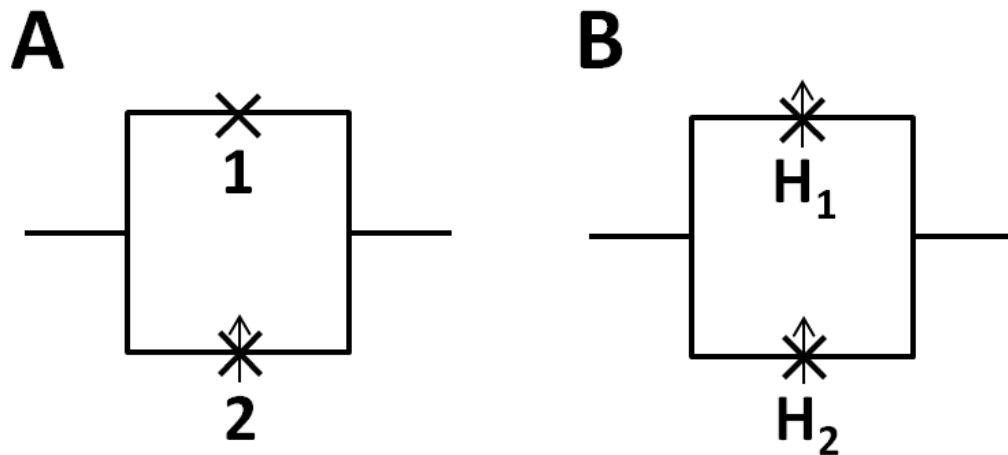


Figure 7.3: A diagram presenting two different methods of controlling a Josephson junction. The lines represent the superconducting leads of a SQUID loop, while crosses represent Josephson junctions. A cross with an arrow represents a controllable junction. A) The first strategy involves using a fixed junction (junction 1) and a controllable junction (junction 2). In this strategy, only one Josephson junction will change during the experiment. B) The second strategy involves fabricating a pair of Josephson junctions that can both be switched. One junction would have a switching field of  $H_1$ , while the second would have a switching field  $H_2$ , where  $H_1 < H_2$ .

one “controllable” that can change state, it would be possible to measure the phase change of the free junction. The circuit diagram for this strategy is shown in Figure 7.3a. While this is a very convenient strategy, and, in fact, makes for a particularly simple measurement, there is a serious weakness with this plan. Fabricating a fixed triplet junction into the same SQUID as a controllable triplet junction is not simple. It would require two different bottom layers, separately defined and sputtered. That makes this an unfavorable strategy.

Figure 7.3b suggests a more palatable strategy for the measurement. Rather than having fixed and free junctions, it is much easier instead to fabricate two controllable junctions. By taking advantage of shape anisotropy, described in Section 2.1.2, we can force the switching field of one junction to be a bit higher than the other. This would allow us to design the switching characteristics during fabrication so as to separate the behavior of each junction in field. Figure 4.10 presents an image of what these ultimately look like after fabrication. The small elliptical features are the Josephson junction, which utilize different elliptical shapes, referred to as “aspect ratios”, or the ratio between the long and short axis of the ellipse, to control the switching fields.

The switching fields can be estimated by following the work of Osborne in 1945 [84]. If we consider the case of an ellipsoid with semi-major axis length  $a$ , semi-minor axis length  $b$ , and thickness  $c$ , then  $a \geq b \gg c$  is the condition for a very flat ellipsoid. This should act as a good estimate for our thin magnetic multilayers. The eccentricity can be written as,

$$e = \left(1 - \frac{b^2}{a^2}\right)^{1/2} \quad (7.1)$$

which can be rearranged to solve for  $b/a$ ,

$$\frac{b}{a} = (1 - e^2)^{1/2} \quad (7.2)$$

From Osborne, the demagnetizing factors in cgs units along the semi-major axis is,

$$\frac{L}{4\pi} = \frac{c}{a} (1 - e^2)^{1/2} \frac{K - E}{e^2} = \frac{cb}{a^2} \left( \frac{K - E}{1 - \frac{b^2}{a^2}} \right) \quad (7.3)$$

along the semi-minor axis is,

$$\frac{M}{4\pi} = \frac{c}{a} \left( \frac{E - (1 - e^2)K}{e^2 (1 - e^2)^{1/2}} \right) = \frac{c}{b} \left( \frac{E - \frac{b^2}{a^2}K}{1 - \frac{b^2}{a^2}} \right) \quad (7.4)$$

and along the thickness of the film is,

$$\frac{N}{4\pi} = 1 - \frac{c}{a} \left( \frac{E}{(1 - e^2)^{1/2}} \right) = 1 - \frac{c}{b}E \quad (7.5)$$

all of which must sum to 1. The factors  $K$  and  $E$  within these equations are complete elliptic integrals of the eccentricity, where the first kind takes the form,

$$K(e) = \int_0^{\frac{\pi}{2}} \frac{d\theta}{\sqrt{1 - e^2 \sin^2(\theta)}} \quad (7.6)$$

while the second kind is,

$$E(e) = \int_0^{\frac{\pi}{2}} \sqrt{1 - e^2 \sin^2(\theta)} d\theta \quad (7.7)$$

These functions can be integrated in Mathematica to solve for the demagnetizing factors

of each direction. For coherent rotation within the plane of the film, the a-b plane, the switching fields are,

$$H_S = (M - L)M_S \quad (7.8)$$

where  $H_S$  is the switching field, and  $M_S$  is the saturation magnetization of the ferromagnetic material.

From this, we can estimate the switching fields for our soft ferromagnetic films. Since we're using PdFe for this entire chapter, we can focus on that material.  $M_S$  for PdFe is no bigger than 40 emu/cm<sup>3</sup>. For a PdFe film that is 16 nm thick, and is 800 nm by 400 nm in diameter, a junction with an aspect ratio of 2, the switching field comes out to 1.2 mT. For an aspect ratio of 1.25, with the same junction area, the switching field is 0.2 mT, while for an aspect ratio of 3, the switching field is 1.8 mT. This gives a rough sense for how strong the fields need to be in order to see switching.

In order to measure a SQUID, it is necessary to apply a flux through the loop of the device. With the SQUID lying flat against the substrate, the external field is applied along the face of the SQUID and therefore cannot be used to generate flux. It would be possible to run a current along the the length of the bottom lead to generate a flux through the SQUID, but it was suspected that this could generate noise in the full SQUID measurements. Therefore a second line, 10  $\mu\text{m}$  wide with a 7  $\mu\text{m}$  wide gap between it and the bottom lead, was added to the design to provide a source for the magnetic flux.

Characterization of a SQUID device is performed with a four-terminal measurement to observe the current-voltage relationship of the junctions, which should behave as the overdamped Josephson junctions described in Section 2.2.3. The critical current measured in these overdamped junctions will vary periodically with the applied flux through the SQUID,

from the sum of the critical current through each junction when both junctions possess the same phase, to the difference of the critical currents when the junctions possess opposite phases. By plotting the variation of  $I_c$  with the change in  $I_\Phi$ , the current through the flux generating line, the modulation of the SQUID device can be determined. It is then possible to identify the relative state of the two junctions in the device. If the  $I_c$  is maximum at zero flux current, then the two junctions occupy the same state. However, if  $I_c$  is a minimum at zero flux current, then the two junctions are in precisely opposite states.

The sample is mounted on a quick dipper and slowly inserted into a liquid Helium-4 storage dewar. Once cold, all of the layers will be ferromagnetic in character, including the soft ferromagnetic materials, which tend to have very low Curie temperatures. Following the cooling process, the device is checked for a SQUID modulation signature, which verifies that both junctions are carrying supercurrent. The characteristics of the modulation, such as the quantity of supercurrent or the state of the SQUID, are irrelevant in this stage as the magnetic layers are likely in a random configuration. This is because the system needs to be optimized before it can be properly measured.

If the SQUID passes the check, a large field of 260 mT is applied in the negative direction. This initializes the magnetizations of the layers. The Ni and soft ferromagnets will both align with the applied field. If the central ferromagnet is the Co/Ni multilayer, then it won't be seriously affected by the external field. If, however, the central ferromagnet is the Co/Ru/Co layer, then the applied field will set it into its optimized state through the spin-flop transition described in Chapter [67]. The sample is then immediately measured at zero field. This checks the initialized state of the junctions. If the two junctions are initialized as expected, then they should both be in the  $\pi$  state. In this case the SQUID will have a maximum signal at zero flux current. This is shown in Figure 7.4

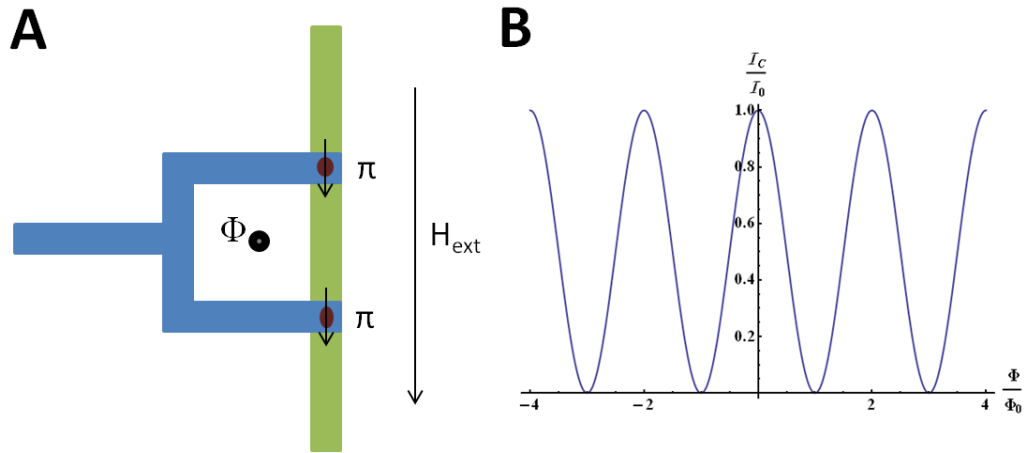


Figure 7.4: A diagram of the Josephson junctions in their initial configuration. A) The Josephson junctions have been magnetized by a large external field  $H$ . They now possess magnetizations that are aligned with the external field. The arrow specifically represents the direction of the soft ferromagnetic layer. Both junctions are in the  $\pi$  state because the Ni and soft ferromagnets point in the same direction. B) The expected response of  $I_c$  vs.  $\Phi$  in this state, normalized to the maximum critical current. Note that the critical current is a maximum at zero flux current.

At this point, the external field is applied in the positive direction to change the magnetic state of the junctions. This is typically done in steps of 0.5 or 1 mT, with the field applied for a short period of time, and then removed. The SQUID is then remeasured to check for any changes in the junction states. By removing the field, it is possible to extract the permanent behavior of the magnetic layers without interference from the Josephson behavior in a magnetic field (i.e. the Fraunhofer pattern). This significantly simplifies the interpretation of the SQUID data, as the only variations in the SQUID should be entirely a result of the changes in the magnetic layers.

This process, increasing the field, removing it, and then measuring the SQUID, continues one step at a time. Eventually, the field will reach  $H_1$ , which is the switching field of the first junction. At this point, the first junction will switch into the 0 state, while the first junction is still in the  $\pi$  state. The SQUID will therefore register the signature of a minimum at zero

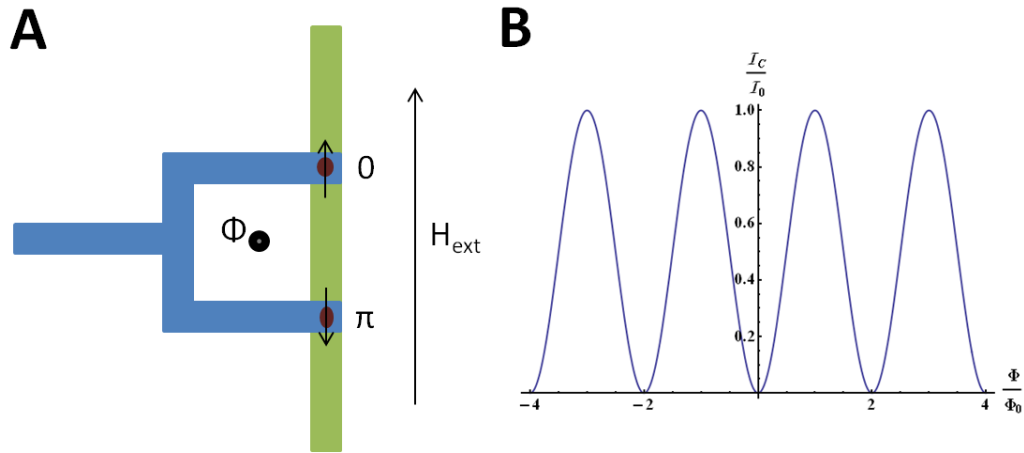


Figure 7.5: A diagram of the Josephson junctions when one of the two junctions has switched. A) The Josephson junctions have now experienced a large enough field in the positive direction that one of the two has switched, with the other held in place by shape anisotropy. The one that has switched is now in the 0 state, because its soft ferromagnet points opposite to the bottom Ni layer. B) The expected response of  $I_c$  vs.  $\Phi$  in this state, normalized to the maximum critical current. Note that the critical current is now a minimum at zero flux current, a result of the interference between the junctions.

flux field. This is shown in Figure 7.5. The field can then continue to be increased until  $H_2$ , the switching field of the second junction, is reached. Here, the two junctions will again be in the same state, and so the SQUID will output a maximum current at zero flux.

The field is then incremented in the negative direction to switch the junctions back. If the magnetic layers are well behaved, the switching fields for each junction will be the same in both positive and negative directions. Thus, when  $-H_1$  is reached, the first junction will switch into the  $\pi$  state. Since the second junction is still in the 0 state, the SQUID will output a minimum current at zero flux. The process is continued until the field arrives at  $-H_2$ , at which point the entire device will have been reset, with both junctions in the  $\pi$  state, and the SQUID back to outputting a maximum at zero flux. Here, the system is again in the configuration shown in Figure 7.4.

The measurement itself is entirely automated. Once the junctions are optimized, a max-

imum field is set and the computer told to run the measurement. The data can then be analyzed after each run for magnetic characteristics. The LabVIEW program was developed by Yixing Wang and has been an invaluable tool for these measurements, allowing for almost continuous around-the-clock measurements of each SQUID.

Because we hope to use these SQUIDs for applications, the switching fields cannot be too high. Eventually, the switching fields will have to be applied by an on-chip line, which has limitations in the quantity of current it can carry and remain superconducting. This sets a limit, based on the designs of our collaborators, of 12 mT to the optimum switching field that would be acceptable for a junction in a working device. However, switching at higher fields are still interesting for study, at least from a proof-of-concept perspective.

### 7.3 First Measurements

The first attempts at measuring these SQUID devices were performed on junctions that were  $1 \mu\text{m}^2$  in area. At the time, these were by far and away the smallest junctions yet measured in our group. Previous students had measured junctions no smaller than  $3 \mu\text{m}$  diameter circles, so this experiment was significantly pushing our fabrication techniques and experience. It was understood that these junctions were too large to be single-domain, but it was important to verify that the fabrication process was working and that the SQUIDs would be measurable before advancing to smaller junctions.

The first measurements, performed on samples containing 1.2 nm Ni for the bottom ferromagnet, the Co/Ni multilayer for the central ferromagnet, and 12 nm PdFe for the soft ferromagnetic layer, confirmed that the SQUID geometry was working as expected. Figure 7.6 shows one of our first SQUID measurements, with Josephson junctions of area  $1 \mu\text{m}^2$ ,

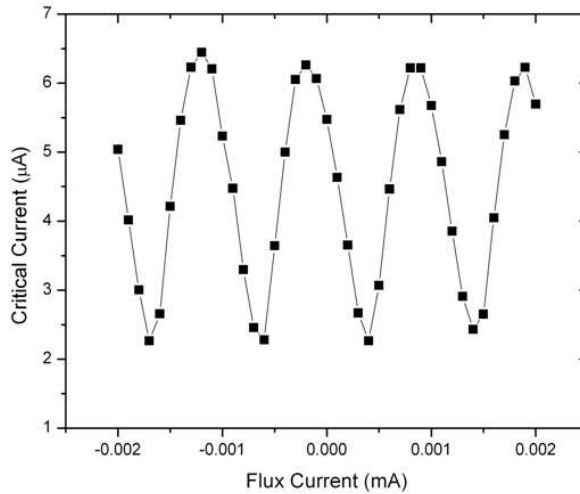


Figure 7.6: *The first measurement of our SQUID design.* The modulations do not entirely approach zero because the junctions are not precisely identical due to the inclusion of the ferromagnetic materials. The SQUID was in the virgin (unmagnetized) state when this data was taken, which explains why the maximum is slightly shifted to the left from the zero in flux current. The oscillation period, which represents a single flux quantum, is very nearly identical to 1 mA of flux current.

demonstrating the modulations indicative of the interference device. Note that the current doesn't go completely to zero as would be expected for a SQUID with two identical junctions. This is a result of the fact that the junctions contain ferromagnetic materials. While they have identical areas, and therefore it would be expected that  $I_c$  would be the same through each, but we always observe sample-to-sample fluctuations in  $I_c$  in our S/F/S junctions.

The vertical axis in the figure is  $I_c$  measured for the SQUID, with each  $I_c$  the result of a current-voltage curve. The horizontal axis is  $I_\Phi$ , rather than the actual flux through the SQUID. However, the SQUID's were designed such that 1 mA of current down the flux line would generate exactly one flux quantum through the SQUID. A least-squares fit of the data plotted in Figure 7.8b gives a period of  $1.036 \pm .006$  mA. The SQUID modulates exactly one period for each flux quantum that enters the SQUID, which suggests that our design methodology was reasonable.

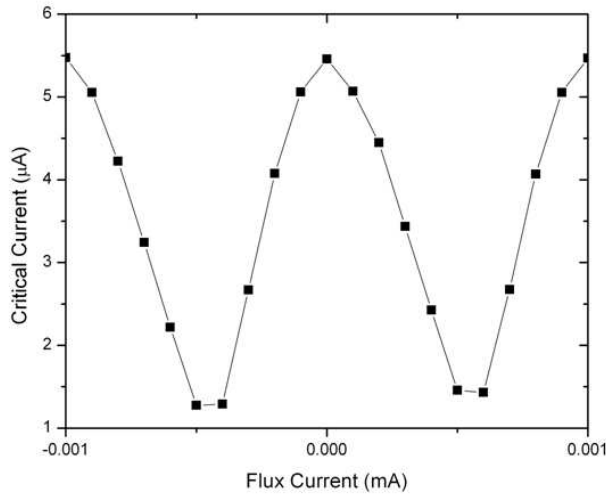


Figure 7.7: *The first measurement of our SQUID design with a maximum at zero flux.* The SQUID was measured at 18 mT here, a technique that was abandoned so as to eliminate the Fraunhofer effects on the critical current. Because the SQUID response has a maximum critical current at zero flux field, this suggests the pillars are in the same state.

These early experiments did not follow the procedure discussed in Section 7.2. That technique was developed as a result of what we learned during these tests. The method we employed here was similar to our measurement strategy used in Chapter . The Fraunhofer pattern of the SQUID was measured first with the applied field in the positive direction, then in the negative direction to attempt to observe changes in the pattern between the two. These changes are the result of switching in the magnetic layers, as we’ve learned that the Fraunhofer patterns can be affected by the magnetic fluxes present inside the pillars.

When a change occurred in the behavior of the pattern,, the SQUID characteristics were then measured just above the field where the potential switch was seen. Figure 7.7 shows the early switching behavior in these SQUIDs. The first curve was measured at 18 mT, demonstrating that the SQUID has shifted from where it was in Figure 7.6. It now suggests that the two pillars are in the same state. By increasing the field, it appears that the magnetic layers have arranged their magnetizations so that the system is now properly

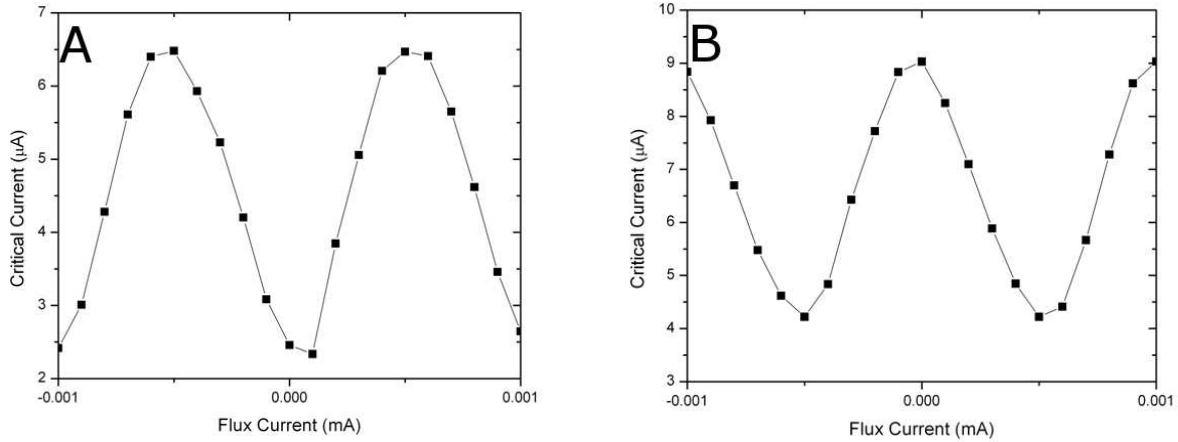


Figure 7.8: *Measurements of  $I_c$  vs.  $I_\Phi$  for the  $1 \mu\text{m}^2$  SQUID.* A) The SQUID was first taken to positive fields where a switch was seen at 30 mT. The SQUID was then measured at zero field to eliminate any magnetic behavior from the measurement. The critical current is clearly a minimum at zero flux, suggesting the two pillars are in opposite states. B) Following the measurement in A, the SQUID was taken to negative fields. A switch was found at -45 mT, and again the SQUID was measured at zero field. Note that it again possess a maximum critical current at zero flux. A least squares fit of this plot gave an oscillation period of  $1.036 \pm .006 \text{ mA}$ .

initialized. This measurement was originally done with the 18 mT field still applied, before it had been realized that the Fraunhofer behavior would be simultaneously sampled with the permanent magnetic behavior during the experiment.

Figure 7.8a shows the results of continuing to increase the field to 30 mT after finding the initialized state. This time, the measurement of the SQUID was performed by applying the field, and then measuring in zero applied field. It is obvious that the device is now in a state where the two junctions are no-longer in the same state. This suggests that we have successfully switched one of the junctions.

We then tried to go to negative field and measure the Josephson junction switching back. Figure 7.8b shows the measurement done at zero field after magnetizing to -45 mT. It appears again that the SQUID has switched, as the critical current is back to a maximum at zero field. This is a particularly exciting result, as it suggests that the system is entirely under

control.

However, the story did not remain so simple. Continued measurements of the same device demonstrated some strange behavior as we tried to switch the junctions. The biggest concern in the observations was the switching fields, which seemed to change as we switched back and forth. A device with real magnetic switching might show some variation in switching field early on, as the initial state might not be perfectly optimized, but after the first switch, all subsequent switches should be at a reproducible field.

This occurred for several devices fabricated in the same batch, suggesting that this was more than a fluke. Because the devices were so large, it is likely that the switching fields were low enough that the shape anisotropy had little effect. Therefore, any real switching was likely unobservable in these samples.

## 7.4 Flux Trapping

One might ask then why switching behavior was seen at all in the earliest devices. The answer is that what was being observed was *flux trapping*. Flux trapping, also known as flux pinning, is the capability of a Type-II superconductor to allow magnetic field lines to penetrate its surface. Unlike Type-I superconductors, which go entirely normal when their critical field is reached, Type-II's can have a small region of their bulk enter the normal (i.e. non-superconducting) state, allowing flux to pass through the normal region. This allows the superconducting state to survive at higher fields.

Unfortunately, it also has the effect of pinning flux lines within the bulk of the superconducting material. This means that if there are regions of trapped flux, then flux lines could be penetrating the SQUID loop. The problem is that since flux trapping is a somewhat

random event in terms of spacial location, then it will result in a random quantity of flux penetrating the SQUID loop. The SQUID then behaves as if one of the two junctions is in a random state.

One way to tell that there is flux trapped in the system is to lift the quick dipper out of the Helium 4. By measuring the resistance across the superconducting bottom leads, it is possible to tell when the superconductor has gone completely normal. This causes the trapped currents, which are what create the pinned flux fields, to decay out due to the sudden reemergence of the resistance. Then, when the superconductor is returned to the Helium 4, it can be remeasured. If the state has remained the same, then it reflects the actual magnetic state of the junctions. However, if the SQUID response is different, then the observed changes were due to trapped flux.

This method of detecting trapped flux is imperfect, however. Because of their small size, we do not know the exact Curie temperatures of our thinnest ferromagnets. It is possible that the Curie temperatures are low enough that this method of warming up the superconductors can send the ferromagnets normal. Then, when the sample is again dipped, the signal will have changed because the ferromagnet will have reordered randomly from its paramagnetic state. This is a particularly vexing problem, and is worrisome considering the big initial applied field required for setting up the experiment.

One other method of avoiding the problem of flux trapping is to never reach fields strong enough to trap flux in the first place. Figure 7.9 demonstrates a sample that showed no signature of state change in the SQUID all the way up to 25 mT. In fact, studies of the flux trapping problem in our samples demonstrated that flux trapping did not occur until fields at least as high as 28 mT. This provides a solid choice for the maximum field in our automated measurements. Any changes in the SQUID that occurs at fields lower than 28

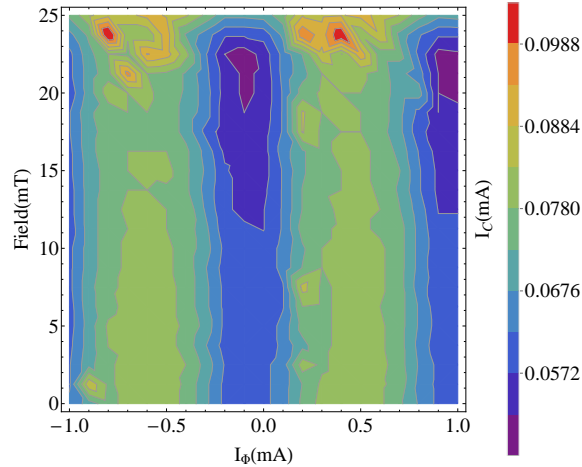


Figure 7.9: *A measurement of a SQUID to positive field from 0 to 25 mT. This particular SQUID measurement demonstrated no state change at all in this field range, which strongly suggests a lack of flux trapping. It is extraordinarily unlikely that trapped flux would perfectly cancel, or provide an unobservable 360 degree shift in phase.*

mT will be due to magnetic behavior without question.

## 7.5 Smaller Junctions

For the next batch of samples we reduced the area of the junctions by a factor of four, to  $.25 \mu\text{m}^2$ . The reduction in size reduces the quantity of supercurrent capable of flowing through the junction, but also reduces the quantity of magnetic domains within the soft ferromagnetic layer. The soft ferromagnetic material remained 12 nm PdFe for these samples. The SQUIDs were also patterned using Aluminum as the milling mask, as described in Chapter .

A number of SQUIDs were measured, but one in particular behaved in a very interesting way. This sample had a junction of 800 by 400 nm in diameter, and another of dimensions 600 by 533 nm. The aspect ratios, therefore, were 2 and 1.25, with the latter being the most circular junctions we fabricate. Any more circular than this and there is a worry that the junction will have no magnetic control via shape anisotropy at all. The junction with an

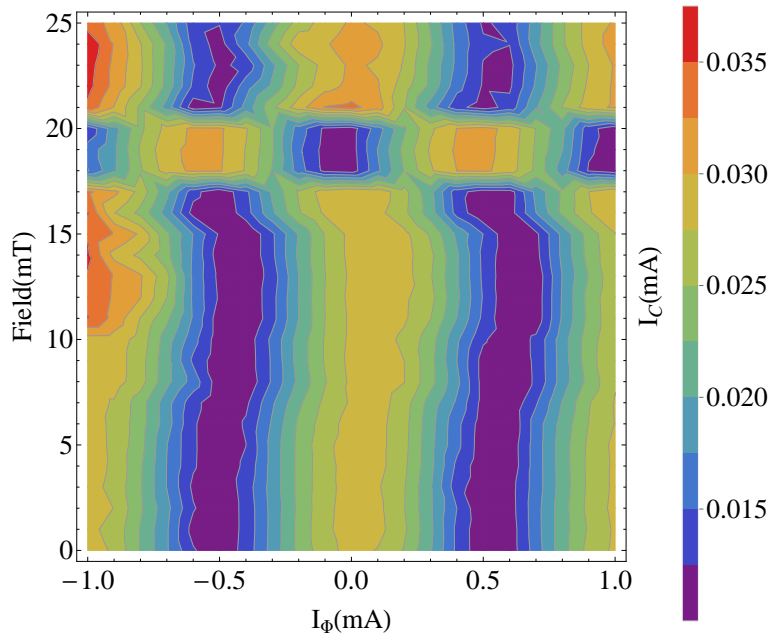


Figure 7.10: A plot of the behavior of the SQUID in positive fields with 12 nm PdFe for the top ferromagnet. The junction aspect ratios were 2 and 1.25, with an junction area of  $.25 \mu\text{m}^2$ . The color represents the magnitude of the critical current at each point, with the blue end of the spectrum representing a minimum. Note that the system begins in a state with a maximum at zero flux field. The system switches at 18 mT and 21 mT. Note also the small shift in phase starting at 7 mT.

aspect ratio of 2 is roughly in the middle of the ranges fabricated. From the calculations above, these two junctions should switch at 0.3 mT, and 0.8 mT respectively.

Plotted in Figure 7.10 is the first measurement of the SQUID from 0 to 25 mT. The spectrum represents the quantity of supercurrent through the junction, with colors on the red end of the spectrum larger than colors on the blue end. The bottom axis plots the change in the flux current, and the vertical axis plots the applied external field. Recall that what is plotted here is the field that was applied before the measurement. All of the measurements were actually performed in zero external field. This is the standard for all of the future three dimensional plots.

The SQUID obviously starts out with a maximum signal at zero flux current. It maintains

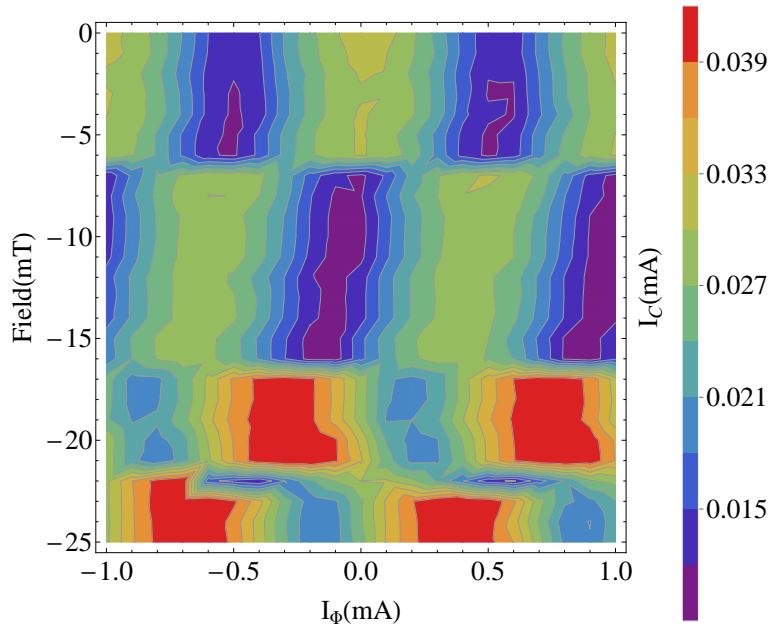


Figure 7.11: *The same SQUID as Figure 7.10 measured to negative fields from 0 to -25 mT. Note that the system begins in a state with a maximum at zero flux field. The system switches at 7, 17, and 22 mT. Note also the shift in phase starting at 7 mT.*

this state, for the most part, up to 18 mT when it rapidly switches. For the next 3 mT it is at a minimum at zero flux current. Finally, at 21 mT, it switches back to a maximum at zero flux current. This is beautiful switching data, exactly what was expected for the behavior of these devices in the experiments. There are some unusual behaviors in the data, for example the sudden increase in the signal strength visible on the left side of the plot, and the small “wiggle” in the data starting around 7 mT. That these occur at nearly the same time suggests that there is some magnetic reordering going on in the sample.

Figure 7.11 displays the data for the same SQUID measured from 0 to -25 mT. Unfortunately, despite the beautiful data to positive fields, the negative field data are confusing. There are three apparent switches, one at 7 mT, one at roughly 17 mT, and one at 22 mT. There is also a dramatic change in the critical current after the second switch. Most strangely, there is a slow shift in the SQUID state starting at the first shift and ending at

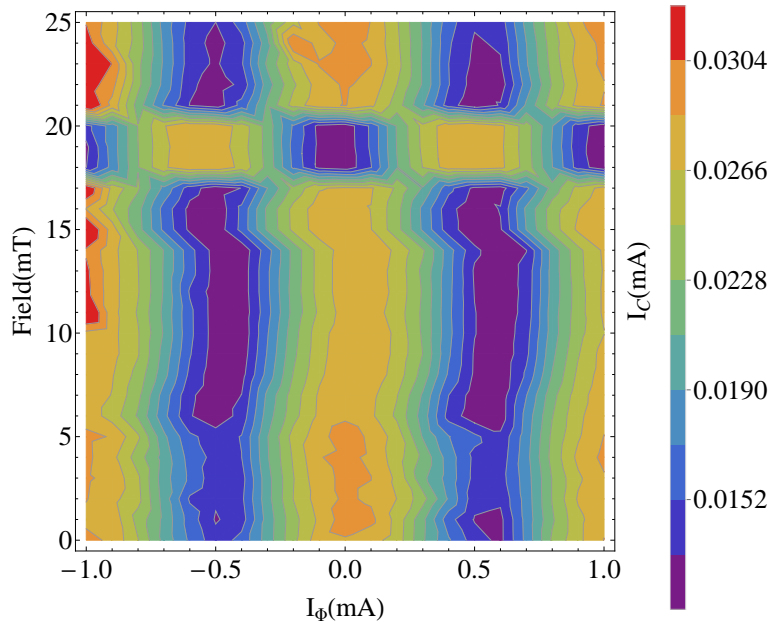


Figure 7.12: A plot of the repeated measurement of the SQUID to positive fields, again up from 0 to 25 mT. Note the similarities to the original measurement of the SQUID.

the second. That shifted “intermediate” state then persists through the last two switches. There is a lot more magnetic behavior going on here than in the first measurement, and it is disappointing that the characteristics to positive and negative field are so different.

A second measurement of the positive field direction yielded an even bigger surprise, shown in Figure 7.12. Again measuring from 0 to 25 mT, the system started out in the state with the maximum critical current at zero. This, despite the fact the sample had ended the previous run offset from this state by a phase of roughly 90 degrees. Even more amazingly, the sample again demonstrated two switches, one at 18, and one at 21 mT. It even possessed a small wiggle in the phase state of the junction starting at roughly 7 mT!

Compare again the data in Figure 7.10 to that in Figure 7.12. Other than small variations in the value of the critical current from point to point, variations that emphasize that they are different measurements, the two plots are very nearly identical. The magnetic behavior is the same in both plots, right down to the wiggle that occurs before the switch. Clearly

the sample is behaving reproducibly, so this can't be chalked up to flux trapping. This can very strongly be called a magnetic switch.

But it begs the question why the negative data seemed to behave so strangely. Why did we see three switches, and why are there these strange shifts in the magnetic data? The answer appears to be domain motion, possibly in the PdFe, but also possibly in the other magnetic layers. Because we have three different ferromagnetic layers, and the current depends on all three as it flows through the junction, it is very difficult to divine exactly what is transpiring in each of the layers. Now, it is largely irrelevant which magnetic layer moves in the context of claiming that the change in the SQUID is the result of changing magnetic chirality, but it becomes a problem when attempting to generate reproducibility from sample to sample.

One might also ask why the switching fields are so high. They were predicted to be 0.3 and 0.8 mT, so why do the switches occur at 18 and 21 mT? This gets at one of the major discoveries of our work in Chapter . Recall that when we attempted to perform Giant Magnetoresistance studies of the Niobium-doped Permalloy, the first samples demonstrated no GMR data whatsoever. This was a result of the Copper spacer layers being 5 nm, which was deemed insufficient to properly magnetically decouple the layers.

These samples used 5 nm of copper for their spacer layers. That may explain some of the surprising results we see here, and in other samples which behaved more erratically, or not at all. For example, the switching fields are higher because the PdFe could be magnetically bound to the Co/Ni layer beneath it, which wants to hold the PdFe in place. Therefore it requires a bigger field to get the PdFe to swing around. This also explains why we see lower switching in the negative direction, as less field is needed to bring it back.

There are other sources of anisotropy that could influence our junctions as well. Recall

the discussion in Chapter on magnetism, where we discussed magnetocrystalline anisotropy. It is possible that the magnetizations within the junctions want to align to a crystallographic direction rather than follow the imposed shape anisotropy. We suspect that this shouldn't be a strong effect, as magnetocrystalline anisotropy is strongly related to spin-orbit scattering, and PdFe is not a strong spin-orbit scatterer. However, it is still possible that a small magnetocrystalline anisotropy would be sufficient to cause some issues.

There are also other sources of anisotropy that could play a role. Strain, which can be induced on a film due to a mismatch in lattice parameters between the ferromagnetic material and layer it is grown on, can have an anisotropic effect. Another source is magnetostriction, where the shape of the magnetic material changes as the moments rotate within the film. Both of these are undesirable effects upon which we have very little control, and could be playing a role in the unusual magnetic behavior.

It is also interesting to consider the stray fields generated by the ferromagnetic layers. Typically stray fields occur at the edges of a ferromagnetic film. However, if domain walls exist, as they surely do in extended films like the Ni and Co/Ni, then stray fields will attempt to close the flux loops around the edges of the domain walls. Because Co/Ni has perpendicular magnetic anisotropy, its flux loops may extend much further than those from a material with entirely in-plane magnetization. Perhaps the use of Co/Ni leads to increased magnetic binding between the various layers, and therefore a degradation in switching performance.

## 7.6 Co/Ru/Co Central Ferromagnet

To combat the issues seen in previous samples, several changes were made to the sample fabrication process. The first change was to increase the thickness of the copper spacing

layers to 10 nm, hopefully improving the magnetic switching characteristics. The second change was to improve our fabrication of the Aluminum junctions, as described in Chapter . A big concern for us was the shape of the edges of the pillars. If the junctions were particularly rough, then there would be places for the magnetization to become pinned, preventing it from moving at fields lower than 25 mT. By increasing the rate of the Aluminum deposition, the edge roughness effect was reduced.

The third major change was to switch from the Co/Ni multilayer, to Co/Ru/Co, the synthetic anti-ferromagnet (SAF). Part of the reason was mentioned in the previous section; that the stray fields from the Co/Ni could be interfering with the switching behavior of the PdFe. The other reason involves the complication mentioned in Section 7.1. The intermediate states seen in the previous samples were a big concern, and appeared to complicate the data analysis. Because the Co/Ru/Co lies in the plane of the sample like the other ferromagnets, it was believed that it would not suffer from the same intermediate state problem. Instead, it was expected that when the layers switched, the SQUID modulations would be suppressed due to the loss of triplet current in one of the two junctions. In other words, the SQUID would act briefly like a single Josephson junction while the magnetic layer in the other junction completed its switch.

An example of these flavor of SQUIDS is shown here. The junctions in this SQUID each had a area of  $.25 \mu\text{m}^2$ , with 1.5 and 2.4 for their aspect ratios. The sample was measured only to 7 mT, and from the behavior seen it was decided that this was sufficient to test the behavior. Figure 7.13 displays the first positive sweep of the sample. The sample clearly starts properly initialized, and then demonstrates the suppression of the SQUID modulations between 3 and 5 mT. When the SQUID signal returns, the critical current has increased in magnitude by a factor of two or more. What's more, the system has found itself in an

intermediate state! This is an enormous surprise, as there was no expectation that the intermediate state would appear in devices with the Co/Ru/Co layer.

Figure 7.14 shows the attempt to reset the system, demonstrating that it is not reproducible to negative field. While there is clearly a suppression of the SQUID modulations, though at lower field, there is no switch back into the initial state of the SQUID. It is also curious that the maximum critical current was initially so low before increasing dramatically at higher fields. It is very apparent that magnetic states are moving around, but their motions are merely enhancing the critical current, not switching the devices.

Figure 7.15 attempted to demonstrate reproducibility in the positive direction similar to the last section. Unfortunately, while the state remained the same initially, there was no

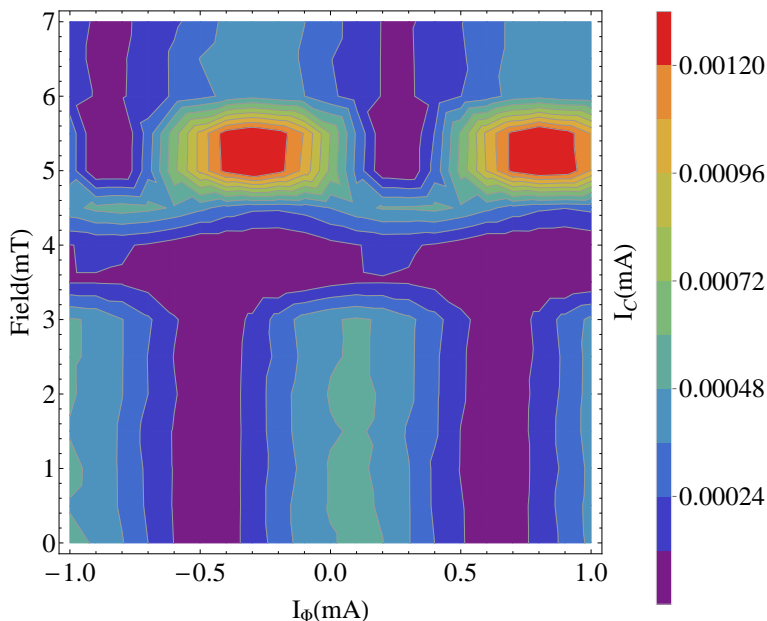


Figure 7.13: A plot of critical current through a SQUID containing Josephson junctions with a Co/Ru/Co central ferromagnet. The vertical axis is the positive external field applied before each measurement, while the horizontal axis is the current applied to generate the flux field through the SQUID. The system appears to start in the properly initialized state before transitioning into an intermediate state. The transition demonstrates the suppression in the SQUID modulation expected for this system of ferromagnets.

similarity at all in the behavior of the SQUID. It remained in the intermediate state, like it did in the negative direction, but did not act the same way. Instead of one apparent switch (i.e. modulation suppression) there were two. Surprisingly, the maximum critical current appeared to change between the two measurements. It is unclear why that change occurred.

Unfortunately, while these samples were expected to simplify matters for these measurements, they actually made them more complicated. Instead of getting rid of the strange intermediate states, we still have to deal with them. This suggests that the interplay between the magnetization directions of the top and bottom ferromagnets plays a bigger role than we've so far considered. In the same breath, we've now added the further complication of the SQUID modulation decay to the data, which is even more bizarre. We occasionally see the SQUID modulations disappear, as we expected to see when a junction switches states, but the same SQUID signal sometimes returns afterwards! One might argue that both junc-

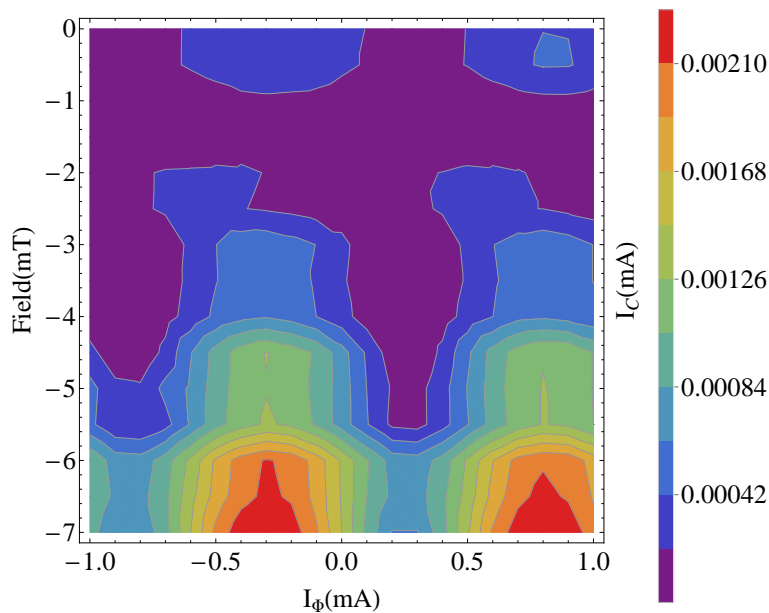


Figure 7.14: A plot of critical current through the same SQUID shown in Figure 7.13. The SQUID was magnetized to negative fields in this case in an attempt to reset the SQUID. While the system apparently goes through another switch, characterized by the suppression of the SQUID modulations, the system remains locked in the intermediate state.

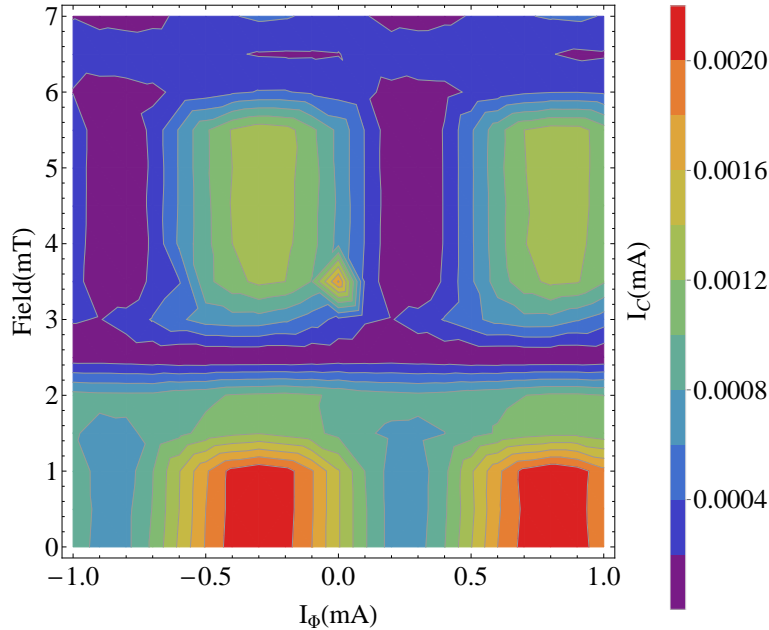


Figure 7.15: A plot of the second measurement of positive fields of the SQUID plotted in Figure 7.13. Unlike the SQUID from the previous section, the behavior at positive field was not repeated in this sample. Somehow, the system is still locked into the same intermediate state. A switch still occurs, but again the state does not change following the switching signal.

tions could be switching simultaneously, but we would expect to see no critical current at all, or perhaps a much smaller critical current than we do see in these gaps.

Normally these issues wouldn't be enough to chase us away from using the SAF as a central ferromagnet. However, it seems as if we've taken a step backwards instead of a step forwards. There's also the problem of magnetic behavior in the other ferromagnetic layers. One solution to this would be to pattern all three ferromagnetic layers into the same elliptical shape. Unfortunately, if the Co/Ru/Co were patterned into the same elliptical shape as the other ferromagnets, it would align its magnetizations with the shape anisotropy. This would completely suppress the triplet generation. Therefore, a return to the Co/Ni multilayer is required.

## 7.7 Full Milling

One of the significant changes moving forward to these samples was the return to the Co/Ni multilayer. This was done so that the samples could be milled through all three ferromagnetic layers in the hopes of controlling the magnetic behavior more fully. Another significant change to these samples was the use of the ma-N 2401 negative E-Beam resist process instead of the Aluminum junctions. This was a further attempt to improve the smoothness of the outer edges of our ferromagnets, which still showed some small defects in the Aluminum method. Lastly, we changed the thickness of the PdFe layers from 12 to 16 nm to account for more recent data on the material as discussed in Chapter .

The last change was a significant one. One of the problems with Nb is that it tends to have a very rough surface texture, typically on the order of 5 Å. Yixing Wang borrowed a method from Reza Loloee to attempt to solve that problem [62]. By adding thin layers of Aluminum intermittently in the Niobium, the Nb roughness can be reduced to roughly on the order of 2 Å, while not seriously suppressing the superconductivity in the material. The roughness of the material makes a big difference in the fabrication of the ferromagnetic materials. Ferromagnets with a wavy characteristic can couple in ways that are hard to predict experimentally. An external field will also not move their magnetizations around in an ideal way, driving switching fields higher, or leading to unusual magnetic characteristics. It was deemed particularly important to try to eliminate this problem from our samples.

The Nb/Al multilayer was grown first by alternating 40 nm thick Nb layers with 2.4 nm of Aluminum three times, capped off with another 40 nm of Nb and 2 nm of Au to prevent oxidation. Because there weren't enough sputtering guns to account for all of the materials, the sputtering system was opened to allow the Aluminum gun to be replaced by another

material. During this process, the top of the sputtering system, which contains the samples, was enclosed by a bag and kept at positive pressure by continuously flowing nitrogen into it. This keeps the samples clean for a short time, long enough to replace the gun. The sputtering system was then reclosed, baked, and the fabrication proceeded as normal.

The result of these changes for one SQUID is presented in Figure 7.16, which is for a SQUID with junctions of area  $.25 \mu\text{m}^2$ , and 1.5 and 2 for the junction aspect ratios. Consider first the initial sweep up in field from 0 to 25 mT. Notice that all of the magnetic behavior occurs at very low field. In fact, the “switch” occurs at around 1 or 2 mT. This is much more in line with our expectations from the Stoner-Wohlfarth calculations earlier in this chapter, and from the small scale GMR switching data from Chapter . Unfortunately, the switch is only a “half switch”, a 90 degree phase shift in the SQUID signal. It then persists in that state up to 25 mT.

Going to negative field, as shown in Figure 7.16b, we see another half switch, but this time it’s a half switch back to its initial state. It also occurs at the same field as the switch to positive field. This suggests that this device is behaving reversibly to positive and negative field, a marked change from the sample presented in Section 7.5. We then see in the other two figures, 7.16c and 7.16d, that when we go positive, and then negative again, we see identically reproducible switching behavior in the sample. This was, in fact, repeated five times for this SQUID device in order to prove that the behavior wouldn’t change due to the magnetic configuration settling down into some stable state.

There are a number of promising signs in this sample that suggest that we have taken a step forward. The first is reduction in the switching field to much lower fields, closer to those anticipated both by calculation and by measurement. This suggests that we’ve finally eliminated some of the troubles plaguing the earlier samples. Also promising is the

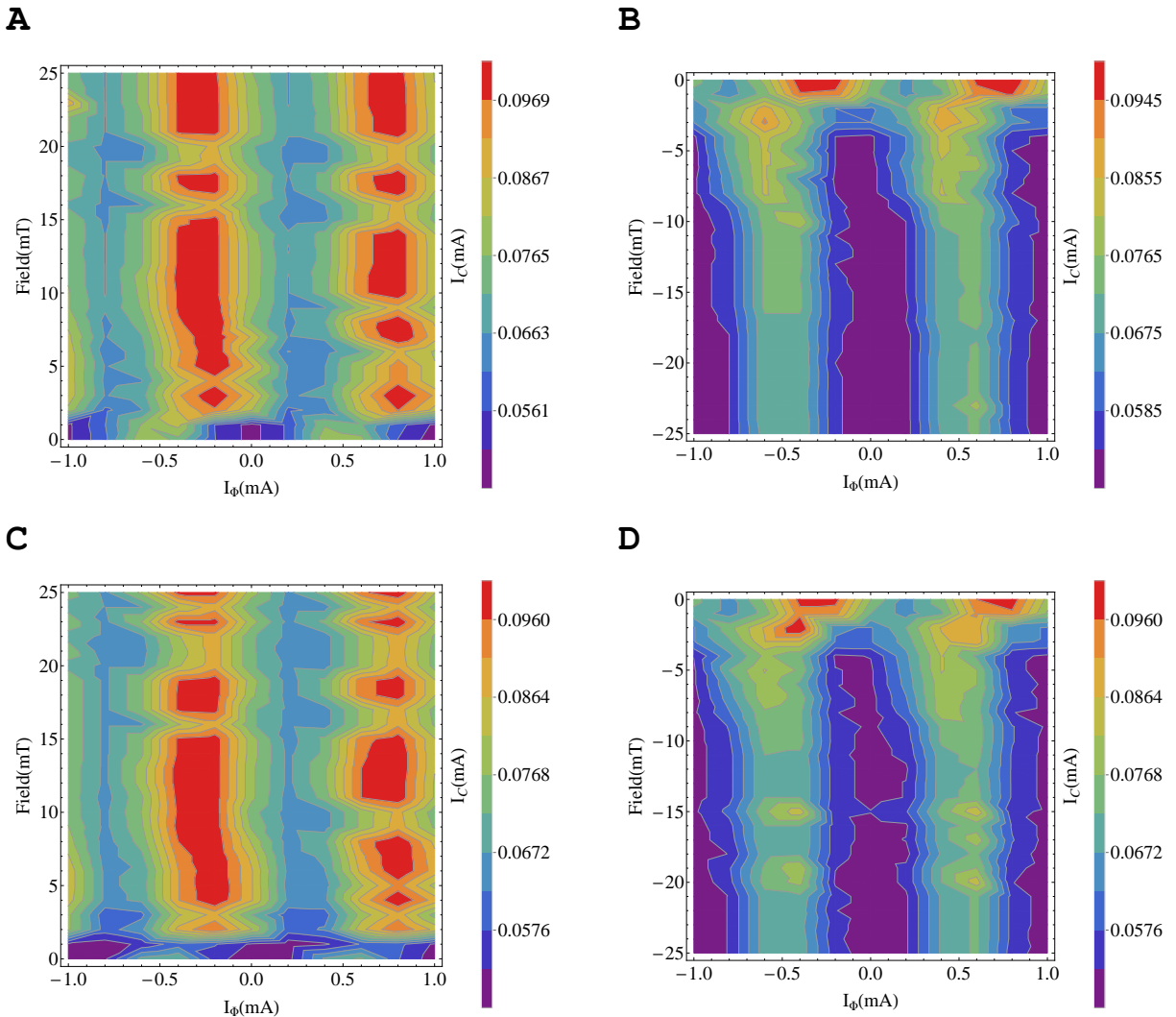


Figure 7.16: Plot of critical current against external field and flux field for a SQUID that has had all 3 ferromagnets patterned. Plots of the left are for positive field, plots on the right are for negative fields. A) The first measurement of the SQUID, which is done to positive field from 0 to 25 mT. The system starts in a state where the two junctions are in opposite states. It then reacts at low field, switching to an intermediate state where it persists to 25 mT. B) The SQUID demonstrates perfect reversibility, switching back from its intermediate state into its original starting state. This switch again occurs at a low field that is roughly equivalent to the switching field in A. C) The positive field is remeasured, demonstrating reproducibility. D) A second measurement of negative field confirms reproducibility.

reproducibility of the sample, both in repetitions of the same field sweeps, but also switching positive to negative. This was an important trait for a device to possess if it was to be eventually developed into applications.

But there are still a couple of concerns. The first is that the sample only seemed to engage in a single switch, and that switch was only a half step. Perhaps both junctions switched together, and one magnetization got stopped halfway. Perhaps one junction's state was frozen, and the other only switched halfway. Unfortunately, it's impossible to say for certain at this time without further studies. At the moment we're simply led to significant questions about the current reliability of these devices.

The other concern is in the starting state of the SQUID. For a reason as yet unknown to us, sometimes our SQUIDS initialize into a state that suggests the two junctions have different phase states. This shouldn't be possible, considering we're magnetizing to a large negative field, and both junctions should end up in the  $\pi$  state, generating a maximum signal at zero flux field. The GMR data in Chapter suggest that perhaps one of the junctions could be switching before we reach zero field, but that doesn't explain why we can't get it to switch back again during the negative sweep. This is a very curious mystery that we simply don't have an answer to at this time.

## 7.8 Conclusion

A large number of changes have been implemented in an attempt to fabricate SQUIDS that work as memory bits. These changes include: reducing the junction size to get closer to single-domain ferromagnets, increasing the copper spacer thickness to 10 nm to reduce magnetic coupling, switching to Co/Ru/Co to eliminate intermediate states, increasing the

PdFe thickness to reduce the switching fields and improve the superconducting properties, milling through all three ferromagnetic layers to constrain the magnetic behavior of the bottom ferromagnetic materials, smoothing the surface of our bottom Nb in order to grow more uniform ferromagnetic films, and switching to a negative E-beam resist to improve the smoothness of our junction edges.

Obviously, some of these changes have been more successful than others. The synthetic anti-ferromagnet was a disappointment, particularly that it overcomplicated the results of the data. Also, the reduction in the junction sizes had mixed success. It was successful in that we got better magnetic behavior, but suffered from the fact that we discovered that we were suppressing the supercurrent sufficiently to make the measurements difficult. This is a serious problem for the use of NbPy, discussed in the previous chapter, which we worry won't pass a measurable supercurrent for the smaller junctions, and is the reason it has not yet been tried.

However, some of the changes appear to have been beneficial to the experiment. The thicker copper layers clearly made a big difference in the GMR samples, and though we don't have direct evidence here, it is hard to believe this was not a positive step. The smoother ferromagnetic layers, and the patterned magnetic layers, seem to have helped a great deal in bringing the switching fields more in line with our expectations. This may also have been helped by increasing the PdFe thickness, which should reduce the switching fields, but we have no way of identifying which detail played the biggest role in the data presented in Section 7.7.

To this point this experiment has not been completed. There are a wide-ranging set of ideas still to try, and the work on this project continues. Seeing the perfect switching data in a SQUID is unfortunately not enough. It is necessary to be able to reproduce it in multiple

SQUIDs across multiple samples. Demonstrating its reproducibility is key to demonstrating convincing control of the systems. However, once the perfect switching data is found, it's simply a matter of study to find the right fabrication conditions to be able to recreate the effect.

Despite being incomplete, there are a number of conclusions that can be reached. The data in Section 7.5 demonstrate conclusively that we have seen the signs of magnetic switching independently in two junctions fabricated into a SQUID geometry. The data conclusively demonstrate signs of a phase change within the SQUID that is at fields lower than where flux trapping is observed. This change must be caused by magnetic switching. We are also confident that this switching is the result of the change in magnetic chirality of the junctions due to an external field. Since this is the only source for a phase change in the spin-triplet junction, the phase shift observed in the SQUID must be a result of the changing magnetic chirality. These statements are particularly promising signs of SQUID control.

We can also go one step further. With the experiment in Section 7.6, we have demonstrated that the critical current in a junction is suppressed when the magnetization changes states. Because we have only observed this effect in samples possessing the in-plane magnetization of the Co/Ru/Co, and not in samples with the perpendicular magnetic anisotropy, it is safe to say that the relative alignment of adjacent ferromagnetic layers does influence whether the triplet is generated or not. This means that we have also demonstrated the feasibility of the on-off control strategy discussed in the introduction to this chapter. This also provides indirect evidence for what we have believed about the generation of the spin-triplet current, that non-collinear magnetizations are required to form spin-triplet supercurrent.

# Chapter 8

## Outlook

### 8.1 Summary of Results

Throughout this work we have continued studies on S/F/S Josephson junctions generating spin-triplet supercurrent. The ultimate goal has been to develop applications for the spin-triplet state, and to create a working device that meets the goals of corporations pursuing magnetic random access memory (MRAM) technology. To that end we have found it necessary to perform a wide range of experiments to improve our understanding of the material properties within our junctions.

While the group had originally discovered the spin-triplet state in the Co/Ru/Co synthetic antiferromagnet (SAF), it was decided that another multilayer might be needed. This decision was based on a number of perceived weaknesses with the SAF. These included: the lack of available guns in the sputtering target, fabrication difficulties, and the need to magnetize it in order to optimize the supercurrent. As a replacement, we studied the Ni/[Co/Ni]<sub>n</sub> multilayer as a new central ferromagnet for generating spin-triplet supercurrent. When properly fabricated, the Co/Ni possesses a strong perpendicular magnetic anisotropy that enabled spin-triplet Josephson junctions to be optimized in the virgin state.

From our studies of the superconducting properties of the Co/Ni multilayer, we discovered that it is particularly effective at generating triplet supercurrent as a central ferromagnet.

$I_c R_N$  products as high as  $6 \mu V$  were seen, as much as 200 times those seen in singlet junctions with the same thickness of Co/Ni. To date, the Co/Ni multilayer possesses the strongest signals seen through S/F/S Josephson junctions in our group. This makes it favorable to the Co/Ru/Co multilayer.

However, it turned out that the advantages we originally expected to gain over the Co/Ru/Co turned out to be largely irrelevant. Therefore, the Co/Ni multilayer has not replaced the Co/Ru/Co multilayer as planned. That said, the multilayer has instead provided a high quality second option for triplet generation. This has been advantageous for work in other experiments in the group, most recently the triplet density of states experiment, where a strong signal strength was deemed valuable. It is also possible that someday this multilayer could be used as one of the outer ferromagnets in an S/F'/F/F''/S Josephson junction, but no such work is yet planned.

Also necessary to the development of functional devices was a thorough characterization of the soft ferromagnetic materials we could choose for a switching layer. We first utilized Electron Dispersive Spectroscopy to quantify the atomic concentrations of the alloyed materials we were sputtering. This was done to confirm that we were achieving atomic percentages of ferromagnetic elements that were in line with the quantities used in previous works, both by us and by other groups. We also performed magnetic studies on bulk films to verify their ferromagnetic properties.

Of critical importance to the future experiments were the magnetic and superconducting properties of these films when they were patterned into Josephson junctions. By fabricating spin-triplet generating junctions with different thicknesses of these materials, the conduction of supercurrent was studied. A plot of the peak of the resulting Fraunhofer curves versus the thickness typically provides a peak  $I_c$  at a specific thickness. By looking for this peak

for the various materials, we were able to optimize the material thickness to guarantee our future junctions would generate the maximum possible supercurrent.

To study the magnetic switching properties required us to create single exchange-biased spin-valves on both the large and small scales in order to study the Giant Magnetoresistance of our materials. The large scale samples were fabricated and tested in order to measure the GMR signal generated with these soft ferromagnetic materials. A soft ferromagnetic material that demonstrated no GMR signal would be problematic for use in further GMR studies, so it was important to verify the GMR generation of all of our soft ferromagnets.

If a GMR signal was observed in large scale samples, we were then able to pattern small elliptical pillars to test the switching characteristics. These samples allowed us to measure how those switching fields varied with the thickness of the soft ferromagnet, and how they varied with the aspect ratio of the elliptical pillars. This also gave us a rough glimpse at the formation of domains within our materials, enabling us to know if the pillar size is sufficiently small to force the material to be in a single domain state. To date, none of the sizes have been small enough to force the magnets into a single domain.

Putting all of this into actual devices was the primary thrust of the experiments discussed here. The goal was to build a device that possessed multiple states, and could be readily switched between those states through some controllable means. While we haven't yet fully achieved a controllable device to the standards necessary to call this an unqualified success, we can say that we have seen enough to claim a proof of concept. There is no question that these devices can be made to work, it's just a matter of finding the right material combinations.

We have fashioned Superconducting Quantum Interference Devices (SQUIDs) containing a pair of Josephson junctions capable of generating spin-triplet supercurrent. The Josephson

junctions are comprised of two superconducting layers, between which are three ferromagnetic materials: two hard, and one soft. The magnetizations of the layers are all arranged so that they are orthogonal to the magnets adjacent to them. We have experimentally demonstrated that by applying a magnetic field to the junctions, we can switch the state of the junction through the use of an external field. This was observed in the current-voltage characteristics of the SQUID, which change depending upon the state of each pillar.

The state of the pillars is governed by the magnetic chirality of the ferromagnetic layers. When the magnetic chirality between the layers changes, the current picks up a phase related to the angle between the bottom and top ferromagnets in the junction. The SQUID causes the two currents to interfere, whether constructively or destructively, which gives an output current. That interference can then be modulated by applying a magnetic flux through the SQUID loop. By observing this phase change in our SQUID devices, we have successfully measured the phase change in a Josephson junction through the change in magnetic chirality. This was one of the primary predictions on which the entire experiment was based.

Finally, we studied SQUID junctions containing Co/Ru/Co as the central antiferromagnet. These junctions were expected to carry no triplet supercurrent when the top ferromagnet became aligned with the central ferromagnet. This is because of the requirement of non-collinear magnetizations for the generation of the spin-triplet state. The expectation is that this would lead to a suppression in the SQUID modulations as the soft ferromagnet of one of the junctions switched. We observed that suppression in these systems, providing indirect evidence of one of the significant predictions, within a single sample, of the original theoretical works by Bergeret *et al.* on spin-triplet junctions.

## 8.2 Future Work

Despite the successes in our measurements, there is still a plethora of work to be done in developing these devices. At the most basic level, everything can be boiled down to one root concept: *make one of these things work*. To make that happen, we have to understand better how and why these SQUIDs are behaving as they are. We also need to consider other strategies and materials that may improve the behavior of the devices, or improve our ability to conceptualize what is happening within the devices.

A wide range of questions have arisen during the course of our experiments. One of the most significant is how exactly these ferromagnetic layers are switching. While we know that the phase change observed in the SQUIDs is the result of a change in magnetic chirality, what we don't necessarily know is which layer has changed. Part of the point of patterning all three ferromagnetic layers in our more recent experiments was to reduce the possibility that we were seeing domain motion in the bottom two ferromagnets rather than in the top ferromagnet.

Further study of the switching characteristics of our soft ferromagnets will help answer some of these questions. Additional Giant Magnetoresistance (GMR) studies will provide better statistics of the switching fields required for a soft ferromagnetic layer. Specifically, we could find how the switching fields vary with the thickness of the material, and how the switching fields vary by changing the aspect ratio. Knowing these would provide future SQUID work with a solid baseline not only for deciding what thicknesses and aspect ratios to work with, but also for knowing what fields ranges to expect to see switching behavior.

Also important for the GMR work would be in the hunt for the domain size of the soft ferromagnetic materials. Roughly speaking, the domain size for a given ferromagnet is the

largest size of pillar that can be fabricated and still generate a single domain signature. The signature would be a sharp change in the resistance of the GMR pillars with changing field. Any rounding in the hysteresis curves would be a result of domain motion, and a signal that the pillars are too large. Since the current strategy of SQUID control requires single-domain coherent switching, it would be useful to know beforehand what the maximum pillar area that is single-domain, and if enough supercurrent can be passed through such a pillar to be observable at our operating temperature of 4.2 K.

The limiting factor for the size of our pillars is when the Josephson energy, Equation 2.26, is on the order of the thermal energy  $k_B T$ . The critical current can be estimated from the  $I_c R_N$  product of a particular multilayer stack, since the product is independent of the size of the junction. If we consider the maximum  $I_c R_N$  from NbPy from Chapter , which is 55 nV, and the known normal state resistance of a 10  $\mu\text{m}$  pillar, which is 100  $\mu\Omega$ , we can estimate the critical current in a 100 nm junction. The resistance of the junction follows an inverse ratio of areas to resistances,

$$\frac{\pi(10\mu m)^2}{\pi(100nm)^2} = \frac{R}{100\mu m} \quad (8.1)$$

as the product of area and resistance should be identical for a given multilayer stack, regardless of the size of the pillar. This gives an estimate of 1  $\Omega$  for the resistance of the junction. Knowing this, the critical current in the junction can be calculated,

$$I_c = \frac{I_c R_N}{R} = \frac{55nV}{1\Omega} = 55nA \quad (8.2)$$

We can then calculate the Josephson energy for this device,

$$E_J = \frac{\hbar I_c}{2e} = 1.813 \times 10^{-23} J \quad (8.3)$$

The thermal energy at 4.2 K is  $5.8 \times 10^{-23} J$ . This junction would be sufficiently small that thermal broadening would wash out any supercurrent in the junction. We must either use a material other than NbPy, one with a larger  $I_c$  product, or perform experiments that do not require such small junction sizes.

Both of the GMR studies mentioned will be worked on in a variety of soft ferromagnetic materials. Those that are found to be capable of supporting supercurrent at single-domain sizes will be fabricated into the SQUID devices. They will then be measured as discussed in Chapter . If they are found to work, the next step would be to develop an array of these devices with on-chip field lines to apply the switching fields. We would then test the devices in a *fast switching* environment using microwave signals. This would be a necessary benchmark test to decide if the devices could function as commercial memory bits.

Another option that is being considered for this experiment is to avoid the difficulties associated with single domain switching altogether. One way to solve the problem is by using a sample cell geometry with an on-chip field line. The geometry of the cell is then designed so that the field switches only a single magnetic moment on the chip, and none of the others. This could be done by developing a SQUID loop where one of the two pillars in the SQUID lies above a field line. When a current is passed down the line, the field generated will switch the pillar back and forth. The other pillar in the SQUID would be out away from the line in a place where the generated field would point perpendicular to its favored axis. This would allow for switching in one of the magnetic bits without causing switching in the other, and

would eliminate the need for single-domain magnetization in this experiment.

Lastly, we are beginning to perform experiments similar to the ones in this thesis, but on spin singlet Josephson junctions. These devices, called *Spin Toggle* devices [85, 86], make use of a synthetic antiferromagnet to improve the switching characteristics of a memory bit. Instead of having a very narrow writing window for the applied fields, the SAFs allow for substantial more leeway in the writing. The changes in the state are controlled by magnetic switching, but are made possible by very careful control of the thickness of the ferromagnetic materials. It is important to note that this method still requires the use of single-domain nanomagnets in the synthetic antiferromagnet.

After decades of only narrow interest, superconducting devices containing ferromagnetic materials are starting to pick up steam as an exciting branch of studies. The ability to enhance the critical current in S/F/S Josephson junctions by adding more ferromagnetic layers is a rare example of Nature giving us a helping hand. With the fact that ferromagnetic materials possess states that are easy to change, this provides an easy control mechanism that is drawing a large amount of attention. The applications of such junctions for superconducting memory devices will drive interest in this field for some time to come.

# APPENDIX

# Magnetic Oscillations in Semi-Metals

This appendix covers experiments that were performed at MSU and at the National High Magnetic Field Laboratory in Tallahassee, Florida from August 2010 through August 2011. Because these experiments were only preliminary, the data is not sufficiently thorough or polished for publication in a more public journal. However, it is still data, and therefore it still deserves a place somewhere in the published works. Thus, our decision to drop it at the tail end of the thesis.

The measurements were performed on bulk and thin film samples of a class of semi-metals. These samples are suspected to be *topological insulators* (TIs), materials who possess a bulk insulating state, but a 2-dimensional surface conducting state that is topologically protected. This is a particularly active field of study, generating wide interest in transport, scanning probe, and materials studies.

The most exciting aspect of these materials is the potential physics arising through their interactions with superconductors or ferromagnets. The eventual intention was to combine TIs with these materials and study the effects. Some options included: forming an S/TI/S Josephson junction, where S was a superconductor like Nb or Al [87], grow a ferromagnetic insulator on the surface and look for the “topological magnetoelectric effect” predicted by Zhang *et al.* [88], perform control experiments on the TI surface by changing the magne-

tization of one or more ferromagnetic insulators [89, 90], and combine both ferromagnetic insulators and superconductors to produce and detect the Majorana fermion - a particle that is its own anti-particle [91, 92].

Of course, to get to these goals, we needed to start by performing transport studies of the topological insulators. The exciting studies mentioned above are pointless unless you can first confirm that you can grow a TI to begin with. Therefore, it was important to start by measuring low-temperature transport, quantum transport effects, and high-field magnetotransport. The signature for a TI would appear most readily in the high-field magnetotransport studies, and we will discuss in Section why this is. At this point, we will not delve any further into the details of topological insulators, as they are not critical to the remainder of the chapter.

The first section will discuss the formation of Landau levels due to the application of a magnetic field. Section covers the physics behind the Shubnikov-de Haas Oscillations. Section gives the form of the frequency of the oscillations. Sections and present the results of our measurements. Section concludes the discussion and presents possible future directions for the research.

## Landau Levels

The origins of magnetic oscillations are particularly easy to understand, and can even be described semi-classically in a way that is at least satisfactory on an elementary level [93]. This is the treatment that will be taken here, both in the two-dimensional and three-dimensional cases. While the cases are not particularly different, conceptualizing them is not necessarily straight forward. We will begin with the simplest case of a two dimensional electron gas

(2DEG).

Consider a single electron with velocity  $v$  moving in a uniform magnetic field  $B$ . Classical Electrodynamics tells us that the electron experiences a force proportional to the cross product of the velocity and field,

$$F_l = e(v \times B) \quad (\text{A.1})$$

where  $e$  is the fundamental charge. This force, which is part of the Lorentz Force Law, causes the path to be circular with centripetal force,

$$F_c = \frac{mv^2}{r} \quad (\text{A.2})$$

Equating A.1 and A.2 gives the radius as,

$$r = \frac{mv}{eB} \quad (\text{A.3})$$

With the *cyclotron frequency* defined as  $\omega_c = eB/m$ , this can be rewritten more simply as,

$$r = \frac{v}{\omega_c} \quad (\text{A.4})$$

This describes a continuum of possible states for the electron to reside in, since it can possess any velocity. However, we know the electron is quantum mechanical in nature, and that therefore the circumference of the circles defined by the electron must be integer multiples of the electron wavelength,

$$\lambda_e = h/p \quad (\text{A.5})$$

where  $h$  is Planck's constant, and  $p$  is the particle momentum  $mv$ . Therefore, the circumference must be,

$$2\pi r = \frac{nh}{mv} \quad (\text{A.6})$$

Substituting Equation A.4 into A.6 and rearranging gives us,

$$mv^2/2 = n\hbar\omega_c/2 \quad (\text{A.7})$$

This implies that the kinetic energy of the electrons is quantized, being forced into integer values of  $\hbar\omega_c/2$ . Therefore, the energy of the electronic states are,

$$E_n = E_s + n(\hbar\omega_c/2) \quad (\text{A.8})$$

where  $E_s$  is the lowest energy of the conduction band. This result is not strictly correct, but it does at least provide an accessible picture into the physics involved.

When a magnetic field is applied to a material, the electrons will coalesce into discrete states separated by energies of  $\hbar\omega_c$ . The quantum mechanically correct treatment of this provides the result,

$$E_n - E_s = (n + 1/2)\hbar\omega_c \quad (\text{A.9})$$

which looks identical to the harmonic oscillator energies. The energy levels  $E_n$  are called *Landau levels*, and are magnetic subbands that form within the density of states. In fact, in the case of no scattering processes at all, the density of states within the material evolves from a continuum of states into a series of delta functions with a center-to-center distance

of  $\hbar\omega_c$ .

$$N_s \approx N_0 \sum_{n=0}^{\infty} \delta \left[ E - E_s - \left( n + \frac{1}{2} \right) \hbar\omega_c \right] \quad (\text{A.10})$$

The effect of scattering processes is to smear out these delta functions in energy into gaussian peaks. Eventually the smearing becomes severe enough to wash out the appearance of the Landau levels, which is why these are observable only at low temperatures.

## Shubnikov-de Haas Oscillations

Oscillations can occur in a variety of different measurable quantities in metals when magnetic fields are applied. When the oscillations are observed in the longitudinal resistivity of the

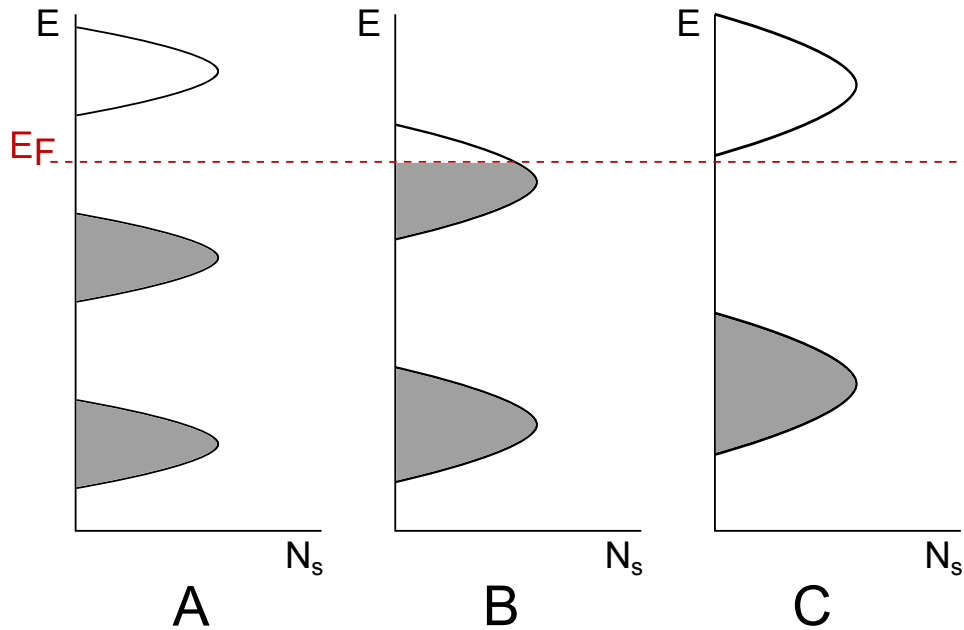


Figure A.1: *The behavior of Landau levels as the magnetic field is increased. A) Initially, the Fermi energy  $E_F$  lies between two Landau levels. All the levels below the Fermi energy are completely filled (colored gray), and all levels above the Fermi energy are empty. B) A Landau level passes through the Fermi energy. It is now partially filled. C) The level has completely passed through the Fermi energy and is now totally depleted of electrons. Note that the states have grown in size, this is to account for the electrons that were forced out of the higher Landau level.*

material, they are referred to as “Shubnikov-de Haas” (SdH) Oscillations. These oscillations were originally observed in bulk materials in the 1930s, and have since been seen in two dimensional electron gases, such as in the Quantum Hall Effect experiments [94]. How these arise are directly related to the Landau Levels discussed in the previous section.

Consider what happens to the Landau levels as the magnetic field is increased. Because  $B$  is increasing, this implies that  $\omega_c$  is increasing as well. This means that the spacing in field between the Landau levels grows. However, the Fermi energy, the energy level to which states are occupied by electrons, does not change with increasing field. This means that eventually a Landau level will pass through the Fermi energy, changing the filling of that level until it is completely empty. This is shown schematically in Figure A.1.

The states at the heart of each Landau level are “extended” states, or states available to conduct current ballistically. All other states are “localized” states, which are incapable of conducting current. When the Fermi energy lies between two Landau levels, the transverse resistivity passes through a plateau, while the longitudinal resistivity sees a minimum. This is because the states whose occupation is changing are entirely localized states. Therefore they do not contribute to conduction through the sample.

However, when the Fermi energy lies inside the Landau level itself, the occupation of states that contribute to conduction change. This leads to an increase in the longitudinal resistivity, and to a similar increase in the transverse resistivity with field. This change in resistance is a result of there being empty states available for electrons to scatter into. These empty states were made available as the occupation changed with the passing of the Fermi energy. Once the Fermi energy is again between two adjacent Landau levels, there are no longer states available to scatter in to, and the longitudinal resistivity will again drop to a minimum.

## Frequency

Now let us consider what happens when the Fermi surface is 3-dimensional. In the simplest case, the Fermi surface is a sphere in  $k$ -space. Under the influence of a magnetic field, the sphere will break into a series of concentric cylindrical “tubes”. Each tube is the analog of a Landau level extended in height along the field direction. These are typically referred to as “Landau tubes”.

The frequency of SdH oscillations follows the form [95],

$$F = \left( \frac{c\hbar}{2\pi e} \right) A \quad (\text{A.11})$$

where  $A$  is the “extremal” area of the Fermi surface. This means the largest, or smallest, cross section of the Fermi surface bisected by planes normal to the applied field  $H$ . Because of this fact, it is possible to determine the shape of the Fermi surface by the behavior of the frequency. By changing the angle of the sample within the field, in other words changing the orientation of the Fermi surface to the applied field, the entire extremal area of the surface can be observed.

For a sphere, the extremal area is identical in all directions, meaning that the frequency of the oscillations will not change at all with angle. However, an elliptical Fermi surface, for example, would show variations in frequency as the angle changes. This becomes even more apparent with a 2-dimensional surface, because the extremal area varies as  $1/\cos\theta$ , with  $\theta$  the angle between the normal to the Fermi surface and the field direction.

This provides a mechanism for measuring the shape of the Fermi surface. By measuring the resistivity as a function of field for various angles, the changes in the SdH frequency can be observed. Then, by plotting the frequency changes against angle, the shape of the Fermi

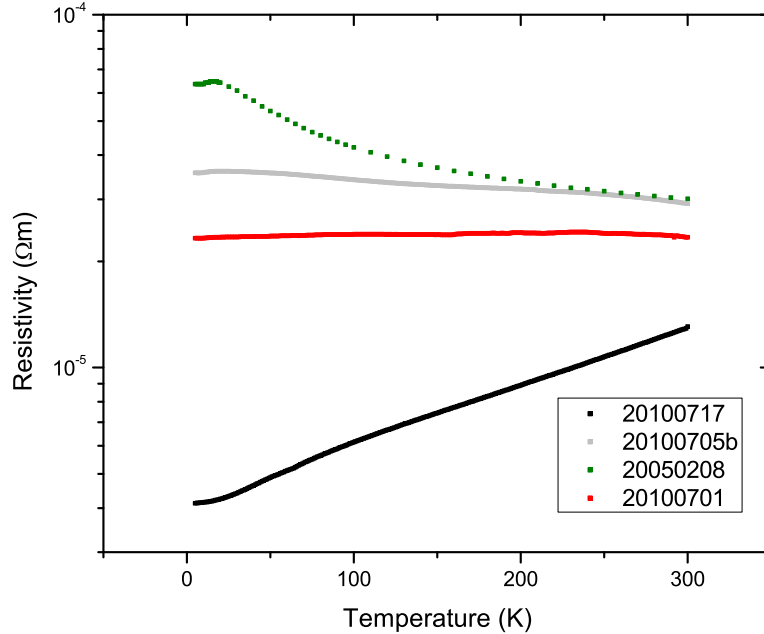


Figure A.2: *Resistivities of samples fabricated by Ctirad Uher's group at the University of Michigan.* Sample 20100717 is the only sample with a resistivity that clearly drops with decreasing temperature, making it the only metallic sample. 20050208 is clearly insulating. The other two show very little change with temperature, but are likely also insulating.

surface can be gleaned by the behavior of the SdH oscillations.

## First Results

Our first attempts to measure these oscillations were performed on thin film samples of  $\text{Sb}_2\text{Te}_3$ , and were performed at Michigan State University. The measurements were performed in an Oxford He3 Dilution Refrigerator with an American Magnetics 9 Tesla superconducting magnet. At the time of the experiments, the dilution refrigerator was not operating at peak condition and was therefore only able to reach a temperature of 300 mK rather than its designed 50 mK. This was not a critical problem considering these measurements were intended to be preliminary in nature, but they did limit some of what we had hoped to do early on.

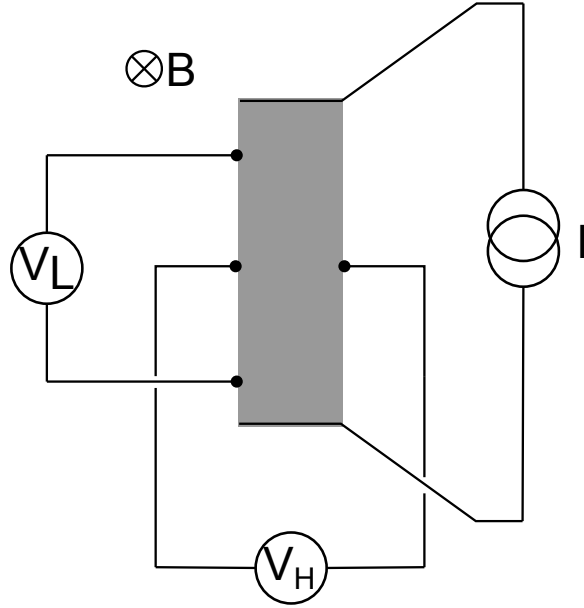


Figure A.3: *Geometry of the hall bar measurements of our semi-metal materials.* Positive  $B$  is defined into the page (the sample sits upside-down in the dilution refrigerator).  $I$  is the current driven across the sample,  $V_L$  is the longitudinal voltage, and  $V_H$  is the Hall, or transverse, voltage.

The  $\text{Sb}_2\text{Te}_3$  samples were grown on corundum substrates by Ctirad Uher's group at the University of Michigan. The samples exhibited a spread in conductive properties, from metallic to insulating. Figure A.2 plots the sample resistivities as a function of temperature. If the resistivity rises with decreasing temperature, it is an insulating sample as fewer electrons have been excited into conducting states. If the resistivity drops with decreasing temperature then the sample is metallic, as the conduction electrons experience fewer thermal scattering events.

The samples, which possess a roughly rectangular shape, were mounted in a hall-probe geometry as shown in Figure A.3. Early on, the leads were mounted with Indium. Because Indium superconducts below 3.2K, care was taken to make certain that the leads were properly mounted using silver paint, which does not superconduct in the temperature regimes we were interested in. The current leads at each end were held in place such that they made

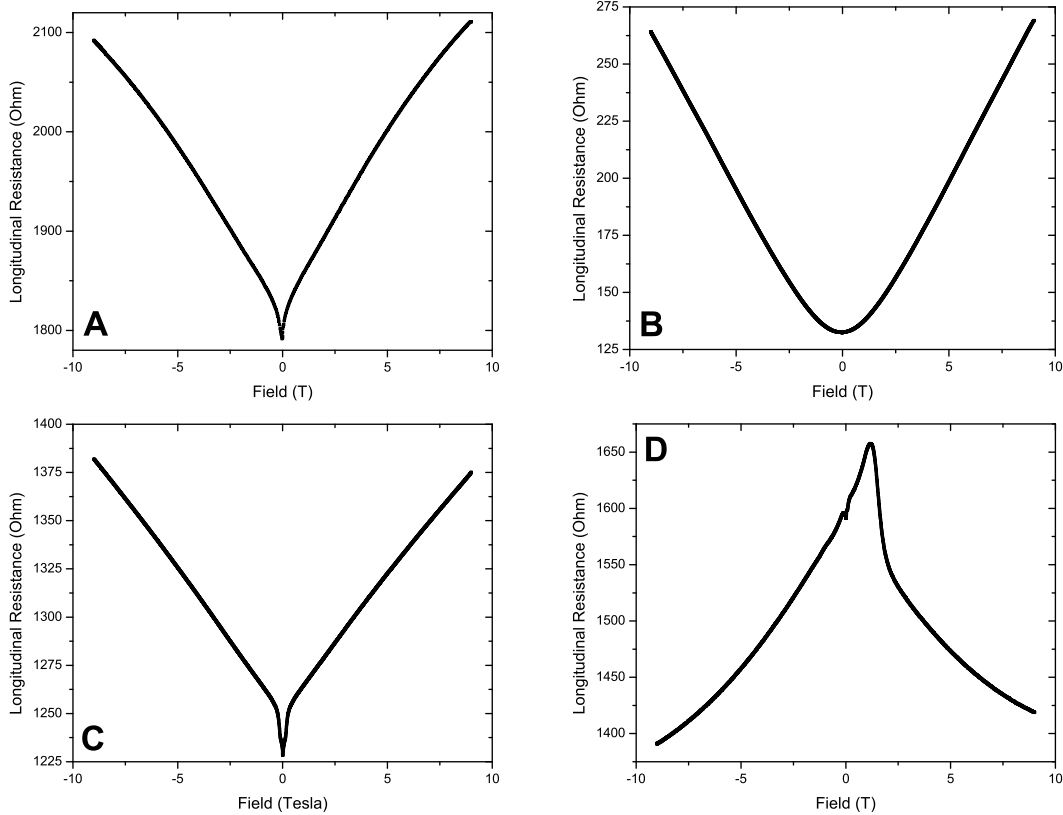


Figure A.4: *Longitudinal Resistances for thin film  $Sb_2Te_3$  samples.* A) Sample 20100705b, which clearly displays an insulating behavior. B) Sample 20100717, which is metallic. C) Sample 20100701, which is insulating. D) Sample 20050208, which is insulating, but unusually inverted.

contact along the entire short edge of the sample. This ensured roughly uniform current flow across the entire sample. The four voltage leads were mounted so as to be symmetric across the sample, specifically that leads across the short dimension of the sample were mounted as close to opposite each other as possible. This minimized the quantity of longitudinal signal picked up by the hall voltage measurement. It was also important to keep the spot size as small as possible in order to improve the accuracy of the measurement.

Figure A.4 presents the longitudinal resistance as a function of field. Each plot was measured at 300 mK, and swept in field from -9 T to 9 T. Three of the samples exhibit a sharp discontinuity at zero field, which has been observed in topological insulator samples

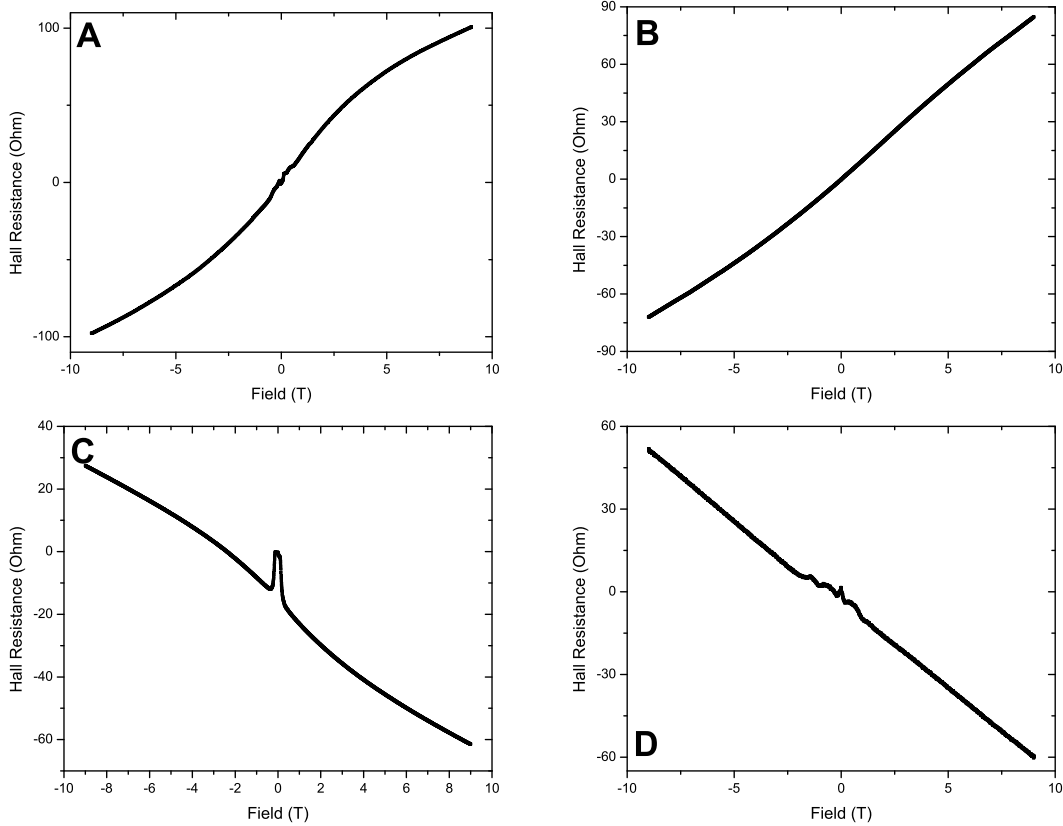


Figure A.5: *Hall Resistances for thin film  $Sb_2Te_3$  samples.* A) Sample 20100705b, which is p-type. B) Sample 20100717, which is p-type. C) Sample 20100701, which is n-type. The feature at zero field is particularly strong, but was suspected to be a result of the Meissner effect in the indium contacts. D) Sample 20050208, which is n-type.

[96, 97]. It was suspected that this had to do with weak antilocalization [97], but the amplitude of the signal observed in our data is much larger than might be expected, which may suggest something else is at work. However, recent thinking suggests that the Berry phase associated with the Topological Insulator state produces a quantum correction that exactly matches the characteristics of weak antilocalization [98, 99, 100, 101]. The only sample that does not show the sharp feature is the metallic sample, and therefore would not display characteristics of topological insulators. The inverted signal in the sample presented in Figure A.4d is particularly unusual, and was never explained.

After measuring the longitudinal resistance, the hall resistance was measured across the

sample as shown in Figure A.5. The signal was expected to have zero resistance at zero field, any non-zero signal would be a result of an imbalance in the position of the leads on the sample. A ratio transformer was used to subtract out the component of the longitudinal signal present in the transverse signal during the measurement. This ensured that the data taken was purely the transverse signal, and no rebalancing of the data was required during the analysis.

The Hall resistance will take a sign related to the sign of the field direction. This is a result of the behavior of the charge carriers within the sample. If the field changes direction, the direction the sign carriers move will change direction because the direction of the Lorentz force has changed. The voltage across the sample is related to the quantity of charges along each side, and to their relative sign. The hall voltage should be a quantity linearly proportional to the field, but in our case there is a non-linear behavior. This is possibly a result of the existence of multiple conduction bands within the sample.

The total quantity of charge carriers can be calculated from the measured hall voltage. If the sample has a width  $w$  and thickness  $t$ , the Hall Coefficient is defined as,

$$R_H = \frac{E_y}{J_x B} \quad (\text{A.12})$$

where  $E_y$  is  $V_y/w$ , and  $J_x$  is  $I_x/(tw)$ . We can rewrite the hall coefficient as,

$$R_H = \frac{R_{xy}t}{B} \quad (\text{A.13})$$

Sample	Doping Type	Carrier Density (1/cm <sup>3</sup> )
20100705b	p	4.738 E18
20100717	p	1.032 E19
20100701	n	1.017 E19
20050208	n	7.88 E18

Table A.1: *List of thin film Sb<sub>2</sub>Te<sub>3</sub> sample properties.* The sample names are the year, month, and day that the film was grown. The doping is realized from the slope of the hall voltage when compared to the polarity of the voltage and current leads on the sample. The carrier density is calculated from A.14.

where  $R_{xy}$  is  $V_y/I_x$ . We can write this as,

$$R_H = \frac{R_{xy}t}{B} = \frac{1}{ne} \quad (\text{A.14})$$

with  $n$  the carrier density and  $e$  is the fundamental charge. Therefore, if we know the thickness of the sample, we can calculate the carrier density from the Hall resistance data.

The results for all four samples are presented in Table .

The wiggles at low field are a result of the use of indium pads in a couple of the samples. The silver paint, while a better method of mounting, had not been used by the University of Michigan for their tests. The leads that were already present, which were mounted with indium, were frequently used in the early measurements. The wiggles themselves are a result of the Meissner effect in the indium, which superconducts under 3 Kelvin. It appears from the data that the critical field for the indium was around 1 Tesla. Therefore, it was important to make certain that no calculations were based on the data below 1 T in field.

Both the longitudinal and hall voltages are particularly smooth. To bring out possible oscillations, it is handy to take a derivative of the voltage (or resistance) with respect to field. The derivative will enhance the size of any oscillations within the data. It will also remove the linear background of the hall voltage so that the data can be expanded to search

for any oscillations that may be present. An example of this is shown in Figure A.6

As it turns out, the only sample that demonstrates any oscillations at all is the metallic sample. This is likely because the mean free path within the sample is much longer than in the insulating samples. If the mean free path is too short, the momentum scattering spreads out the Landau levels too much for the formation of discrete states. It was suspected at the time that a higher field strength could bring out oscillations within the insulating samples, but that was not possible on the system at Michigan State.

## NHMFL Results

This preliminary data was sufficient to generate interest in further studies of the thin film samples. In order to perform a proper measurement, a larger magnetic field was desirable in order to attempt to beat the mean free path problems suspected from the MSU data. The

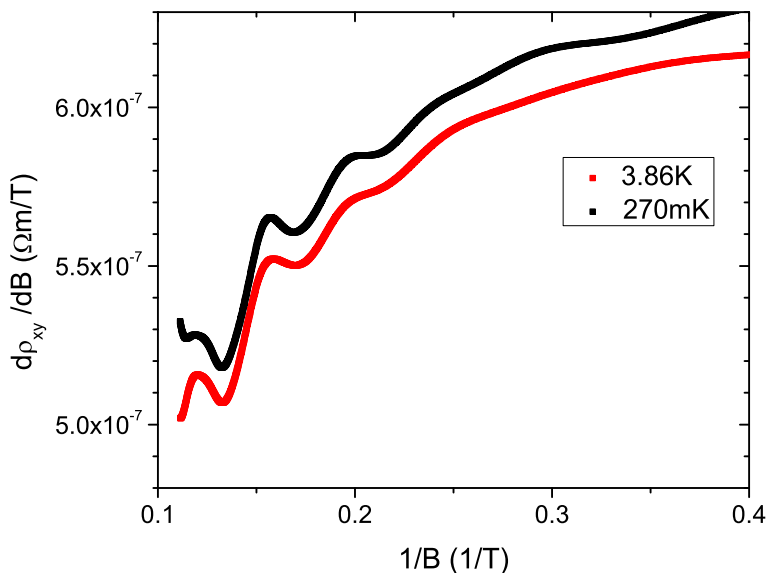


Figure A.6: *Plot of the derivative of Resistivity with respect to field against inverse field for sample 20100717. The data was taken at two temperatures to see the behavior of the oscillations. Note that the oscillations reproduce perfectly at both temperatures, but that the amplitude of the oscillations at 4K are smaller than at 300mK. This is solid evidence that these are SdH oscillations.*

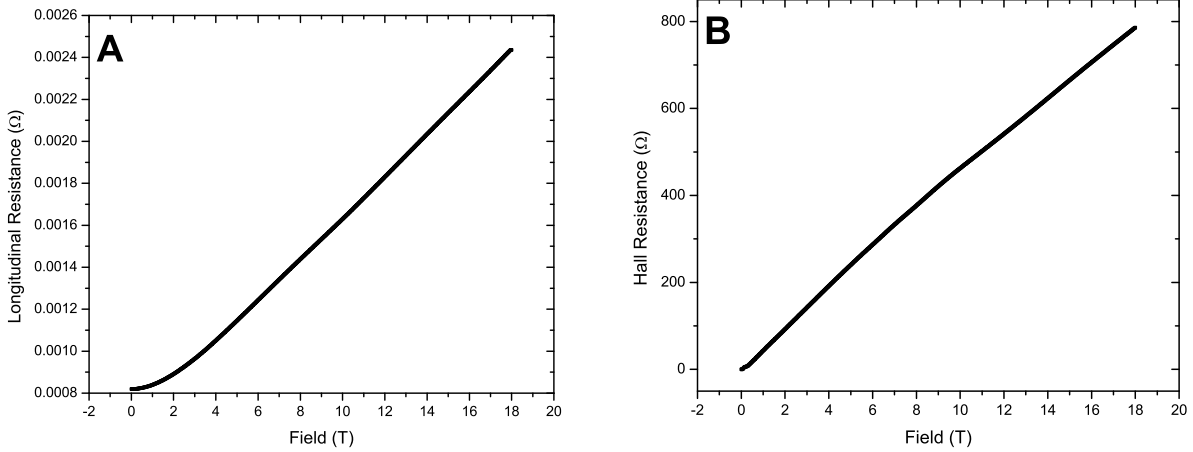


Figure A.7: *Raw data from sample 20100717 taken at the National High Magnetic Field Laboratory.* A) Longitudinal resistance. Note the rounded behavior near zero field, suggesting a metallic sample. B) Hall resistance.

setup at the NHMFL also included a motorized, computer controlled system for rotating the sample in the field while cold - something that could not be done at MSU. Being able to measure the angular dependence of the Fermi surface of the samples was a huge step forward for our analysis of the experiment.

The results from MSU were also sufficient to drive interest in measuring a batch of bulk samples, which were also obtained from Ctirad Uher's group. There were four samples provided, one  $\text{Sb}_2\text{Te}_3$ , two  $\text{Bi}_2\text{Se}_3$ , and one  $\text{Bi}_2\text{Te}_3$ . All of these materials are of the same general class, and all are expected to potentially possess properties of topological insulators. This was an excellent opportunity to demonstrate the collaboration's ability to fabricate and test these materials, as well as a chance to practice the types of measurements that would be regularly required by the experiment.

Of the thin film samples, despite the higher field, only the metallic sample demonstrated any sort of oscillations. The oscillations remained too small to see in the raw data, and so the derivative was required to bring them out, exactly as before. Measurements were

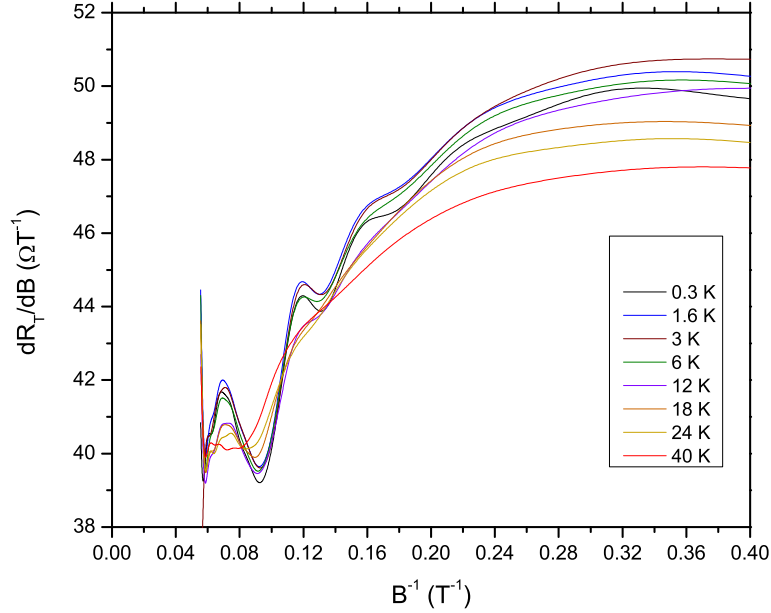


Figure A.8: *Plot of the Temperature dependence of hall resistance plotted against inverse field for sample 20100717. The oscillations clearly decay with increasing temperature, and appear to have completely vanished by 40K.*

performed at a variety of angles between 0 and 90 degrees, and at several temperatures from 300 mK as high as 40 K. By examining the height of the oscillation peaks at varying angles and varying temperatures it is possible to learn several different important quantities. These include: the effective mass of the carriers, the relative shape of the Fermi surface, and the “Dingle Temperature”, or an effective temperature experienced by the carriers due to scattering events with impurities.

The plots in Figure A.7 show the raw resistance data in the Transverse and Longitudinal directions, demonstrating the metallic behavior of the sample. By taking the derivative of the Transverse data for varying temperatures, Figure A.8 emerges, which demonstrates the decay of the oscillation peaks with temperature. This is an extension of the work shown in Figure A.6 and demonstrates most conclusively that these oscillations are strongly temperature dependent.

The plan had been to use the highest temperature, where the oscillations should have

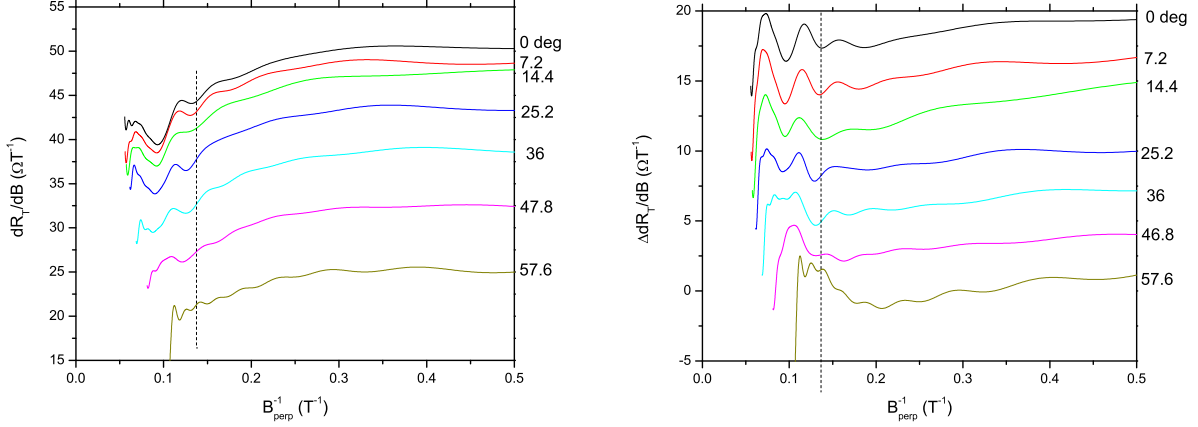


Figure A.9: *Angular dependence measurements for sample 20100717.* A) The base data before background subtraction. B) After subtracting a background curve calculated using a 200 point FFT filter. Note the artifact at the end of data, which is a result of the filtering process. The dashed line is a guide to the eye for the valley at  $0.14 T^{-1}$  in the  $\theta = 0^\circ$  curve.

been completely washed out by thermal effects, to subtract out any background signal in the data. This would then give us a flat background on which to perform fitting, and, more importantly, a zero baseline for measuring the relative peak heights of the oscillations. Unfortunately, as can be seen in Figure A.8, the highest temperature curve does not follow precisely the same background curve as the other temperatures. This is an unfortunate problem that increased the difficulty of analyzing the data. To overcome it, a 200 point Fast Fourier Transform filter was applied to each set of temperature data in the hopes of flattening out the SdH oscillations completely, and leaving the general shape of the smooth background behind. This was then used to subtract off the background signal. The results of this can be seen in Figures A.9a and A.9b, which demonstrate the Transverse derivative of the measurements at different angles. The data has been artificially spaced out in resistance for clarity. Using the 200 point FFT creates a large artifact at the high field end of the data, an unfortunate, and unavoidable, side-effect of the process.

The plots in Figure A.9 are important for another reason. The dashed line provides a

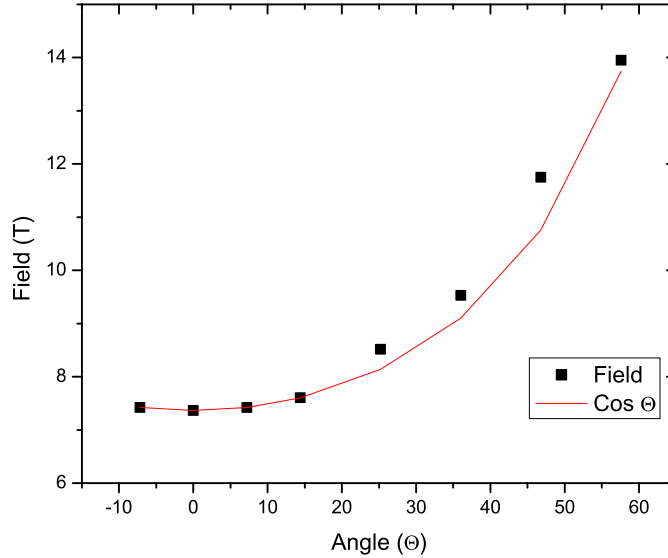


Figure A.10: *Analysis of the angular dependence of the amplitude of a peak in the oscillations of sample 20100717.* The red curve is not a fit to the data, but demonstrates the form of  $1/\cos\theta$ , which is the dependence of the behavior of a two-dimensional Fermi surface on angle.

guide to the eye for the minimum of the oscillation at zero degrees of angle between the magnetic field and the normal of the sample. It is clear that the minimum does not move for the first three angles, and then slides to the left slightly before becoming hard to discern. Figure A.10 plots the angle of the measurement against the field of the minimum of the oscillation. The red curve plots  $1/\cos\theta$ , which is the behavior of a two dimensional Fermi surface with angle. These data points seem to follow that curve, but increase more steeply with angle. As it turns out from an analysis of the angular dependence of the Fermi surface, no Fermi surface can climb more steeply than  $1/\cos\theta$  [95].

The reason why our data seems to climb more steeply is very likely an artifact of the uncertainty in measuring the angle with the field. The data here used the angle set by, and recorded by, the computer in driving the motors. Because this is a mechanical system, there is likely some “slop” in the motion of the motors, creating a large uncertainty in the actual angle to the measured one. One way to overcome this would have been to place a simple

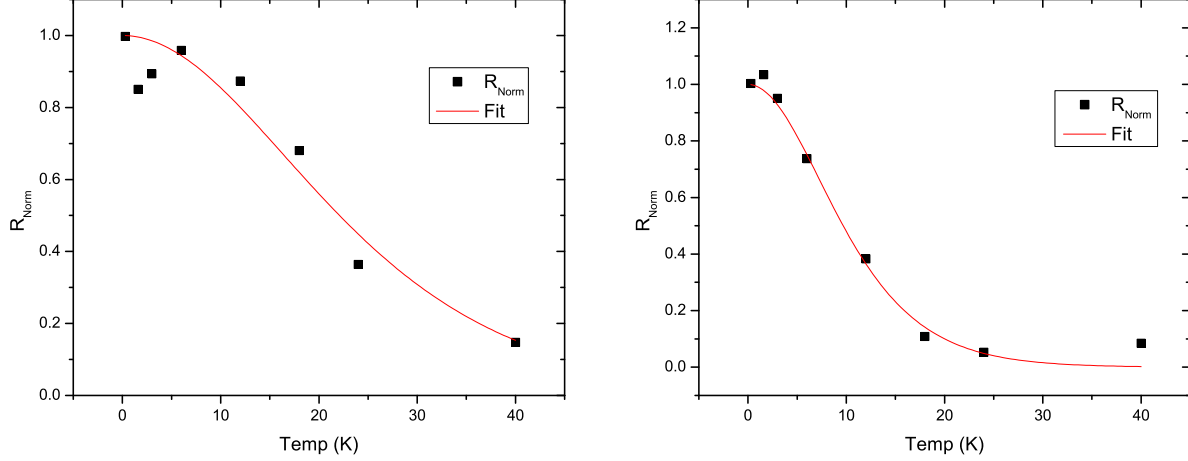


Figure A.11: *Determination of effective mass of carriers in sample 201007177.* A) Determination of the mass for the peak at  $0.08 \text{ T}^{-1}$ . The result of the fit suggests a mass of 7.85 percent of the electron mass. B) Mass determination for the peak at  $0.10 \text{ T}^{-1}$ . The result of the fit suggests a mass of 14.34 percent of the electron mass.

hall-effect sample in with the other samples (four samples could be measured at once) and use that to more accurately measure the angle with the field. Unfortunately, that was only realized in hind-sight. Therefore, it is impossible to know exactly the behavior of the Fermi surface for any of our samples, and only rough estimations can be suggested.

The figures in A.11 show the analysis of the peak height against temperature for two different peaks. Figures A.11a and A.11b show the determination of the carrier mass for the peak at  $0.08$  and  $0.10 \text{ T}^{-1}$  respectively. The maximum resistance of each peak has been normalized to the lowest temperature data and plotted against Temperature. It is possible to extract the effective mass of carriers by fitting this to [95],

$$R = \frac{ATm}{\sinh(ATm)} \quad (\text{A.15})$$

where  $T$  is the temperature,  $m$  is the effective mass, and  $A$  is a collection of constants that includes the cyclotron frequency. The constant  $A$  was forced to a particular value, and the

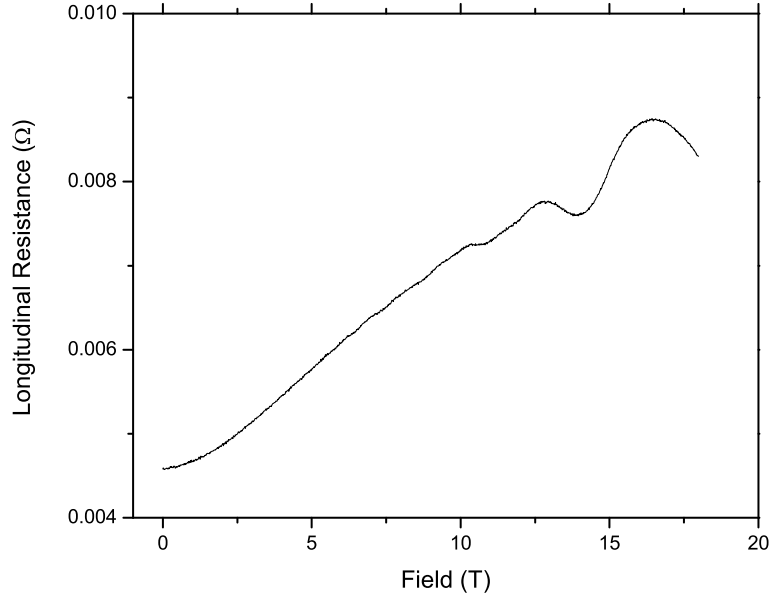


Figure A.12: *Raw longitudinal resistance of a bulk sample of  $Sb_2Te_3$ .* The Shubnikov-de Haas oscillations are strong enough to be easily visible even in the raw data. These appear at high fields, starting at around 10 T.

program allowed to fit the data to the curve using  $m$  as a parameter. For the first set of peaks, the effective mass was determined to be 7.85 percent of the electron mass, while the second set suggests an effective mass of 14.34 percent. These widely different values could be a result of errors in the background subtraction.

The bulk sample data was equally exciting. The only sample that suggested any obvious SdH oscillations was the  $Sb_2Te_3$  data, and we will focus on the analysis of that here. Interestingly, as shown in Figure A.12, the SdH Oscillations were large enough to appear obviously in the raw data. This was a particularly exciting result, and exactly what we were hoping to see when performing the measurements. It is also worth mentioning that the longitudinal resistance is rounded at the bottom, suggesting that this sample is also metallic in characteristic.

The high temperature data, taken at 45K in this case, provided a much better method of subtracting off the background. Shown in Figure A.13 is the longitudinal resistivity taken

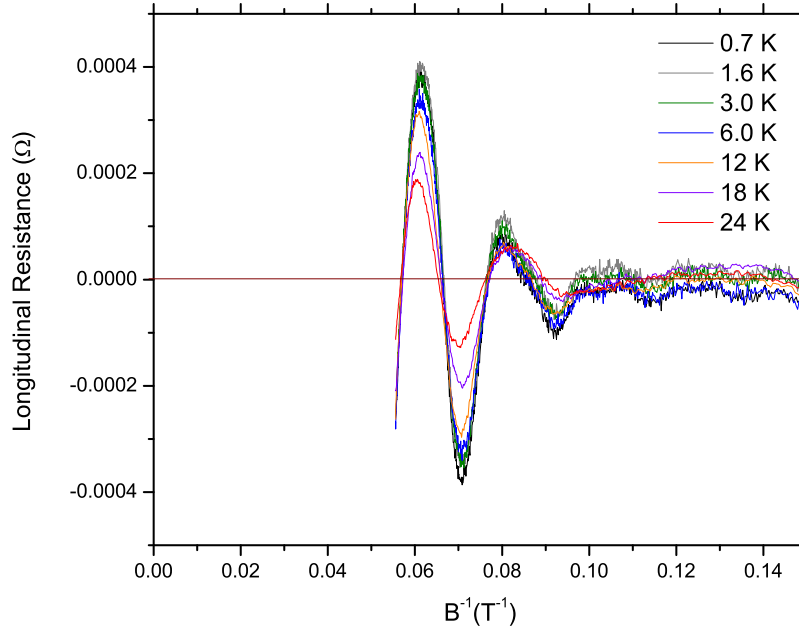


Figure A.13: *Temperature dependence of longitudinal resistance of a bulk  $Sb_2Te_3$  sample.* The background has been removed from these curves using a measurement of the same sample at 45K, where the oscillations had been completely killed by thermal effects.

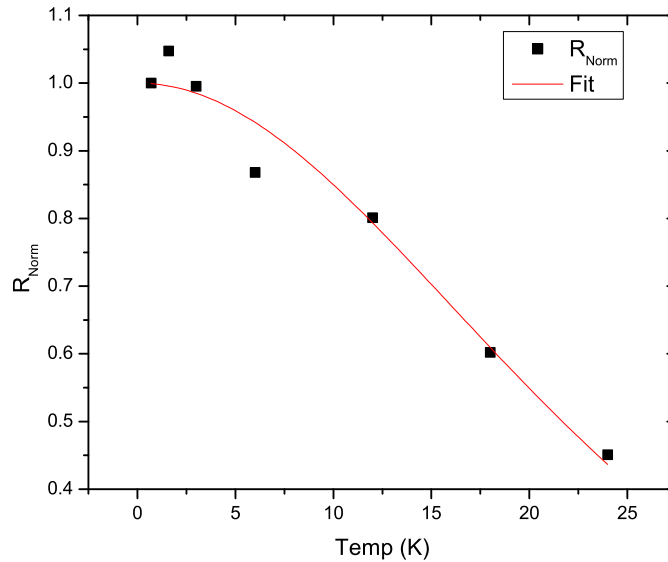


Figure A.14: *Determination of the effective mass of carriers in a bulk  $Sb_2Te_3$  sample.* The fit suggests a effective carrier mass of 11.2 percent of the electron mass.

a different temperatures with the background subtracted off. There is clearly some residual signal that the background was not able to remove, but the oscillations nicely wiggle around zero giving us more confidence in the peak heights of this data.

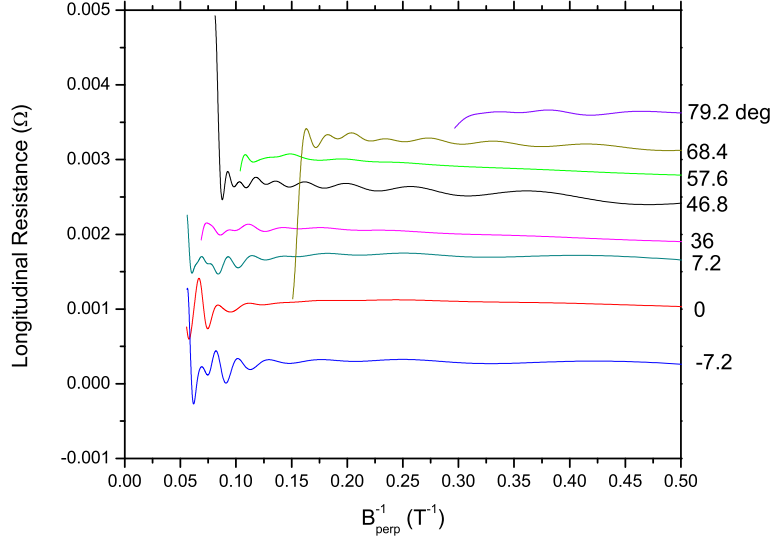


Figure A.15: *Angular dependence of resistance in a bulk  $Sb_2Te_3$  sample.* The movement of the oscillations in these curves is too great to properly pin down the behavior of the Fermi surface.

As before, we examined the peak height against temperature and fit to the function A.15. Again, the value for A was set by the constants and fixed in the fitting function. The mass of the carriers in this case, shown in Figure A.14 was found to be 11.2 percent of the electron mass. Similarly, we analyzed the angular dependence of the data, as shown in Figure A.15. Unfortunately, this demonstrated that the behavior of the oscillations as a function of angle were far too complicated to be able to analyze rigorously. Smaller angular step sizes would have been a big help in tracking the movement of individual peaks, and may have allowed us to determine if multiple different sets of oscillations were present. We can only say that the Fermi surface was not simple in this sample, was likely three-dimensional, and may have possessed multiple extremal areas, which produced several sets of overlapping, and interfering, SdH oscillations.

## Conclusions

These samples demonstrate very interesting properties that are well worth further study. This is just a sampling of the rich physics possible with this class of materials, and hopefully further work will be able to be done. We were only able to scratch the surface of this project in the short time given to us to pursue it, and it is too bad that the studies were not able to be continued due to lack of funding.

There are a number of places where the studies could be substantially improved. First, as mentioned in the last section, a reference sample in the shape of a simple hall bar would be very helpful for accurately measuring the relative angle of the field with respect to the sample. That one change alone would have provided significantly improved accuracy that turns out is necessary to properly pin down the behavior of the Fermi surface. Similarly, a finer angular step size would make a big difference in understanding the changes in the SdH oscillations during the sweep.

One of the big problems with these materials is that the conduction is expected to happen in a two-dimensional plane on the surface. While it is thought that the conducting surface is robust, it turns out that this is not entirely the case. If the surface is not a pristine sheet, free of lattice defects and other inclusions, the conducting surface is hard to observe - if it forms at all. This means that the sample must be properly cleaved before leads are mounted, and preferably done in a clean environment, surrounded by a non-volatile gas atmosphere - for example, Nitrogen, or Argon. This is a particularly tricky environment that would have required major changes to our measurement methods. The sample would have to be cleaved, leads mounted, and immediately inserted into the dewar entirely *in-situ*.

Further work on these materials would require these basic changes in the experimental

procedure. That would enable a more thorough investigation of the material properties, particularly of the insulating samples. With any luck, one of those samples would display the characteristics of a two-dimensional conducting surface despite being a bulk insulator. This is the characteristic transport signature of a topological insulator, which is a highly sought-after material in condensed matter physics today.

Once such a material had been found, further experiments could be performed. Other materials could be patterned on the surface, such as superconductors, and ferromagnets. This would enable the search for the Majorana fermion in these materials. Other experiments could involve growing such a material into a Josephson junction, or growing them as part of an insulating tunnel barrier for performing tunneling spectroscopy experiments.

This concludes the sum total of the work done on these samples. While the data was quite interesting, it remains only preliminary, and as such they were not in a state to be published. They are listed here in the hopes that someone else may be interested in pursuing further work on these materials, providing them a solid basis from which to start. If not, the data is at least here in case it ever becomes useful in any way, shape, or form.

# BIBLIOGRAPHY

# BIBLIOGRAPHY

- [1] H. Kamerling Onnes, Leiden Comm. **120b**, **122b**, **124c** (1911)
- [2] H. Fröhlich, Proc. Roy. Soc. (London) **A215**, 291 (1952)
- [3] L.N. Cooper, Phys. Rev. **104**, 1189 (1956)
- [4] J. Bardeen, L.N. Cooper, J.R. Schrieffer, Phys. Rev. **108** 1175 (1957)
- [5] J.G. Bednorz, K.A. Muller, Z. Phys. B **64**, 189 (1986)
- [6] D.J. Scalapino, Phys. Rep. 250, 329 (1995)
- [7] C.C. Tsuei, J.R. Kirtley, Phys. Rev. Lett. 85, 182 (2000)
- [8] I. Eremin, D. Manske, S.G. Ovchinnikov, J.F. Annett, Ann.Phys-Berlin **13**, 149 (2004)
- [9] V.L. Berezinskii, JETP Lett. **20**, 287 (1975)
- [10] F.S. Bergeret, A.F. Volkov, K.B. Efetov, Phys. Rev. Lett. **86**, 4096 (2001)
- [11] A.F. Volkov, F.S. Bergeret, K.B. Efetov, Phys. Rev. Lett. **90**, 117006 (2003)
- [12] F.S. Bergeret, A.F. Volkov, K.B. Efetov, Rev. Mod. Phys. **77** 1321 (2005)
- [13] M. Giroud, H. Courtois, K. Hasselbach, D. Mailly, B. Pannetier, Phys. Rev. B **58**, R11872 (1998)
- [14] M. Lawrence and N. Giordano, J.Phys: Cond. Matt. **11**, 1089 (1999)
- [15] V. Petrashov, I. Sosnin, I. Cox, A. Parsons, C. Troadec, Phys. Rev. Lett. **83**, 3281 (1999)
- [16] R.S. Keizer, S.T.B. Goennenwein<sup>1</sup>, T.M. Klapwijk, G. Miao, G. Xiao, A. Gupta, Nature (London) **439**, 825 (2006)

- [17] D. Sprungmann, K. Westerholt, H. Zabel, M. Weides, H. Kohlstedt, Phys. Rev. B **82**, 060505(R) (2010)
- [18] J.W.A. Robinson, J.D.S. Witt, M.G. Blamire, Science **329** 59 (2010)
- [19] M.S. Anwar, F. Czeschka, M. Hesselberth, M. Porcu, J. Aarts, Phys. Rev. B **82** 100501(R) (2010)
- [20] T.S. Khaire, M.A. Khasawneh, W.P. Pratt, Jr., N.O. Birge, Phys. Rev. Lett. **104**, 137002 (2010).
- [21] M. Houzet, A.I. Buzdin, Phys. Rev. B **76**, 060504(R) (2007)
- [22] D.S. Holmes, A.L. Ripple, M.A. Manheimer, IEEE Trans. Appl. Supercond. **23**, 1701610 (2013)
- [23] M.I. Khabipov , V.P. Koshelets , K.K. Likharev , O.A. Mukhanov , V.K. Semen , L.I. Serpuchenko, A.N. Vystavkin, IEEE Trans. Magn. **25**, 861 (1988)
- [24] V.P. Koshelets, S.A. Kovtonyuk, I.L. Serpuchenko, L.V. Filippenko, A.V. Shchukin, IEEE Trans. Magn. **27**, 3141 (1991)
- [25] Q.P. Herr, A.Y. Herr, O.T. Oberg, A.G. Ioannidis, J. Appl. Phys., **109**, 103903 (2011)
- [26] S.A.Wolf, Daryl Treger, Almadena Chtchelkanova, MRS Bulletin **31**, 400 (2006)
- [27] Albert Fert, Jean-Marie George, Henri Jaffrs, Richard Mattana, Pierre Seneor, Europhysics News **34**, 227 (2003)
- [28] Stuart A. Wolf, Jiwei Lu, Mircea R. Stan, Eugene Chen, Daryl M. Treger, Proc. IEEE **98**, 2155 (2010)
- [29] N.D. Rizzo, D. Houssameddine, J. Janesky, R. Whig, F.B. Mancoff, M.L. Schneider, M. DeHerrera, J.J. Sun, K. Nagel, S. Deshpande, H.-J. Chia, S.M. Alam, T. Andre, S. Aggarwal, J.M. Slaughter, IEEE Trans. Magn. **49** 4441, (2013)
- [30] A. Y. Herr, Q. P. Herr, US Patent 8 270 209 B2, Sept. 18 2012

- [31] B. Baek, W. H. Rippard, S. P. Benz, S. E. Russek, P. D. Dresselhaus, arXiv:1310.2201
- [32] Nicola A. Spaldin, *Magnetic Materials, Fundamentals and Applications* (Cambridge University Press, Cambridge, 2011)
- [33] David Jiles, *Introduction to Magnetism and Magnetic Materials* (Taylor & Francis, Boca Raton, 1998)
- [34] Robert C. O'Handley, *Modern Magnetic Materials, Principles and Applications* (John Wiley & Sons, Inc., New York, 2000)
- [35] B.D. Cullity, *Introduction to Magnetic Materials* (University of Notre Dame, 1972)
- [36] E. C. Stoner, F.R.S. and E. P. Wohlfarth, Phil. Trans. R. Soc. Lond. Ser. A: Math. Phys. Sci. **240** 599, (1947)
- [37] L.D. Landau, E.M. Lifshitz, *Electrodynamics of Continuous Media, 2nd Ed.* (Elsevier, Amsterdam, 1984)
- [38] I. Giaever, Phys. Rev. Lett. **5** 147 (1960)
- [39] Michael Tinkham, *Introduction to Superconductivity, Second Edition* (Dover Publications, Inc., New York, 1996)
- [40] B. D. Josephson, Phys. Lett. **1**, 251 (1962)
- [41] B. D. Josephson, Adv. Phys. *14*, 419 (1965)
- [42] Laurent-Patrick Lévy, *Magnetism and Superconductivity* (Springer, Berlin, 1997)
- [43] T.S. Khaire, Ph.D. thesis, Michigan State University, United States, 2010.
- [44] A.F. Andreev, Sov. Phys. JETP **19**, 1228 (1964)
- [45] R.D. Parks, *Superconductivity, Vol. 2* (Marcel Dekker, Inc., New York 1969)
- [46] E.A. Demler, G.B. Arnold, M.R. Beasley, Phys. Rev. B **55**, 15174 (1997)

- [47] A.I. Buzdin, L. N. Bulaevskii, S. V. Panyukov, JETP Lett **35** 178 (1982)
- [48] A.I. Buzdin, M. Yu Kupriyanov JETP Lett **53** 321 (1991)
- [49] Z. Radovi?, M. Ledvij, L. Dobrosavljevi?-Gruji?, A.I. Buzdin, J.R. Clem Phys. Rev. B **44** 759 (1991)
- [50] V. Ryazanov, V. Oboznov, A. Rusanov, A. Veretennikov, A Golubov, J. Aarts, Phys. Rev. Lett. **86**, 2427 (2001)
- [51] T. Kontos, M. Aprili, J. Lesueur\*, F. Gent, B. Stephanidis, R. Boursier, Phys. Rev. Lett. **89**, 137007 (2002)
- [52] Y. Blum, A. Tsukernik, M. Karpovski, A. Palevski, Phys. Rev. L **89**, 187004 (2002)
- [53] H. Sellier, C. Baraduc, F. Lefloch, R. Calemczuk, Phys. Rev. B **68**, 054531 (2003)
- [54] J. Robinson, S. Piano, G. Burnell, C. Bell, M. Blamire, Phys. Rev. Lett. **97**, 177003 (2006)
- [55] J. Robinson, S. Piano, G. Burnell, C. Bell, M. Blamire, Phys. Rev. B **76**, 094522 (2007)
- [56] Matthias Eschrig, "Spin-polarized supercurrents for spintronics." Physics Today **64** 43 (2011)
- [57] R. C. Jaklevic, J. Lambe, A. H. Silver, J. E. Mercereau, Phys. Rev. Lett. **12** 159 (1964)
- [58] Terry P. Orlando, Kevin A. Delin, *Foundations of Superconductivity* (Addison-Wesley, Reading, 1990)
- [59] Dror Sarid, *Scanning Force Microscopy* (Oxford University Press, 1994)
- [60] Private communication with Bill Martinez.
- [61] S. L. Flegler, J. W. Hickman, K. L. Klomparens, *Scanning and Transmission Electron Microscopy: An Introduction* (W. H. Freeman & Company, New York, 1993)

- [62] Y. Wang, Ph.D. thesis, Michigan State University, United States, 2013.
- [63] D. Edmunds, W.P. Pratt, Jr., J. Rowlands, *Rev. Sci. Instrumen.* **51**, 1516 (1980)
- [64] T. Khaire, W.P. Pratt Jr., N.O. Birge, *Phys. Rev. B* **79** 094523 (2009)
- [65] M. Khasawneh, W.P. Pratt Jr., N.O. Birge, *Phys. Rev. B* **80**, 020506(R) (2009)
- [66] S.S.P. Parkin, N. More, and K.P Roche, *Phys. Rev. Lett.* **64**, 2304 (1990)
- [67] C. Klose, T.S. Khaire, Y. Wang, W.P. Pratt, Jr., N.O. Birge, B.J. McMorran, T.P. Ginley, J.A. Borchers, B.J. Kirby, B.B. Maranville, J. Unguris, *Phys. Rev. Lett.* **108**, 127002 (2012)
- [68] G.H.O. Daalderop, P.J. Kelly, F.J.A. den Broeder, *Phys. Rev. Lett.* **68**, 682 (1992)
- [69] V. Ambegaokar, B.I. Halperin, *Phys. Rev. Lett.* **22**, 1364 (1969)
- [70] S. Mangin, D. Ravelosona, J.A. Katine, M.J. Carey, B.D. Terris, Eric. E. Fullerton, *Nat. Mater.* **5** 210 (2006)
- [71] W. Chen, J.-M.L. Beaujour, G. de Loubens, A.D. Kent, J.Z. Sun, *Appl. Phys. Lett.* **92** 012507 (2008)
- [72] W.H. Rippard, A.M. Deac, M.R. Pufall, J.M. Shaw, M.W. Keller, S.E. Russek, G.E.W. Bauer, C. Serpico, *Phys. Rev. B* **81** 014426 (2010)
- [73] M.A. Khasawneh, T.S. Khaire, C. Klose, W.P. Pratt, Jr., and N.O. Birge, *Supercond. Sci. Technol.* **24**, 024005 (2011)
- [74] J.W.A. Robinson, S. Piano, G. Burnell, C. Bell, and M.G. Blamire, *Phys. Rev. Lett.* **97**, 177003 (2006)
- [75] E.C. Gingrich, P. Quarterman, Y. Wang, R. Loloee, W.P. Pratt, Jr., N.O. Birge, *Phys. Rev. B* **86**, 224506 (2012)
- [76] J.J. Hauser, H.C. Theuerer, N.R. Werthamer, *Phys. Rev.* **136**, A637 (1964)

- [77] H. Kurt, R. Loloee, K. Eid, W.P. Pratt, Jr., J. Bass, Appl. Phys. Lett. **81**, 4787 (2002)
- [78] Richard M. Bozorth, *Ferromagnetism* (D. Van Nostrand Company, Toronto, 1951)
- [79] Makram Abd El Qader, R. K. Singh, Sarah N. Galvin, L. Yu, J. M. Rowell, and N. Newman, App. Phys. Lett. **104**, 022602 (2014)
- [80] T. Valet, A. Fert Phys. Rev. B **48**, 7099 (1993)
- [81] B.M. Niedzielski, S.G. Diesch, E.C. Gingrich, Yixing Wang, R. Loloee, W.P. Pratt, Jr., Norman O. Birge, To Appear in IEEE Trans. Appl. Supercon.
- [82] H.Z. Arham, Trupti S. Khaire, R. Loloee, W.P. Pratt, Jr., Norman O. Birge, Phys. Rev. B **80** 174515 (2009)
- [83] K.M. Boden, W.P. Pratt, Jr., Norman O. Birge, Phys. Rev. B **84**, 020510(R) (2011)
- [84] J.A. Osborne, Phys. Rev. **67**, 351 (1945)
- [85] J.M. Slaughter, Annu. Rev. Mater. Res. **39**, 277 (2009)
- [86] B.N. Engel, J. Åkerman, B. Butcher, R.W. Dave, M. DeHerrera, M. Durlam, G. Grynkewich, J. Janesky, S.V. Pietambaram, N.D. Rizzo, J.M. Slaughter, K. Smith, J.J. Sun, S. Tehrani, IEEE Trans. Magn. **41**, 132 (2005)
- [87] H. le Sueur, P. Joyez, H. Pothier, C. Urbina, D. Esteve, Phys. Rev. Lett. **100** 197002 (2008)
- [88] X.L. Qi, T.L. Hughes, S.C. Zhang, Phys. Rev. B **78**, 195424 (2008)
- [89] T. Yokoyama, T. Tanaka, N. Nagaosa, Phys. Rev. B **81**, 121401(R) (2010)
- [90] J. Gao, W.-Q. Chen, X.-Y. Feng, X.C. Xie, F.-C. Zhang, arXiv:0909.0378
- [91] L. Fu, C.L. Kane, Phys. Rev. Lett. **102**, 216403 (2009)

- [92] A.R. Akhmerov, J. Nilsson, C.W.J. Beenakker, Phys. Rev. Lett. **102**, 216404 (2009)
- [93] Supriyo Datta, *Electronic Transport in Mesoscopic Systems* (Cambridge University Press, Cambridge, 1995)
- [94] K. von Klitzing, G. Dorda, M. Pepper, Phys. Rev. Lett. **45** 494 (1980)
- [95] D. Shoenberg, *Magnetic Oscillations in Metals* (Cambridge University Press, Cambridge, 1984)
- [96] Toru Hirahara, Yusuke Sakamoto, Yasuo Takeichi, Hidetoshi Miyazaki, Shin-ichi Kimura, Iwao Matsuda, Akito Kakizaki, Shuji Hasegawa, Phys. Rev. B **82**, 155309 (2010)
- [97] J. Chen, H.J. Qin, F. Yang, J. Liu, T. Guan, F.M. Qu, G.H. Zhang, J.R. Shi, X.C. Xie, C.L. Yang, K.H. Wu, Y.Q. Li, L. Lu, Phys. Rev. Lett **105**, 176602 (2010)
- [98] H. Suzuura, T. Ando, Phys. Rev. Lett. **89**, 266603 (2002)
- [99] E. McCann, K. Kechedzhi, V.I. Fal'ko, H. Suzuura, T. Ando, B.L. Altshuler, Phys. Rev. Lett. **97**, 146805 (2006)
- [100] G. Tkachov, E.M. Hankiewicz, Phys. Rev. B **84**, 035444 (2011)
- [101] Y. Takagaki, A. Giussani, J. Tominaga, U. Jahn, R. Calarco, J. Phys.: Condens. Matter **25** 345801 (2013)